REMOVAL OF SELECTED IONIC AND HALOGENATED ORGANIC POLLUTANTS FROM WATER BY ZEOLITIC ADSORBENTS: COMPUTATIONAL AND EXPERIMENTAL STUDY

Fred Wanyonyi Sifuna

A Thesis Submitted in Partial Fulfillment of the Requirements for the Award of Doctor of Philosophy in Chemistry Degree of Masinde Muliro University of Science and Technology.

February, 2024

DECLARATION

This thesis is my original research work prepared with no other than the indicated sources and support and has not been presented elsewhere for a degree or any other award.

Signature……Date….....

Fred Wanyonyi Sifuna

REG NO: SCH/H/01-55929/2017

CERTIFICATION

The undersigned certify that they have read and hereby recommend for acceptance of Masinde Muliro University of Science and Technology a thesis entitled **"Removal of Selected Ionic and Halogenated Organic Pollutants from Water by Zeolitic Adsorbents: Computational and Experimental Study".**

Signature……Date….....

Prof. Francis Orata Omoto

Department of Pure and Applied Chemistry

Masinde Muliro University of Science and Technology

Signature……Date….....

Dr. Gershom Mutua

Department of Pure and Applied Chemistry

Masinde Muliro University of Science and Technology

Signature……Date….....

Dr. Anthony Pembere

Department of Physical Sciences

Jaramogi Oginga Odinga University of Science Technology

COPYRIGHT

DEDICATION

This thesis is dedicated to my wife madam Sylvia and children Wendy Nasimiyu, Ezrah Wafula, and Ethan Simiyu, who have shown me love, encouragement, and strength in order for me to achieve my goal. This is also a dedication to God for his blessings throughout my life.

ACKNOWLEDGEMENTS

I would like to express my heartfelt gratitude from so many wonderful people who helped me in my educational pursuit to make this thesis possible. I wish to express my deepest gratitude to my supervisors, Prof. Francis Orata, Dr. Anthony Pembere and Dr. Gershom Mutua for their patience, suggestions, encouragement, and priceless guidance since the conception, execution and completion of the project. Their immense knowledge, constructive critiques and superb guidance have mentored me into an independent scholar. Special appreciation goes to Prof. Ramasami, Dr. Louis for their expertise in molecular simulation. Also, thank Dr. Pembere, the Principal Investigator for the Centre of High-Performance computing, South Africa for running the input files using Material Studio and Gaussian Software. I express my sincere appreciation to all staff and administration office from the Department of Pure and Applied Chemistry, Masinde Muliro University of Science and Technology for the assistance accorded to me.

To Sylvia, my wife, for her love, care, concern, patience, under-standing, moral support and encouragement. Last but not least, i want to thank my parents and the rest of my family for being the best anyone could wish to have. To everyone whose names are not mentioned but have significant and special roles in my life, for your prayers and for helping make it through. The support of my parents Mr. and Mrs. Sifuna and the entire family contributed in no small measure to the completion of this work. Their patience, prayers and continued encouragement in the face of several adversities was second to none. And most of all, to our Almighty God, the author and finisher of my faith; this research would not have been successful without the strength, grace and ability that come from Him. To God be the glory. I also place on record, my sense of gratitude to one and all, who directly or indirectly, have lent me their hand in this venture

ABSTRACT

The presence of contaminants such as toxic anions, heavy metals, halogenated pesticides and pharmaceuticals in various water compartments has caused environmental concern due to the toxicological effects. Conventional water treatment systems are unable to completely remove a large class of these pollutants. It therefore, necessitates the development of more cost effective and environmentally safe methods to remove these pollutants from water. This study explores the use of zeolites as adsorbents for the removal of selected ionic (heavy metals and anions) and organic (halogenated pharmaceuticals and pesticides) pollutants from water. This study was done through computational simulations and batch experiments. In the assessment of zeolite frameworks for the sorption of Pb^{2+} and Cd^{2+}, 242 zeolites were investigated by employing molecular simulations and machine learning technique. The results showed that only the zeolites with high pore diameter exhibited appreciable loading of the two cations (CLO, FAU, PAU TSC and MWF). It was also observed that the adsorption energy of the cations on the zeolite framework is directly related to the loading capacity, whereby a trend of $Pb^{2+} > Cd^{2+}$ is observed. The sorption of Pb^{2+} and Cd^{2+} in all the zeolites gave a negative average total energy, showing that the sorption is exothermic. From the machine learning results, pore size and total energy are the most important factor in adsorption of the metal ions onto the zeolites. Therefore, CLO and MWF are recommended for adsorption of Pb^{2+} and Cd^{2+}, respectively. Furthermore, the capacity of Heulandite **(**HEU**)** zeolite to remove Pb^{2+} and Cd^{2+} ions from water was investigated using batch experiments and from the results the percentage removal of Pb^{2+} and Cd^{2+} ions were 98 and 77 %, respectively. The adsorption of Pb^{2+} and Cd^{2+} onto the HEU zeolite follows the Freundlich isotherm model. For the anions (NO_3^- and PO_4^{3-}), a screening process involving based on the pore-limiting diameter was done, followed by simulations to identify high-performing zeolites for their removal. CLO, LTN, MWF and TSC zeolites are the best performing. From machine learning the important descriptors that has influence on the removal of the two anions in water were overall cavity diameter, mass and accessible pore volume. From the batch experiments, it was observed that HEU zeolite was able to removal of 59 and 51% of 4 ppm of NO_3^- and PO_4^{3-}, respectively after 120 minutes. The adsorption of anions followed the *pseudo*-first order (PFO) kinetics indicating a physisorption-mediated rate-determining step. The adsorption of NO_3^- and PO_4^{3-} onto the HEU zeolite follows the Freundlich isotherm model and the adsorption process was multi-mechanistic spontaneous and exothermic. From the computational results, CLO zeolite was the most suitable for the adsorption of diuron, imidacloprid and chlorpyrifos. From the batch experiments, the adsorption of imidacloprid and chlorpyrifos adsorption were best described by the Freundlich isotherm. The percent removal of imidacloprid and chlorpyrifos by HEU zeolite were 50 and 48 %, respectively. The adsorption kinetics followed both *pseudo*-first order and second order kinetics indicating both physisorption and chemisorption. For the adsorption of selected pharmaceutical products (diclofenac, ciprofloxacin and chloramphenicol, it was observed that CLO was the best zeolite adsorbent. On the HEU zeolite, the percent removal of diclofenac, ciprofloxacin and chloramphenicol were 82, 69 and 51 %, respectively. The adsorption of the pharmaceuticals was best described by Freundlich and Sips isotherm models. The kinetics followed *pseudo*-first order for diclofenac and ciprofloxacin, while *pseudo*-second order for chloramphenicol predicting physisorption and chemisorption, respectively. HEU zeolite removed 99, 87 and 70 %, of Ciprofloxacin, imidacloprid and chlorpyrifos, respectively from environmental water samples. The study has

established that HEU is a good adsorbent for the removal of pollutants from water. This study forms the background for the innovative use of zeolites adsorbents in development of water purifier gadgets and in wastewater treatment technology.

TABLE OF CONTENTS

LIST OF TABLES

LIST OF FIGURES

LIST OF APPENDICES

LIST OF ABBREVIATIONS AND ACRONYMS

AAS	Atomic Absorption Spectroscopy
AC	Activated Carbon
CD	Cyclodextrins
CLO	Cloverite
COSMO	Conductor-like screening model
CVD	Chemical Vapour Deposition
DFT	Density Functional Theory
DO	Dissolved Oxygen
EDX	Energy Dispersive X-ray Spectroscopy
EDX	Energy dispersive X-ray
EPA	Environmental Protection Agency
EU	European Union
FAU	Faujasite
FTIR	Fourier Transform Infrared Spectroscopy
GCMC	Grand Canonical Monte Carlo
HEU	Heulandite
HPLC	High Performance liquid chromatography
HR-TEM	High Resolution Transmission Electron Microscopy
IZA	International Zeolite Association
LOD	Limit of Detection
LOQ	Limit of Quantification
NZ	Natural Zeolite
POPs	Persistent Organic Pollutants

PXRD	Powder X-Ray Diffraction
SCRF	Self Consistent Reaction Field
SEM	Scanning Electron Microscopy
SSE	Sum of Square Error
UV-Vis	UltraViolet -Visible
V	Volume
W H O	World Health Organizations
WWTPs	Wastewater Treatment Plants
XRD	X-Ray Diffraction

LIST OF UNITS

cm	Centimeter
g	Grams
mg	Miligram
mg/L	Milligrams per litre
mL	Millitre
µg/g	Microgram per gram
µg/L	Microlitre per litre
ppb	parts per billion
ng	Nanogram
nm	Nanometre
^{o}C	Degree Celsius
Kg	Kilogram
µl	Microlitre
M	Molar
χ^2	Chi-square

CHAPTER ONE

INTRODUCTION

1.1 Background Information

Water is crucial and essential for all forms of life because it is a vital universal solvent (Rathi & Kumar, 2021) and used for metabolic processes within the living organisms (Shultana & Khan, 2022). Over the last few years, water related issues such as chemical pollution are of major global concern (Lee *et al.,* 2023). Pollutants of surface water include; dissolved solids, minerals, heavy metals, toxic anions, organic and inorganic substances which adversely affects flora and fauna (Borah *et al.,* 2020; Lee *et al.,* 2023). Wastewater pollutants usually consist of an array of cationic and anionic chemicals, oils and organics, mostly posing deleterious effects on the ecosystem.

A major class of the organic pollutants are the halogenated pesticides and pharmaceutical products. Halogenated pesticides are widely used in farms, forests, parks, industrial sites, sport fields, and educational facilities for control of pests (George & Shukla, 2011; Ojha, 2020). For example, in Kenya, chlorpyrifos and diuron are among the pesticides used in sugarcane farming (Mirenga, 2018).

On the other hand, halogenated pharmaceutical products are used for the treatment of different ailments. Subsequently, pharmaceutical product residues have been found in water. This is attributed to dumping of expired pharmaceuticals in the environment, incomplete metabolization in human body and inefficient wastewater treatment plants (WWTPs) that cannot completely remove the pollutants (Tambosi *et al.,* 2010; Sharma *et al.,* 2023; Chopra *et al.,* 2020). These halogenated pollutants enter surface and ground water through runoffs and infiltration processes, as well as from wastewater treatment plants. A major concern of the halogenated pesticides and pharmaceuticals residues is their

persistent and potential to cause chronic abnormalities in organisms (Anju *et al.,* 2010; Letsoalo *et al.,* 2022).

Toxic anions present in water include; phosphates and nitrates. Phosphorus plays an important role as building block for cells, storage and processing of genetic information (Shrestha *et al.,* 2020). The major sources of phosphates and nitrates in water are high application of phosphorus and nitrogen-based fertilizers. Their presence in water results in eutrophication (Berkessa *et al.,* 2019)

Similarly, heavy metals are considered to be among the major pollutants in source and treated water due to their non-biodegradable nature and their bioaccumulation potential. For example, chromium has also been found to cause lung cancer (Steinmaus *et al.,* 2010). Heavy metal of interest in wastewater management include; Pb, Cr, Cd and Ni ions (Chai *et al.,* 2021; El Ouardi *et al.,* 2015; Shikuku *et al.,* 2017).

Removal of these contaminants requires convenient, simple, cost-effective and environmentally friendly technologies (Zhao *et al.,* 2010). To this end, a variety of techniques dealing with wastewater treatment have been developed in the past decades by the global scientific community to remove these pollutants from water bodies. Naturally occurring zeolites have shown promising results in the removal of pollutant from water systems due to their large surface areas (Cabrera-Lafaurie *et al.,* 2014; Rad & Anbia, 2021).

Zeolites are three-dimensional crystalline aluminosilicate materials with specific microporous structures of cavities and pore dimensions with physicochemical properties such as sorption, cation exchange, molecular sieving, catalysis and adsorption (De Araujo *et al.,* 2022; Foo & Hameed, 2011; Shikuku, *et al.,* 2015). Unlike their synthetic

counterparts, natural zeolites which commonly occur in volcanic active areas and are highly varied in chemical composition. Both synthetic and natural zeolites have been widely used separately as adsorbents and molecular sieves for pharmaceuticals remediation from wastewaters (Grela *et al.,* 2021). Computational studies, including molecular dynamics, quantum mechanics and Monte Carlo tools, have a key function in understanding and predicting the adsorption behavior of adsorbents development for pollutants removal (Jiménez *et al.,* 2021).

Computational simulations are becoming essential in understanding chemical reactions and processes. In particular, molecular simulations hold great significance when it comes to the adsorption processes. They have been utilized in understanding adsorbate-adsorbent interactions, energy changes and adsorption sites as well as predicting viability of chemical process before proceeding with the experimental reactions (Hira *et al.,* 2023; Jiménez *et al.,* 2021). This study explores the use of zeolites as adsorbents for the removal of selected ionic (heavy metals and anions) and halogenated organic (pharmaceuticals and pesticides) pollutants from water employing combined computational and experimental approach.

1.2 Statement of the Problem

The rate of technological advancement, growing industrialization, and extensive use of chemicals has resulted in the release of contaminants such as toxic anions (phosphates and nitrates), heavy metals (lead and cadmium), halogenated pesticides (diuron, chlorpyrifos and imidacloprid) and pharmaceuticals (diclofenac, ciprofloxacin and chloramphenicol) into various water sources. Pollution is one of the major problems facing both developing and developed economies with a wide range of environmental contaminants being reported. Toxicity testing has predominantly been assessed on anions, heavy metals ions,

pharmaceuticals, pesticides and their effects have been intensively studied. Solutions to these contaminants must be sought because it has been recognized as an issue of growing global concern. Several processes to remove have been reported which include oxidation technologies and precipitation for the case of heavy metals (Vardhan *et al.,* 2019). The conventional treatment plants systems are unable to completely remove a large class of pollutants especially persistent organic pollutants (POPs) and heavy metals that are present in WWTPs (Mahmood *et al.,* 2022).The chronic health effects associated with long term ingestion of mixtures of these pollutants necessitates the invention of more cost effective and environmentally safe methods of removing these pollutants from WWTPs and aquatic environment so as to reduce the risk they pose to humans and biota.

1.3 Objectives

1.3.1 General Objective

To study the efficiency of zeolitic adsorbents in the removal of selected ionic and halogenated organic pollutants from water

1.3.2 Specific Objectives

i. To evaluate the adsorption of Pb^{2+}, Cd^{2+}, NO_3^- and PO_4^{3-} onto experimentally available zeolite frameworks using computation simulations
ii. To simulate the adsorption of selected halogenated pharmaceuticals and pesticides onto experimentally available zeolite frameworks
iii. To determine the kinetics and mechanisms of adsorption of the selected pollutants onto the natural heulandite zeolite
iv. To evaluate the removal of selected pollutants from water samples.

1.4 Justification of the Study

Zeolites present varying characteristic depending on their sources and have high adsorption capacity, great cationic exchange capacity and stability. In this study, zeolites were applied to demonstrate the adsorption capacity on selected ions, and other halogenated organic pollutants, suggesting the potential of zeolites in providing a cost-effective solution to the challenging environmental management problems.

The molecular simulation showed great potential to predetermine the adsorption capacity of the adsorbent before proceeding with the actual process, which was costly and time-consuming to be realized from experimental interrogation. Moreover, the molecular dynamic simulation provides a platform where the adsorption phenomenon was studied microscopically within a sufficient time period, economical means and space. It has therefore become critically important to develop sustainable methods that can reduce the concentrations of these pollutants by removing them from polluted water. Therefore, this study aimed to develop sorbents that are effective, affordable and readily available to adsorb the ionic and halogenated organic pollutants from wastewater.

1.5 Significance of the Study

The potential of the various zeolites for remediation of the selected ionic and halogenated organic pollutants from water is established and would help in treatment of these chemicals in water systems. Therefore, the study will benefit the world by developing green, effective and economical technology aimed at remediating environmental matrices. This will create employment, mitigate environmental pollution and boost the economy. The findings of this study form a basis for development of environmental management implication policy which will involve treatment of contaminants like anions, heavy metals, pesticides and advice to manufacturers, hospitals staff and general public on the proper disposal.

Furthermore, the outcomes can be used to reorganize WWTPs to address unconventional contaminants found in wastewater and effluents. This research provides points of reference for both academics and industry involved in material development and water purification.

CHAPTER TWO

LITERATURE REVIEW

2.1 Introduction

Water pollution is one of the most critical global issues, which represents a risk to human and the environment (Lin *et al.,* 2022). The increasing industrialization and human activities have caused an increased levels of pollutants in water resources (Chowdhary *et al.,* 2020; Lee *et al*., 2023). Water is essential for the survival of life on earth; effective management, distribution, storage, recycling and purification of water is critical to ensure sustainable use of this resource. Water is necessary for many human activities such as agriculture, industrial processes, recreation and most importantly consumption. Some of the major pollutants found in water are; pharmaceuticals, pesticides, polyaromatic hydrocarbons, per-fluorinated compounds, heavy metals and anions (Chirikona *et al.,* 2015; Lisouza *et al.,* 2011; Okello *et al.,* 2017; Orata, 2020; Ouma *et al.,* 2018).

2.2 Water Pollution

2.2.1 Heavy Metal Pollution

Heavy metal pollution within various environmental segments is of great global concern (Elbehiry *et al.,* 2020; Ren *et al.,* 2019). This is because heavy metals are toxic, non-biodegradable, with a large dispersal capability, high rates of bioaccumulation in plants, fish, and human (Buaisha *et al.,* 2020; Orata, 2020). Therefore, it is crucial to remove heavy metals from water and other environmental matrices (Bolisetty *et al.,* 2019; Kumar *et al.,* 2019; Lin *et al.,* 2020; Tinkov *et al.,* 2018). Heavy metals become concentrated in soil, water or air and they are taken in by plants and ingested by humans or animals (Ali & Khan, 2019; Chepkorir, 2022).

The concentration of heavy metals in water is directly related to the degree of pollution in the environment. Streams, rivers, surface runoffs and through the discharge of sewage, industrial effluents and farms. Cadmium, chromium and lead ions are environment pollutants of great concern because their toxicity is a problem of increasing significance for evolutionary, ecological, nutritional and environmental reasons (Rahman *et al.,* 2019). It is important to note that water regulations were established to minimize human and environmental exposure to these hazardous chemicals. This includes limits on the types and concentration of heavy metals that may be present in the discharged water (Björklund *et al.,* 2018).

Due to that, safe limits or maximum contaminant levels have been defined for drinking water by different organizations. Table 2.1. show the standards and guidelines in drinking water recommendation by the National Environment Management Authority (NEMA), World Health Organization (WHO), Environmental Protection Agency (EPA) and the Council of European Union (EU) for cadmium, chromium and lead ions (Mohod *et al.,* 2013)

Table 2. 1: The maximum concentration for heavy metals in drinking water recommended by the WHO, EPA and EU

Metal	NEMA	WHO (mg/L)	EPA (mg/L)	EU (mg/L)
Cd	0.05	0.003	0.005	0.005
Cr	0.5	0.05	0.10	0.05
Pb	0.1	0.01	0.015	0.01

Table 2.2. lists the common sources of heavy metal pollutants found in water and their associated health risks. Even at low concentrations these metal ions may interfere with

normal biological processes hence becoming toxic and resulting in either heavy metal poisoning or genetic disorders (Rahman *et al.,* 2019).

Table 2. 2: Common sources of heavy metals and the associated health risks

Metal	Sources	Health risks	Reference
Cadmium	Electroplating, smelting, alloy manufacturing, refining processes, pigments, plastics, phosphate industry and battery mining.	loss of appetite, lung fibrosis, cancer, kidney damage, bronchitis, fibrosis, lumbago and dyspnea	(Ebelegi *et al.,* 2019; Igberase *et al.,* 2015; L. Wang *et al.,* 2022; Wekesa *et al.,* 2015)
Chromium	Chrome plating, electroplating, leather tanning, photography, metal cleaning, oxidative dying, fertilizes and steel production.	Oxidative stress, DNA damage, skin cancer	(Agrafioti *et al.,* 2014; Ouma *et al.,* 2018; Shraim, 2017)
Lead	Lead-acid batteries, bullets, solder, pewter and alloys and fertilizers.	Kidney damage, memory disorders, mental disorders.	(Cheng & Hu, 2010; Shraim, 2017)

2.2.1.1 Cadmium

It's divalent ion that possess a relatively higher degree of mobility in the environment in comparison to other heavy metallic species (Haider *et al.,* 2021). These ions are readily bioavailable and bioaccumulate in many organisms, particularly microorganisms and molluscs where the bio-concentration factors are in the order of thousands. In aquatic systems, cadmium is readily absorbed by organisms directly from the water in its free ionic form Cd^{2+}. This element is not essential for plant or animal life (Maheshwari *et al.,* 2015).

Studies have shown that cadmium is very toxic to humans even at low concentration (Rahimzadeh *et al.,* 2017). It causes damage to the human body cells through the generation of reactive oxygen species which interrupts the synthesis of nucleic acids and proteins (Ebelegi *et al.,* 2019). High concentrations cause gastrointestinal tract erosion, pulmonary, renal injury and obstructive lung disease (Ebelegi *et al.,* 2019). The chronic exposure to Cd produces a wide variety of acute and chronic effects in humans. It accumulates in the human body, especially in the kidneys, resulting in renal tubular damage, which is a critical health effect (Idrees *et al.,* 2018). Other effects of Cd exposure are disturbances in calcium metabolism, hypercalciuria and the formation of kidney stones. High exposure to Cd can lead to lung, pancreas and prostate cancer (Othmani *et al.,* 2022).

In Kenya, the level of cadmium in water, soil and food has been reported in different areas. For example; in Nairobi County, cadmium level in Nairobi River ranged from 0.04 to 0.06 mg/L which was beyond the permissible limit of 0.03 mg/L according to WHO levels. In river Nzoia and lower parts of river Kuywa the levels of cadmium ranged from 0.003 to 0.02 mg/L which was below the permissible limit and this was attributed to agrochemicals (Wasike *et al.,* 2019). In Thika, cadmium contamination levels in the food samples ranged between 0.001 and 0.010 mg/kg (Mwove *et al.,* 2023). In Nairobi waste water the reported levels ranged between 0.12 and 52.4 µg/L (Kinuthia et al., 2020; Munene, 2019). In Embu County, Sayo *et al.,* (2020) reported Cd concentrations of 0.015 to 0.353 mg/L in the sewage effluent which were above the WHO permissible levels in wastewater for irrigation (Sayo *et al.*, 2020). In the Winam Gulf in Kisumu City reported comparatively high mean values of Cd^{2+} in lake water. Elsewhere, higher level of Cd has been reported. For example; in New Zealand waste water irrigated soil, the levels were 0.45 mg/kg (Abraham, 2020).

In India cadmium levels of 1.5 µg/L were reported in water (Iyer *et al.,* 2020), which was slightly above the WHO recommended levels of 0.1 µg/L.

Vegetable plants watered with wastewater from Nyatsime and Mukuvisi rivers in Zimbabwe had the highest cadmium tissue concentration of 1.47 and 1.43 mg g^{-1}, respectively (Tibugari *et al.,* 2020).

2.2.1.2 Chromium

Chromium occurs in a number of oxidation states, but Cr(III) and Cr(IV) are of main biological relevance. It has several applications such as; metal plating, leather processing, surface treatments, silk printing, inks, paints, in the manufacture of green varnishes, ceramic industry, as fuel, a propellant additive and in refractories. Sources of chromium ions in water include effluents from industries, emission from vehicles and incinerators. Chromium is necessary for the metabolism of insulin. It is also essential for animals, whereas it is not known whether it is an essential nutrient for plants, but all plants contain the element (Sharma *et al.,* 2020).

Cr(VI) ions are greatly harmful to humans. Chromium can be ingested, inhaled, or absorbed via the skin by any organism. When ingested the ions accumulate in bones, blood and liver. Studies have shown that chromium affects human health in many ways leading to kidney and liver damage, skin rashes, respiratory defects, weakened immune systems, dysfunction of the digestive and gastrointestinal systems, stomach ulcers, stomach cancer, alteration of genetic materials among others (Mangwandi *et al.,* 2020). Cr(VI) has been shown to be mutagenic, carcinogenic and a strong oxidant (Yuan *et al.,* 2010).

Chromium occurrence and levels in Kenya have been reported in different environmental matrices. In waste water treatment plants , levels of 87.6 and 3.08 µg/L have been reported

in Embu and Nairobi County, respectively (Sayo *et al.,* 2020). In coastal city of Mombasa, levels ranging between 0.015 and 0.026 μg/L in seawater along the coastline (Mwatsahu *et al.,* 2020).

In groundwater, levels ranging between 0.01 and 0.19 mg/L have been reported in South India (Kubier, Hamer, Pichler, & Management, 2020) and 14.60 mg/L in wastewater in Nigeria (Obasi & Akudinobi, 2020).

2.2.1.3 Lead

Lead is ranked position two in the top twenty list of most toxic and hazardous substances according to the Agency for Toxic Substances and Disease Registry. It is harmful to organisms even at low concentrations. Lead and its compounds are released into water, soil and air by different industrial activities such as manufacturing industries of matches, explosives, pigments, photographic materials, printing, storage batteries, television tube, and paint industries (Kumar *et al.,* 2020). It is also released into the environment by automobile emissions, sewage discharge, combustion of fossil fuels, urban and agricultural runoff, forest fires and volcanic eruptions (Chowdhury *et al.,* 2022). The widespread use of lead has caused significant environmental contamination and health problems in various parts of the world (Ara & Usmani, 2015). Disposal of lead containing waste products, removal of lead-based paints from bridges, buildings and damaged battery from industries further results into the accumulation of lead in municipal landfills (Collin *et al.,* 2022). Lead is not essential for plant or animal life. Of particular concern is the effects of lead on the central nervous system, renal system and the brain. Some of the effects are reversible, whereas chronic exposure to high lead levels may result in continued decreased kidney function and possible renal failure. Lead has been shown to interfere with

haemoglobin synthesis. It is easily absorbed by the body. Children absorb higher amounts of lead than adults which is highly dangerous as they are developing (Collin *et al.,* 2022). In children lead is not absorbed by the bones unlike adults therefore children are at a higher risk of poisoning since it is the soft tissues that absorb excess lead.

Low concentrations of lead in children's blood can cause hearing and learning problems, anemia, behavioral anomalies, slowed growth, lower intelligence quotient, and hyperactivity. Adults exposed to lead can suffer from cardiovascular effects, increased blood pressure and incidence of hypertension, decreased kidney function, and reproductive problems (Chowdhury *et al.,* 2022).

In the environment, lead binds strongly to particles such as soil, sediment and sewage sludge (Afzaal *et al.,* 2022). Because of the low solubility of most of its salts, lead tends to precipitate out of complex solutions. High level of Pb have been reported in fishes an indication that they are secondary predators, showing rich magnification of a trophic structure of an aquatic ecosystem (Pandiyan *et al.,* 2021).

In Kenya, contamination of water, soil and food by lead ions have been reported. For example; Outa and coworkers (2020) reported lead levels of 20 µg/L in Lake Victoria water near Kisumu city which was above the maximum allowable limits (Outa *et al.,* 2020). In a related study by Mwatsahu *et al.,* (2020) concentration upto 0.01 µg/mL were reported along the Mombasa coastline (Mwatsahu *et al.,* 2020. Also, Munene and Mwaniki, (2019) in their analysis of heavy metals in the Nairobi wastewater reported a very high mean levels of lead metal in the wastewater ((Munene, 2019),13.62 ± 2.91µg/L wastewater (Kinuthia *et al.,* 2020).

In wastewater treatment plants in Nairobi and Embu County, the levels of lead ranging between 1.2 -75.5 µg/L and 0.011 – 2.123 mg/L, respectively were reported. In air, lead concentration of 0.07, 0.34 and 1.10 µg/m^3 were reported for residential, controlled and industrial areas, respectively in Nairobi city county (Mutua *et al.,* 2021). The level of Pb^{2+} ion contamination in food ranged between 0.271and 1.891 mg/kg with groundnuts recording higher level than other food samples within Thika town in Kiambu County (Mwove *et al.,* 2023).

Previous studies in different regions in the world reported lead levels of 11.42 mg/L (water) in Nigeria (Obasi & Akudinobi, 2020), 0.47mg/L (ground water) in India (Alghobar &Suresha, 2015) and 0.21 mg/L (waste water) in Sudan (Musa *et al.,* 2020). In vegetables watered with contaminated waste water, lead tissue concentration as high as 13.4 mg/L was reported in Zimbabwe (Tibugari *et al.,* 2020).

2.2.2 Anions as Water Contaminants

The occurrence of anions in the aquatic environment has become a worldwide issue of increasing concern (John *et al.,* 2011). One of the important classes of pollutants found in aquatic environments are the nutrients that exist in the form of toxic anions (John *et al.,* 2018). They include; nitrate, fluorides, bromides, phosphates, chlorides, cyanides, and dichromate. These anions are widely used in the industry. For example; phosphates and nitrates are widely used in many industries such as food, agriculture, beverage and detergent.

They are of importance to flora and fauna. However, when they are beyond the permissible dose over a prolonged period, they can cause detrimental effects to humans, animals and aquatic environment, such as severe eutrophication which contributes to aquatic species

death, algal bloom, various types of cancers in humans, diabetes and parasitic infections (Gizaw *et al.,* 2021; Glibert, 2020). Eutrophication associated with nitrogen and phosphorus can lead to unhealthy ecosystems. In addition, eutrophication leads to the reduction of biodiversity, increased water toxicity and increased turbidity of water bodies (Berkessa *et al.,* 2019).

2.2.2.1 Nitrates

Nitrates are contaminants that are abundant in various environmental compartments. They are naturally occurring compounds that are obtained after the decomposition of animal waste (Arnnok & Burakham, 2014). Due to their high solubility in water, they are the most widely spread contaminants in the world (Bhatnagar *et al.,* 2015). Nitrates are mostly available at moderate concentrations in most natural waters; however, excessive use of fertilizers has resulted in an increase in their concentration in the environment which has been identified as an issue of growing concern (Craswell, 2021)

The presence of high concentration of nitrates can be detrimental to the environment (Bhatnagar *et al.,* 2015). To be specific, elevated levels of nitrates causes diabetes, interferes with fetal development, causes water anoxia and interferes with growth of algae. It is a precursor for carcinogen (Kostraba *et al.,* 1992; Wolfe & Patz, 2002). For example; a significant association between colorectal cancer and nitrates in men has been reported (Nasseri Maleki et al., 2022). The carcinogenic risk of nitrates is concentration-dependent (Mehta *et al.,* 2014). Drinking water with nitrates increases the risk of colorectal cancer (Schullehner *et al.,* 2018). Due to the various environmental problems related to the high concentration of nitrates in drinking water, WHO set the standard permissible level of nitrate in drinking water to be 50 mg/L

In Kenya, contamination of water by nitrates has been reported. For example; in Molo river basin, Nakuru County levels of 1.73 to 6.16 mg/L were been reported (Chebet *et al.,* 2020). In a related study, in river Isiukhu, Kakamega county, high nitrate levels were reported in water (0.15 to 0.75 mg/L) and sediments (0.75 to 1.93 mg/L) (Oremo *et al.,* 2020).

In west Africa, Kouakou et al (2022) reported nitrate ions concentrations ranging from 0.93 to 28.13 mg/Lin drinking water (Kouakou *et al.,* 2022). In ground water nitrate concentrations of in 24 to 78 mg/L and 0.80 to 109.57 mg/L have been reported in India and China, respectively (Ramalingam *et al.,* 2022).

2.2.2.2. Phosphates

Phosphates are emerging pollutants of environmental concern. Phosphates have been released into water bodies in organic and inorganic forms as a result of domestic, mining, industrial, and agricultural activities, as well as municipal discharges (Hussain *et al.,* 2011). Phosphate is not considered harmful to humans, but elevated levels in aquatic ecosystems can promote microbial and algae growth leading to eutrophication (Douterelo *et al.,* 2020; Glibert, 2020).

Phosphate ions contamination in water and sediments have been documented in Kenya. In river Isiukhu concentrations ranging between 1.18 and 3.28 mg/L (water) and 2.30 to 4.51 mg/L (sediments) have been reported (Oremo *et al.,* 2020). Chebet *et al.,* (2020) reported phosphate levels above the maximum allowable limits in river Molo basin (0.13 to 11.16 mg/L) (Chebet et al., 2020). In Maumau stream, a tributary of Nairobi River reported high phosphate levels ranging from 0.043 to 0.57 mg/L (Wilson *et al.,* 2021) .

2.2.3 Environmental Pollution by Halogenated Organic pollutants

Halogenated organic pollutants are often associated with pharmaceutical drugs and pesticides. Pharmaceutical drugs are widely used in health care, injecting a large number of them into the environment in unused or metabolized form (Akhtar *et al.,* 2016; Patel *et al.,* 2019). Their emergence has increased due to the growth in population, industrial activities, and climate change (Qalyoubi *et al.,* 2022) The main sources of pharmaceuticals in the environment are sewage treatment plants, landfill leaching, WWTPs and direct disposal of pharmaceuticals (Ghosh *et al.,* 2023). Their presence in the aquatic environment is considered a potential toxicological hazard because they pose long-term risk to aquatic organisms and their dependents through endocrine destruction and the development of drug-resistant bacterial strains (Kairigo *et al.,* 2020; Tambosi *et al.,* 2010). Some of commonly used pharmaceutical drugs are: diclofenac, chloramphenicol and ciprofloxacin.

2.2.3.1 Diclofenac

Diclofenac (2-[(2,6-dichlorophenyl) amino] benzene acetic acid) is one of the most commonly used non-steroidal anti-inflammatory drugs in human medical care. It serves as an analgesic, antiarthritic, and antirheumatic compound, effectively reducing inflammation. Additionally, it is employed for fever reduction and acts as a painkiller, offering relief from mild to moderate pain, including headaches, backaches, and postoperative pain (Qalyoubi *et al.,* 2022). Figure 2.1 shows the molecular structure of diclofenac.

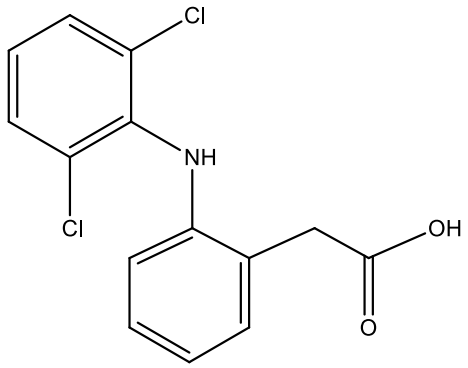

Figure 2.1: Molecular structure of diclofenac

Diclofenac has molecular weight of 296 g/mol, water solubility of 2.37mg/L, pka value of 4.1 and log Kow of 45. It can be found as a generic drug in a number of formulations, including diclofenac diethylamine, which is applied topically. Over-the counter use is approved in some countries for minor aches and pains and fever associated with common infections (Lonappan *et al.,* 2016).

Diclofenac is considered as a persistent pharmaceutical product which has low removal efficiency from sewage treatment plants (Lee *et al.,* 2012). Therefore, its concentrations has been reported to increase after sewage treatment (Aly, 2023).

A study by Jeele *et al.,* (2023) showed that acute administration of diclofenac deteriorated renal function in patients with coronary artery disease and heart failure (Jeele *et al.,* 2023). Diclofenac affects organ histology and gene expression in fish when exposed to a concentration of l µg/L of this drug (Madikizela & Chimuka, 2017). It is one of the most widely studied pharmaceuticals in the environment, due to its persistence in nature and known toxicity to vultures, as well as aquatic species for example, in fish it destroys the liver and lungs (Gilbert, 2012). It is one of the first pharmaceuticals that could be detected in the aquatic environment (Buser *et al.,* 1998). Microbial degradation of diclofenac was reported to be very slow resulting in formation of two metabolites, which later was reported

to be deconjugated to form diclofenac within seven days. Hence, indicating that the biological removal of diclofenac is not likely to occur in convectional WWTPs (Lee *et al.,* 2012). Since its initial commercial introduction, diclofenac has been used by more than one billion patients and ranks as the eighth largest selling drug in the world (Gan & opinion, 2010). Globally, diclofenac is consumed in huge amount (1443 tons) per year (Lonappan *et al.,* 2018).

In Kenya, diclofenac levels have been reported, for example, concentrations ranging from 3 to 18 ng/g have been reported in Nairobi River sediments (Vane *et al.,* 2022). In lake Victoria water levels upto 160 ng/L were reported (Nantaba *et al.,* 2020).

In wastewater levels of 9.68 µg/L in Egypt and 19.0 µg/L in South Africa have been reported (Akawa *et al.,* 2021; Agunbiade *et al.,* 2016). In India diclofenac levels of 68 µg/L were reported in wastewater (Praveenkumarreddy *et al.,* 2021). In seawater, levels ranging between 843 ng/L have been reported in China (Kubier *et al.*, 2020) and 13.48 µg/L in groundwater in Nigeria (Sathishkumar *et al.,* 2020). In waste waters concentrations ranging from 0.079 to 3.6 µg/L have been reported in Egypt (Abdallah *et al.,* 2019). In the environment diclofenac is broken down through biodegradation and photo transformation (Angosto *et al.,* 2020). Figure 2.2 shows pathways for diclofenac biodegradation

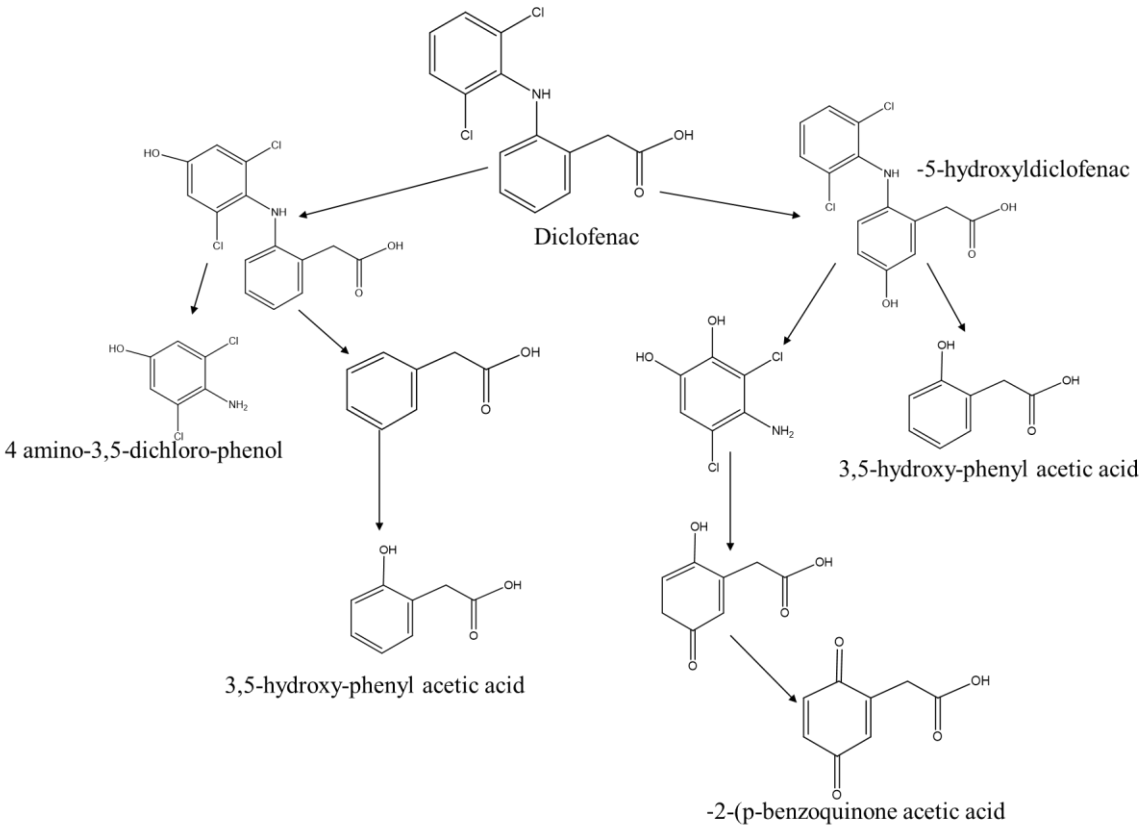

Figure 2. 2: Proposed pathways for diclofenac biodegradation (Aguilar Romero, 2021)

2.2.3.2 Chloramphenicol

Chloramphenicol,2,2-dichloro-N-[(IR,2IR)-1,3-dihydroxy-1-(4-nitrophenyl)propan-2-yl acetamide, is a broad-spectrum antibiotic which is considered as both affordable and easy to manufacture, and thus frequently used in developing economies. It is effective against a wide variety of gram-positive and gram-negative bacteria, including most anaerobic organisms which cause brain abscesses and meningitis (Berendsen, 2013). It is also used for veterinary purposes as well as in human medication, hence after administration un-metabolized and un-adsorbed parent compounds will be excreted and enter the environment via urine and excrement (Tan *et al.,* 2022). Figure 2.3 shows the molecular structure of chloramphenicol.

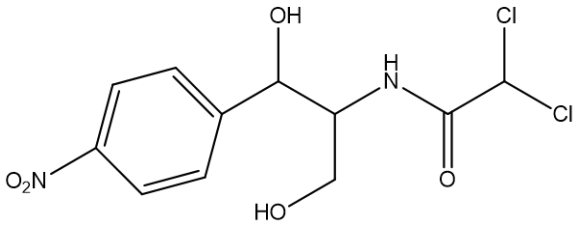

Figure 2. 3: Molecular structure of Chloramphenicol

Unregulated exposure to chloramphenicol results in bone marrow suppression and aplastic anaemia which is idiosyncratic. The intravenous utilization of chloramphenicol is associated with grey baby syndrome (Singhal *et al.,* 2023). Chloramphenicol has been monitored in multiple environmental contexts, such as river water, domestic wastewater, sediment and soil.

In Kenya, significant chloramphenicol concentration has been detected in hospital waste, for example; Kimosop *et al.,* (2016) reported concentration ranging from 60 ng/ L to 100 ng /L in wastewater samples from hospitals in Kakamega, Mumias, Bungoma, and Eldoret in Lake Victoria Basin, Kenya (Kimosop *et al.,* 2016). Chloramphenicol level have been reported to be 0.42 µg/L in wastewater in Barekese reservoir, Ghana (Gyesi *et al.,* 2022). Similarly, Zhou et al. showed that chloramphenicol at an average level of 4.89 ng/L existed in shallow lakes in the Yangtze River basin, China (Zhou *et al.,* 2019). In Malaysia, chloramphenicol levels were found to be the highest in the Selangor River of 24.35 ng/L, followed by the Gombak River of 23.37 ng/L, and finally the Lui River of 18.03 ng/L (Praveena *et al.,* 2018).

Chloramphenicol cannot be adsorbed and metabolized completely by human beings and animals, hence after administration un-metabolized and un-adsorbed parent compounds is excreted into the environment via urine and excrement (Ma *et al.,* 2019). In the

environment, this drug can undergo different degradation pathways; amido bond hydrolysis, nitro group reduction, acetylation, aminoacetylation, dechlorination, and oxidation as shown in Figure 2.4.

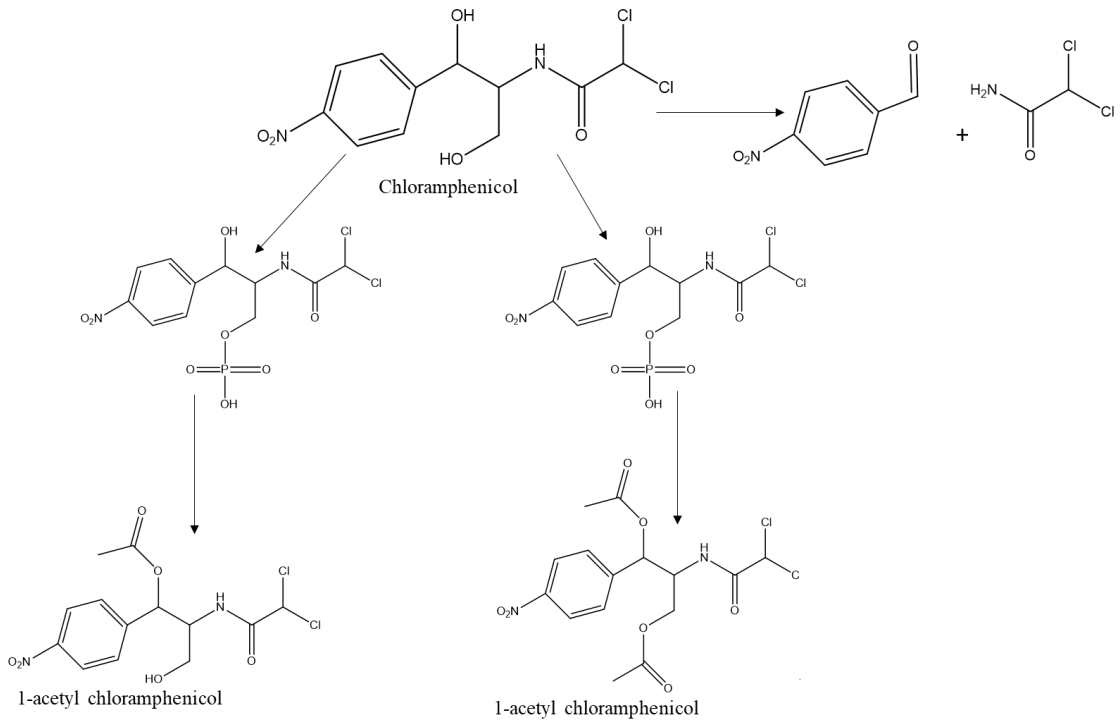

Figure 2. 4: Structures of Chloramphenicol and the degradation products (Wu *et al.,* 2023)

2.2.3.3 Ciprofloxacin

Ciprofloxacin, 1-cyclopropyl-6-fluoro-1,4-dihydro-4-oxo-7-(1-piperazinyl)-3quinolinecarboxylic acid, is a synthetic chemotherapeutic antibiotic that belongs to fluoroquinolone class of pharmaceutical antibiotic. It has a molecular weight of 331.4 g/mol. It is used to treat different types of bacterial infections, including skin infections, bone and joint infections, respiratory or sinus infections, urinary tract infections, diarrhea, gonorrhea and anthrax. Figure 2.5 shows the molecular structure of ciprofloxacin.

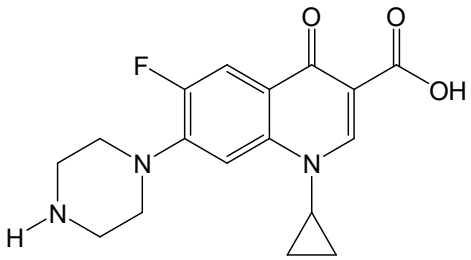

Figure 2. 5: Molecular structure of Ciprofloxacin

It ranks among the most widely utilized antibiotics globally and stands as one of the primary choices within the quinolone class in hospital settings. This versatile antibiotic exhibits a broad-spectrum antibacterial activity, displaying high effectiveness against a wide array of gram-negative bacteria and moderate effectiveness against various gram-positive bacteria. Its mode of action involves the inhibition of bacterial DNA topoisomerases, particularly gyrases, which are crucial enzymes in nucleic acid synthesis. Moreover, their presence in water exceeding certain limits can cause adverse health problems such as brain damage, urinary tract infections, liver impairment, and carcinogenic diseases (Al Sharabati *et al.,* 2021). Thus, ciprofloxacin can reach the environment by sewage, discharges from sewage treatment plants, leaching from landfills, its release from pharmaceutical industries, livestock activities and application of sewage sludge, manure or treated waste water to agricultural land.

Ciprofloxacin was found at the concentrations of 5.3 μg L^{-1} in wastewater in Machakos, Kenya and at concentrations of 14.98 μg L^{-1} in wastewater in Nairobi, county which indicated that it is one of the most prevalent antibiotics (Kairigo *et al.,* 2020). In China, Tran *et al.,* (2018) reported ciprofloxacin concentrations of 6453 ng/L in influent and 524.1 ng/L in effluent (Tran *et al.,* 2018). In wastewater ciprofloxacin concentrations ranging from 2 to 41 ng/L in wastewater, Lake Victoria, Uganda (Nantaba *et al.,* 2020) and

15 µg/L have been reported in hospital wastewater, Ghana (Azanu *et al.*, 2018). Figure 2.6 shows pathways for ciprofloxacin degradation pathways.

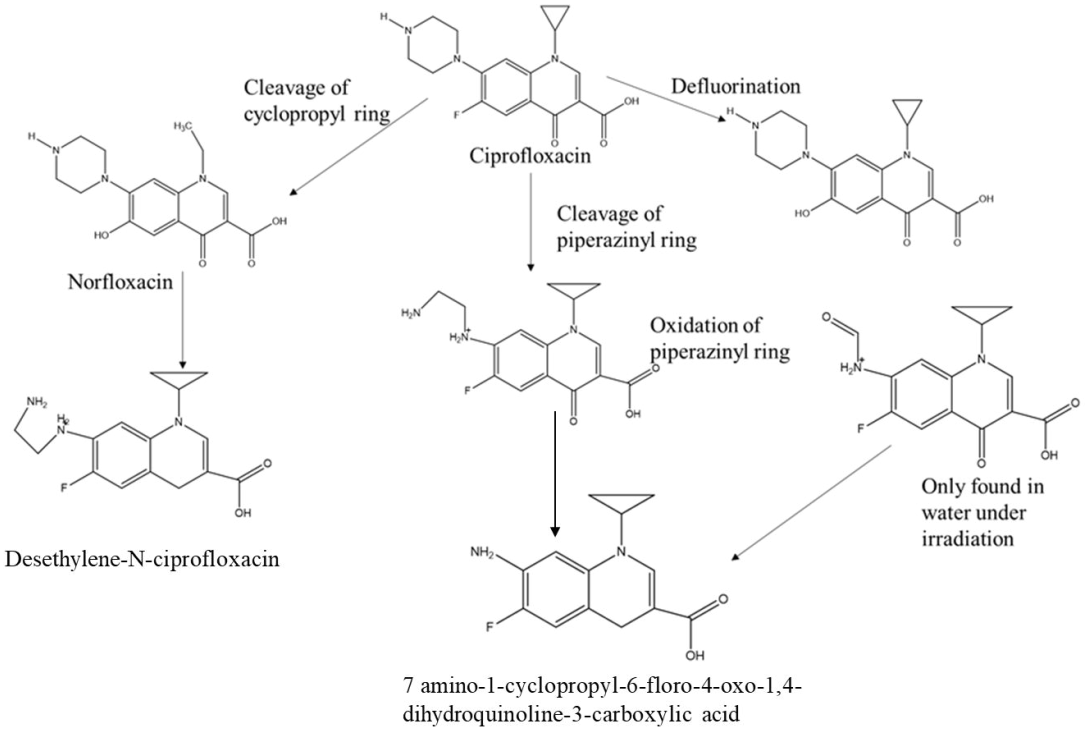

Figure 2. 6: Structures of ciprofloxacin and the degradation products (Lin *et al.,* 2018)

2.2.3.4 Diuron

Diuron (3-(3, 4-dichlorophenyl)-1, 1-dimethylurea) is a phenylurea herbicide used for the control of long-term pre-emergence and post-emergent weeds in both agricultural and non-agricultural areas, such as roads and paths and to control weeds in a range of tree crops (Li *et al.,* 2021). It is commonly used in many parts of the world where agricultural activities are undertaken in large scale with the sole purpose of improving quality and quantity of yields. Figure 2.7 shows the molecular structure of diuron.

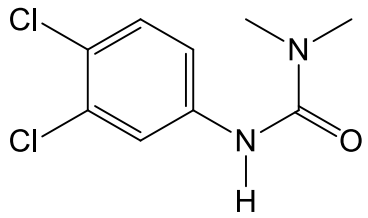

Figure 2. 7: Molecular structure of Diuron

Several reports have confirmed that diuron enters the surface water and groundwater through irrigation, drainage, percolation, and surface runoff. Diuron is characterized as a potential threat to ground water resources due to its moderate solubility and low tendency to adsorb to soil (Wang *et al.,* 2017). It is ranked as the third most hazardous pesticide to ground-water resources in the United States due to its high mobility in soil solution and it is generally considered persistent in the environment. It is reported to have a moderate solubility of 42 mg/L in water and thus able to contaminate both surface and ground water (Safi *et al.,* 2014; Stork *et al.,* 2008). Diuron exposure to animals has been reported to cause toxicological effects, such as growth retardation, increased mortalities and alteration of blood chemistry (Mhadhbi *et al.,* 2012). Diuron causes methemoglobin production in the blood as well as liver and spleen disorders in humans. It is also an endocrine disruptor, interfering with normal hormone release, transport, and disposal systems in the body (Tekin *et al.,* 2020). In mammals, as well as fish, birds, and invertebrates, this chemical is known to produce acute and chronic toxicity, teratogenicity, mutagenicity, carcinogenicity, and genotoxicity (Jayaraj *et al.,* 2016). Microbially facilitated degradation is the major dissipation route of diuron which occurs through successive demethylation of the urea group followed by hydrolysis producing more toxic metabolites (Kaonga *et al.,* 2015). In Kenya, diuron has been reported up to 41 ng/L in river water along river Nzoia basin

(K'oreje *et al.,* 2018). Also, upto 9.43 ng/L concentrations have been reported in sediment obtained from freshwater systems of Western Kenya (Kandie *et al.,* 2020).

Previous studies in different regions in the world reported diuron levels of 86.56 ng L (water) in Mexico (Lagunas-Basave et al., 2022), 100.0 µg/L (water) in India (Al-Shaalan, Ali *et al.,* 2019) and 20 and 100 µg/L (wastewater) in Brazil and Argentina, respectively (de Oliveira *et al.,* 2023). In Costa Rica river basins, the highest diuron concentration in water and sediment samples reported were 22.8 µg/L and 11.75 µg/kg, respectively (Carazo-Rojas *et al.,* 2018)

In an aerobic environment, diuron undergoes ring cleavage is followed by N-demethylation of the urea group and subsequent hydrolysis in the biodegradation of diuron leading to, 4 dichloroaniline (DCA), N-(3,4-dichlorophenyl)-N-methylurea (DCPMU), and 3, 4 dichlorophenylurea (DCPU), with DCA serving as the primary metabolite. The degradation products methyl (3,4-dichlorophenyl-methylurea, DCPMU) and dimethyl (3,4-dichlorophenyl-methylurea, DCPU) have been found in diuron-contaminated environments (Guzzella *et al.*, 2006; Mirenga, 2018; Moretto *et al.,* 2019). Figure 2.8 shows structures of diuron and the degradation products

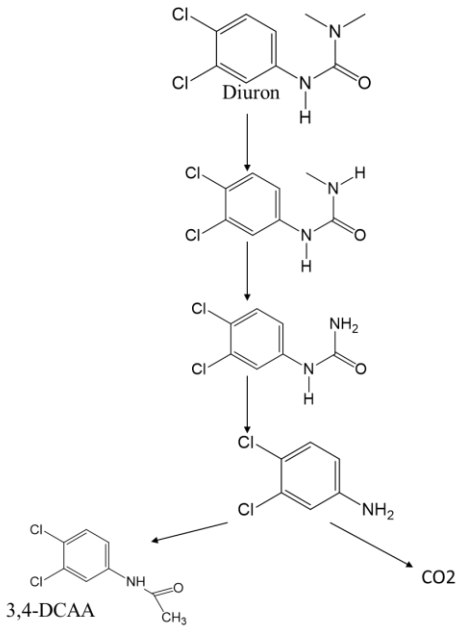

Figure 2. 8: Structures of diuron and the degradation products (Moretto *et al.,* 2019)

2.2.3.5 Chlorpyrifos

Chlorpyrifos [O, O-diethyl O-(3, 5, 6-trichloro-2-pyridyl) phosphorothiate] is a broad-spectrum, widely used organophosphate pesticide (Perry *et al.,* 2020). This compound is applied in various agricultural and horticultural crops and in households to combat biting and stinging-sucking pests. They act on pests by contact, ingestion, and inhalation, and on the plant surface and inside (Wołejko *et al.,* 2022) It is used in protection of agricultural crops such as sugarcane, coffee, tea, cocoa, rice, wheat, potatoes, vegetables, bananas, citrus fruits and cotton. Figure 2.9 shows the molecular structure of chlorpyrifos

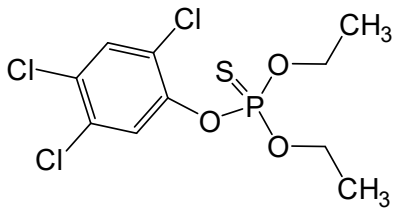

Figure 2. 9: Molecular structure of Chlorpyrifos

It is one of the primary acaricides used by Kenyan dairy producers to manage ticks and insect pests in agriculture (Mutavi *et al.,* 2018). Chlorpyrifos is one of the most widely used organophosphate pesticides worldwide (Giesy *et al.,* 2014). It is available in various brand names, such as Duodip, commonly used as an acaricide in Kenya. It acts on the nervous systems of insects by inhibiting the acetylcholinesterase enzyme.

Its extensive use has led to contamination of different environmental matrices (Lu *et al.,* 2020). In some cases, the contamination is as far as 20 kilometers from the site of application (Lu *et al.,* 2020). Chlorpyrifos has a half-life of between two and four months in the soil, although it can take over a year depending on the climate and soil type (Ambreen *et al.,* 2021)**.**

According to Ambreen *et al.,* (2021), the overuse of chlorpyrifos in agriculture has led to deposition in water, soil, and food resources, resulting in biomagnification in non-target organisms, including humans. Toxic effects of this chemical have been reported, they cause major toxicities such as oxidative stress, and endocrine disruption. Further, it can have adverse hematological, musculoskeletal, renal, ocular, and dermal effects. Excessive use of this compound results in poisoning and potentially kills a non-target species upon exposure including human (Nandi *et al.,* 2022).

In Kenya, contamination of water, soil and food by chlorpyrifos has been reported. For example; Otieno and coworkers (2015) reported chlorpyrifos levels in the range of 2.6 to 24.9 ng/L and 6.8 to 35.8 ng/g dry weight (dw) in water and sediment, respectively in Lake Naivasha (Otieno *et al.,* 2015). In a related study by Chaka *et al.,* (2023) concentration 0.5 µg/L in surface water were reported in Narok and Bomet Counties (Chaka *et al.,* 2023).

Also, Nyabiba, (2022), 11.92 mg/L chlorpyrifos in the surface water have been reported in the Molo subcounty (Nyabiba, 2022).

In river Nile in Egypt, levels of chlorpyrifos of 12.1and 68.7 ppb have been reported during winter and autumn, respectively (Shalaby *et al.,* 2018). 3.35 mg/L (effluent) in fields in Owiro Estate, Tanzania (Kihampa *et al.,* 2010. Also, have been reported up to 30 ug/l in surface water in Brazil (de Oliveira, 2023).

In the soil, available data shows that the chlorpyrifos degrades slowly both under anaerobic and aerobic conditions. Biodegradation of chlorpyrifos mainly occurs through hydrolysis of the P-O alkyl or P-O aryl bond. Under controlled conditions, microbial enzymes can hydrolyze chlorpyrifos and mineralize the two main metabolites, 3, 5, 6- trichloro-2-pyrinidinol and 3, 5 6-trichloro-2-methoxypyridine metabolites (Briceño *et al.,* 2012). The half-life of chlorpyrifos in soil is usually between 10 and 120 days, but can range from 2 weeks to over one year, depending on the soil type, soil pH, moisture content and temperature (Ajaz, 2005; Wolejko, 2022). The persistence of chlorpyrifos in soil may also be attributed to the accumulation of trichloro pyridine-2-phenol, a metabolite with anti-microbial properties which serves as a buffer to prevent the growth of chlorpyrifos degrading bacteria (Ambreen &Yasmin, 2021; Nyabiba, 2022). Figure 2.10 shows structures of chlorpyrifos and the degradation products.

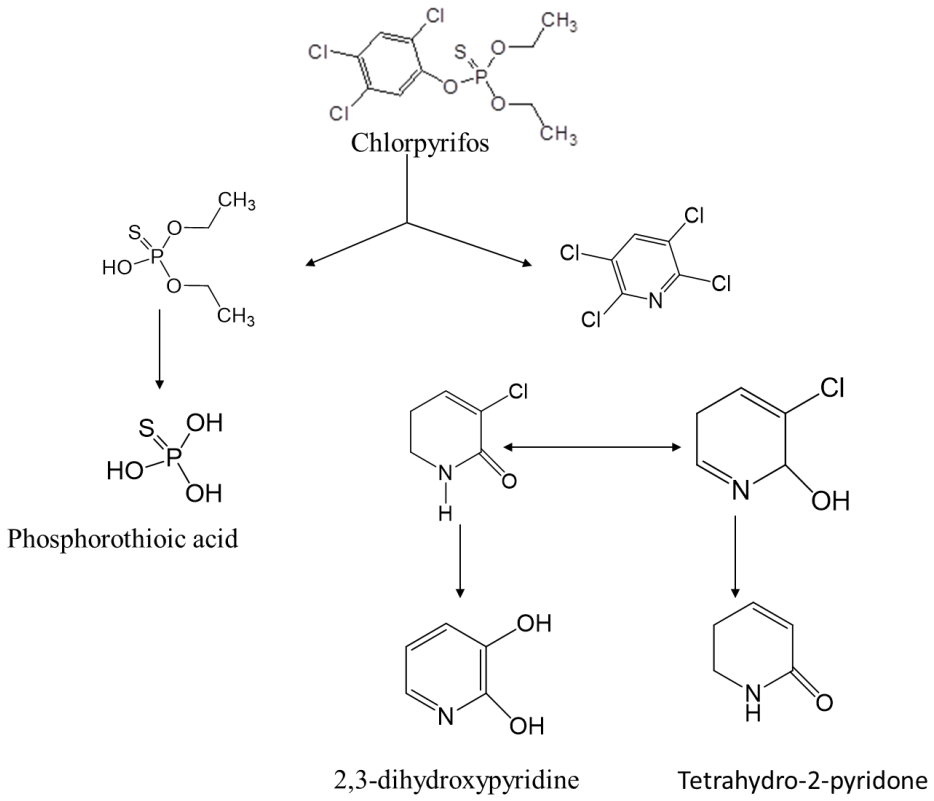

Figure 2. 10: Structures of Chlorpyrifos and the degradation products (Ambreen &Yasmin, 2021)

2.2.3.6 Imidacloprid

Imidacloprid**,** 1-((6-Chloro-3-pyridinyl) methyl)-4,5-dihydro-N-nitro-1H-imidazol-2-amine, is a systemic insecticide that acts as an insect neurotoxin and belongs to the neonicotinoids group which act on the central nervous system of insects. It is commonly used in agriculture to control a wide range of insect pests, as well as in household and veterinary applications (Wakil *et al.,* 2021). The molecular structure of imidacloprid is shown in Figure 2.11.

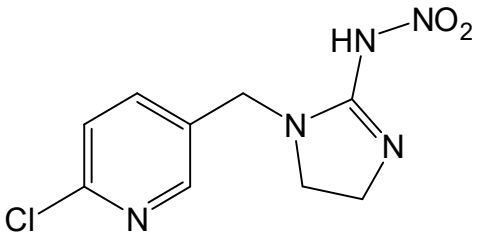

Figure 2. 11: Molecular structure of Imidacloprid

It is effective on contact and via stomach action. Because imidacloprid binds much more strongly to insect neuron receptors than to mammal neuron receptors, this insecticide is more toxic to insects than to mammals. Studies have shown that even low doses of imidacloprid can impair the navigation and foraging ability of bees, leading to decreased colony survival and productivity. As a result, some countries have restricted or banned the use of imidacloprid, particularly for outdoor applications. It is important to carefully consider the potential risks and benefits of using imidacloprid, and to use it in a responsible and sustainable manner (Wakil *et al.,* 2021).

In Kenya, contamination of water, soil and food by imidacloprid have been reported. For example; Kandie and coworkers (2020) reported imidacloprid levels ranging up to 152 ng/L in freshwater, within the Lake Victoria South Basin (Kandie *et al.,* 2020). In Wuhan in southern China, levels of imidacloprid and its degradation products ranging between 0.04 to 32.0 and 438 ng/L have been reported in source water, treated water, and tap water (Wan *et al.,* 2020; Elfikrie *et al.,* 2020). Half-life of imidacloprid has been reported are well-known; it has an aerobic half-life of 997 days and an anaerobic half-life of roughly 27.1 days. The longer half-life period of imidacloprid and its metabolites in soil is attributed to the pesticide's decreased bioavailability to microorganisms that break down

pesticides (Duchet *et al.,* 2018). There are numerous suggested metabolic pathways for imidacloprid degradation in water.

Imidacloprid may breakdown into 6-chloro-3-pyridyl-methylethylendiamine, 6-chloron-icotinaldehyde, 6-chloro-N-methylnicotinacidamide, 1-[(6-chloro-3-pyridinyl)methyl]-2-imidazolidinone(i.e., imidacloprid urea), and 6-hydroxynicotinic acid whereas the minor breakdown product is imidacloprid-guanidine (Sharma & Singh, 2014; Zheng & Liu, 1999). Figure 2.12; shows the structure of imidacloprid and pathway of imidacloprid biodegradation.

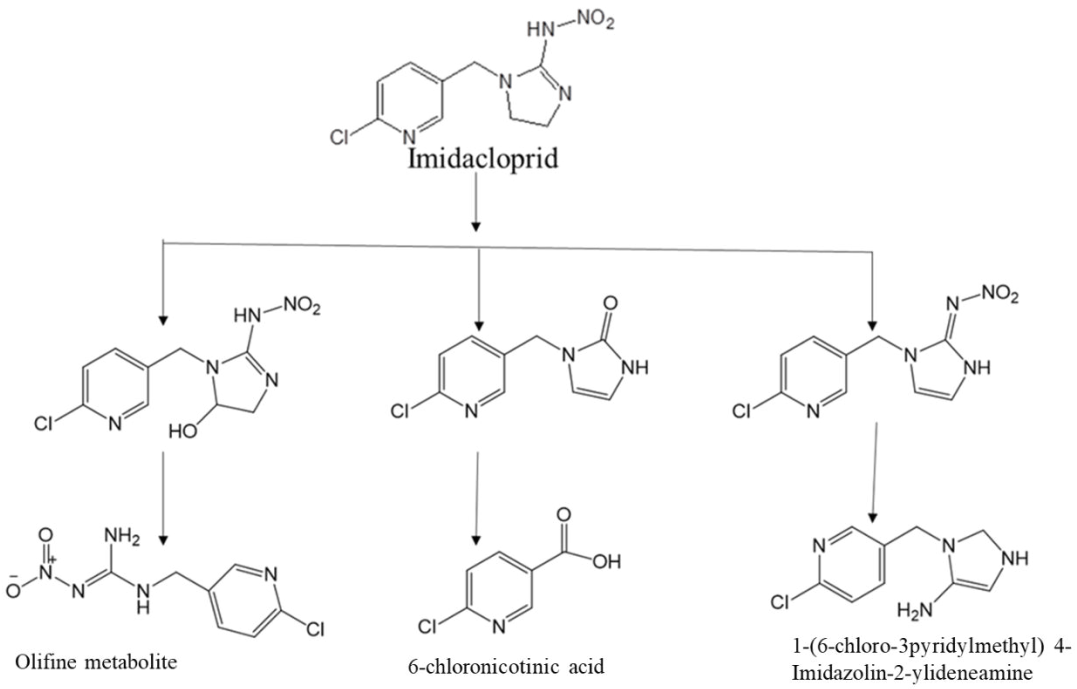

Figure 2. 12: Degradation pathway of Imidacloprid (Sharma & Singh, 2014)

2.3 Remediation Methods of Polluted water

Various conventional methods have been used for the removal of pollutants such as heavy metal ions, anions, pharmaceuticals and pesticides from wastewater. These methods include: chemical precipitation, phytoremediation, ion exchange, membrane filtration,

membrane distillation and bioremediation methods. These are briefly explained in the following subsections.

2.3.1 Chemical Precipitation

Chemical precipitation is widely used for the removal of different pollutants such as heavy metals, anions (nitrates and phosphates), pharmaceuticals and pesticides (Akinnawo, 2022; Huang, 2017; Ibigbami *et al.*, 2016). For example; during the removal of heavy metal ions, after pH adjustment to basic conditions, the dissolved metal ions are converted into insoluble solid phase via a chemical reaction with a precipitant agent. The precipitate formed is then separated from water by sedimentation or filtration. For example; iron sulphide has been used to precipitate copper, lead and cadmium (Zhu *et al.,* 2012). Chemical precipitation is advantageous because it's cheap and relatively simple to operate (Matlock *et al.,* 2002; Izadi *et al.,* 2017). However, the limitation of the above method is that there is production of large amount of residue sludge which increases sludge disposal costs (Kilaru *et al.,* 2019).

Furthermore, few metal hydroxides are amphoteric, and the mixed metals make it problematic in utilizing the hydroxide precipitation since the ideal pH for one metal may return another metal into the solution. Besides, complexing agents being in the wastewater, they will restrain the metal hydroxide precipitation. In addition, it requires a lot of chemicals to decrease the pollutants to an acceptable level that are released in the environment (Kilaru *et al.,* 2019). Slower pollutant precipitation is yet another demerit (Kilaru *et al.,* 2019).

2.3.2 Bioremediation

Bioremediation process is a treatment method whereby biological systems, such as microorganisms, green plants and animals remove and degrade toxic pollutants from the aquatic environment into less toxic forms (Tyagi & Kumar, 2021). The microbe assists bioremediation and phytoremediation methods for the removal of pollutants and the two are financially effective treatment methods. Numerous aquatic plants which include Typha, Eichhornia, Phragmites, Azolla and Lemna have been utilized for the removal of pollutants from the wastewater (Chellaiah, 2018). Phytoremediation is a group of plant based remedial method that removes pollutants or lower their bioavailability and mobility in the soil. Phytoremediation offers a promising technique for removing pharmaceuticals, pesticides and heavy metals from water bodies (Nie *et al.,* 2020). These methods include: phytoextraction, phytostabilization, rhizofiltration and phytovolatilization. Phytoextraction involves absorption of pollutants by plant roots and then transferring them to the shoots. The pollutants are then removed by harvesting plants with accumulated pollutants into the roots, shoots, and leaves. This in turn produces a mass of plants containing pollutants that are further transported for disposal and recycling (Nie *et al.,* 2020). Phytostabilization involves the use of plant roots to limit the movement of pollutants in the soil. The plant purposes to prevent soil erosion thus hindering the transfer of pollutants to other areas while rhizofiltration involves the application of certain plants which are found in both terrestrial and aquatic environments, to absorb, concentrate and precipitate the pollutants from their polluted sources. Rhizofiltration is mainly applied in ground and surface water with low contaminant concentration (Ullah *et al.,* 2015). After removal, the pollutants are volatilized and discharged into the environment (Eid *et al.,*

2020). Macrophytes have been used for the removal of heavy metals, nitrates and phosphates (Qayoom & Jaies, 2023).

This group of methods has promising advantages in comparison to other remediation techniques. The cost-effectiveness of the phytoremediation is higher than that of conventional processes both *in situ* and *ex-situ* (Singh *et al.,* 2022). It is easy to monitor the hyperaccumulating plants and it's a natural method that can protect the surrounding in an environmentally friendly way with soil microbiota and plants. The same can also eliminate long- term viability and enhance soil fertility. The recovery and reuse of valuable metals is possible by the phytoremediation which is an economically and environmentally favorable technique since it utilizes green plants to contain, sequester or detoxify contaminants from contaminated soil and water (Ashraf *et al.,* 2019; Tyagi & Kumar, 2021).

Disadvantages of phytoremediation as a method of pollutant removal include: incomplete pollutant removal, high reagent, high energy requirements and it tends to generate secondary contaminants. It is also time consuming (Tyagi & Kumar, 2021). It is limited to the depth of the roots and surface area covered by the plants. The toxicity of pollutants to plants, incapability to treat organic contaminants due to lack of enzymes for degrading. Because of slow growth, it is not possible to completely prevent the leaching of contaminants into the groundwater. Plant survival depends on the health of soil and growth conditions and due to their bioavailability, they can get incorporated into the food chain. Once the pollutants accumulate in the food chain, they become toxic to plants, animals, and humans'(Tyagi & Kumar, 2021). Certain compounds like metals and chlorinated organic pollutants cannot be broken down by microbes. Microbes can occasionally create

toxic metabolites or byproducts when they break down pollutants. Since bioremediation is a scientifically intensive process, it should be modified to the unique conditions of each site; that is, before using the technique to treat a polluted site.

2.3.3 Ion Exchange

This involves the process of reversible exchange of ions using natural or synthetic ion exchange resins. Ion exchange can be used for the removal of undesirable or recovery of useful anions and cations from wastewater (Maheshwari *et al.,* 2015). Ion exchange also takes place in living materials considering that cell walls, cell membranes, and other physiological structures have charges. Ion exchange being another method for removing pollutants from effluents, it involves transferring or exchanging ions with the same charge between a medium and an electrolyte solution (Maheshwari *et al.,* 2015). This technique involves the stoichiometric exchange of weak electrostatically attracted ions on the resin with ions in solution (Indarawis & Boyer, 2013). Ion exchange resins have functional groups which create a fixed charge. Anion exchange, cation exchange or a combined anion and cation exchange have been used for the purification of drinking water as well as water softening and in the production of ultrapure water (Abdulgader *et al.,* 2013).

Ion exchange resin possesses cationic exchangers which are able to exchange ions with positively charged ions in aqueous solutions and has high removal efficiency and fast kinetics. Metal ions from dilute solutions are exchanged with ions held by electrostatic forces on the exchange resin. The above method has various limitations. For example, it is expensive and requires pretreatment for wastewater as the exchanger matrices get clogged with the organics in the wastewater (Yuan & Wood, 2018).

Furthermore, the method cannot handle concentrated metal solution as the matrix gets easily fouled by organics and other solids in wastewater. Moreover, ion exchange is nonselective and highly sensitive to pH of the solution (Maheshwari *et al.,* 2015; Al-Asheh *et al.,* 2020).

2.3.4 Membrane Filtration

Membrane filtration entails the use of filter membranes which permit some particles to pass through the filter membranes but does not permit others to pass through. Examples of membrane filtration include: ultrafiltration, nanofiltration and reverse osmosis (Obotey *et al.,* 2020). Synthetic organic polymers are used to make filter membranes for pressure-driven separation such as; cellulose acetate, polypropylene, polyethylene, and polytetrafluorethylene (PTFE). Materials like silica, zeolites, metals, and ceramics are used to make inorganic membranes (Aliy*u et al.,* 2018). There are several studies reporting that membrane filtration has been used in removal of pharmaceuticals, pesticides, and heavy metals from polluted water (Mukherjee *et al.,* 2020). The advantage of membrane filtration is that it is chemically and thermally stable. However, this method has quite a number of disadvantages which include: formation of sludge, rapid membrane fouling and plugging when pollutants are deposited on the membrane resulting into decreased permeate flux, high energy consumption, more time for filtration, high cost of buying and maintaining of filtration (Mukherjee *et al.,* 2020). Additionally, it is not suitable for dissolved inorganics apart from the fact that pretreatment process is required with regular cleaning.

2.3.5 Reverse Osmosis

Reverse osmosis is a pressure-driven membrane separation process that forces a solution to pass through a semi-permeable membrane for the removal of toxic pollutants from the

wastewater (King *et al.,* 2020). This process was used for the removal of pollutants using a polyamide thin-film composite membrane (Arezoo *et al.,* 2016; Bakalar *et al.,* 2009). The membranes of the recent reverse osmosis system are commonly a homogeneous thin bolstered polymer with a permeable support structure. The permeability of the membrane through which the pollutants pass and the rejection of the same pollutants mainly depend upon the chemical and physical properties of the membrane (Huang *et al.,* 2017). The reverse osmosis membrane technologies are very efficient for the treatment of wastewater containing anions, heavy metal ions, pesticides and pharmaceuticals (Kings *et al.,* 2021). Advantages of pollutants removal by reverse osmosis include: removes salts and other ions in a large percentage, no chemicals addition, no significant pH alteration, no phase change, and it is effective in all concentrations (Jiang *et al.,* 2018). Nevertheless, the notable challenges of this method are: handling of the rejection, high power cost, it's energy intensive and may not be practical for pharmaceuticals and volatile organics (Gupta *et al.,* 2013).

2.3.6 Electrochemical Methods

The anodic and cathodic reactions between the anode and cathode electrodes and the pollutants of interest in the electrochemical cell are the basis of this electrochemical method for wastewater remediation. One of the most popular electrochemical methods that have been effectively applied to the mineralization of stable organic compounds found in wastewater is electrochemical oxidation. According to Turan *et al.,* (2019), direct and indirect oxidation mechanisms are used in chemical oxidation approaches to oxidize pollutants on the anode surface. In order to achieve strong oxidation conditions which

typically show additional potentials, the direct oxidation of pollutants on the anode requires appropriate electrodes.

The anode is the site of the direct oxidation process, where charges are directly transferred between the anode's surface and the organic compound. By generating OH radicals from water on the anode surface, oxidants cause reactive oxygen species to form (in situ) at the electrode's surface, which is how indirect electro-oxidation works (Chavoshani *et al.,* 2020). Once the remediation process is over, the contaminants that are accumulated at the electrodes are eventually extracted by methods such as electroplating. The electrochemical techniques are well known for treating wastewater, especially when it comes to removing pollutants from wastewater (Kilaru *et al.,* 2019). Electrochemical methods have been used for heavy metals, anions, pharmaceuticals and pesticides removal from wastewater (Zhang *et al.,* 2019).

Toxic As (III) ions, for instance, undergo oxidation to become less toxic As (V) ions, which subsequently precipitate out of solution (Ouma *et al.,* 2018). Vela *et al.,* (2019) studied the efficiency of sodium persulfate ($Na_2S_2O_8$) as oxidizing species to remove different pesticides that include imidacloprid, acetamiprid, cymoxanil and thiacloprid (Vela *et al.,* 2019). The method has various advantages: it needs less chemicals, it generates less sludge and provides maximum pollutants removal. On the other hand, it requires higher initial capital, apart from being costly in terms of power supply. Yet another shortcoming is the toxic by-products formed from the oxidizing agents (Kordbacheh & Heidari, 2023; Zhang *et al.,* 2019).

2.3.7 Coagulation-Flocculation

Coagulation processes involve the introduction of a chemical coagulant on colloids causing them to flocculate followed by the precipitation of pollutants on the flocculated matter (Syam *et al.,* 2020; (Syam, 2020). Iron based coagulants have been reported to be more favorable over aluminum-based coagulants due to their stability over a long pH range (Ang & Mohammad, 2020). Coagulation is a stand out amongst the most vital methods for wastewater treatment. Flocculation is the activity of polymers to make the connection between the flocs and tie the particles into huge agglomerates. Suspended solids are flocculated into bigger particles and are easily removed by sedimentation, filtration, and floatation or straining.

The numerous types of flocculants include; poly-aluminum chloride, polyacrylamide, and polyferric sulfate which are utilized in the wastewater treatment but these flocculants cannot be directly utilized for the removal of toxic metal ions from wastewater. Macromolecule flocculants have been utilized as an effective flocculant for the removal of heavy metals from the wastewater (Duan *et al.,* 2010). It has been reported that pesticides and pharmaceuticals can be removed by coagulation-flocculation using aluminum sulfate ($Al_2(SO_4)_3$) (Mohamed *et al.,* 2022; Narayanan *et al.,* 2020).

Generally speaking, coagulation/flocculation treatment method alone cannot remove all pollutants. However, by combining this treatment with other methods to increase removal efficiency, the pollutants can be completely removed (Tokuyama *et al.,*2010). Though it has advantages, coagulation/flocculation has limitations too. For example, high operational costs due to a large amount of chemical utilization and the method may not be applicable

to all soluble pollutants (Kilaru *et al.,* 2019). Also, it produces contaminated sludge which may be difficult to manage resulting in environmental (Mondal *et al.,* 2013).

2.3.8 Adsorption

Adsorption is a technique that has been established for the treatment of potable water, urban wastewater, ground water and industrial effluents (Awad *et al.,* 2020). Hence, it's a well-known, low-cost purification method that is very reliable and environmentally friendly (Al-Ghouti & Da'ana, 2020). It is a surface process that involves the deposition of pollutants on the surface of the adsorbents (Grass *et al.,* 2012) . This method was declared as one of the most excellent wastewater treatments techniques, among others by the United States Environmental Protection Agency (Anil *et al.,* 2020). Several factors affect the efficiency of adsorption.

They include; pH, the presence of other pollutants, temperature, the nature of the adsorbent, the nature of the adsorbate, the particle size of the adsorbent, concentration of the adsorbate, surface area, contact time and adsorbent dose (Grassi *et al.,* 2012). The most common method for the removal of dissolved organic substances is the adsorption using activated carbon, a product that is produced from a variety of carbonaceous materials, including wood, pulp mill char, peat, lignite, etc. Adsorption is the physical and/or chemical process in which a substance is accumulated at an interface between phases (Awad *et al.,* 2020). Adsorbents are materials that have the ability to stimulate the process of adsorption on their surfaces. The process of adsorption has led to the production of various adsorbents. Adsorbents are widely used as separation media to remove inorganic and organic pollutants from contaminated water in water purification process. A good adsorbent material must have properties such as; high internal accessible volume, a high

surface area and a good pore size distribution. Its also important that the adsorbent has good mechanical properties such as strength and resistance to destruction. Chemical properties of the adsorbent such as, its degree of ionization at the surface, functional groups present, and the degree to which these properties change in contact with the solution are important considerations in determining the adsorption capacity of the adsorbent. The most widely used adsorbents for the removal of pollutants from water is activated carbon; this is attributed to the fact that it is thermally stable, highly porous and allows rapid adsorption (Dias *et al.,* 2007). Various kinds of adsorbent materials have been used for water remediation. These includes; carbon-based materials, clays, biological materials, bentonite, zeolites, metal oxide, magnetic nanoparticles, agricultural residues.

2.3.8.1 Conventional Adsorbents

Various adsorbents derived from locally available materials have been employed for the removal of pollutants such as heavy metal ions, anions, pharmaceuticals and pesticides from water (Singh *et al.,* 2020).

The effectiveness of the adsorbent depends on the number of binding sites available, their porosity, accessible surface area, and the interactions with the target pollutant (Amalina *et al.,* 2022). These adsorbents include; clay, activated carbon, biochar, metal oxides and zeolites as discussed (*vide infra*).

2.3.8.1.1 Clay Adsorbents

As a multilayered natural adsorbent clay contains minerals like; vermiculite, smectites (saponite and montmorillonite), pyrophyllite, mica, kaolinite, serpentine and sepiolite (Kumari & Mohan, 2021) . Clay's adsorption is due to the minerals' net-negative charge,

which allow it to adsorb positively charged ions. The high porosity and broad surface area account for clay's sorption capacities. Clay-based nanocomposites, for example, have been deployed as adsorbents for the removal of heavy metals (Kinoti *et al.,* 2022), pharmaceutical products and pesticides (Al-Wabel *et al.,* 2020). As an adsorbent, clay has a number of advantages like high adsorption, stability, high ion exchange capacity, and large specific surface area, however it is riddled with a number of challenges such as low surface area, regeneration, and recovery limit, limit the use of clay as an adsorbent for wastewater treatment.

2.3.8.1.2 Activated Carbon

Activated carbon typically consists of around 80% carbon with the rest being hydrogen, nitrogen, oxygen, and sulfur, alongside main functional groups such as phenols, carbonyl, carboxyl, quinones, lactones *inter alia*. Activated carbon can either be powdered or granular. Activated carbon is characterized as carbon-rich material with a well-built internal porous structure that is usually created *via* the pyrolysis and chemical treatment of natural sources including wood, coal, rice husks, sugarcane bagasse, orange peel, bamboo, and other organic wastes.

Tang *et al.* (2020) reported the removal of pharmaceuticals, pesticides and other pollutants from water using activated carbon (Tang *et al.,* 2020; Wong *et al.,* 2018). Pharmaceuticals such as acetylsalicylic acid and sodium diclofenac have been removed by activated carbon (Cimirro *et al.,* 2020; Maged *et al.,* 2020). While the removal of the antibiotic sulfonamide was reported by Wan et al. using magnetic activated carbon although it was discovered that this process is highly pH dependent. Berges *et al*., (2020) reports on the use of adsorption in the elimination of antibiotics from water onto activated carbon. The elimination of

sulfadiazine, amoxicillin, trimethoprim, and enrofloxacin has also been ascertained (Kordbacheh & Heidari, 2023). Activated carbon is an environmentally friendly and has a large internal surface area and a high degree of surface reactivity that is available for adsorption process (Singh *et al.,* 2017).

However, as an adsorbent activated carbon has certain demerits including costly chemical and thermal regeneration method and a notable adsorbent loss during regeneration (Moosavi *et al.,* 2020). Furthermore, the interaction between the pollutants and activated carbon is unpredictable because its adsorption mechanism depends on a number of factors such as electrostatic, dispersive, and chemical interactions as well as intrinsic properties of the solute and adsorbent (Chai *et al.,* 2021). Despite its high adsorption capacity it can only hold onto pollutants until the adsorption sites are completely filled (Chai *et al.*, 2021) thus leading to loss of adsorption efficacy upon regeneration, there is the possibility of secondary contamination due to pollutants being separated from the activated but not eliminated. It is therefore imperative that research on the availability and use of alternative adsorbents is done thus this study.

2.3.8.1.3 Biochar Adsorbents

Biochar is a carbon-rich product with high porosity, large surface area, enhanced capacity for ion exchange, and abundance of functional groups *(*Ambaye *et al.,* 2021*).* The ability of biochar to remove various pollutants including potentially toxic heavy metals, organic pollutants (like phenols, herbicides, and antibiotics), phosphorus, and nitrogen compounds has been documented (Chen *et al.,* 2011). Biochar derived from eucalyptus wood chips has been applied in the removal of imidacloprid from water (Srikhaow *et al.,* 2022) with the maximum adsorption capacities for the investigated pesticides being 14.75 mg/g for

imidacloprid (Srikhaow *et al.,* 2022). In addition, biochar-based adsorbents for pesticides, pharmaceuticals, phosphorus, and heavy metal removal from polluted water have been reported (Bocșa *et al.,* 2023; Puga *et al.,* 2016; Ambaye *et al.,* 2021)). Equally, the use of biochar derived from grapefruit husk for removal of pharmaceuticals has been documented (Cheng *et al.,* 2020). The adsorption performance of biochar is limited by the need for multiple modification techniques to produce biochar composite materials with enhanced adsorption capabilities in addition to its high energy consumption. Thus, producing biochar typically calls for high energy and temperature inputs. While various surface modifications for biochar can boost its adsorption capacity, they may also hinder the regeneration process.

2.3.8.1.4 Metal Oxides

Due to their low toxicity, high thermal stability, large surface area, porous structures, ease of recovery, and the presence of lewis acid-base sites in their structures, metal oxide nanoparticles do exhibit momentous potential for wastewater remediation (Nagpal *et al.,* 2019). It has been demonstrated by earlier research that metal oxide nanoparticles are capable of effectively removing a wide range of pollutants from aqueous environments, including heavy metals, dyes, and naturally occurring organic matter. The Fe_3O_4 and $MgFe_2O_4$ nanoparticles have been used for the removal of ciprofloxacin and chlorpyrifos from wastewater *via* a batch technique (Aydin *et al.,* 2019; Sharma *et al.,* 2017; Fallah *et al.,* 2021).

Metal oxides can be used as absorbents in water treatment, luckily there aren't many restrictions. For instance, reducing metal oxide to a nanoscale size increases surface area but due to Van der Waals interactions, this increase may also cause the metal oxide to become unstable and more susceptible to agglomeration. The metal oxide may then loose

its high capacity, mechanical strength and selectivity as a result of this interaction. Furthermore, the application of certain metal oxides in water treatment is restricted due to their wide energy gap and low quantum yield caused by a rapid recombination of photogenerated charge carriers.

2.3.8.1.5 Zeolites

Zeolites are a family of crystalline aluminosilicates materials with interconnected micropores that exhibit tremendously narrow pore-size distribution (Cao *et al.,* 2022). The zeolite frameworks are built from an infinitely extending three-dimensional tetrahedral network of silicate (SiO_4) and aluminate (AlO_4) linked to each other by the shared oxygen atoms (Moshoeshoe *et al.,* 2017). The framework atom is usually silicon (Si) and aluminum (Al), however other metals such as sodium (Na), calcium (Ca), gallium (Ga), germanium (Ge), boron (B) and titanium (Ti) can take the place of Si and Al (Panda $ Dash, 2020). It should be noted that the charge can be balanced by the presence of exchangeable extra-framework cations. Tetrahedral molecules have the ability to form a variety of oligomers, such as 3-, 4-, 5-, 6-, 8-, 12-, and 20-rings, which can then be combined to form the secondary building units that constitute different cylinders or cages. As a result, different topologies with different pore diameters that may be small, medium, or large as well as pore systems with one, two, or three dimensions and internal cages where pollutants may react or be entrapped.

Zeolites have garnered significant attention in the scientific community due to its exceptional physicochemical properties, widespread availability, and cost-effectiveness (Abdelwahab & Thabet, 2023). Zeolites present compelling potential as adsorbents and

catalyst carriers in water treatment processes, thanks to their distinctive adsorption characteristics and their substantial ion exchange capacity.

Zeolites, due to their distinct pore structure, are highly ordered microporous tetrahedron structural materials with highly hydrophobicity, good thermal stability, hydrothermal stability, accessible surface modification, good ion exchange capacity, high specific surface area, and high pore volume (Dehmani *et al.,* 2023).

The pore size of zeolites varies with zeolite species, allowing selective adsorption for molecules of different sizes. Zeolites' unique properties make them attractive for a wide range of applications, particularly in water purification. They serve as effective adsorbents for removing contaminants like heavy metals, organic compounds, and radioactive materials through various interactions such as van der Waals forces, electrostatic forces, and chemical bonding (Dehmani *et al.,* 2023).

2.3.8.1.5.1 Classification of Zeolite

Presently the International Zeolite Association (IZA) recognizes 255 unique zeolite frameworks which are either found in nature or with synthetic origin (Bukowski *et al.,* 2021). Each zeolite framework is assigned a three-letter acronym code for identification as shown in Table 2.3

The FTC acronym which is used to identify each distinctive zeolite framework is derived from the name of the zeolitic material identifying the unique topology. For instance; FAU stands for Faujasite, CLO refers to cloverite zeolite, HEU means haulandite and MTN designates the synthetic zeolite ZSM-39 (Zeolite Socony Mobil – Thirty-Nine) (Baerlocher, McCusker, & Olson, 2007). These symbols describe all variants of a

framework with a given topology, irrespective of composition, Si, and Al distribution, cell dimension and symmetry.

Table 2. 3: Approved Framework Type codes (FTC) by the structure Commission of International Zeolite Association (IZA) (McCusker & Baerlocher, 2019)

	FTC	**Name**		**FTC**	**Name**		**FTC**	**Name**
1.	AET	ALPO-8	13	BRE	Brewsterite	25	TSC	Tschortnerite
2.	MER	Merlinoite	14	MEI	ZSM-18	26	FER	Ferrierite
3.	ANA	Analcite	15	ERT	ECR-34	27	CHA	Chabazite
4.	ETR	ECR-34	16	MWW	ZSM-25	28	MON	Montesommaite
5.	AFN	AIPO-14	17	FAR	Farneseite	29	LTA	Linda type A
6.	CHI	Chiavennite	18	IFO	ITQ-51	30	LAU	Laumontite
7.	GME	Gmelinite	19	BOG	Boggsite	31	SBE	UCSB-8CO
8.	DFO	Decamethonium	20	BOZ	Berylium-10	32	HEU	Heulandite
9.	IRY	ITQ-40	21	SBS	UCSB-6Gaco	33	PAU	Paulingite
10.	MFI	Zsm-5	22	MOR	Mordenite	34	NAT	Natrolite
11.	CLO	Cloverite	23	MRE	Zsm-48	35	AWW	AIPO-22
12.	FAU	Faujasite	24	DAC	Dachiardite	36	LAU	Laumontite

2.3.8.1.5.2 Micropore System of Zeolites

The known applications of zeolites as molecular sieves, adsorbents and catalysts are based on their micropore systems (Pérez-Botella *et al.,* 2022). The micropores of each type of framework are characterized by their diameter or pore size, shape and channel dimensions. The minimum number of interlinked T-sites that surround the pore provides an indication of the micropore diameter. The micropore is then referred as an n-membered ring (n-MR), where n is the number of T-sites forming the pore.

However, these values can change from one framework to another depending on structural distortions. For example; some of the pore diameters are: 7MR (MEI), 9MR (CHI), 11MR (JSR), 14MR (AET), 15MR (IRY), 16MR (IFO), 18MR (ETR), 20MR (CLO) and 21MR (EWT) (Hernandez, 2017).

The micropore can also be straight or sinusoidal as observed in zeolites of lower symmetry. The pore system of zeolites is also characterized by the number of Cartesian directions or dimensions that a molecule can span within the channels. For instance; a molecule may be only able to diffuse along a pore, unable to move to another pore at an intersection. In this case, the pore system of the zeolite is defined as one-dimensional (Schulman *et al.,* 2020). Some examples of framework types with one dimensional channel are AWW and ABW. The next level in this classification comprises in the two-dimensional pore system. Here, the molecule can move in the two-dimensional plane formed by a network of inter-linked pores (Hernandez, 2017). The UEI and ZON framework types are examples of zeolites with two-dimensional channels. Finally, in the three-dimensional pore system a molecule can cover the entire volume of the crystal by moving through the pores. The CLO, PAU, FAU, MWF, TSC and HEU framework types contain three-dimensional channels.

2. 3.8.1.5.3 Application of zeolites in the removal of heavy metal ions, anions and Organic Pollutants

In the past few decades, several experimental studies on the removal of anions from water by zeolite materials have been reported. For example, removal of CrO_4^{2-}, AsO_4^{3-}, and PO_4^{3-} using CHA, MON, FER, and HEU zeolites was investigated (Barczyk *et al.,* 2014) and the adsorption of sulphate, hydrogen chromate and dihydrogen phosphate anions on surfactant-modified clinoptilolite studied (Barczyk *et al.,* 2014). Likewise, the removal of chromate from water using surfactant modified pohang clinoptilolite and haruna chabazite and the use of hydrophobic Fe-Zeolites in the removal of MTBE from water by combination of adsorption and oxidation has been reported (Gonzalez-Olmos *et al.,* 2013). Mažeikiene *et al.,* (2008) as well did report the removal of nitrates and ammonium ions from water using clinoptilolite. The treatment of drinking water containing excess amount of nitrate using a functionalized natural zeolite (Onyango *et al.,* 2010) and the adsorption of asenate ions on surfactant-modified natural zeolites has been reported (Chutia *et al.,* 2009).

Also, Datt et al used quantum calculations to understand the nature of intermolecular interactions between the zeolite host and the aspirin (Lee *et al.,* 2018). It was established that the release of the aspirin from the zeolite was dependent on the hydrophobicity of the zeolite host with more hydrophobic zeolites releasing the aspirin less readily. Adsorption of butanol isomer, toluene and chlorofluorocarbons on zeolites using molecular simulation has also been investigated by several authors (Lee *et al.,* 2018). However, there are limited studies on the adsorption of anions and in particular CrO_4^{2-}, AsO_4^{3-}, NO_3^- and PO_4^{3-} by zeolites. For example an investigation on the Phosphate ($H_2PO_4^-$ and HPO_4^{2-})

and phosphoric acid adsorption in zeolite clinoptilolite by electronic structure methods has been done (Uzunova & Mikosch, 2016).

They established that the B-channel of clinoptilolite, which is accessible via eight-member ring windows, provides more favorable coordination to phosphates and phosphoric acid in presence of cations. In a similar manner, Tribe *et al., (*2012) studied the interactions of HNO_3 and NO_3^- with kaolinite surfaces, and the results were compatible with the ranges assigned in the literature for NO_3^- on mineral surfaces for the frequency of the vibrational symmetric stretches and for the low-frequency branch of the asymmetric stretches.

2.4 Type of Adsorption Mechanism

The adsorption mechanisms reported in the literature are exclusively either chemisorption or physisorption, based on the strength of interactions between sorbate and sorbent (Gusain *et al.,* 2020)

2.4.1 Physisorption Mechanism

Physisorption is an ionic interaction that is relatively non-specific and occurs due to the operation of weak forces between molecules. It occurs when intermolecular forces are responsible for binding the pollutant to the adsorbent surface. These forces usually occur as a result of particular geometric and electronic properties of the adsorbent and adsorbate (Sawyer *et al.,* 2003; Thommes *et al.,* 2015; Rodriguez-Reinoso *et al.,* 2015). The adsorption is dependent on the temperature, pressure, and the nature of the adsorbent and adsorbate. It is characterized by low adsorption activation energies (< 20 kJ mol^{-1}) and ease of desorption hence it is a reversible process (Yang *et al.,* 2011).

2.4.2 Chemisorption Mechanism

Chemisorption is also based on electrostatic forces, but much stronger forces play a major role on this process. In chemisorption, the attraction between adsorbent and adsorbate is due to a covalent bond or electrostatic forces among atoms (Sawyer *et al.,* 2003). It involves the exchange of electrons between the adsorbent surface and the adsorbent resulting in the formation of chemical bonds (Sharma *et al.,* 2016). It is mostly characterized by the enthalpy of the system being endothermic as energy is used up during the formation of new chemical bonds.

It requires more energy than physisorption and is characterized by high adsorption activation energies (40 to 800 kJ mol^{-1}) (Cantu *et al.,* 2014). Ion exchange may also be responsible for some chemical adsorption processes whereby the ions present on the adsorbent surface are replaced by ions from the adsorbate. This process is characterized by intermediate adsorption energies (20 to 40 kJ mol^{-1}(Cantu *et al.,* 2014). Adsorption free energy (E) is another distinguishing factor for the type of adsorption and is classified as $E < 8$ kJ mol^{-1} (physisorption), $8 > E < 20$ kJ mol^{-1} (chemical ion exchange), and $E > 20$ kJ mol^{-1} (chemisorption).

2.5 Adsorption Isotherm Modelling

Adsorption data is modelled to determine the optimum parameters for adsorption and determine the nature of binding between the adsorbent and the adsorbate. The evaluation of adsorption efficiency using isotherm, kinetic models, and thermodynamic parameters is very effective in predicting the adsorption mechanism (Fallah *et al.,* 2019).

2.5.1 Thermodynamic Modelling

Thermodynamic modelling of adsorption data provides information about the type and mechanism of adsorption (Alnajrani & Alsager, 2020; Qu *et al.,* 2020).To calculate adsorption parameters, isotherm models are applied and used to evaluate the adsorption data. The conventional adsorption isotherms are used to determine the relationship between the equilibrium adsorption capacity and the equilibrium concentration at a certain temperature (Chakraborty *et al.,* 2021). Adsorption isotherms are very useful for determining the adsorption capacity and the interactions between adsorbate and adsorbent (Alnajrani & Alsager, 2020). The most common isotherms are the Langmuir and Freundlich which indicate whether the adsorption is monolayer or multilayer in nature and can be used to calculate the maximum adsorption capacity of the adsorbent (Chakraborty *et al.,* 2021).

Redlich-Peterson and Sips isotherms are three parameter models which are more versatile and are often used to confirm homogeneity or heterogeneity of the adsorption system. Dubinin-Raduschkevich and Flory-Huggins models are used to determine the mean adsorption energy, change in Gibbs free energy, enthalpy and entropy of the system which provide information on the adsorption mechanism (Chakraborty *et al.*, 2021; Ouma *et al.,* 2018).

2.5.1.1 Langmuir

The Langmuir model assumes that the adsorbed molecules form a monolayer and that adsorption can occur at a fixed number of homogeneous adsorption sites (Meena, *et al.,* 2005). Moreover, it assumes that every molecule has constant enthalpy and sorption activation energy, meaning that all molecules have equal affinity to all adsorption sites

(Chakraborty *et al.,* 2021).The non-linear expression is given by equation 2.1 (Almasri *et al.,* 2018; Chakraborty *et al.,* 2021; Qu *et al.,* 2020).

$$q_e = \frac{q_m K_L C_e}{1 + K_L C_e} \tag{2.1}$$

where; q_e is the adsorption capacity of pollutants at equilibrium (mg g $^{-1}$), C_e is the concentration of adsorbate at equilibrium (ppm), K_L is the Langmuir constant (L mg^{-1}) and q_m is the monolayer adsorption capacity(mg g^{-1}) (Chakraborty *et al.,* 2021; Langmuir, 1918; Majd *et al.,* 2021).

2.5.1.2 Freundlich Adsorption Model

The Freundlich adsorption model is used to describe the adsorption of pollutants that occur on heterogeneous adsorbent surfaces and active sites. It is an empirical equation with little theoretical basis used to describe the distribution of solute between solid and aqueous phases at a point of saturation (Meena *et al.,* 2005).

It is used to describe the strength of pollutants adsorption towards the adsorbent surface. The basic assumption of Freundlich adsorption model shows an exponential variation in site energies of adsorbent (Choy *et al.,* 2004; Khatoon *et al.,* 2013; Pan, *et al.,* 2012). It is based on a reversible adsorption process on a heterogeneous surface but it is not restricted to monolayer coverage and assumes increasing adsorption with an increase in solution concentration (Sheikhi & Rezaei, 2021). The Freundlich isotherm is derived by assuming a heterogeneous surface with a non-uniform distribution of heat of adsorption over the surface (Odoemelam *et al.,* 2015). It can be expressed by the nonlinear equation 2.2 (Almasri *et al.,* 2018; Edet & Ifelebuegu, 2020; Mahmoodi *et al.,* 2011).

$$q_e = K_F C_e^{1/n} \quad (2.2)$$

where; q_e (mg g^{-1})is the amount adsorbed in terms of equilibrium adsorption capacity, C_e (mg L^{-1}) is the equilibrium concentration of adsorbate, K_F is the Freundlich isotherm constant and n is the adsorption intensity (L g^{-1}) are constants related to adsorption capacity and intensity respectively

2.5.1.3 Temkin Adsorption Model

The Temkin isotherm explains the nature of adsorption in a heterogeneous system. It assumes that the adsorption heat decreases linearly with increasing adsorption capacity. The Temkin adsorption model is as shown in equation 2.3.

$$q_e = B_1 lnKT + B_1 lnC_e \quad (2.3)$$

where; B_1 = RT/b, T is the absolute temperature (K) and R is the universal gas constant (8.314 J/$mol^{-1}K^{-1}$). B_1 is a constant related to the heat of adsorption (J/mol), K_T is the equilibrium binding constant (L/g) corresponding to the maximum binding energy (Albadarin *et al.,* 2011; Rupa *et al.,* 2019)

2.5.1.4 Redlich-Peterson Model

Redlich-Peterson (R-P) isotherm model incorporates three parameters into an empirical equation. This model is versatile and can be applied to either homogenous or heterogenous systems. It has a high concentration dependence with a linear relation in the numerator and exponential dependence in the denominator. It is described by equation 2.4

$$q_e = \frac{K_R C_e}{1 + \alpha_R C_e^{\beta}} \quad (2.4)$$

where; K_R (L/mg) is a constant related to adsorption capacity, α_R (L/mg) is a constant related to binding site affinity and β is an exponent related to the adsorption intensity (Kupeta *et al.,* 2018; Lee *et al.,* 2017).

When the exponent β =1 the equation reduces to Langmuir isotherm and it approaches Freundlich equation at high concentrations (Kupeta *et al.,* 2018).

2.5.1.5 Sips Adsorption Model

The Sips isotherm also referred to as Langmuir-Freundlich isotherm, is derived from both Langmuir and Freundlich isotherm models (Rostamian and Behnejad, 2016). Sips isotherm is described by equation 2.5

$$q_e = \frac{q_{\max} K_S C_e^{1/n}}{1 + K_S C_e^{1/n}} \tag{2.5}$$

where; q_e (mg g^{-1}), $q_{\max}$ (mg g^{-1}) and C_e (mg L^{-1}) are the adsorption capacity at equilibrium, maximum adsorption capacity and solution concentration at equilibrium, respectively. K_S (L mg^{-1}) is the Sips isotherm constant related to the affinity of binding sites and 1/n is the heterogeneity index.

The heterogeneity factor in this model is used to distinguish between the two isotherm models. Heterogeneity values close to 1 indicate a homogenous system while lower values indicate a heterogenous system. (Albadarin *et al.,* 2013; Cao *et al.,* 2014; Pakade *et al.,* 2017).

2.5.1.6 Dubinin-Raduschkevich

Fitting experimental data using the Dubinin-Radushkevich (D-R) model (equation 2.6) allows for the calculation of the mean adsorption energy from which the determination of either physical or chemical adsorption can be made (Argun *et al.,* 2007). The linear relation is given by equation 2.7

$$\ln q_e = \ln \mathrm{q}_m - \beta\varepsilon^2 \tag{2.6}$$

$$\varepsilon = RT \ln (1 + {}^{1}\!/\!_{C_e}) \tag{2.7}$$

$$E = {}^{1}\!/\!_{\sqrt{2\beta}} \tag{2.8}$$

where; q_e (mg g^{-1}) is the adsorption capacity at equilibrium, q_m (mg g^{-1}) is the maximum adsorption capacity, β (mol^{-2} kJ^{-2}) is a constant related to adsorption energy and ε (eq 2.8) is the potential of the surface, R is the gas constant (8.314 J K^{-1} Mol^{-1}) and T (K) is the absolute temperature of the system (Almasri *et al.,* 2018).

2.5.1.7 Flory-Huggins

The Flory-Huggins (F-H) model is used to calculate the parameters necessary for thermodynamic evaluation of an adsorption process. The model is described by equation 2.9.

$$\log {}^{\theta}\!/\!_{C_0} = \log K_{FH} + n_{FH} \log(1-\theta) \tag{2.9}$$

where; θ is the degree of surface coverage (equation 2.10), C_0 (mg L^{-1}) and C_e (mg L^{-1}) are the initial and equilibrium solution concentrations, respectively, K_{FH} (L g^{-1}) is the model equilibrium constant and n_{FH} is the model exponent representing the number of ions occupying adsorption sites (Nechifor *et al.,* 2015).

$$\theta = (1 - {C_e}/{C_0}) \tag{2.10}$$

The change in Gibbs free energy (ΔG) (kJ mol^{-1}) can be determined using the F-H equilibrium constant (K_{FH}) (L g^{-1}) (equation 2.11)

$$\Delta G = RT \ln K_{FH} \tag{2.11}$$

where; R is the gas constant (8.314 $Jmol^{-1}K^{-1}$) and T (K) is the absolute temperature

Equation 11 can be applied in the calculation of the change in enthalpy (ΔH) (kJ mol^{-1}) and change in enthalpy (ΔS) ($Jmol^{-1}K^{-1}$) (equation 2.12).

$$\Delta G = \Delta H - T\Delta S \tag{2.12}$$

2.6 Adsorption Kinetics Models

Kinetics provide information regarding the mechanism of adsorption that is important for the efficiency of the process (Dehbi *et al.,* 2020). It is important to know the rate of adsorption in the removal of contaminants from wastewater for design optimization. This is because the kinetics of adsorption determines the adsorbate residence time and adsorption column dimensions. As a result, predicting the rate at which adsorption takes place for a given system is probably the most important factor in adsorption system design (Baccar *et al.,* 2010).

Kinetic studies are generally described by the following stages: (i) External diffusion; defined by diffusion of molecules from the bulk phase to the interface, (ii) Internal diffusion; Diffusion of molecules inside pores, (iii) Surface diffusion; diffusion of molecules on the surface of the adsorbent (Sahoo & Prelot, 2020). These stages are important in the determination of the rate limiting step in the adsorption process thereby increasing the understanding of the adsorption mechanism. Kinetics studies also aid in the determination of physical or chemical adsorption allowing for the comparison of different adsorbents used in adsorption of similar pollutants (Agrawal & Singh, 2016).

To understand adsorption kinetics models such as *pseudo*-first order, *pseudo*-second order, Elovich and intra-particle diffusion are used to fit the data and the model parameters are then used to evaluate the adsorption process (Ho, 2006; Rupa *et al.,* 2019).

2.6.1 *Pseudo*-First Order Model

This model describes adsorption kinetics preceded by the diffusion through a boundary layer (Enos *et al.,* 2010). It assumes that the adsorption rate depends only on the adsorbate concentration (Shikuku *et al.,* 2018). It is given by equation 2.13.

$$q_t = q_e(1 - e^{-k_1 t}) \tag{2.13}$$

where; q_t (mg g^{-1}) is the adsorption capacity at time t (min), q_e (mg g^{-1}) is the equilibrium adsorption capacity and k_1 (min^{-1}) is the pseudo-first order rate constant.

2.6.2 *Pseudo*-Second Order Model

This model assumes that (i) the rate of reaction is proportional to the number of active sites on the adsorbent surface, (ii) the adsorption process occurs in two steps where the first is a

fast reaction equilibrating quickly followed by a slow step, (iii) the rate limiting step is a chemical process involving the sharing or exchange of electrons between the adsorbate and the adsorbent surface (Albadarin *et al.,* 2011; Enos *et al.,* 2018).

Pseudo-second order kinetics is described by equation 2.14.

$$q_t = \frac{k_2 q_e^2 t}{1 + k_2 q_e t} \tag{2.14}$$

where; k_2 (g mg^{-1} m is the *pseudo*-second order rate constant and h (mg g^{-1} min^{-1}) is the initial sorption rate (equation 2.15

$$h = k_2 q_e^2 \tag{2.15}$$

A higher initial sorption rate, indicates a higher affinity of the adsorbent for the adsorbate (Cheng *et al.,* 2016).

2.6.3 Elovich Model

This model describes the variation in chemical adsorption and is based on the assumption that the adsorbent surface consists of heterogenous energies and there are no interactions between the adsorbed molecules (Elovich, 1962; Han *et al.,* 2016). The model is given by equation 2.16.

$$q_t = \frac{1}{\beta} \ln(1 + \alpha\beta t) \tag{2.16}$$

where; α (mg g^{-1} min^{-1}) is the initial rate of chemisorption and β (g mg^{-1}) is the desorption constant (Namasivayam & Sureshkumar, 2008).

Activation energy for chemisorption and the extent of surface coverage are also related to the constant β. A higher value for α than β is desirable as it indicates viability of the adsorption process.

2.6.4 Intra-Particle Diffusion

According to the intraparticle diffusion relation, a plot of adsorption capacity versus the square root of time yields a straight line if it controls the adsorption process. However, intraparticle diffusion is the only rate limiting step if the line passes through the origin (Shikuku *et al.,* 2015). A high correlation coefficient for the intra-particle diffusion model implies that adsorption occurs in the pores of the adsorbent (Shikuku *et al.,* 2015). The model is described by equation 2.17.

$$q_t = k_{id} t^{0.5} + C \tag{2.17}$$

where; k_{id} (mg g^{-1} $min^{-0.5}$) is the intra-particle diffusion rate constant and C is the intercept reflecting the thickness of the boundary layer.

2.7 Modelling Sorption via Computational Simulations

Quantum chemical computations have been used to elucidate the adsorption sites where molecules are adsorbed on the adsorbents. This can be achieved by determining the adsorption isotherms, binding sites, binding energy and identification of the geometrical changes that occur on the adsorbent after adsorption (Nakhli *et al.,* 2020).

It is worth noting that molecular simulations provide theoretical framework which is based on statistical mechanics that model the properties of the adsorption process. It provides a molecular-level interpretation of thermodynamic quantities like free energy, entropy, heat or work (Singh *et al.,* 2022). For example, with molecular simulations one can compute

the number of molecules that are adsorbed into a surface pore at a given pressure, detect phase transitions or calculate stability

Using statistical quantum mechanics, one is able to comprehend and interpret further the measurable macroscopic properties of materials in terms of the properties of their constituent particles and therefore the interactions that they have with each other. This connect the microscopic world of molecular interactions with the macroscopic world of collective properties (e.g., pressure, density or free energy) (Ge *et al.,* 2013). This connection is made through ensemble averages or time averages as described by classical statistical mechanics (Fainerman *et al.,* 2012).

The molecular mechanics (MM) method, also known as the force-field method, uses the classical type of model to predict the energy of a molecule as a function of its conformation. It allows the prediction of equilibrium geometry along with its transition states and relative energies between and within the molecules (Singh *et al.,* 2022). This method applies Newtonian mechanics to predict the minimum static energy structure of a system. Despite being able to supply the potential energy for larger molecules, the MM method is not appropriate for bond breaking reactions (Massobrio & Blandin, 1996).

Another important technique in molecular simulation is Molecular Dynamics (MD). The idea behind MD is to generate a representative trajectory of the system over time (Massobrio & Blandin, 1996). To do so, calculation of forces between the atoms explicitly and calculates how the system evolves in time using Newton's equations of motion. At each time step, the forces on the atoms are calculated and combined with their current positions and velocities to create new positions and velocities. The atoms are moved to their new positions, the forces updated and a new cycle begins (Singh *et al.,* 2022). These

dynamically generated states are averaged in time to determine the system properties. A simulation must be carried out for a large number of time-steps to obtain reliable averages. The starting conditions are the positions and the velocities of the constituent atoms. The velocities can be generated from a previous run or by using random numbers and later scaled to the desired temperature (Singh *et al.,* 2022). The Maxwell-Boltzmann distribution is rapidly reached by molecular collisions typically within a few hundred-time steps. In the context of adsorption of pollutants on mesoporous materials, MD simulations can be used to study the adsorption process at the molecular level and to understand the mechanisms that control it (Bukowski *et al.,* 2021). Mesoporous materials are materials like zeolites with pores of intermediate size (2-50 nm) and high surface area, which makes them ideal for use in adsorption applications. By studying the adsorption of pollutants on mesoporous materials using MD simulations, insights into the factors that affect the adsorption process are gained, such as the size and shape of the pores, the chemical composition of the material, and the nature of the pollutant molecules. One potential application of MD simulations in this context is the design of more efficient mesoporous materials for pollutant removal. By simulating the adsorption process on a range of different materials and under different conditions, the optimal material properties and conditions for efficient pollutant removal are identified. Another potential application of MD simulations is the prediction of the adsorption capacity of mesoporous materials for different pollutants. By simulating the adsorption of different pollutant molecules on a given mesoporous material, the maximum amount of pollutant that can be adsorbed under different conditions are determined. Overall, MD simulations can provide valuable insights into the adsorption of

pollutants on mesoporous materials and help in the development of more efficient and effective strategies for pollution alleviation (Zeng *et al.,* 2022) .

MD simulations show various aspects that affect the adsorption process, such as the electrostatic interaction, binding energy, Gibbs free energy, adsorption energy and loading value. The binding energy affects the molecule's structural stability, whereby the negative value of the binding energy shows that the structure is stable. Studies have shown that the higher the adsorption energy, the more the adsorption capacity of the adsorbent and hence the better the adsorbent (Sholl, 2006).

Gibbs free energy help in understanding the adsorption process by indicating the thermodynamic feasible interaction of the adsorbent with sorbate (Sholl, 2006). A negative value of Gibbs free energy indicates a spontaneous reaction, which demonstrates feasibility of the adsorbent to adsorb the pollutant and vice versa.

While molecular simulation has evolved over time, driven by the rapid increase of raw computing power, the invention of clever algorithms, and the development of efficient and user-friendly software packages, it is still some distance away from the grand. It may not be possible to understand and accurately predict emergent phenomena all the way from the atomistic to the macroscopic scale. For instance, the precise prediction of phase diagrams of materials from first principles is often out of reach of current capabilities and so is the simulation of many biomolecular processes (Bukowski *et al.,* 2021).

Molecular simulation methods play an important role in the study of the behavior of microscopic and macroscopic processes. A well-designed computer simulation can predict thermodynamic properties and can be a substitute for experiments (Salahshoori *et al.,* 2023). Molecular simulation can also provide data that is inaccessible through

experimental methods or when the experiment has components that are too dangerous or too expensive (Bukowski *et al.,* 2021). At the same time, they offer the possibility to create hypothetical scenarios and to test theories. Computer simulations can also help to provide a molecular understanding of why the observed events occur.

Simulation applications can be used to model and optimize the performance of zeolites in water purification. For example, molecular dynamics simulations can be used to study the adsorption behavior of water molecules and contaminants on zeolite surfaces at the atomic level. This information can then be used to design more efficient and effective zeolite structures for water purification applications.

Computational fluid dynamics (CFD) simulations can also be used to model the flow of water through zeolite beds and to optimize the design of zeolite water purification systems. CFD simulations can help predict the flow patterns, pressure drop, and residence time distribution of water in zeolite beds, which can be used to optimize the design of zeolite-based water treatment systems for maximum efficiency. In addition, simulations can be used to study the impact of different operating conditions on the performance of zeolite water purification systems. For example, they can be used to study the effect of temperature, pH, and flow rate on the adsorption capacity and selectivity of zeolites. Overall, simulation applications can play an important role in the design and optimization of zeolite water purification systems, helping to improve the efficiency and effectiveness of these systems for providing safe and clean water.

2.8 Laboratory Based Adsorption Studies

The laboratory-based adsorption studies can be classified into two; batch and continuous system. A batch system involves the agitation of the adsorbent and adsorbate mixture for a

specific period of time without a continuous inflow and outflow. A particular weight of the adsorbent is used with a specific volume of the contaminated water. After agitation, the residual concentration is then quantified, and the adsorbent material is regenerated for subsequent use. This system is mostly employed in the treatment of a small volume of contaminants (Thommes *et al.,* 2015).

On the other hand, continuous flow system does not involve the agitation of the adsorbent and adsorbate mixture. A particular weight of the adsorbent is packed into a column, and the fluid containing the contaminant is run continuously through it. In this system, there is room for varying the flow rate of the fluid. The spent adsorbent can also be regenerated for subsequent use. It can be applied in the treatment of a large volume of wastewater. The types of continuous flow system include: fixed bed adsorption system, fluidized bed adsorption system and moving bed adsorption system (Thommes *et al.,* 2015).

2.8.1 Factors Affecting Adsorption

The adsorption of pollutants onto the adsorbent is affected by several factors as discussed below.

2.8.1.1 Contact Time

Adsorption in the initial step occurs at a rapid rate where their capacities exhibit a quick rise at the start of the experiment as a result of large surface area and large amount of unoccupied adsorption active sites of the adsorbent. Also, with the duration of adsorption process, the active sites which were available turn saturated ultimately reaching an equilibrium state (Han *et al.,* 2022).

2.8.1.2 Solution pH

Solution pH is an important factor affecting adsorption especially in ionic based systems since adsorption efficiency of these systems is highly dependent on solution pH (Pan *et al.,*

2012). Metal oxidation states as well as adsorbent surface functional group ionization are pH dependent and therefore affect the adsorption of the pollutants. Surface groups are either protonated or deprotonated depending on the solution pH (Singh *et al.,* 2016). Also, extremely low pH indicates a higher concentration of H^+ free ions in the solution, in the ion exchange action of the zeolite, improving the clash among the H ions and the metal getting adsorbed, causing their damage due to competition between the chemical species and metal to be adsorbed, which decreases the rate of adsorption.

2.8.1.3 Adsorbent Mass

The mass of adsorbent used plays an important role on the amount of pollutant adsorbed. It affects the number active sites on the surface and the available surface area. Generally, an increase in adsorbent mass results in an increase in the adsorption to a certain limit, beyond which, adsorption may remain unaffected or even reduce if there is an interference due to hindered mass transfer due to altered solution viscosity (Adeli *et al.,* 2017).

2.8.1.4 Adsorbate Concentration

Increasing the adsorbate concentration generally increases the competition for available adsorption sites. This increases the concentration gradient between the adsorbent surface and the adsorbate solution resulting in increased adsorption capacities (Ouma *et al.,* 2018).

2.8.1.5 Temperature

When using zeolites for adsorption, temperature is also a significant factor. The temperature causes the ions to become more mobile and encourages the zeolite's crystalline structure to expand, both of which raise the adsorption rate (Somashekara & Mulky, 2023). A rise in the temperature leads to a rise in the removal strength, which supports the point that the elimination methods were impulsive, attainable, and endothermic in nature, and

can be further stated by the active sites of adsorbent available in addition to the expansion of the pores and surface area at elevated temperatures. With respect to the thermodynamic properties and their temperature-related behavior, suggests that the adsorption reaction is enhanced by decreasing temperature, while the desorption reaction can be favored by increasing the temperature (Raza *et al.,* 2021).

2.8.2 Methods of Characterizing of Adsorbents

The characterization of adsorbent materials is crucial in understanding their properties and their application in adsorption of pollutants. Specific techniques are used to analyze morphology, particle size, structures of the materials, physical and chemical properties of the adsorbent. Commonly used instrumental techniques for characterization of adsorbent are discussed below.

2.8.2.1 Energy Dispersive X-ray Spectroscopy

Energy Dispersive X-ray Spectroscopy (EDX) is a technique used for the elemental analysis of materials. It works by measuring the energy of X-rays emitted by a sample when it is bombarded with high-energy electrons or X-rays. When the X-rays interact with the sample, they cause the electrons in the sample to be excited and jump to higher energy levels. As these electrons return to their original energy levels, they emit X-rays of characteristic energies, which can be detected and used to identify the elements present in the sample. EDX analyses provide information about the relative abundance of elements present in the sample, as well as their distribution within the material. This information can be used to identify the types of elements present in the adsorbent, as well as any impurities or contaminants that may be present. In addition to elemental analysis, it can also be used to perform mapping and line scans of the sample. Mapping involves collecting data on the

elemental composition of the sample over a defined area, while line scans involve collecting data along a specific line on the sample surface (Von-Kiti, 2012).

2.8.2.2 Powder X-ray Diffraction (PXRD)

Powder X-ray Diffraction (PXRD) is a technique used to analyze the structure of crystalline materials. It involves illuminating a beam of X-rays onto a powdered sample and measuring the resulting diffraction pattern. When the X-rays hit the sample, they interact with the electrons in the material, causing them to diffract in different directions.

This diffraction pattern is then captured by a detector and analyzed to determine the crystallinity of the sample. PXRD can be used to determine crystal structure, and investigate the purity and quality of adsorbents. XRD is a non-destructive technique that requires extremely little amounts of sample. Due to the random orientation of the material, all potential diffraction directions for the lattice can be found by scanning the range of samples, the range of 2ɵ angles. Because each material has a unique set of d-spacings, converting the diffraction peak to d-spacings enables for sample identification. This is often accomplished by comparing the d-spacing to the usual reference pattern (Von-Kiti, 2012).

2.8.2.3 Scanning Electron Microscopy

Scanning electron microscopy (SEM) is used to detect and analyse the surface structures of the sample of interest. The electron gun generates a beam of electrons down the column. The generated electrons are then accelerated down a vacuum column. The beam of electrons is then directed to the electromagnetic lenses which are wrapped with solenoid. Beam of electrons are then focused onto the stage where the sample is placed. The interaction between the incident beam and the surface of the sample is determined by the acceleration rate of the incident electrons. Upon the incident electrons coming into contact

with the sample, energetic electrons are released from the sample surface (Von-Kiti, 2012). This then leads to the formation of the scattering patterns which gives information on the external morphology (texture), chemical composition, crystalline structure and orientation of materials making up the sample (Manjunatha *et al.,* 2019).

2.8.2.4 Fourier Transform Infrared (FTIR) Spectroscopy

FTIR spectroscopy provide information on fundamental vibrations of characteristic functional groups present in an adsorbent. Analysis by IR spectroscopy is limited to energies between 4000 – 400 cm $^{-1}$ to some extent the far IR region of electromagnetic spectrum (Kuehl, 2021).

The analysis by FTIR spectroscopy is limited to molecules having permanent dipole moments or phonons in crystalline materials. The FTIR spectrum is collected as absorbance or the percent transmittance of light as a function of wavelength or often its inverse, the wavenumber, cm^{-1} is usually used (Younis *et al.,* 2021). Quantitatively, the amount of energy absorbed at a given frequency depends on both molecular concentration and molecular structure. FTIR is used to identify functional groups in the sample. Data interpretation of characteristic bands is a simple correlation and reference to charts of characteristic group frequencies (Asiedu, 2016).

CHAPTER THREE

MATERIALS AND METHODS

3.1 Computational methods

Objective 1; To evaluate the adsorption of $Pb^{2+,}$ Cd^{2+}, NO_3^- and PO_4^{3-} onto zeolite frameworks using computation simulations

Methodology; The structures of the zeolites were taken from the International Zeolite Association (IZA) structure database (Baerlocher, 2008). The structures of the selected ions were obtained from Pubchem. Prior to sorption simulation the structures of the ions and zeolites were optimized by $Dmol^3$ and Forcite, respectively. To study adsorption, grand-canonical Monte Carlo (GCMC) simulations were performed using the continuous fractional component algorithm (CFCMC) (Shi & Maginn, 2007). In the grand-canonical ensemble, the chemical potential, volume and temperature were fixed. Fugacity coefficients were assumed to be 1. Each point on the adsorption isotherm was obtained by running 5×10^5 production cycles preceded by 5×10^4 equilibration cycles. The IRASPA software was used to quantify the characteristic features of Machine learning via Boruta Algorithm, (Kursa & Rudnicki, 2010) embedded in R software (Team, 2017) environment for statistical computing, was used to gain more chemical insights into loading capacity of selected ion onto the zeolites by ranking and analysing the importance of calculated parameters (density, mass, helium void fraction, accessible pore volume, gravimetric surface area, dimensionality of the pore system). The algorithm was implemented as wrapper algorithm around random forest classification which helps to out all relevant variables (Kursa & Rudnicki, 2010).

Objective 2; To evaluate the adsorption of halogenated pharmaceuticals (diclofenac, ciprofloxacin and chloramphenicol) and pesticides (diuron, chlorpyrifos and imidacloprid) onto zeolite frameworks using computation simulations

Methodology; Material Studio 17.0 software was used for the molecular simulations. The structures of the zeolites were obtained from the IZA structure (Baerlocher, 2008). The molecular structures of selected pesticides and pharmaceuticals were obtained from PubChem database (Kim *et al.,* 2019). The structures were then loaded into the DS Biovia Materials Studio 2017 software (Dassault Systemes BIOVIA, Release 2017). Geometry optimization and frontier molecular orbital analyses of the selected pesticides and pharmaceuticals was done using first-principles $DMol^3$ method (Delley, 1990) while the zeolites were optimized using forcite force field. The generalized gradient approximation (GGA) with the PDW exchange-correlation functional and the double-numerical basis set were used for adsorption in different levels of theory (Delley, 1990).Visualization of the HOMO, LUMO and energy gap were done with CHEM CRAFT program version 1.5. All the calculations were done at density functional theory (DFT) using the Gaussian 09W suite of the programs. To study adsorption, grand-canonical Monte Carlo (GCMC) simulations were performed using the continuous fractional component algorithm (CFCMC) (Shi & Maginn, 2007). In the grand-canonical ensemble, the chemical potential, volume and temperature were fixed. Fugacity coefficients were set at 1. Each point on the adsorption isotherm was obtained by running 5×10^5 production cycles preceded by 5×10^4 equilibration cycles. Finally, Natural bond orbital (NBO) calculation for the investigation of the stabilization energy was conducted with the help of the NBO 3.1 module entrenched in Gaussian (Frisch *et al.,* 2009). The quantum theory of atoms-in-molecules (QTAIM)

investigations and all other wave function analyses were conducted by Multiwfn 3.7 dev (Chen, 2012).

3.2 Experimental methods

3.2.1 Chemicals and reagents.

High purity standards of heavy metal salts ($Pb(NO_3)_2$ (≥99.95%) and $Cd(NO_3)_2$ (99.9%), anions (KNO_3 and KH_2PO_4), halogenated pesticides (chlorpyrifos and imidacloprid) and pharmaceuticals (diclofenac, chloramphenicol and ciprofloxacin), NaOH, HCl, NaCl were supplied by Merck Ltd through Kobian Kenya. Analytical grade and high-performance liquid chromatography (HPLC) grade solvents for extraction and analysis were purchased from Fluka Chemicals. Other expendable materials such as solid phase extraction cartridges and nylon microfilters were also purchased from Merck Ltd. All stock solutions were prepared using HPLC-grade solvents.

3.2.2 Preparation of the Heulandite zeolite

The natural heulandite (HEU) zeolite was obtained from Pratley mining company, South Africa. The zeolite was then ground and sieved using a 200 µm mesh sieve. It was then washed with deionized water and oven-dried at 100 ℃ for 24 h. No additional treatment was done prior to characterization and adsorption studies.

3.2.3 Characterization of HEU zeolite

The HEU zeolite was characterized by the following instrumental techniques; Energy dispersive X-ray spectroscopy (EDX) (Shimadzu EDX-800HS) for chemical composition, powder X-ray diffraction (XRD) (Rigaku Model-MiniFlex 600) for surface morphology, and Fourier transform infrared spectroscopy (FTIR) (Nicolet 6700 FT-IR) for functional

groups and scanning electron microscopy (SEM) (FEI Nova Nano SEM 230) for the morphological analyses.

For the EDX analyses, 2.0 g of dry powder sample was placed into a plastic cuvette and placed into the energy dispersive spectrometer.

For XRD (Rigaku Model-MiniFlex 600) analyses, the ground zeolite was placed in sample holder and the crystalline phases were evaluated using Phillips X-ray diffractometer with Cu-Kα radiation. The XRD operating conditions as given in Table 3.1.

Table 3. 1: The XRD operating parameters

Radiation Wavelength	104
Range	$1.54 < \theta < 80^0$
Time constant (s)	1
Presets (counts/s)	1000
Voltage	40
Current	25°
2θ range	4°
2θ /step	0.1°
Anti-scatter	4°

Identification of phases present in the zeolites was performed by searching and matching obtained spectra with powder diffraction files from the data base with the help of the Joint committee of powder diffraction standards files for inorganic compounds. Data evaluation was done using EVA software from BRUKER (PDF database 1999). The patterns were

collected and phase identification was done using X'Pert High Score software containing ICDD (International Centre for Diffraction Data) files for comparison.

For the SEM analyses, this was done using (FEI Nova Nano SEM 230) instrument at varying magnifications, with a field emission gun to analyse particle size of heulandite zeolite. A small amount of the sample was sprinkled onto a 12 mm aluminum SEM stub covered with carbon glue to make their surfaces conductive. The excess sample was blown off with compressed air, and the samples were carbon coated before being loaded into the SEM equipment. The loaded sample was then imaged using a high-resolution immersion lens. On the other hand, the FTIR (Nicolet 6700 FT-IR) was used. The spectra were recorded using a horizontal plate crystal cell at room temperature. The sample was placed on the crystal cell, which was mounted on the FT-IR spectrometer with a pressure of 50 MPa, for the spectra analysis. The IR measurements were recorded between (400 – 4000 cm^{-1}) wavenumber and conducted by exposure of the crystal cell containing the heulandite zeolite at 750 K for 2 hours, and the automated signals collected.

3.3 Adsorption studies

3.3.1 Stock solutions

0.159 g of $Pb(NO_3)_2$ and 0.274 g of $Cd(NO_3)_2$ were used to prepare of 1000 mg/L stock solutions of lead and cadmium respectively. 1.805 g and 1.094 of KNO_3 and KH_2PO_4 were used to prepare 250 mg/L stock solution of NO_3^- and PO_4^{3-}, respectively. Lastly, 0.1 g of pharmaceuticals (diclofenac, ciprofloxacin and chloramphenicol) and pesticides (imidacloprid and chlorpyrifos) standards were used to prepare 100 mg/L stock solution. For environmental water samples analysis stock solutions were prepared by dissolving accurately weighted standards in methanol to make 5 mg/L concentration. These stock solutions were refrigerated at – 4 °C, awaiting further analysis.

3.3.2 Effects of operating parameters on adsorption

3.3.2.1 Contact time

The contact time was varied while the other factors were maintained constant. For lead (II) and cadmium (II) ions, 10 and 1.5 mg/L solutions were prepared in 100 and 50 mL volumetric flasks, respectively. 1.0 g of heulandite zeolite was added to each solution containing Pb^{2+} and Cd^{2+} ions. The solutions of heavy metals were then agitated on an orbital shaker at 150 rpm and aliquots of the filtrate drawn from the flasks after predetermined interval of 0, 30, 60, 90, 120, 150, 180, 210 and 240 min. While, 0.1 g of heulandite was added to 4 mg/L of the anions and pesticides in 100 mL were drawn after 15, 30, 45, 60, 75, 90, and 120 minutes. Lastly, for the diclofenac, ciprofloxacin and chloramphenicol, 1.0 g of HEU zeolite was equilibrated with 100 ml of the of 10 mg/L at 25 ^{o}C during internal between 0 to 180 minutes. The resultant solutions were filtered then subjected to AAS and UV-VIS measurements for selected heavy metals and anion determination, respectively.

3.3.2.2 Effect of initial solution concentration

The concentration of analytes was varied while the other factors were maintained constant. 1.0 g of zeolite was dispersed into flasks with 50 mL of various concentrations at 25 ^{o}C and a contact time of 60 minutes. The concentration of Pb^{2+} were 5, 10, 20, 30 and 40 mg/L and the incase of Cd^{2+} the concentration were 1, 1.5, 2, 2.5, 3 and 4 mg/L. For the selected anions and pesticides, the concentrations were (2, 2.5, 3, 4,5 and 6 ppm) and pharmaceuticals concentrations were 5, 10, 15, 20, 30 and 40 mg/L. After equilibration time, the residual compounds were analyzed using AAS (heavy metals) and UV-Visible spectrophotometer (selected anions and halogenated pesticides and pharmaceuticals). The

equilibrium concentrations were used to determine the adsorption isothermal characteristics of the adsorption process. The obtained experimental data was fitted to non-linearized Langmuir, Freundlich Sips and Peterson adsorption isotherm models.

3.3.2.3 Effect of adsorbent dosage

The adsorbent dosage was varied while the other factors were maintained constant at their best levels. 50 and 10mL aliquots solutions having initial concentration of 10 and 1.5 mg/L of Pb^{2+} and Cd^{2+} solutions, respectively were placed in conical flasks. Varying amount of (0.3, 0.5, 0.8, 1.0, 1.5 and 2.0 g) of the heulandite was added to each set of the conical flasks and agitated (150 rpm) for 60 minutes with orbital shaker. The adsorbent dosage (0.5, 0.8, 1.0, 1.5, 2.0 and 2.5 g) with 100 mL of 4 mg/L solution were used for anions (PO_4^{3-} and NO_3^-) and for the pesticides (imidacloprid and chlorpyrifos) the adsorbent dose ranged from 0.05 to 0.2 g in 10 mL of the solution. For the pharmaceuticals (diclofenac, ciprofloxacin and chloramphenicol), the adsorbent dose were 0.5, 0.8, 1.0, 1.5 2.0 and 2.5 g. After shaking, the solution, was separated from the adsorbent using filter papers. The concentration of analyte in the supernatant was determined using AAS for heavy metals and UV-Visible spectrophotometer for other pollutants

3.3.2.4 Effect of temperature

Temperature was varied incrementally from (25 ºC, - 75 ºC) while the other factors were maintained constant. 1.0 g of heulandite zeolite was added into 100 mL of 4 ppm of PO_4^{3-} and NO_3^- solutions, respectively. 0.1 g of HEU zeolite was added into 10 mL of 4 ppm of imidacloprid and chlorpyrifos solutions. Then the contents were shaken at speed of 150 rpm.After equilibrations time the residual contaminants amounts of each anion and pesticides were analyzed by UV-VIS spectrophotometry. The equilibrium concentrations

were used to determine the thermodynamic functions and feasibility of the adsorption process. All experiments were performed in triplicates.

3.3.3 Removal of pesticides and pharmaceuticals residues from wastewater using Heulandite

This section involves collection, sampling, extraction, analysis and removal of the selected halogenated pharmaceuticals and pesticides from wastewater samples using HEU.

3.3.3.1 Sample collection for halogenated pharmaceuticals and pesticides

The wastewater samples for the halogenated pharmaceuticals and pesticides were collected from Kisumu and Juja wastewater treatment plants, respectively in triplicate into pre-cleaned amber glass bottles which were then tightly covered and preserved in an icebox to limit microbial activities (Ouma *et al.,* 2021). Prior to the sample collection, the sampling bottles were rinsed with the waste water to be sampled. In the laboratory, the samples were spiked with 5mL formaldehyde and stored in a refrigerator at - 4 ^{o}C and analyzed within 48 hours.

3.3.3.2 Sample extraction for pharmaceuticals and pesticides

The analyte was extracted from wastewater following the method described by Ouma *et al*., (2021) with slight modifications. The samples were thoroughly mixed by shaking and then allowed to settle before extraction. 100 mL aliquots were then filtered through 0.45 µm glass microfiber filters to remove suspended particles and particulate debris. The filtered effluent samples were then extracted using 5 mL Oasis HLB (200 mg) SPE cartridges. The SPE cartridges were first activated and conditioned with 3 mL methanol and 3 mL water at a flow rate of approximately 3 mL min^{-1}. Elution was performed with 3 mL methanol. The eluents were evaporated to dryness under a gentle stream of nitrogen.

The sample were reconstituted to 0.5 mL methanol. All the analyses were carried out in triplicate (Gawad *et al.,* 2022). The supernatant was filtered using a 0.22-micron syringe filter into an auto-sampler vials and the clean sample was the prior to analysis with LC-MS/MS.

3.3.4 Adsorption studies for wastewater sample using Heulandite zeolite

The adsorption studies were carried in triplicates using 100 ml of the waste water and 1.0 g of the HEU zeolite for 60 minutes at 150 rpm. The samples were then filtered to remove the adsorbent then followed by extraction using SPE catridges (*supra*) and analyzed using LC-MS/MS. The amounts of analytes adsorbed were determined from the initial and final concentrations of the pollutant in solution. The percent (%) removal was then done to establish the effectiveness of HEU zeolite in the removal of analytes from wastewater samples.

3.5 Instrumental analyses

3.5.1 AAS analysis

The heavy metal ions concentration in solution were determined by atomic adsorption spectrophotometry (Shimadzu AA-7000 Series). The ions were aspirated into the spectrophotometer, then the ions present in solution were ionized in an air and acetylene flame environment until a corresponding concentration was recorded (Outa *et al.,* 2020). The wavelengths and slit widths were varied to suit the optimum working range required for the particular metal ion. Before every run, the equipment was calibrated using known high grade standard solutions and the appropriate lamp until a curve was obtained, which was in agreement with the calibration curves in the AAS working manual. Pb^{2+} and Cd^{2+} were analyzed at this wavelength of 283.3 and 228.8 nm, respectively.

3.5.2 Ultraviolet Visible Spectrophotometric analysis

Shimadzu UV-800 series Spectrophotometer was used to analyze the residual concentration of selected anions and halogenated organic pollutants during adsorption studies. The anions (PO_4^{3-} and NO_3^-) residual concentration were determined at wavelength of 214 and 880 nm, respectively. On the other hand, imidacloprid and chlorpyrifos were determined at wavelength of 270 and 250 nm, respectively. The λmax used were 275, 278 and 280 nm for diclofenac, ciprofloxacin and chloramphenicol, respectively. Quartz single cuvettes were used and deionized water were used as a blank during the analyses.

3.5.3 LC-MS/MS analysis

Agilent HP1100 LC-MS/MS was used to determine the concentrations of pharmaceuticals and pesticides from water samples obtained from the WWTPs as well as the residual levels of the organic pollutants in the real water samples after adsorption studies. The operating conditions was as follows; a quaternary LC pump coupled to a waters Quattro Ultima- MS system. The system was operated using Masslynx Version 4.1 software. The separation was conducted on EVO C_{18} column (100 mm × 3.0 mm, 5µm particle size and 100 A^0). The mobile phase consisted of ultrapure water (solvent A) and methanol acidified (solvent B), both containing 0.1 % (v/v) formic acid. The mass spectrometric detection was operated in the multiple reactions monitoring (MRM) mode and performed in the positive electrospray ionization mode (Ouma *et al.,* 2019). The collusion and desolvation gases were argon and nitrogen, respectively. The flow rate was held constant at 1 mL/min the injection volume was 20.0 µL and data was acquired in a full-scan positive-ion mode using a 100 to 1500 *m/z* scan range. The time for each ion was 50 ms. Other parameters of the mass spectrometer were as follows: capillary voltage, 3.0 kV; cone voltage, 70 V; extract

voltage, 5 V; RF voltage, 0.5 V; source temperature, 100 ºC; nitrogen gas temperature for desolvation, 350 ºC; and gas flowrate at 700 L/h. After this, the full scan MS mode was used to record the product ion. For each standard, both the negative and positive electrospray ionization modes were tested.

3.6 Quality Control and Assurance

In the computational experiments different forcefield such as Universal, Dreiding, were evaluated and the best forcefields was used in the computational analyses. The structure of different zeolite and pollutants (heavy metals, anions and halogenated pesticides and pharmaceuticals) were optimized by Forcite and $Dmol^3$ which are embedded in Material Studio software. For the laboratory experiments, each study was conducted in triplicate.

For quality control in AAS, UV-Vis Spectrophotometry analyses, analytical blanks and a sample with known concentrations of selected pollutants were prepared and analyzed. The linearity was measured by standard solutions of different concentrations.

For LC-MS/MS, the external standards calibration was used for quantification. The calibration curves were obtained by preparing individual standards using black solvents. The linearity of the calibration was evaluated based on coefficients of determination(R^2) of the calibration curves. In all the cases, R^2 was greater than 0.99. The precision of the LC-MS\MS methods for pesticides and pharmaceuticals analyte investigated was determined by analyzing all the samples in triplicates.

With each set of samples to be analyzed, a solvent blank and a standard was run in sequence to check for background contamination, peak identification and quantification. In addition, internal standards for pesticides (imidacloprid, chlorpyrifos) and pharmaceutical ciprofloxacin were added to all the samples to monitor matrix effects and recoveries. Limit

of detection (LOD) and limit of quantitation (LOQ) were calculated based on the standard deviation of the response and slope of the calibration curve plots.

3.7 Data analysis

Data processing and analysis was done using Microsoft Excel program and OriginPro software 2018.

CHAPTER FOUR

RESULTS AND DISCUSSION

4.1 The computational studies on the adsorption of Pb^{2+} and Cd^{2+} onto zeolites

In this work, the adsorption of Pb^{2+} and Cd^{2+} onto 242 zeolites has been investigated by employing molecular simulations, where the role of pores, topology and chemical characteristics in the sorption of the two heavy metal ions has been examined. For the 242 zeolite structures, data showing loading capacity, adsorption isotherms and sorption fields was generated. Machine learning algorithm (boruta package) was employed to rank how and to what extent each of the parameter (total energy, pore size, and average volume) influence the loading capacity of the selected heavy metal ions onto the zeolite framework. For detailed methodology of this section, refer, to subsection 3.1

4.1.1 Results

The IZA structure database (Baerlocher, 2008) contains around 242 zeolite structures that have been discovered in nature or synthesized in the laboratory. The domains of these structures are characterized by several structural features such as the framework density, topological density, ring size, channel dimensionality, pore size, total volume, accessible volume and the type of composite building unit.

Material studio has various forcefields embedded in it such as universal, dreiding, compass and the consistent-valence forcefield (CVFF) (Dassault *et al.,* 2017). Universal forcefield has full coverage of the periodic table. Universal forcefield is accurate for predicting geometries and conformational energy differences of organic molecules, main-group inorganics, and metal complexes. It is recommended for organometallic systems and other systems for which other forcefields do not have parameters (Golchoobi & Pahlavanzadeh,

2017). The dreiding forcefield has good coverage for organic, biological and main-group inorganic molecules. It is only moderately accurate for geometries, conformational energies, intermolecular binding energies and crystal packing (Mayo *et al.*, 1990). On the other hand, the consistent-valence forcefield (cvff) parameters are provided for amino acids, water, and a variety of other functional groups (Ritschl *et al.,* 2002). The Compass forcefield has broad coverage in covalent molecules including most common organics, small inorganic molecules, and polymers. Compass is able to predict various solid-state properties: unit cell structures, lattice energies, elastic constants, and vibrational frequencies. The combination of parameters for organics and inorganics makes it possible the study of interfacial and mixed systems. In this study, the results of the different forcefield were as shown in Figure 4.1. In agreement with Golchoobi and Pahlavanzadeh, (2017), it was found that the universal forcefield fit the systems used in this study.

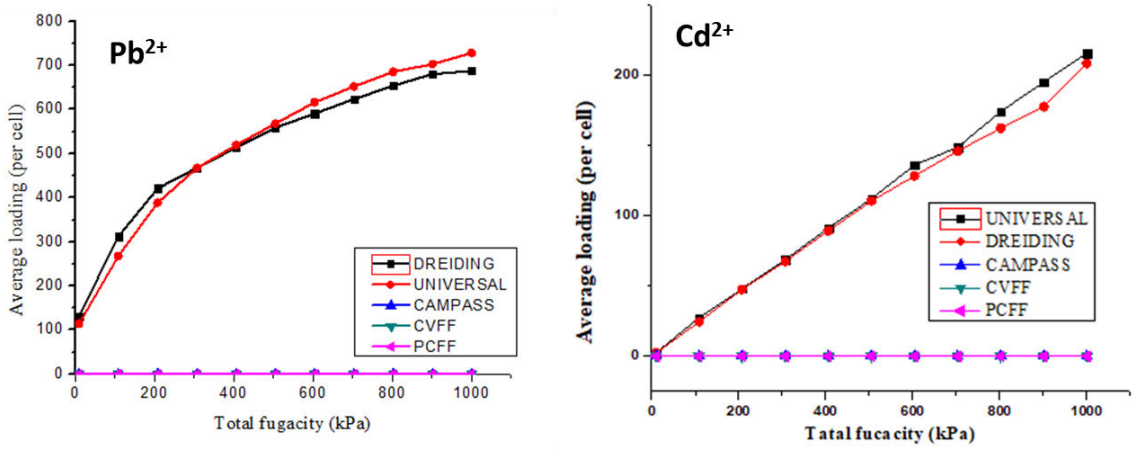

Figure 4. 1: Loading of Pb^{2+} and Cd^{2+} onto CLO in terms of force fields

Although there are such a variety of zeolites with different microporous systems, the zeolite with optimal structure can find utilization in adsorption applications. Table 4.1 shows the best performing zeolites among the 242 zeolites, in terms of loading of Pb^{2+} and Cd^{2+} ions verses pore size, and structure (Appendix Table 1)

Table 4. 1: The best performing zeolites among the 242 zeolites, in terms of loading verses pore size and structure

Code	Structure	Mass of zeolite (g)	Pore size (A^0)	Accessible volume %	Loading Pb^{2+}	Percent weight (% wt) – Pb^{2+}	Total Energy Pb^{2+} kcal/mol	Loading Cd^{2+}	Percent weight (% wt) – Cd^{2+}	Total Energy Cd^{2+} (kcal/mol)
TSC	Cubic	23072	16.45	27.85	231	78.64	-2000.6	67	24.71	-198.6
CLO	Cubic	11728	15.72	33.76	728	92.78	-4807.2	216	66.82	-1902.3
PAU	Cubic	40377	10.48	12.39	247	55.88	-2897.1	196	35.42	-605.6
FAU	Cubic	11536	11.24	27.42	128	69.67	-1062.2	32	23.86	-77.66
MWF	Cubic	86521	10.64	11.44	464	51.28	-5573.5	441	36.55	1530.3
LTN	Cubic	46144	10.13	0	170	43.27	-3047.4	180	30.59	-651.4
ITV	Cubic	11792	9.32	37.82	146	71.92	-987.1	16	13.29	-86.5
DFO	Hexagonal	7932	11.29	22.01	111	74.34	-974.3	33	31.98	-76.18
LTA	Cubic	1442	11.05	21.43	102	93.60	-1005.4	3	74.86	-92.91
SBE	Tetragonal	7691	12.54	26.41	69	64.99	-619.5	17	19.99	-51.84
SBT	Trigonal	8652	11.17	27.25	77	64.80	-676.3	21	21.52	-49.16
IRY	Hexagonal	4598	11.33	40.9	67	75.10	-512.0	10	19.73	-13.09
IMF	Orthorhombic	17304	7.34	12.12	62	42.58	-703.9	16	09.46	-39.15
JSR	Cubic	5768	7.83	28.09	60	68.39	-563.2	4	07.26	-8.64

Different zeolite properties play key roles in the adsorption of Pb^{2+} and Cd^{2+} uptake. From the data presented in Table 4.1, it is evident that mass, density, helium void fraction and surface area are useful properties in determining Pb^{2+} and Cd^{2+} uptake in zeolites besides pore sizes.

Heavy metal adsorption capacity of a zeolite is defined as the mass of heavy metal ions taken up by a given quantity of zeolite at equilibrium. This is an important performance indicator and depends on a number of factors that include zeolite topology and adsorption temperature. Out of the 242 zeolites, CLO, FAU, PAU, TSC, LTA LTN and MWF zeolites exhibited the highest percentage weight (%wt.) capacity for Pb^{2+} and Cd^{2+} uptake.

It is observed that cloverite (CLO), with a cubic structure and framework density of 11.1 T/1000 $Å^3$ has the highest loading of 728 Pb^{2+} per cell. It also has the largest ring size (20 - ring pore) and the lowest observed framework density, with an accessible volume of 33.76%. Other cubic structured zeolites (FAU, PAU, TSC, LTA LTN, and MWF) also gave a relatively high loading of lead (II) ions per cell. Among the cubic structured zeolites, it is also observed that PAU with a chemical formula, **[**$Al_{152}Si_{520}O_{1344}$**],** gave a higher loading compared to FAU since PAU has a higher topological density and volume. On the other hand, the pore size of FAU zeolite is almost double that of the LTA zeolite and it exhibited almost double loading of Pb^{2+} per cell, in comparison to LTA. This was also observed by Yuna, (2016) . In addition, FAU having the lowest Si/Al ratio of 1:1, exhibits high cation exchange capacity and sorption performance. The LTA structure has a primitive cubic unit cell (a = 12.3 Å) with one sodalite cage in each corner of the cube and a 4-4 unit on each edge of the cube. In each unit cell the total volume of LTA is 416 $Å^3$, using a T-O-T distance of 2.7 Å and assuming that the sodalite cage is spherical with a

radius of 4.4 Å. This corresponds to the 22.3% of the framework volume. In the case of FAU zeolites, the structure has a face centered cubic unit cell (24.7 Å). The sodalite cages are linked by 6-6 units with a tetrahedral distribution. Using the same assumptions as in the previous case, the inaccessible volume to the metal cations is 3674 $Å^3$, which is 24.4% of the volume of the unit cell.

ITV, a mesoporous, crystalline zeolite with a 30-ring channel has the lowest framework density of all zeolite framework types. The very large pore volume of the germanosilicate and its chiral framework structure allows high loading of 146 Pb^{2+}ions which is almost double that of SBT and SBS (loading of 77 and 69, respectively). As seen in Table 4.1 (and S1, supporting information appendix 1), only the zeolites with high diameter of sphere/pores exhibited appreciable loading of the Pb^{2+} ions (CLO, FAU, PAU, TSC, LTA LTN and MWF). Majority of the zeolites have small pores hence low loading. A few that exhibited zero loading have extremely small pores. In a related study by Ouki *et al, 1997* it was observed that metal uptake capacity of chabazite exceeded that of clinoptilolite since chabazite window and channel sizes were larger than those of clinoptilolite (Ouki & Kavannagh, 1997).

In the case Cd^{2+}, MWF exhibited the highest loading compared to the other zeolitic structures. MWF is accessible to the Cd^{2+} that can pass through the 8-rings cavities, and so it is potentially useful as a small-ion adsorbent. Moreover, MWF has expanding structural complexity and an embedded isoreticular structure. MWF with a chemical formula of $C_8H_{20}N^+)_{38}(H_2O)_{812}|$ **[**$Al_{334}Si_{1106}O_{2880}$**]** has less limiting ring channels <100> 8 ring 3.8 x 3.8 which makes it better for adsorption of both Pb^{2+} and Cd^{2+} ions while CLO with a chemical formula of $(C_7H_{13}N)_{248}$ $|_8$ **[**$Ga_{96}P_{96}O_{372}(OH)_{24}$**]**$_8$, has greater limiting ring

channels <100> 20 ring, 13.2 x 3.5 <100> 8 ring, 3.8 x 3.8, which makes it better for adsorption of Pb^{2+} ions. While the adsorption of Pb^{2+} is predominantly determined by cation exchange by the zeolite framework composition, the adsorption of Cd^{2+} exhibited strong pore-geometry dependent behavior. This may explain why MWF exhibited higher loading for Cd^{2+} in comparison to Pb^{2+}, since Cadmium has a lower relative atomic mass (48) compared to Lead. Otherwise, the rest of zeolites exhibited a similar trend as that of lead although in each case, there is a lower loading as shown in Table 4.1. TSC, PAU, FAU, SBE, CLO, SBS, SBT, LTN MWF, MTN, LTA, IFT and DFO exhibited a loading of 67, 196, 32, 21, 209,13, 21, 180, 441, 36, 37, 13, and 33 ions of cadmium (II) ions per unit cell. The sorption of Pb^{2+} and Cd^{2+} ions in almost all the zeolites gave a negative average total energy, showing that the sorption process is an exothermic process.

The sorption isotherms for representative zeolites that gave the best loading is shown in Figure 4.2. Among the various zeolites, only CLO and MWF exhibited the L-shape isotherm with a pronounced inflection at maximum loading. The loading of Pb^{2+} ion at each step for CLO is higher when compared to MWF and the rest of zeolites at a given total fugacity.

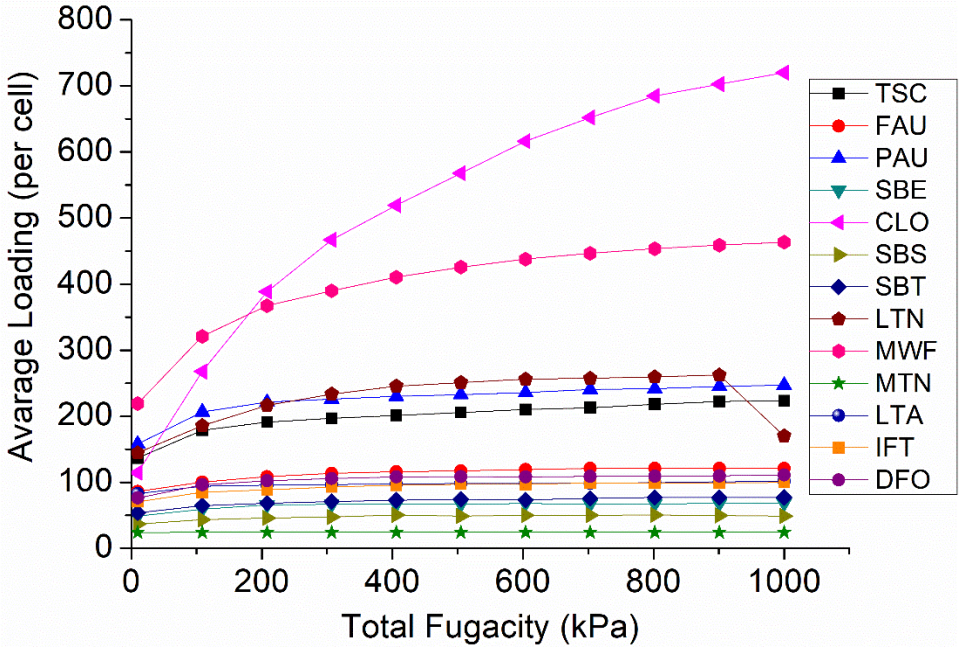

Figure 4. 2: Adsorption isotherms of Pb^{2+} ions on the best performing zeolites at 298 K

Figure 4.3 shows structures of the most stable configuration of Pb^{2+}, PbO and $Pb(OH)_2$ adsorbed onto CLO alongside the respective binding energies (B.E).

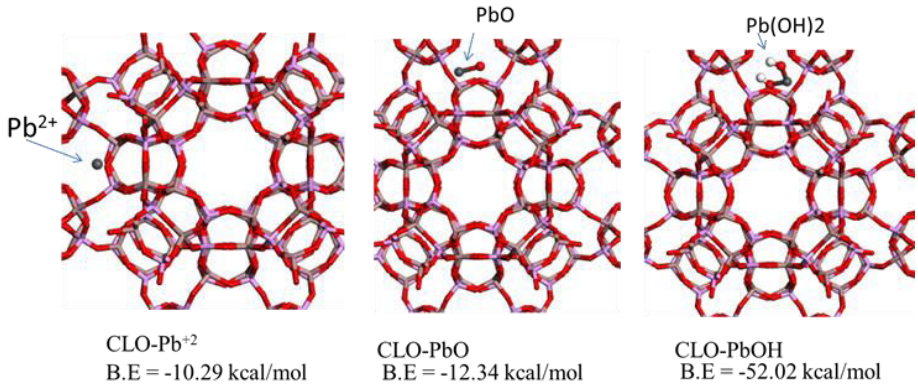

Figure 4. 3: Structures of the most stable configuration of Pb^{2+}, PbO and $Pb(OH)_2$ adsorbed on CLO alongside the respective binding energies (B.E).

From figure 4.3, it was observed that Pb^{2+} is located at the pore closer to the oxygen atom of the zeolite with a binding energy of -10.29 kcal/mol. Since divalent Lead also exists in

the environment in form of various species such as PbO and $Pb(OH)_2$ among others (Chadwick, 1988; Pembere, 2014), the binding energies alongside their most stable configurations of these species were studied for comparison. $Pb(OH)_2$ has the highest binding energy of -52.02 kcal/mol, followed by PbO with the binding energy of -12.34 kcal/mol. The lead ion in PbO and $Pb(OH)_2$ tend to bind towards oxygen atoms in the CLO zeolite while oxygens towards gallium atoms. While the binding energy of Pb^{2+} ion is less negative than those of $Pb(OH)_2$ and PbO when compared, hence less stable.

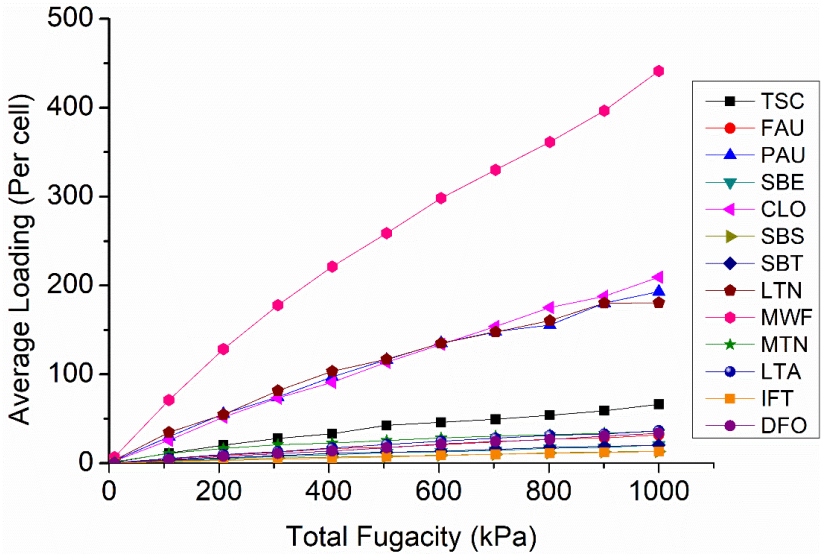

Figure 4. 4: Adsorption isotherms of Cadmium (II) ions on the best performing zeolites at 298

In Figure 4.4 the loading of Cd^{2+} ion at any fugacity is higher for MWF than for all other zeolites types. To understand this observation,

the binding energies of adsorbed Cd^{2+} ions onto CLO and MWF zeolite was compared as shown in Figure 4.5. It was found that the most stable configuration of Cd^{2+} ion had a binding energy of -2.69 kcal/mol in CLO and -4.31 kcal/mol in MWF which are lower than that of lead (II) ions. The higher binding energy of Cd^{2+} on MWF compared to CLO, implies that MWF has more loading for Cd^{2+} ion, in agreement with the above adsorption isotherm results.

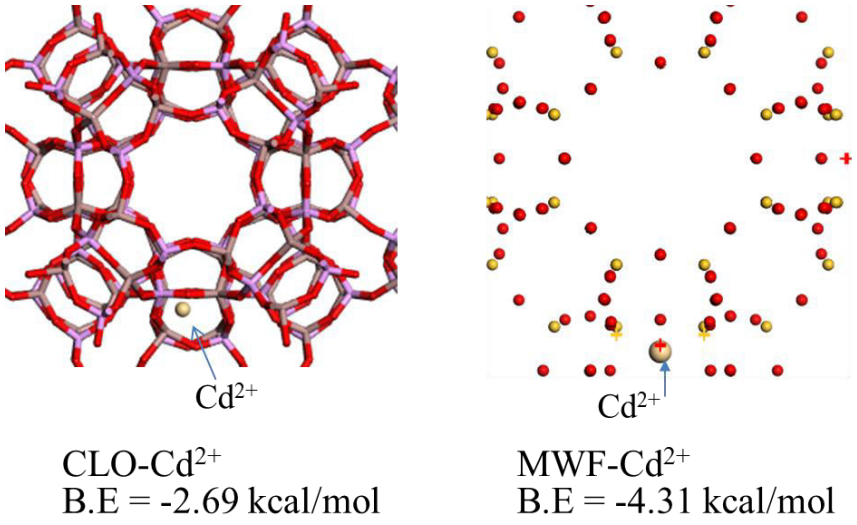

Figure 4. 5: Structures of the most stable configuration of Cadmium (II) ions on MWF and CLO zeolites, alongside the respective binding energies (B.E).

Just like Pb^{2+} and its compounds, cadmium can exist as either CdO or $Cd(OH)_2$. However, $Cd(OH)_2$ has a binding energy of -42.94 kcal/mol compared to CdO whose binding energy is -50.83 kcal/mol. From the binding energies of Cd^{2+} (-2.69 kcal/mol) and Pb^{2+} (-10.29 kcal/mol) on CLO, it is clear Cd^{2+} are less stable. Cadmium ion in CdO and $Cd(OH)_2$ bind to oxygen atoms in the CLO zeolite while oxygen atoms in the cadmium compounds bind to gallium atoms. $Pb(OH)_2$ is more stable on CLO than $Cd(OH)_2$ as shown by the binding energies of -52.02 kcal/mol and -42.94 kcal/mol, respectively. It is interesting to note that CdO (-50.83 kcal/mol) on the other hand is more stable compared to PbO (-12.34 kcal/mol) as shown in Figure 4.6.

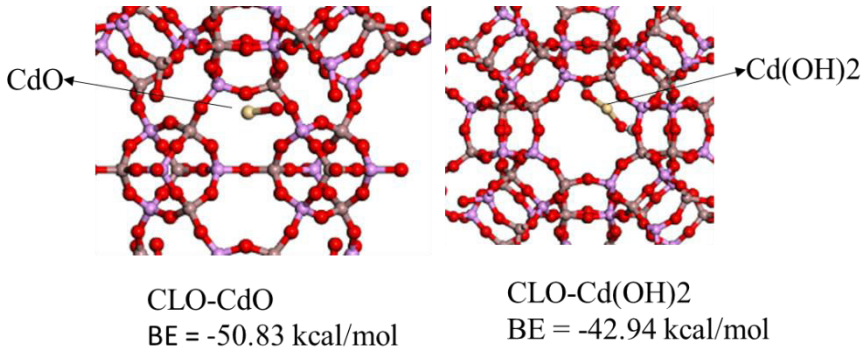

Figure 4. 6: Structures of the most stable configuration of CdO and $Cd(OH)_2$ adsorbed on CLO alongside the respective binding energies (B.E).

Figure 4.7 compares the most stable configuration in terms of binding energy for CdO and $Cd(OH)_2$ onto CLO and MWF. It was observed that the most stable configuration of CdO and $Cd(OH)_2$ had a binding energy of -51.61 and -43.39 kcal/mol, respectively in MWF which are higher than that of CLO. This shows that MWF is the most suitable adsorbent compared to CLO for Cd^{2+}, CdO and $Cd(OH)_2$ adsorption. This is corroborated by the higher number Cd^{2+} ions loaded on MWF (441) than in CLO (209) in Table 4.1.

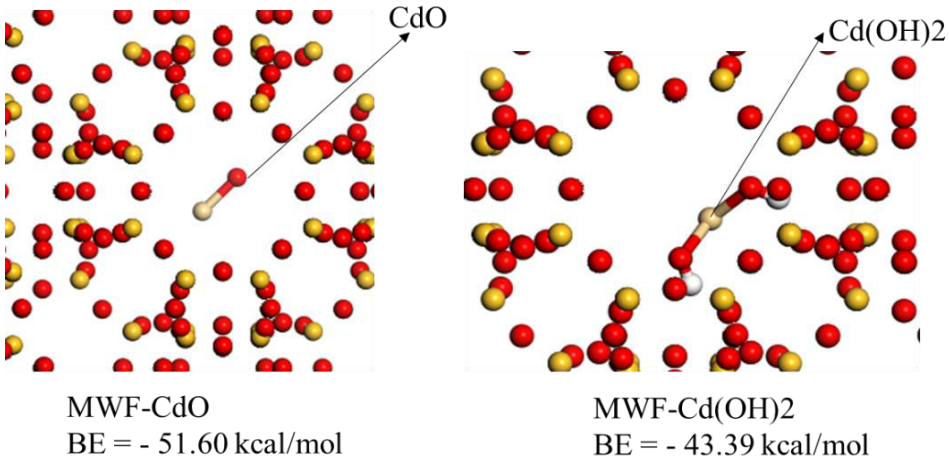

Figure 4. 7: Structures of the most stable configuration of CdO and $Cd(OH)_2$ adsorbed on MWF alongside the respective binding energies (B.E)

4.1.2 Machine Learning

To confirm the findings using the molecular simulation, machine learning employing boruta algorithm was used. This was done to gain more insights into loading capacity of the heavy metals onto the zeolites framework by ranking how important each of the parameter is in the loading capacity of the best performing zeolite structures. Pb^{2+} was used as a representative of the heavy metals. As depicted in Figure 4.8, out of the three parameters, total energy appeared as the most important parameter followed by the pore size. This is consistent with the view that topology captured an important chemical information about zeolite structures. Similarly, the negative values of the total energy further confirmed that the adsorption process is exothermic and this energy is inversely related to the density of the zeolites.

The pore size on the other hand implies that, zeolite's topology with high sphere cavity as well as inter channel cavities exhibit high tendency for heavy metal loading compare to zeolite with small diameter pore sizes. This however indeed is in conformity with the molecular simulation results. Compared to the pore size, the average volume was rejected by the random forest classier algorithm, which implies that the individual pore size on the surface of each of the best performing zeolite framework is responsible for the adsorption of heavy metals with relatively high sphere diameter instead of total volume for each zeolite.

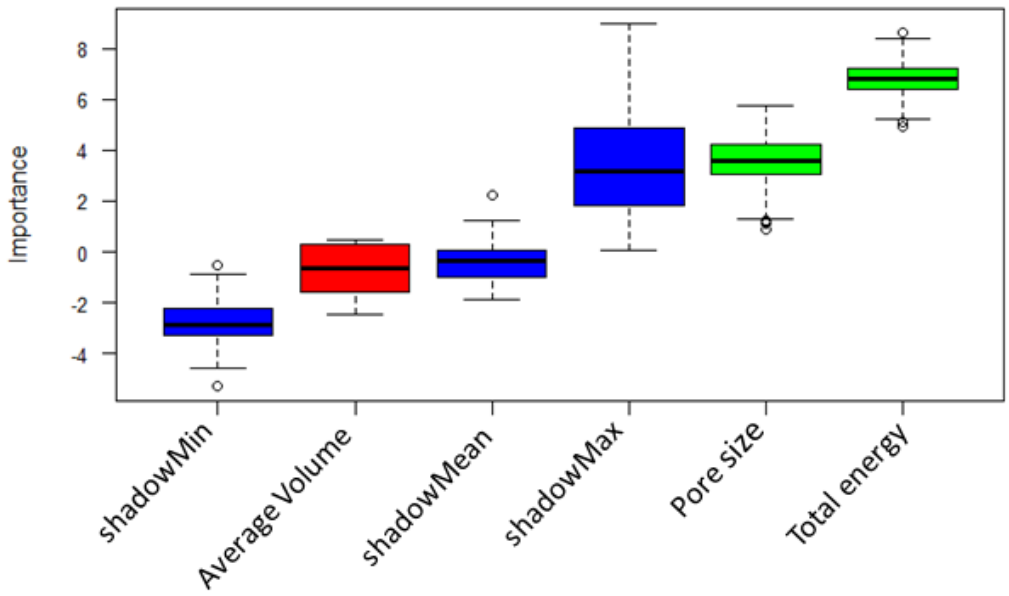

Figure 4. 8: Ranking of importance of parameters (descriptors) plot using Boruta algorithm for zeolites data. Green boxplots correspond to Z score of important descriptors, red boxplot correspond to unimportant descriptor while blue boxplots correspond to minimum, mean and maximum Z score of a shadow descriptor.

Accordingly, the data frame listed in Table 4.2 with each parameter *Z* score shows the value of each parameter of which both total energy and pore size are above the value of maximum shadow parameter with the values of 0.61 and 0.88 for pore size and total energy, respectively. This means that pore size is 61% higher than the showdown parameter while for total energy yield 87% higher the shadow parameter. For the average volume, the value (0) is below 50% which apparently is below the value of the shadow parameter, thus rejected and tagged to be unimportant parameter in determining the loading capacity of the selected heavy metals on the zeolite structures.

Table 4. 2: The attStats function shows the data frame with each descriptor Z score statistics as the function of random forest iteration to rank which descriptor was more important than the most important shadow descriptor

Descriptor	MeanImp	MedianImp	MinImp	MaxImp	NormHits	Decision
Pore size (Å)	3.5535	3.5608	0.9136	5.7251	0.6161	Tentative
Average volume	-0.7945	-0.6511	-2.4668	0.4517	0.0000	Rejected
Total energy (kcal/mol)	6.7610	6.7960	4.9208	8.6116	0.8788	Confirmed

Conclusion

According to the molecular simulation results, only the zeolites with high diameter of pores exhibited appreciable loading of the cations (CLO, FAU, PAU, TSC, LTA LTN and MWF). CLO and MWF exhibited highest loading of 728 and 441 of lead (II) and cadmium (II) ions per unit cell, respectively. It is observed that the adsorption energy of the cations on the zeolite framework is directly related to the loading capacity, whereby a trend of Pb^{2+}> Cd^{2+} is observed. The sorption of lead (II) and cadmium (II) ions in all the zeolites gave a negative average total energy, showing that the sorption is an exothermic process. From the machine learning results, pore size and total energy are the most important factor in adsorption of the metal ions onto the zeolites. Therefore, CLO and MWF are recommended for adsorption of Pb^{2+} and Cd^{2+}ions, respectively.

4.2 Computational Adsorption Studies of Anions on Zeolite

In this work, the aim was to apply molecular simulations and machine learning for a prediction of the adsorption of PO_4^{3-} and NO_3^- onto zeolites. Binary and five-component GCMC simulations were used to evaluate the performance of the zeolite structures obtained from the IZA structure database (Baerlocher, 2008). A screening process was used involving an initial selection of zeolites based on the pore-limiting diameter, followed GCMC simulations to calculate relevant descriptors and equally identify the high-performing zeolites. Statistical quantum mechanics was used to comprehend and interpret further the measurable macroscopic properties of zeolites in terms of the properties of their constituent particles and therefore the interactions that they have with each other. Finally, machine learning algorithm was employed to rank the importance of the various descriptors (Density, mass, helium void fraction, accessible pore volume, gravimetric surface area, and dimensionality of the pore system) that has influence on the removal of anions from water by zeolite. The approach does provide insight for a feasible approach for adsorption of pollutants aimed at alleviating water pollution. For detailed methodology of this section, refer, to subsection 3.1

4.2.1 Effect of Forcefield on Loading

Different forcefields were evaluated for the loading of PO_4^{3-} and NO_3^- onto the zeolites. It was found that Universal forcefield provided the highest loading for both PO_4^{3-} and NO_3^-. Figure 4.9 shows a typical loading of PO_4^{3-} and NO_3^- onto zeolite using different forcefields.

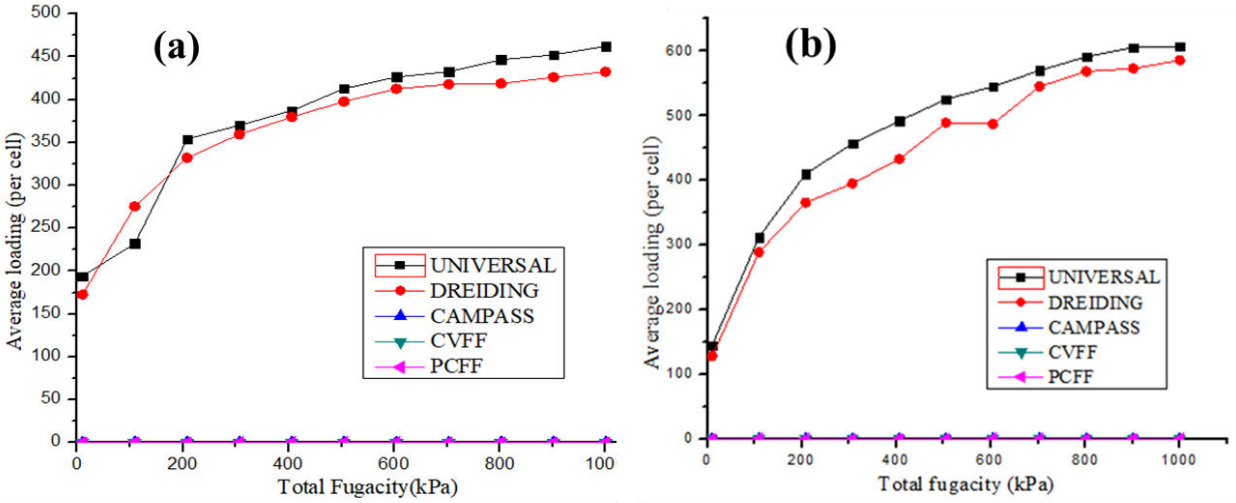

Figure 4. 9: Loading of (a) PO_4^{3-} and (b) NO_3^- onto CLO in terms of force fields

It was found that the dreiding and universal force fields fit the systems used in this study in comparison to CAMPASS, CVFF and PCFF. The universal forcefield has been found to be moderately accurate for predicting geometries and conformational energy differences of organic molecules, compounds of the main-group, and metal complexes and it is recommended for organometallic systems and other systems for which other forcefields do not have parameters (Golchoobi & Pahlavanzadeh, 2017). On the other hand, the dreiding forcefield has been found to have a good coverage for organic, biological and compounds of the main-group, and it is only moderately accurate for geometries, conformational energies, intermolecular binding energies and crystal packing (Mayo *et al.,* 1990). Thus, the discussion in the main text focused on the universal and dreiding forcefields. Geometry optimization of the zeolite cluster and anions were done at B3LYP/6-31+G(d) level of theory (Becke, 1988; Lee *et al.,* 1988), using Gaussian 09 software (Frisch *et al.,* 2009).

4.2.2 Zeolite Structural Screening and its Effect on Loading

The adsorption results from this screening were collected, and the best structures that was selective towards the anions was chosen for the adsorption of NO_3^- and PO_4^{3-}. The

structures of the zeolites were taken from the IZA structure database (McCusker & Baerlocher, 2019), which contains over 242 structures. To eliminate zeolites where diffusional limitations are highly expected, only zeolites with a pore diameter larger than 4 Å were selected. This is based on previous studies on the adsorption of selected heavy metal ions on zeolites where it was established that only the zeolites with larger pore diameter exhibited appreciable loading of the cations (Wanyonyi *et al.,* 2021) . Thus, in the first step of the screening, 141 out of 242 structures (58%) were eliminated. In the second step, the remaining 101 zeolite structures were screened based on selectivity for the PO_4^{3-} and NO_3^- . The GCMC simulations consisting of a total of 5000 cycles (where 1 cycle = max (20, N) with N being the maximum number of adsorbed ions that are split equally into equilibration and production periods were carried out.

Natural bond orbital (NBO) calculation for the investigation of the stabilization energy was conducted with the help of the NBO 3.1 module entrenched in Gaussian (Frisch *et al.,* 2009). The quantum theory of atoms-in-molecules (QTAIM) investigations and all other wave function analyses were conducted by Multiwfn 3.7 dev (Chen *et al.,* 2012).

The capability of PO_4^{3-} and NO_3^- adsorption as determined from GCMC simulations is shown in Table 4.3. The porous domains of zeolites are characterized by several structural features such as mass (M), density (D), helium void fraction (HVF), accessible pore volume (APV), gravimetric surface area (GSA), dimensionality of the pore system (Di) (Appendix Table 7)

.

Table 4. 3: The structural characteristics and loading capacity of PO_4^{3-} and NO_3^- on the best performing zeolites

CODE	Mass	Density	Helium void fraction	Accessible pore volume (cm^3/g)	Volumetric surface area (m^2/cm^3)	Gravimetric surface area (m^2/g)	Dimensionality of the pore system	Largest overall cavity diameter (A)	Loading of PO_4^{3-}	Isoelectric heats of PO_4^{3-}	Loading of NO_3^-	Isoelectric heats of NO_3^-
CLO	11728.18	1128.76	0.55	0.49	2069.69	1833.61	3	15.33	461	13.75	606	8.36
LTN	46144.74	1695.18	0.31	0.18	1181.64	697.06	0	0	103	16.48	128	10.61
MWF	86521.39	1603.83	0.35	0.22	1593.89	993.81	3	10.06	99	15.84	220	11.20
TSC	23072.37	1318.71	0.49	0.37	1472.61	1116.72	3	15.87	89	12.51	137	9.42
ITV	11792.17	1075.18	0.55	0.51	2110.04	1962.51	3	8.54	70	10.74	88	7.62
PAU	40376.65	1585.70	0.36	0.23	1639.21	1033.75	3	10.08	61	15.22	104	10.92
FAU	11536.19	1327.65	0.49	0.37	1615.92	1217.14	3	10.69	60	13.85	82	9.19
DFO	7931.13	1485.63	0.43	0.29	1625.72	1094.30	3	10.89	49	13.25	81	9.64
LTA	1442.02	1414.17	0.47	0.33	1674.58	1184.14	3	10.24	48	14.65	66	9.82
SBT	8652.14	1368.16	0.47	0.34	1585.49	1158.84	3	10.41	37	13.67	52	9.22
SBE	7690.79	1370.15	0.46	0.34	1514.00	1104.99	3	12.09	31	13.57	46	9.79
IRY	4598.41	1115.15	0.60	0.54	1701.51	1525.79	3	10.69	30	11.75	40	8.27
JSR	5768.09	1225.53	0.52	0.42	2271.20	1853.23	3	7.43	29	13.65	40	13.72
EMT	5768.09	1328.95	0.49	0.37	1618.80	1218.11	3	11.00	28	13.49	38	9.33
IMF	17304.28	1744.41	0.30	0.17	1261.47	723.15	2	6.70	28	15.68	49	11.54

IWV	9132.81	1498.62	0.41	0.27	1455.32	971.11	2	8.14	26	13.30	45	10.20
SBS	5768.09	1368.86	0.47	0.34	1585.68	1158.39	3	10.97	24	13.53	36	9.65
BOG	5768.09	1602.00	0.38	0.24	1486.24	927.74	3	7.49	16	14.26	26	10.62
BOZ	5527.76	1290.63	0.46	0.36	2017.67	1563.33	3	8.31	16	12.70	37	10.76
KFI	5768.09	1493.77	0.41	0.28	1638.56	1096.93	3	10.16	16	14.47	26	10.59
HEU	2163.03	1748.00	0.29	0.17	1335.49	764.01	2	5.22	15	13.32	17	14.21

Table key; D=density (kg/m^3), M=mass (g/mol); HVF=helium void fraction; APV=accessible pore volume [cm^3/g]; VSA=volumetric surface area [m^2/cm^3]; GSA=gravimetric surface area [m^2/g]; DPS=dimensionality of the pore system; Di=largest overall cavity diameter [A]; L=loading; isoelectric heats=IH

Among the 101 zeolites, it is noted that CLO has the lowest mass and density with highest helium void fraction (HVF), largest ring pore system and largest volumetric surface area. It exhibits the highest loading of 461 PO_4^{3-} ions per cell. On the other hand, LTN is ranked second in terms of loading with 103 ions per cell. This is a huge difference and may be attributed to the difference in mass, density, helium void fraction and diameter of the two zeolites. LTN is followed closely by MWF (103 verses 99 ions per cell). Although MWF has a higher Di and HVF, it has a higher mass of 86521.39 compared to 46144.74 g/mol of LTN. This may explain why LTN exhibits higher loading in comparison to MWF. TSC has a lower mass, higher HVF and Di compared to MWF. Thus, it is expected to have a higher loading per cell compared to MWF. Contrarily, it exhibits a lower loading of 89 compared to 99 in MWF. This may be attributed to the higher volumetric surface area of MWF (1593.89 m^2/cm^3) compared to TSC (1472.61 m^2/cm^3). TSC is followed closely by ITV (89 verses 70 ions per cell). This is attributed to the higher cavity diameter in TSC compared to ITV (15.87 verses 8.54 Å).

On the other hand, despite the fact that PAU has a larger Di compared to ITV, it has a lower loading capacity (61 ions per cell). This may be attributed to the relatively higher mass and density of PAU. FAU and PAU have almost equal loading (60 verses 61 ions per cell, respectively), this may be due to the similarity in their Di (10.08 verses 10.69 Å). DFO, LTA and SBT exhibit similar loading (49, 48 and 39 ions per cell), and may also attributed to similarity in their HVF and Di. IRY has lower mass and density giving the loading of 30 ions per cell due to having larger HFV and Di.

JSR and EMT exhibit similar loading of 29 and 28 ions per cell, respectively. This may be attributed to similar mass (5768.09) and HFV (0.49). Conversely, IMF has lower mass with

a larger density with a loading of 28 which may be due to its larger density and lower Di. IWV has larger mass with lower density with a loading of 26 ions per cell due to its large HFV. SBS has lower mass and density with a loading of 24 ions per cell because of its larger HFV and Di. BOG, BOZ and KFI show similar loading of 16 ions per cell which may be attributed to similarity in mass (5768, 5528 and 5768 g/mol, respectively) and HFV. Other zeolites (ANA, DFT, BIK, SBN, JNT, MON, PAR, THO, VSV, LIT, ITW, CAS, and APD) exhibited zero loading due to their small HVF, Di, APV and minute pores. Those with loading of 4 PO_4^{3-} ions per cell have larger pore sizes in comparison to those having 3, 2 and 1 ions loading per cell. Furthermore, there is a profound positive relationship between ion loading per cell and the HVF and Di in that those zeolites with appreciable loading have larger HVF and Di. It is also interesting to note that the loading decreases with decrease in the average total energy.

Isosteric heats of adsorption were calculated to determine the strength of each sorbent when interacting with the molecules. The objective is to correlate the heat of adsorption (ΔHads) values of zeolite to the corresponding performance. The stronger the interaction of the anion with the zeolite, the higher sorption energy, and therefore, a higher isosteric heat of adsorption. CLO exhibits the highest ΔHads values as strong adsorption exists between the CLO and the PO_4^{3-} ion (Table 4.3).

The adsorption of NO_3^- onto the different zeolites generally follow the same trend as PO_4^{3-} except on a few zeolites with CLO showing the highest loading. It was observed that the loading for NO_3^- onto the different zeolites was higher than those for PO_4^{3-} . For example, MWF showed a loading of 202 NO_3^- ions per cell compared to 99 PO_4^{3-} ions per cell which shows that its good for smaller adsorbate which is also shown by PAU. Both, MWF and

PAU showed more than double in terms of loading since they are good adsorbent. This is followed closely with TSC with the loading of 137 ions per cell. This shows that both MWF and TSC are good for adsorption of small anions. LTN is followed closely by PAU (128 verses 104 ions per cell). This is attributed to the higher cavity diameter in LTN compared to PAU (15.87 verses 8.54 Å). PAU has a larger Di compared to ITV; hence it has higher loading capacity (104 ions per cell). This may be attributed to the relatively small APV, higher mass and density of PAU this allows more packing. FAU and DFO exhibit similar loading of 82 and 81 ions per cell, respectively. This may be attributed to similar VSA. The rest of zeolites their loading is lower but higher than that of phosphate loading for the same zeolites. Except for HEU and JSR which had lowest loading of nitrates but higher than that of phosphate ions per cell.

The higher loading of NO_3^- compared to PO_4^{3-} onto the different zeolites can be attributed to NO_3^- ion having smaller size than PO_4^{3-} hence it can enter and move in the pores easily and gets attached even within zeolite structure.

4.2.3 Simulation Annealing Configurations for Anions onto Zeolites

The most stable adsorbed configurations of the PO_4^{3-} ion on CLO, LTA, MWF, ITV, PAU and PAU zeolites was studied using the simulated annealing approach (Kirkpatrick, 1983). Figure 4.10, shows the structure of the most stable configuration of PO_4^{3-} adsorbed onto the zeolites

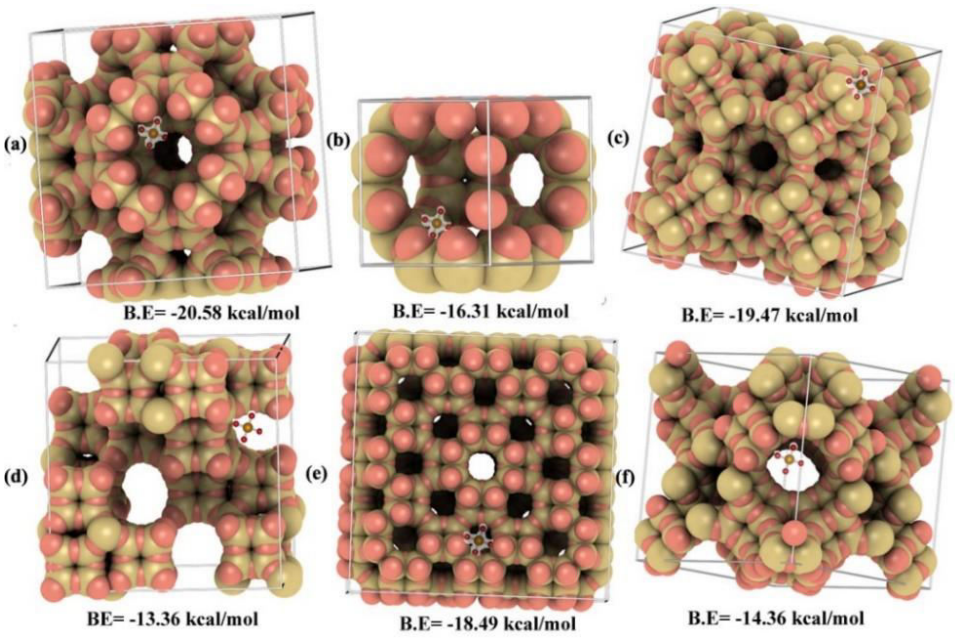

Figure 4. 10: Most stable configuration of the PO_4^{3-} ion on the best performing zeolites; (a) CLO (b) LTN (c) MWF (d) ITV (e) PAU (f) FAU.

The adsorbed PO_4^{3-} on the CLO is located in the upper left of 8-rings (Figure 4.10 (a) with an adsorption energy of -20.58 kcal/mol, which is higher than that on LTA, MWF, TSC, ITV, PAU and PAU. The value reveals that the PO_4^{3-} ion is most strongly bonded to CLO. MWF and PAU have adsorption energies of -19.47 and -18.49 kcal/mol, respectively. On the other hand, ITV has the least adsorption energy of -13.36 kcal/mol hence it has the least stable configuration.

Figure 4.11 shows the most stable adsorbed configurations of the NO_3^- ion on LTA, MWF, TSC, ITV, PAU and PAU zeolites studied.

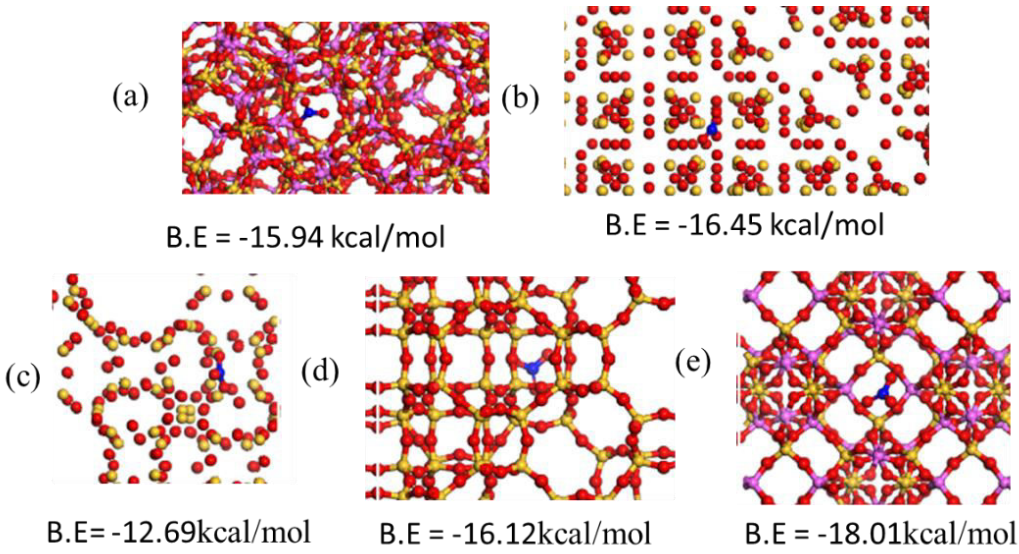

Figure 4. 11: Most stable configuration of the NO_3^- ion on the best performing zeolites; (a) LTN (b) MWF (c) ITV (d) PAU (e) FAU.

From, Figure 4.11 FAU exhibited highest adsorption energy hence more stable configuration in comparison to MWF, ITV, PAU, LTN. Like in the case of PO_4^{3-}, the binding energy for NO_3^- onto MWF and PAU have adsorption energies of -16.45 and -16.12 kcal/mol, respectively which is lower compared to PO_4^{3-} on the same zeolites hence less stable in terms of bonding to the zeolites. Interestingly. ITV has the least adsorption energy of -12.69 kcal/mol

While, Figure 4.12, shows structures of the most stable configuration of PO_4^{3-}, NO_3^-, adsorbed on the CLO. Adsorption energy, also termed binding energy, was computed for molecular structures after sorption of various anions on CLO zeolite. The least negative value was observed for NO_3^- (-11.12 kcal/mol^{-1}). It can be concluded from binding energy results that sorption of PO_4^{3-} (-20.58 kcal/mol^{-1}) was most favorable on the CLO zeolite as it has the lowest energy

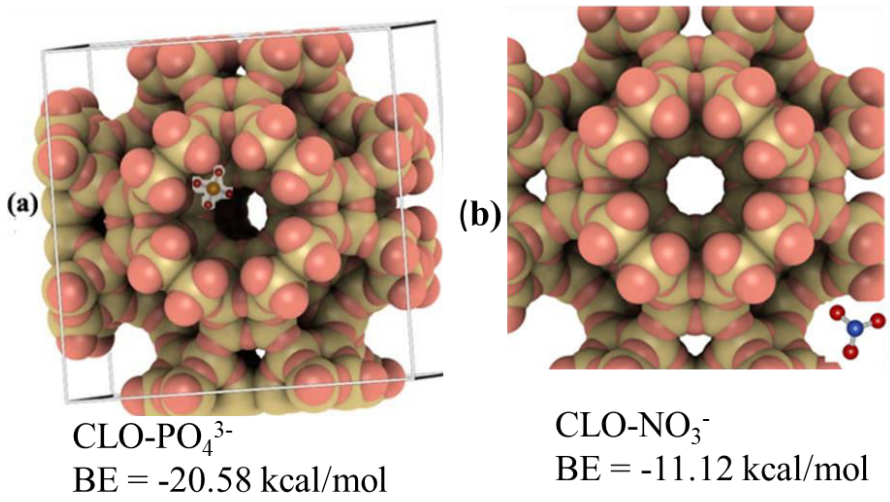

Figure 4. 12: Structure of the most stable configuration of (a) PO_4^{3-} and (b) NO_3^- as adsorbed on the CLO

4.2.4 Quantum Chemical Calculation

Quantum chemical calculations provided a better understanding of the orientation of the anion inside the pore of the best performing zeolite (CLO). Figures 4.13 show the optimized structure of PO_4^{3-} and NO_3^-; alongside the frontier molecular orbitals, electron density and the electrostatic potential. The PO_4^{3-} ion consists of a tetrahedral structure with a central phosphorus atom surrounded by four oxygen atoms. The LUMO and HOMO are rydberg in character, and are located on the oxygen atom with energies of 1.03 eV and -0.38 eV and occupancy of 1.80 and 0.002, respectively (Table 4.4).

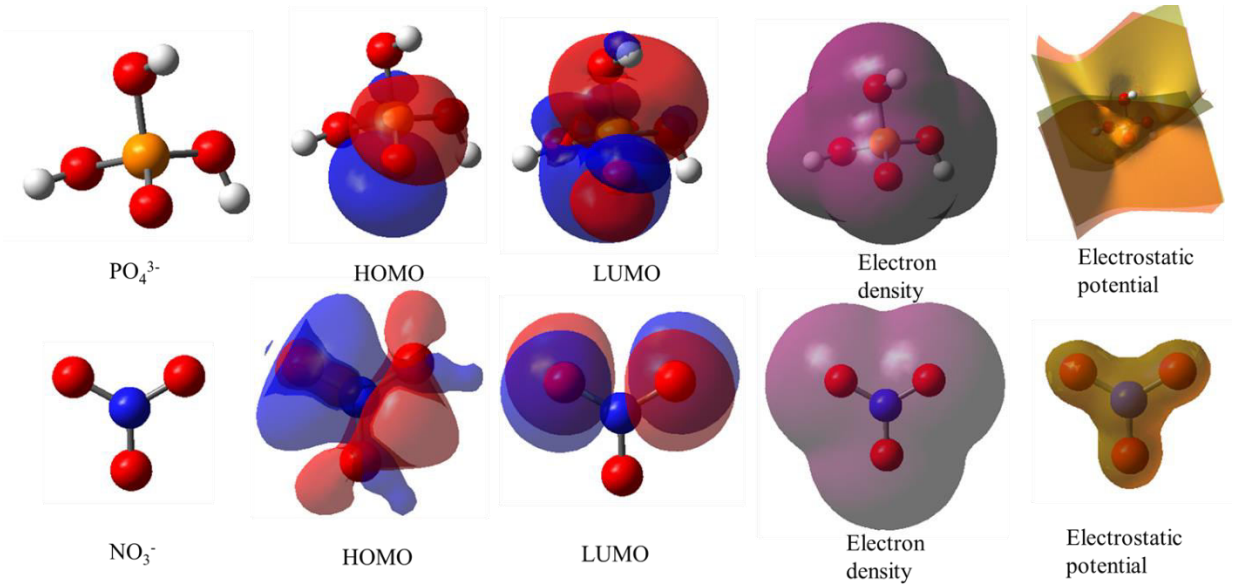

Figure 4. 13: Optimized structures of anions and Frontier molecular orbitals of PO_4^{3-} and NO_3^-. Calculated at DFT/B3LYP/6-31G (d,p) level of theory

Table 4. 4: Energies of the frontier molecular orbitals of PO_4^{3-} and NO_3^-. Calculated at DFT/B3LYP/6-31G (d,p) level of theory

Ion	Orbital	Atom	Type	Occupancy	Energy	**H-L gap (η) (eV)**	**μ (eV)**	**ω (eV)**
PO_4^{3-}	HOMO	O	Ryd(2P)	0.002	-0.38	1.40	0.32	0.16
	LUMO	O	Ryd(3P)	1.80	1.03			
NO_3^-	HOMO	O	Cor(1S)	1.999	-18.71	18.0	-9.71	4.85
	LUMO	O	Val(2S)	1.615	-0.707			

The NO_3^-, is a nitrogen oxyanion formed by loss of a proton from nitric acid, and it's the conjugate base of nitric acid, consisting of one central nitrogen atom surrounded by three identically bonded oxygen atoms in a trigonal planar arrangement.

Its HOMO and LUMO are located on the oxygen atom with energies of -18.71 eV and -0.707 eV and occupancy of 1.99 and 1.65, respectively Table 4.4. From the two anions, it is found that NO_3^- has the largest HOMO-LUMO gap (18.01 eV). It is indicated on Figure 4.13 that the LUMO is mainly distributed around the oxygen atoms in the anions, which indicate the preferred active sites for a nucleophilic attack. From Table 4.4, the chemical properties show that NO_3^- has the highest electrophilicity followed by PO_4^{3-}complexes.

4.2.5 Adsorption of PO_4^{3-} and NO_3^- onto CLO

Since CLO showed the highest loading for the two anions, it was used as the model zeolite for subsequent computational studies. From Figure 4.14, it is observed that CLO exhibited the L-shape isotherm for the two anions, with an almost maximum loading and a pronounced inflection at a maximum loading of 606 and 461 for NO_3^- and PO_4^{3-} per unit cell, respectively.

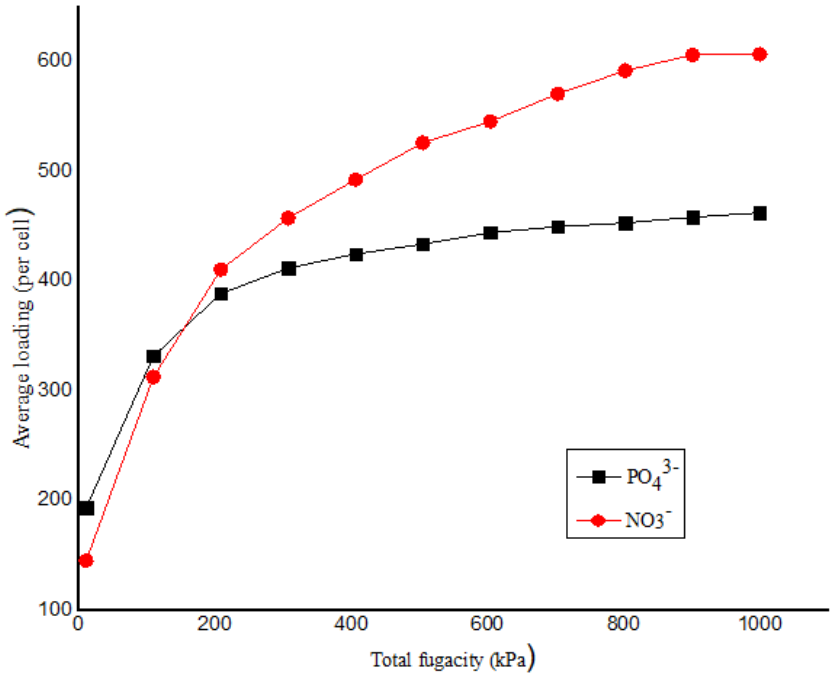

Figure 4. 14: Adsorption isotherms of PO_4^{3-} and NO_3^- onto CLO zeolite

NO_3^- exhibited higher loading onto CLO compared to PO_4^{3-} , due its lower molecular weight hence allowing more packing of the anions in the CLO structure cavities/pores. The oxygen atoms of NO_3^- participate in hydrogen bonds with the CLO framework oxygen atoms which act as basic sites and these bonds have a major impact on the stability of the adsorption complexes. The lower loading of PO_4^{3-} is attributable to its higher molecular weight hence less packing of anions in the cavities. The negative adsorption energy of PO_4^{3-} and NO_3^- onto CLO (-1840.79 and -1632.34 kcal/mol) shows that adsorption is exothermic (Wanyonyi *et al.,* 2021).

Adsorption isotherms were also determined at various temperatures (288, 298, 318 and 348 K) as shown in Figure 4.15.

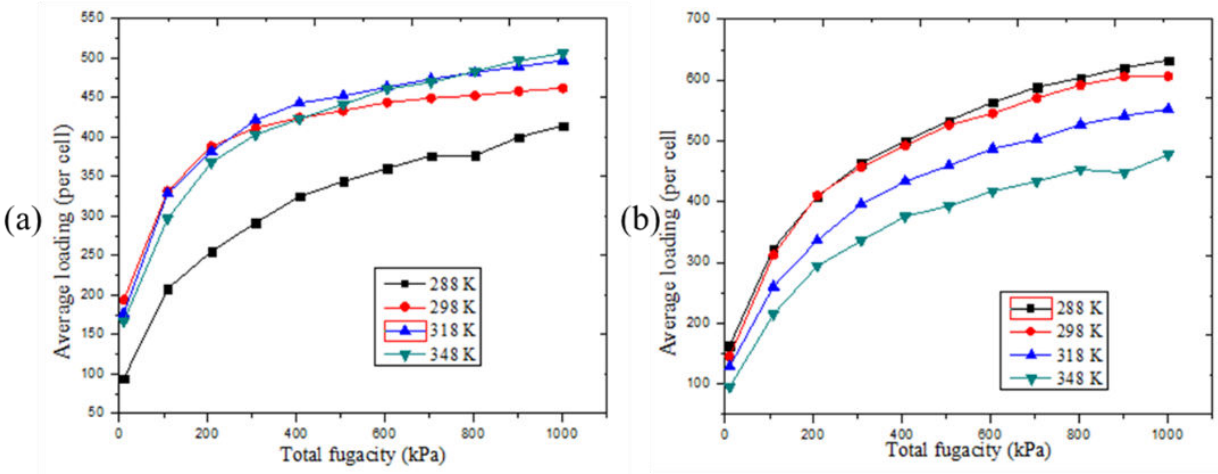

Figure 4. 15: Effect of temperature on adsorption of (a) NO_3 and (b) PO_4^{3-}onto CLO zeolite

It is important to note that as temperature increases, adsorption of PO_4^{3-} ions per cell on the CLO zeolite increase. On the other hand, adsorption of NO_3^- onto the CLO zeolite decreases when temperature increases since higher temperatures can promote desorption,

where previously adsorbed species are released. This could contribute to a decrease in the net sorption of NO_3^- onto the CLO zeolite.

The effect of doping of the CLO zeolite on the loading capacity was also investigated in detail. The phosphorous atoms at various sites with different symmetrical attributes in the CLO unit cell were individually substituted by Lithium, Sodium and Boron atoms to model CLO doped zeolite, which was then optimized. Table 4.5 show loading of NO_3^- and PO_4^{3-} on doped and undoped CLO zeolite.

Table 4. 5: Loading of anions on undoped CLO, CLO doped with Lithium, Sodium and Boron

ANIONS	**Undoped CLO**	**CLO doped with lithium**	**CLO doped with sodium**	**CLO doped with boron**
NO_3^-	606 ions	617 ions	608 ions	594 ions
PO_4^{3-}	461 ions	467 ions	472 ions	485 ions

It is interesting to note that when CLO is doped with Lithium, Sodium, and Boron, the loading of the PO_4^{3-}increased from 461 to 467, 472, and 485 ions per cell, respectively. This demonstrates a remarkable increase, and maybe attributed to the creation of large pores as a result of difference in the atomic radius of Lithium, Sodium and Boron atoms. This proves that the modification of CLO zeolite by doping can effectively improve the loading capacity of the PO_4^{3-}.

Similarly, NO_3^- exhibited higher loading of 617 and 608 of ions per cell respectively for lithium and sodium doped CLO compared to the undoped CLO since a doped CLO is more positively charged than before adsorption. Na-doped CLO showed a lower loading of NO_3^- compared to the undoped CLO. This makes pores to be large hence allows the adsorbate

pass through the pores instead being adsorbed. Doping causes modifications in the interatomic distances which could impact the ion binding. Doping with sodium may alter the zeolite's ion exchange capacity and selectivity, leading to a decreased affinity for nitrate ions.

4.2.6 Machine Learning for Anions

To complement the findings by molecular simulation , machine learning using boruta algorithm, (Kursa *et al.,* 2010) embedded in R software (Team, 2017) for statistical computing, was used to gain more chemical insights into loading capacity of anions onto the zeolites by ranking and analysing the importance of calculated parameters such as density, mass, helium void fraction, accessible pore volume, gravimetric surface area, dimensionality of the pore system.

However, since it is difficult to explicitly decipher which of the parameters obtained from molecular simulations has obvious influence on the zeolites anions sorption, the Boruta algorithm, which is a feature selection machine learning algorithm, was employed to rank the importance of descriptors especially how they impact absorption of anions on the zeolites surface. Therefore, from the pool of the descriptors, seven out of eight descriptors were tagged as important and one was tagged as unimportant and thus rejected as depicted in Figure 4.16, since its value is below the maximum value of a shadow descriptor. Therefore, largest overall cavity diameter (Di) or pore size, mass (M) and accessible pore volume (APV) appeared to be the three most important descriptors after the statistical analysis on the basis of relevant feature selection. This is quite intriguing because the aforementioned three descriptors are related to the framework, mass and volume of the zeolites which undoubtedly correlates with the role of zeolite topology to encode the

chemical information towards anion sorption. The largest overall cavity diameter being an important descriptor, is consistent with zeolite topologies with high sphere cavity which combine with interconnected cavities to exhibit appreciable loading ability for the anion sorption. The building units in zeolites results in the generation of cavities and channels which are classified as small pore (8 MR pore apertures), medium pore (10 MR pore apertures), large pore (12 MR pore apertures), and extra-large-pore (≤ MR pore apertures), zeolites (Gao *et al.,* 2021). Also, multiple pores with different dimensions can exist in zeolites, which results in different dimensional system of channels where the multiple pore systems can be linked or not linked. This is also consistent with our previous report (Wanyonyi *et al.,* 2021) on how the zeolite framework with appropriate pore size and inter channel cavities can affect heavy metal removal from water samples. Similarly, the role of the mass of a zeolite in the absorption of anions is paramount since mass is the product of density and volume of a given material. The pore system of zeolites is also characterized by the number of Cartesian directions or dimensions that a molecule can span within the channels (Schulman *et al.,* 2020). For instance, in a two-dimensional pore system the molecule can move in the two-dimensional plane formed by a network of inter-linked pores. In a three-dimensional pore system, a molecule can cover the entire volume of the crystal by moving through the pores (Baig, 2023). Therefore, density and volume deal with the bulkiness of a zeolite structure and a zeolite with high framework density and accessible pore volume tends to yield high loading for anion removal. Interestingly, accessible pore volume happens to be among the three most relevant descriptors, design of zeolites with accessible pore volumes will enhance harvesting of the anion sorption. In addition, tuning the sphere cavity and diameter, as well as enhancing the accessible volume of zeolite

architectures, are of utmost importance in harvesting the desired anion. Furthermore, other descriptors including gravimetric surface area (GSA), helium void fraction (HVF), density (D), and volumetric surface area (VSA) contribute to the loading of anions on the zeolite surface. GSA and VSA are both surface properties which are important in zeolites in removing anions from water. As already mentioned, the framework density of a zeolite is related to the accessible volume and this enhances anion removal from water. Compared to the other descriptors from the molecular simulation results, zeolites with moderately high HVF displayed high loading, particularly the CLO zeolite. This however is reasonable and in good agreement with the ranking since it proves the inherent nature of HVF in zeolite. As mentioned earlier, one descriptor was rejected –the dimensionality of the pore system (DPS) as shown in red in Figure 4.16 because the value is below the maximum value of a shadow descriptor which served as an index to rank how important descriptors appeared after statistical analysis.

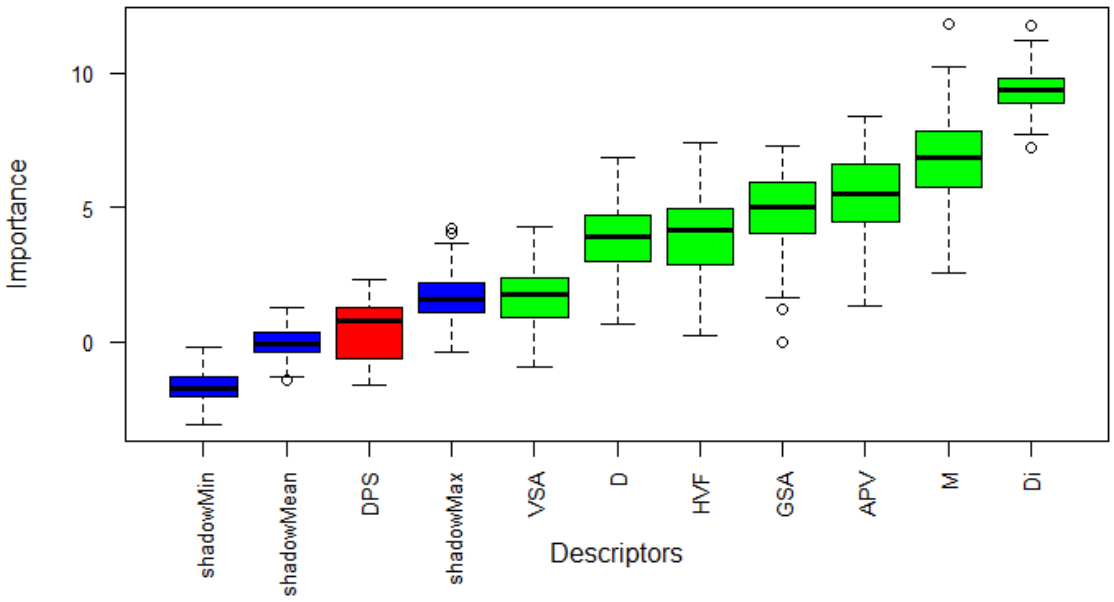

Figure 4. 16: Ranking of importance of parameters (descriptors) plot using Boruta algorithm for zeolites dataset. Green boxplots correspond to Z score of important descriptors, red boxplot correspond to unimportant descriptor while blue boxplots correspond to minimum, mean and maximum Z score of shadow descriptors.

The data shown in Table 4.6 shows all the values of the descriptors on the basis of their importance according to the *Z* score of each descriptor. The *Z* score is a benchmark used to determine the importance of descriptors by comparing with the mean, minimum and maximum *Z* score of the shadow descriptors to decide the importance of descriptors in the selected application. In view of these considerations, the *Z* score of Di, M, APV, GSA, HVF, D, VSA are above the maximum *Z* score of the shadow descriptors with values of 1.0, 1.0, 0.95, 0.98, 0.89, 0.91 and 0.46, thus they are deemed to be important. This implies that Di is 100% more than the shadow descriptor, M is also 100% more than the shadow descriptor, APV is 95% higher than the shadow descriptor, GSA is 98% higher than the shadow descriptor, HVF is 89% higher than shadow descriptor, D is 91% higher than the

shadow descriptor and VSA is 46% higher than the shadow descriptor. VSA is lower than 50% which is the minimum value needed to assign importance to a descriptor, thus it is tagged as a tentative descriptor, meaning a decision is yet to be made as to whether the descriptor is important or unimportant.

However, after running the *Tentative Rough Fix* command in the RStudio, the descriptor was tagged as important. In contrast, DPS was rejected since the value is 0.05 (5%), below the maximum value of the shadow descriptor. Moreover, to examine how independent these descriptors are of each other, the correlation between the seven important descriptors taking each pair of descriptors as well as the correlation with sorption loading was analysed. Accordingly, the correlation coefficients depicted in Figure 4. 17, shows only a single pair of descriptors (GSA, HVF) gave high R^2 values over 0.95, therefore, most of descriptors are independent with each other.

Table 4. 6: The attStats function shows the data frame with each descriptor Z score statistics as the function of random forest iteration to rank which descriptor was more important than the most important shadow descriptor

Descriptor	MeanImp	MedianImp	MinImp	MaxImp	NormHits	Decision
M	6.77	6.88	2.58	11.83	1.00	Confirmed
D	3.83	3.91	0.65	6.85	0.92	Confirmed
HVF	3.97	4.15	0.24	7.41	0.90	Confirmed
APV	5.50	5.50	1.35	8.41	0.96	Confirmed
VSA	1.69	1.77	-0.92	4.27	0.47	Tentative
GSA	4.94	5.04	0.00	7.29	0.99	Confirmed
DPS	0.48	0.81	-1.63	2.31	0.05	Rejected
Di	9.36	9.40	7.21	11.79	1.00	Confirmed

M	1.00	M							
D	0.11	1.00	D						
HVF	0.02	0.04	1.00	HVF					
APV	0.17	0.59	0.06	1.00	APV				
VSA	0.13	0.14	0.07	0.71	1.00	VSA			
GSA	0.17	0.55	0.07	0.95	0.82	1.00	GSA		
Di	0.21	0.44	0.03	0.70	0.45	0.64	1.00	Di	
Load	0.41	0.28	0.01	0.50	0.29	0.47	0.45	1.00	Load

Figure 4. 17: Triangular matrix of the correlation among the selected 7 descriptors and zeolite anion loading

From the study, CLO was the best for PO_4^{3-} and NO_3^- sorption. LTN was the second best for PO_4^{3-} while NO_3^- was second on MWF. Machine learning algorithm has been employed to rank the importance of the various descriptors that has influence on the removal of anions in water. Largest overall cavity diameter, mass and accessible pore volume appeared to be the three most important descriptors. Collectivity, tuning the sphere cavity and inter channel diameter as well as engineering the accessible volume of zeolite architectures are of utmost important toward harvesting the desired anions

4.3 Computational Adsorption Studies of Selected Pharmaceuticals and Pesticides

Objective 2; To evaluate the adsorption of halogenated pharmaceuticals (diclofenac, ciprofloxacin and chloramphenicol) and pesticides (diuron, chlorpyrifos and imidacloprid) on experimentally available zeolite frameworks using molecular dynamic simulations

4.3.1 Computational study on Pharmaceuticals

This work aims at establishing whether molecular simulation approach can be used for an approximate prediction of pharmaceutical pollutant removal efficiency on a large variety of purposefully selected zeolites i.e; CLO, ITV, SBT, MFI, SBE, FAU, TSC, PAR, ITE, CGF, RTH, RUT, DOH, MTF, THO, CZP, AHT, MON, EUO, SAO, SFE, OSI, LTN, MTN, STO, AEL, FRE, MOR, DDR, WEI, SBS, MSO, HEU, KFI, LTA, NAT, RHO, ESV, SAT, BOG and NON (Baerlocher, 2008). The focus on the three pharmaceutical drugs (diclofenac, ciprofloxacin and chloramphenicol) was motivated by the fact that they are largely consumed resulting in their detection in surface water and sewage treatment plants effluents (Kimosop *et al.,* 2016). For detailed methodology of this section, refer, to subsection 3.2

4.3.2 Frontier Molecular Orbitals of Pharmaceuticals

Molecular simulations have been used as a screening tool to identify promising zeolites for the removal of selected pharmaceutical pollutants. The frontier orbitals of the optimized structures of diclofenac, ciprofloxacin and chloramphenicol are shown in Figure 4.18.

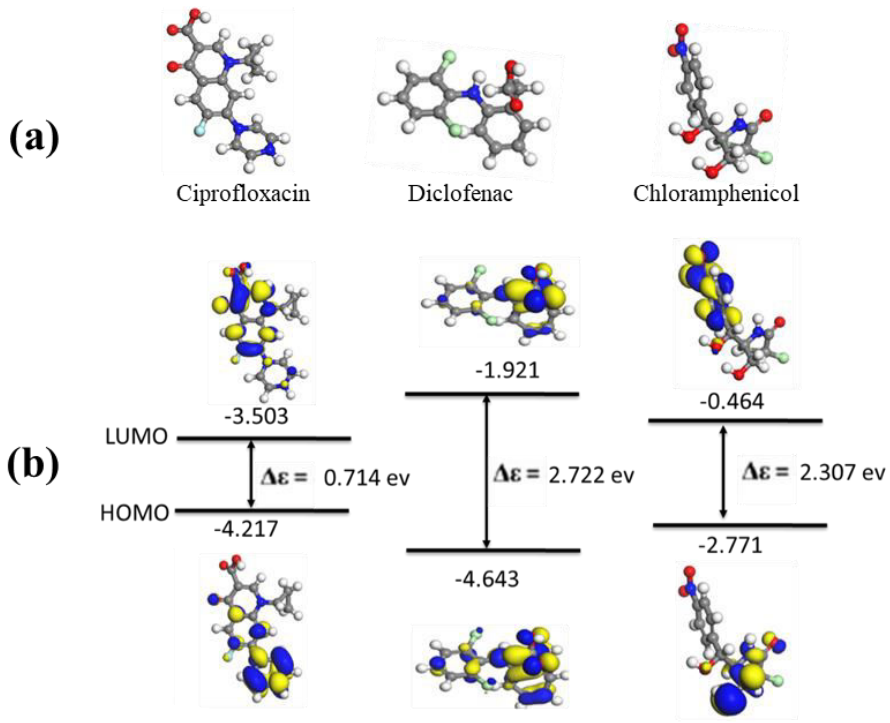

Figure 4. 18: (a) Optimized structures of ciprofloxacin, diclofenac and chloramphenicol (b) Frontier molecular orbitals of ciprofloxacin, diclofenac and chloramphenicol. Atoms in grey, red, white, green, blue color represent Carbon, Oxygen, Hydrogen, Chlorine and Nitrogen respectively. Yellow and blue regions correspond to positive and negative values of the orbital. Calculated at approximation (LDA) with the PDW exchange-correlation functional level of theory

The HOMO energy (E_{HOMO}) is normally related to the electron-donating ability of a molecule whereas LUMO energy (E_{LUMO}) is associated with the electron-accepting ability of a molecule from which the global hardness (η) can be calculated.

The energy gap between HOMO and LUMO also helps to describe the chemical behavior and electrical properties of molecules, with lower energies indicating higher reactivity and lower stability (Mebi, 2011). It can be observed that the HOMO of diclofenac is concentrated on benzene ring and around N- and OH- groups, similar to the LUMO but

less pronounced. In ciprofloxacin the HOMO is localized on lower side on dinitro-phenyl ring, while the LUMO on the upper phenyl ring having nitrogen in the ring extending to OH group and O^-, which are attached to the phenyl ring. For chloramphenicol, the HOMO is also on lower part of the molecule and appears around the benzene ring, OH group and the acetamide group in which δ-interaction bonding system is on semicircle of the ring, while the LUMO is localized on nitro-phenyl ring. Table 4.7 shows the quantum chemical descriptors of the three selected pharmaceuticals products

Table 4. 7: Key quantum chemical descriptors obtained for the three pharmaceutical products.

Pharmaceuticals	**Chemical potential (eV)**	**Chemical hardness (eV)**	**Chemical softness (eV)**
Diclofenac	-3.28	1.36	0.74
Ciprofloxacin	-3.86	0.36	2.80
Chloramphenicol	-1.62	1.15	0.87

The calculations of the energy levels of the electron orbitals allowed quantifying the value of the HOMO and LUMO energies, whereby diclofenac has the lowest HOMO energy (-4.6430 eV) while chloramphenicol has the highest HOMO energy (-2.771 eV). The larger the HOMO–LUMO energy gap, the harder and more stable/less reactive the molecule (Mebi, 2011). In the present study, it is also seen that diclofenac has the highest chemical hardness of 1.3609 eV (Table 4.7). This implies that it has a higher stability and opposing charge transfer.

On the contrary, chloramphenicol and ciprofloxacin molecules have a small HOMO-LUMO gap hence, they are highly polarizable in nature and more reactive (AI-Sehemi *et*

al., 2016). These descriptors determine the interactions of the selected pharmaceuticals with the binding sites on various zeolites. Based on this, we initially screened the adsorption of diclofenac, ciprofloxacin and chloramphenicol on the eleven zeolites (Table 4.8).

Table 4. 8: The loading of diclofenac, ciprofloxacin and chloramphenicol on various zeolites structure

Code	Diclofenac Loading (molecules per cell)	Total Energy (kcal/mol)	Ciprofloxacin Loading (molecules per cell	Total Energy (kcal/mol)	Chloramphenicol Loading (molecules per cell	Total energy (kcal/mol)
CLO	60	10185.83	29	8401.67	48	8512.08
TSC	19	5637.32	8	2051.31	13	2019.38
ITV	11	2527.35	11	3756.83	9	1486.59
FAU	9	2326.61	5	1326.60	8	1242.94
SBT	4	885.23	3	1006.81	3	524.62
SBS	4	616.329	2	665.94	2	441.29
SBE	5	666.36	3	987.32	4	626.45
DFO	3	994.81	2	443.37	2	314.48
LTN	1	12.34	0	0.00	0	0.00
MFI	0	0.00	0	0.00	0	0.00
NON	0	0.00	0	0.00	0	0.00

From Table 4.8, CLO has the greatest diclofenac, imidacloprid and ciprofloxacin loading of 60, 48 and 29 molecules per cell, respectively since, CLO has large diameter, 10.06 A.

Conversely, the loading of all other zeolites was relatively low. For example, TSC, is in second place in terms of loading of diclofenac and chloramphenicol with 19 and 13 molecules per cell, respectively. This is a significant discrepancy that can be attributed to differences in the two zeolites' mass, density, helium vacancy percentage, and diameter. ITV is closely followed by FAU, where loading of chloramphenicol (9 versus 8 molecules per cell) and diclofenac (11 versus 9 molecules per cell) is observed. However, ciprofloxacin's (9 verses 11) indicates that ITV has a higher ciprofloxacin loading than FAU. This shows that ITV is a good adsorbent for ciprofloxacin compared to FAU. DFO, SBT, SBE and SBS recorded lower loading for the three pharmaceuticals due to their small pores. It is important to note that all zeolites exhibited positive total energy showing that the process is endothermic.

4.3.3 Adsorption isotherms of diclofenac, ciprofloxacin and chloramphenicol on various zeolites

According to Kalam and co-workers, (Kalam *et al.,* 2021) adsorption isotherms are classified into four groups. The first group is the C-shaped adsorption isotherm which describes a linear increase of the pollutant's adsorption loading with the equilibrium concentration of pollutant in solution. The second category is the L-shaped isotherm that occurs when the adsorbent has a limited number of adsorption sites, leading to the appearance of a plateau in the adsorption isotherm after a specific equilibrium concentration of pollutants, suggesting the saturation of the adsorbent. Thirdly, the H-shaped isotherms that indicate that the adsorbent have a higher affinity for pollutants, and lastly, the S-shape that is attributed to a higher attraction between the pollutants at the surface of the adsorbent (Inglezakis *et al.,* 2018).

The sorption isotherms for diclofenac on zeolites that gave the best and one with zero loading is shown in Figure 4.19.

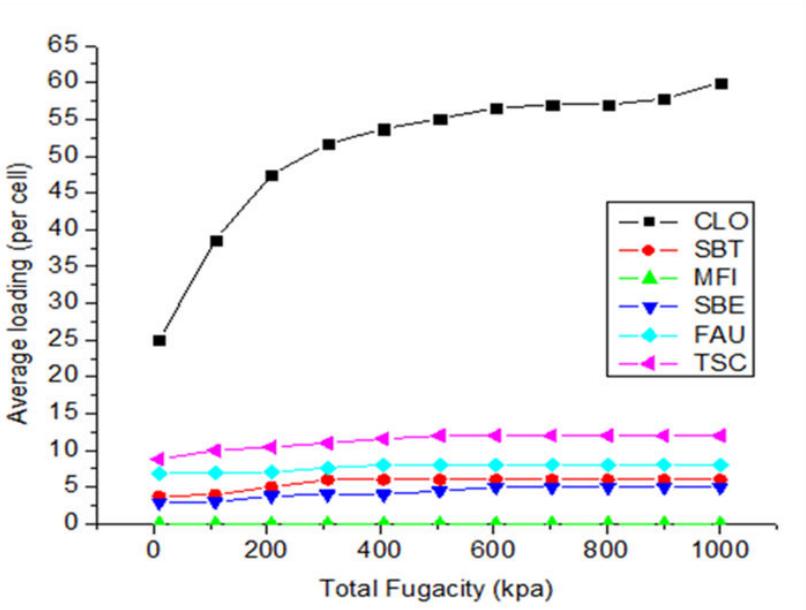

Figure 4. 19: Adsorption isotherms of diclofenac on various zeolites at 298 K

Among the various zeolites tested, it was observed that only CLO exhibited the L-shape isotherm with an almost maximum loading and a pronounced inflection at a maximum loading of 60 molecules per unit cell (Figure 4.19).

Conversely, all the other zeolites exhibited low loading. For example, the MFI zeolite a high silica zeolite, a medium pore zeolite, featuring a 10-ring pore opening with a diameter of approximately 5.5 Å and a chemical formulae $AI_{27}Si_{69}O_{165}$), showed no loading, due to its narrow channel openings (Martucci *et al.,* 2012) and as a result the cations tend to be located in the intersections, blocking the favorable adsorption sites. Also, the UCSB-10Ga29 (SBT), UCSB-8CO (SBE), faujasite (FAU) and Tschortnerite (TSC) type of zeolites with chemical formulae $Ga_{36}Zn_{36}P_{72}O_{288}$, $AI_{32}CO_{32}P_{64}O_{256}$, $Al_{58}Si_{134}O_{384}$ and $Al_{192}Si_{192}O_{768}$ respectively, exhibited low loading of 3, 5, 8 and 12 molecules (Figure 4.19)

of diclofenac per unit cell, respectively. SBT is 3-dimensional structure, with a 12 - ring pore (7.2 × 7.4 nm in diameter) and a cage number of 5, 13 which is small hence low loading of 3 diclofenac molecules per cell.

On the other hand, SBE zeolite is almost the same to SBT though the loading is 5 molecules per cell. Faujasite (FAU) has a 3-dimensional channel system with large pore openings formed by 12 rings (7.4× 7.4 nm in diameter), hence relatively high loading of 8 molecules per cell. The Tschortnerite (TSC) structure contain 8-ring channels or pores (4.2× 4.2 nm in diameter). The channel has intersections, or cavities, and the cavities and cages fused together which makes it have more loading compared to FAU-zeolite.

The adsorption is minimal when the size of pollutant is larger than the pore opening size of zeolite making the zeolites behave as molecular sieves (Pham *et al.,* 2016). Sorption fields of diclofenac on the several representative zeolites are also shown in Figure 4.20.

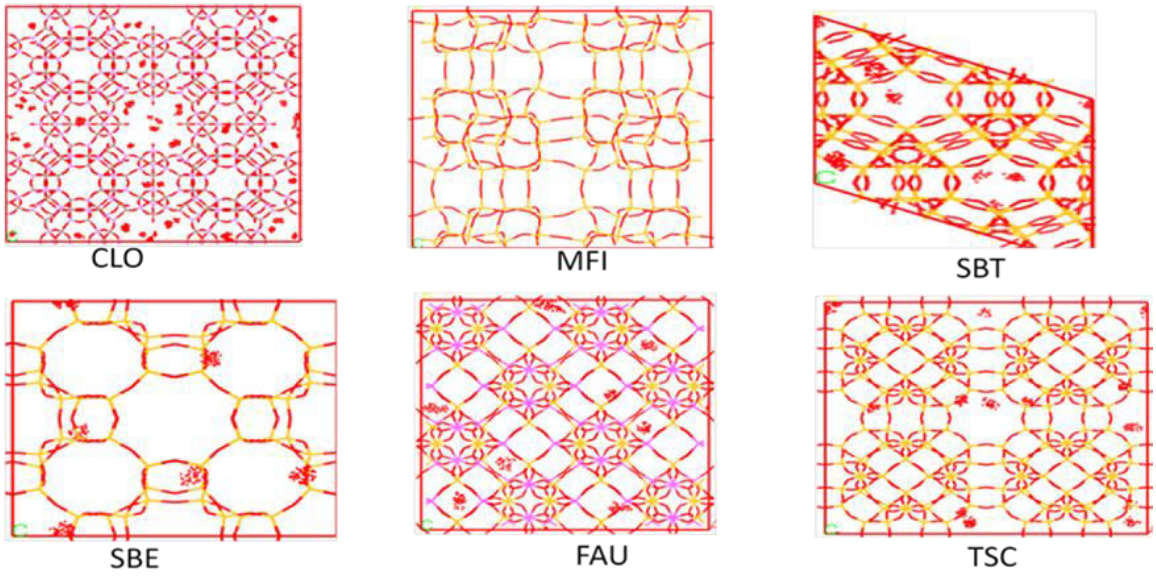

Figure 4. 20: Sorption fields for diclofenac on the zeolites

It is seen that CLO has more sorption fields for diclofenac compared to other zeolites. For the best performing zeolite CLO, the adsorption sites are distributed evenly throughout the framework structure. This fields are attributed to the number of oxygen atoms which are the active sites providers. Then the rest, the active sites are specifically distributed as shown in Figure 4.20, 4.23 and 4.26. For comparison, the adsorption of ciprofloxacin and chloramphenicol was also studied. It shows that the adsorption follows the same trend as discussed for diclofenac. It is clear from Figure 4.21 that the diclofenac molecule prefers to locate at the intersections in CLO zeolite structure. The simulation results indicate that CLO is a promising adsorbent for the removal of diclofenac and it demonstrates that the very good packing of diclofenac is directly related to the probability of crossing and bending at the intersections of CLO. The most stable adsorbed configurations of the pharmaceuticals in the CLO zeolite alongside the corresponding adsorption energies was also probed as observed in Figure 4.21 A

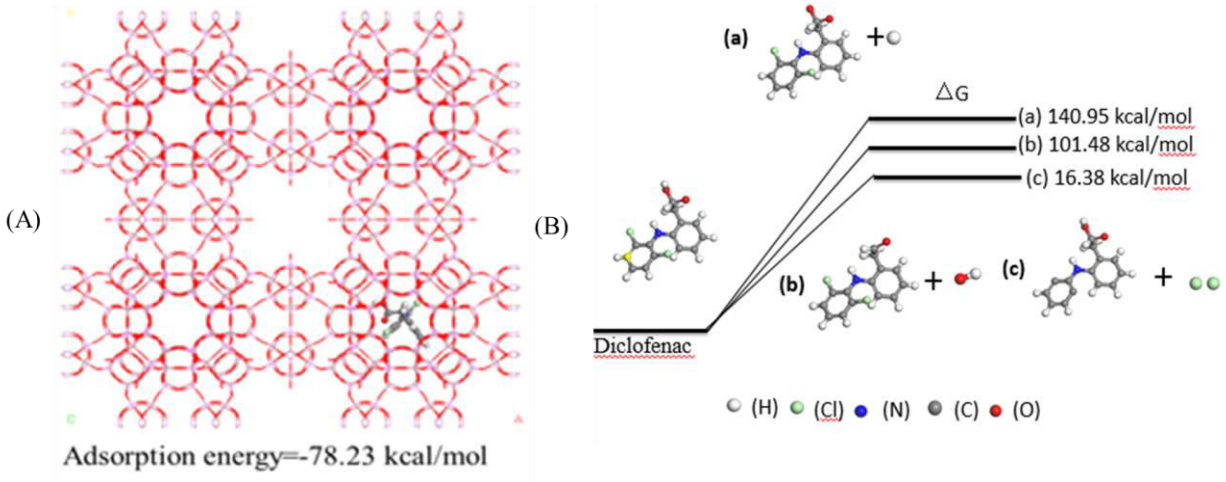

Figure 4. 21: (A) Structures of the most stable configuration of diclofenac adsorbed onto the CLO. (B). Calculated Gibbs energies for the diclofenac desorption processes from CLO.

Diclofenac molecule was observed to be located at the centre of the 20-ring channel, facing the direction of the channel, while the phenyl group directly lie on the phenyl ring. Adsorption energy of -78.23 kcal/mol was observed for the most stable configuration. On the other hand, Figure 4.21 B shows desorption products of diclofenac outside the zeolite structure through dehydrogenation, dehydroxilation and dechlorination. It is seen that dechlorination is the most favoured route with △G of 16.38 kcal/mol.

The adsorption behavior of ciprofloxacin on several representative zeolites were studied. Figure 4.22, shows the adsorption isotherms for ciprofloxacin on CLO, SBT, MFI, SBE, FAU and TSC zeolites.

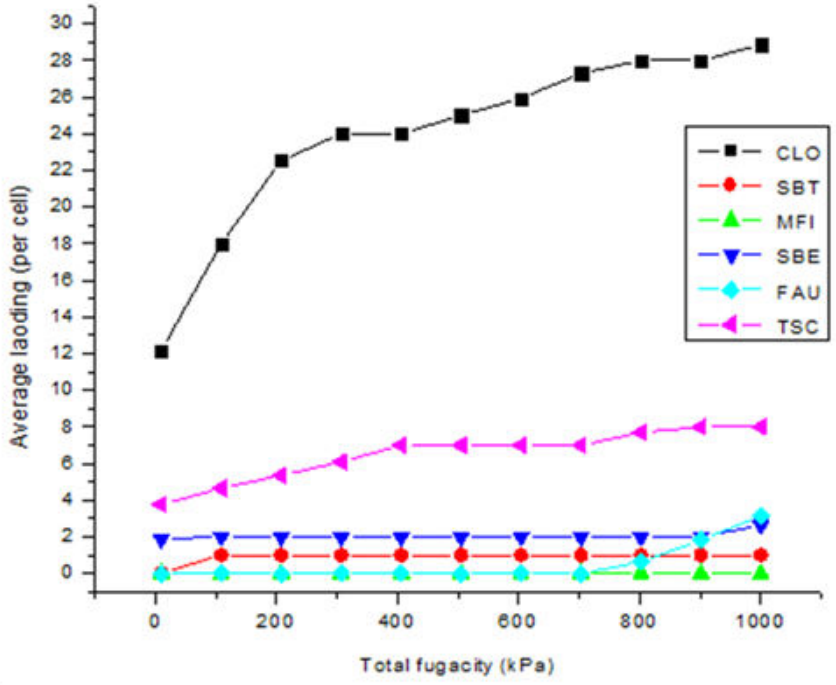

Figure 4.22: Adsorption isotherms of ciprofloxacin onto various zeolites at 298 K

Among the various zeolites, only CLO exhibited the L-shape isotherm with maximum loading and a pronounced inflection at a maximum loading of 29 molecules of

ciprofloxacin per unit cell which is less compared to sorption of diclofenac (60 molecules per cell). It is also seen that MFI showed zero loading. The SBT, SBE, FAU and TSC exhibited low loading of 1, 3, 4 and 8 molecules of ciprofloxacin per unit cell, respectively. The loading on the same zeolites exhibits the same trend as the diclofenac case, however in each instance, a lower loading was noted, most likely because it was larger molecule than diclofenac. Additionally, CLO has more sorption fields compared to SBT, SBE, FAU and TSC. Figure 4.23 shows the sorption fields of ciprofloxacin on different zeolites while Figure 4.24 shows the most stable configuration of ciprofloxacin on CLO zeolite.

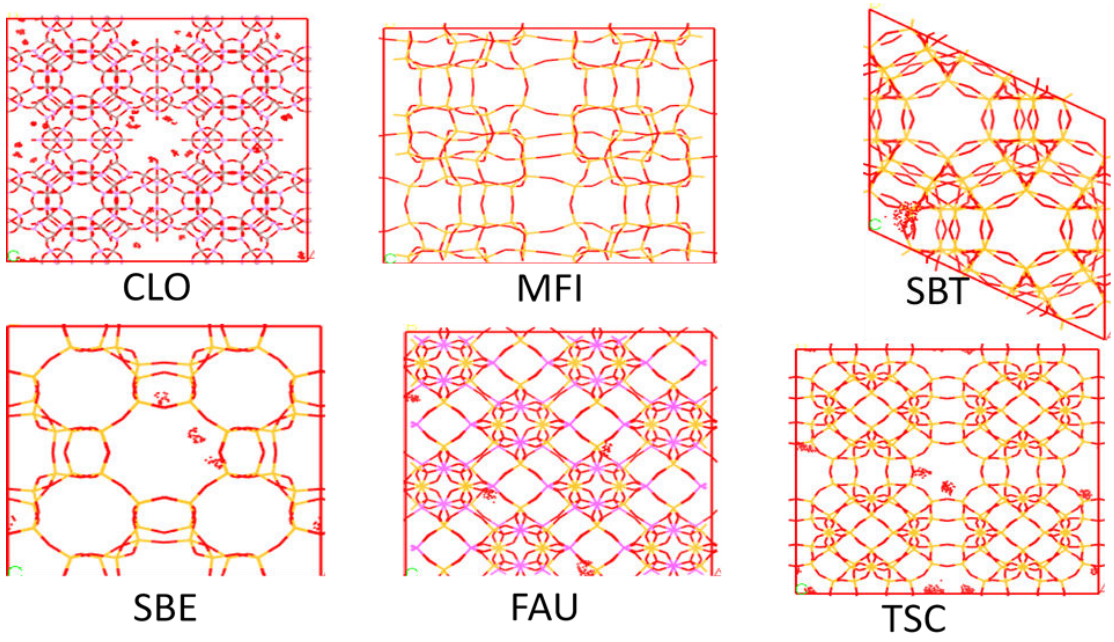

Figure 4. 23: Sorption fields for ciprofloxacin on the zeolites

Figure 4.24A, visualizes the lowest-energy configuration of ciprofloxacin in the CLO structure. The central part of the molecule occupies a 20-ring window connecting two super cages, while the phenyl moieties and the side chain are located to the side assemblies of the 20-rings bordering these cages of the 8 rings. The most stable configuration energy of

ciprofloxacin gave absorption energy of -84.46 kcal/mol compared to -78.23 kcal/mol of diclofenac meaning that it is more stable compared to diclofenac. Figure 4.24 B, shows desorption of ciprofloxacin outside the zeolite structure through dehydrogenation, dehydroxilation and dichlorination where dechlorination is the most favored route with △G of 315.24 kcal/mol.

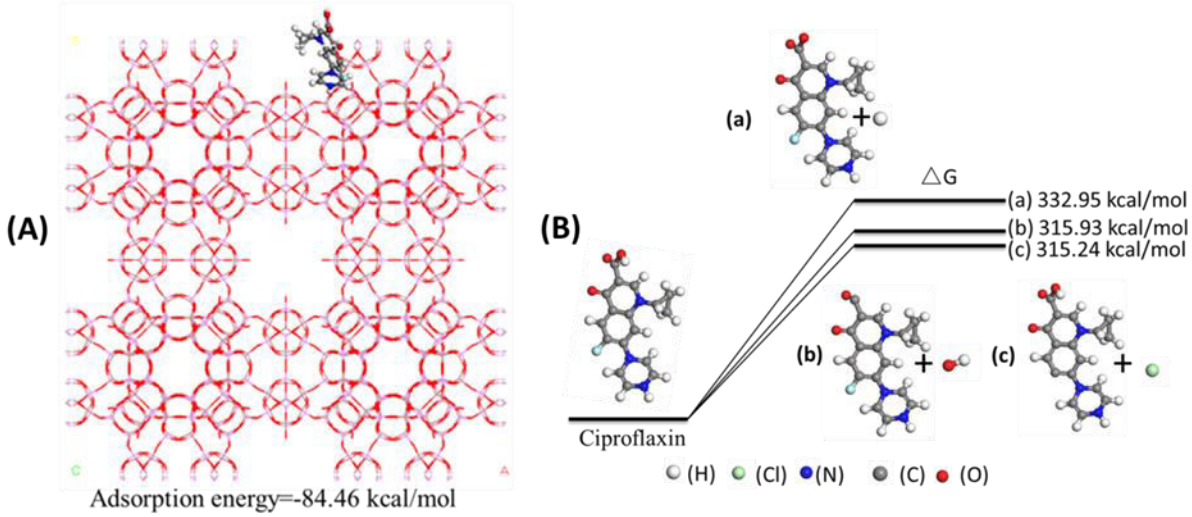

Figure 4. 24: (A) Structures of the most stable configuration of ciprofloxacin adsorbed on the CLO. (B). Calculated Gibbs energies for the ciprofloxacin desorption processes from CLO.

Figure 4.25 shows the adsorption isotherms of chloramphenicol on the CLO, SBT, MFI, SBE, FAU and TSC representative zeolites.

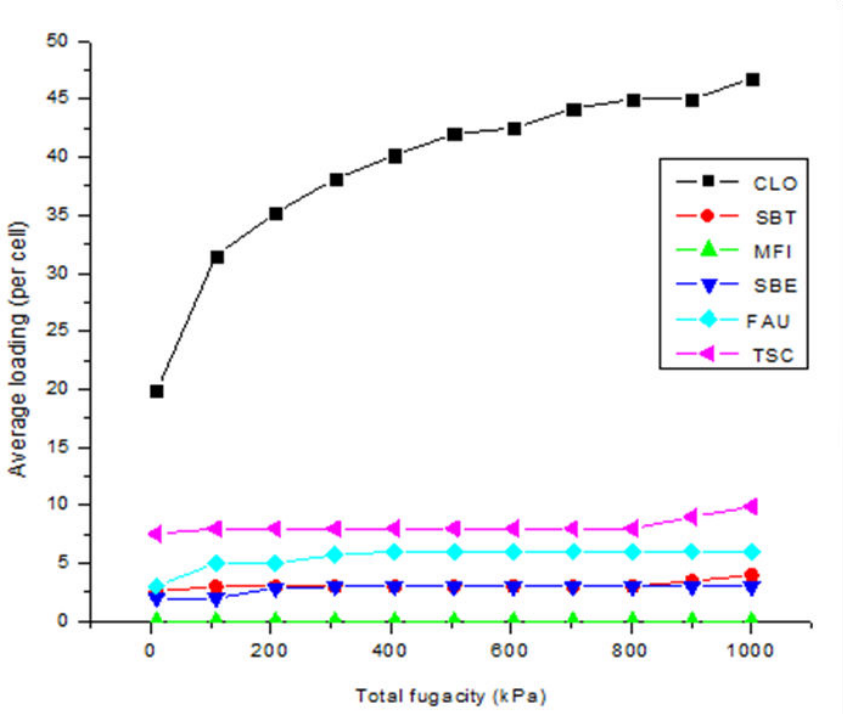

Figure 4. 25: Adsorption isotherms of chloramphenical on various zeolites at 298K

Just like for diclofenac and ciprofloxacin, it is only CLO that exhibited the L-shape isotherm with maximum loading and a pronounced inflection at a maximum loading of 48 molecules of chloramphenicol per unit cell. It is interesting to note that diclofenac sorption on the CLO is higher compared to the ciprofloxacin and chloramphenicol. It is also seen that just like sorption of diclofenac and ciprofloxacin, chloramphenicol showed zero loading on MFI. The SBT, SBE, FAU and TSC exhibited low loading of 4, 3, 6 and 13 molecules of chloramphenicol per unit cell, respectively. It is also seen that CLO has more sorption fields for chloramphenicol compared to SBT, SBE, FAU and TSC as shown in Figure 4.26.

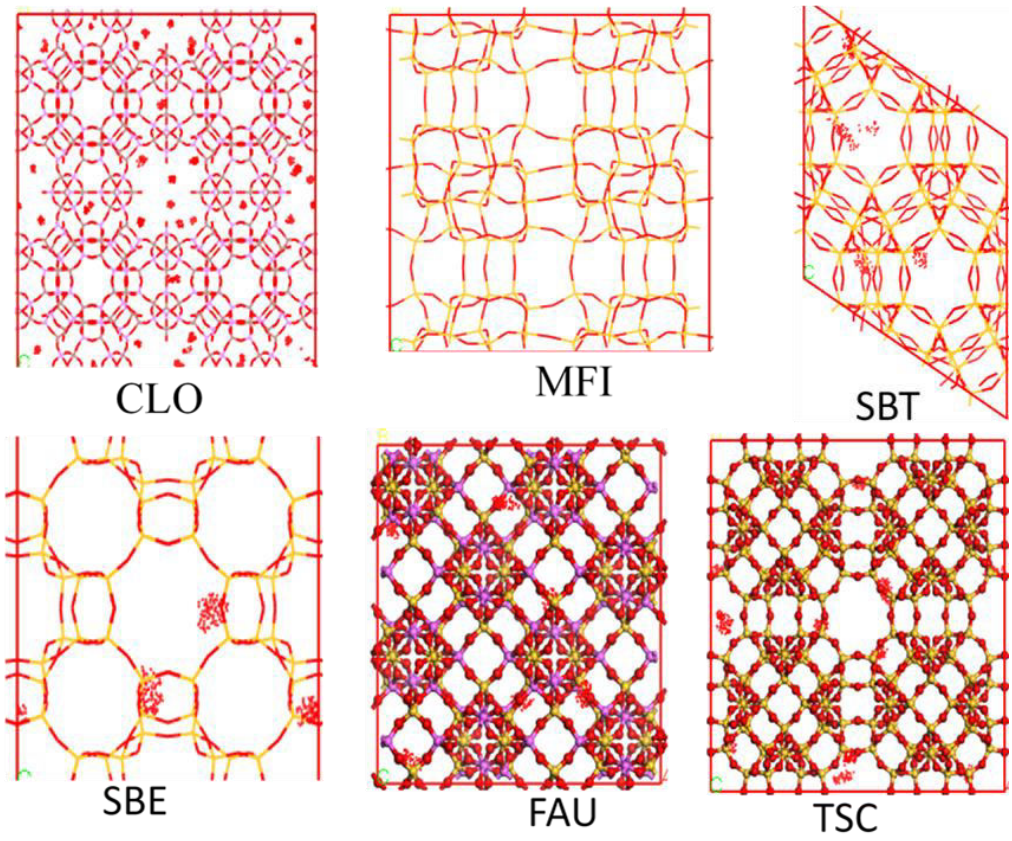

Figure 4. 26: Sorption fields for chloramphenicol on the zeolites

Figure 4.27 A, shows structures of the most stable configuration of chloramphenicol adsorbed on the CLO while Figure 2.27 shows the desorption of chloramphenicol.

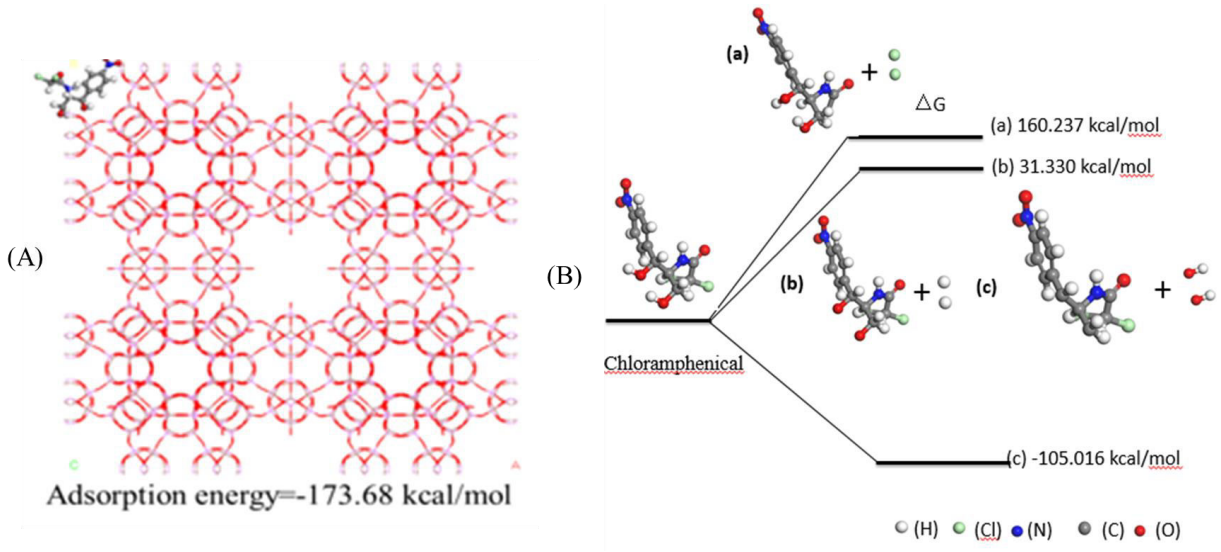

Figure 4. 27: (A) Structures of the most stable configuration of chloramphenicol adsorbed on the CLO. (B). Calculated Gibbs energies for the chloramphenicol desorption processes from CLO.

The conformation of chloramphenicol adsorbed in CLO is very similar to that of the free molecule just like ciprofloxacin. The central part of the molecule occupies a 20-ring window connecting super cages, and both phenyl moieties with the side chain are located to the upper and down assemblies of 20-rings bordering these cages. The most stable configuration gave absorption energy of -173.23 kcal/mol which is two folds lower than that of diclofenac and ciprofloxacin. The desorption of chloramphenicol outside the zeolite structure can be through dehydrogenation, dehydroxilation and dichlorination. Dechlorination is the most favored way of desorption of adsorbed chloramphenicol with △G of -105.016 kcal/mol.

According to the molecular simulation results of this study, CLO zeolite is the most suitable for the adsorption of diclofenac, ciprofloxacin and chloramphenicol. Given the large amount of drug contaminants found in the current environment and the structural

variability of zeolites, this screening strategy has considerable potential to facilitate the development of new adsorptions for wastewater treatment. Looking beyond zeolites, they could also be used to compare the performance of adsorbents from different categories.

4.4 Computational Studies of Selected Organic Pesticides

This study aimed at evaluating the adsorption of diuron, chlorpyrifos and imidacloprid onto several zeolites. The study of the three pesticides were employed as models because of their extensive use and the prevalence with which they have been traced in water. For detailed methodology of this section, refer, to subsection 3.2

4.4.1 Frontier Molecular Orbitals of Pesticides

The frontier orbitals and respective energies of the optimized structures of the selected pesticides are shown in Figure 4.28.

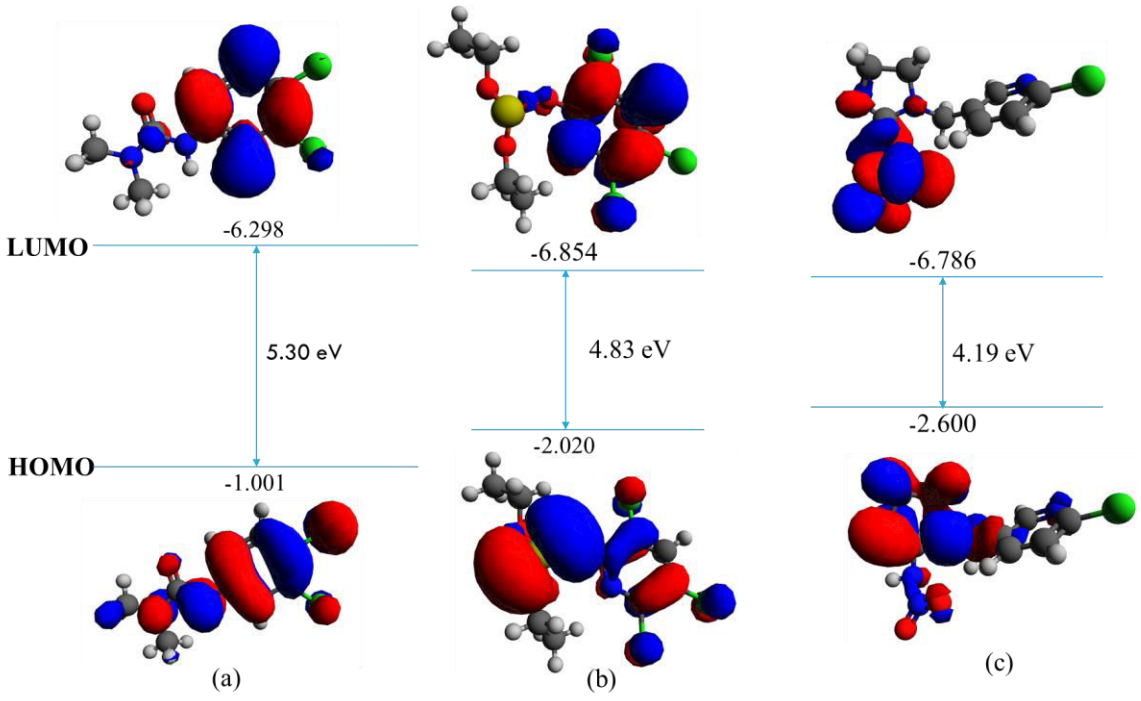

Figure 4. 28: The frontier molecular orbitals of (a) diuron, (b) chlorpyrifos and (c) imidacloprid

Table 4. 9: DFT-calculated Key quantum chemical descriptors for the three pesticides

Compound	Dipole Moment(μ)	Polarizability (α)	E_{HOMO} (eV)	E_{LUMO} (eV)	$\Delta E_{HOMO-LUMO}$ (eV)
Chlorpyrifos	2.06	209.26	-6.85	-2.02	4.83
Diuron	5.77	157.75	-6.30	-1.00	5.30
Imidacloprid	3.31	166.53	-6.79	-2.60	4.19

Analyzing the HOMO and LUMO is very vital in the study of the frontier molecular orbitals. The HOMO-LUMO helps to characterize the chemical reactivity and stability of the molecules. A compound with narrow energy gap indicates less stability and higher chemical reactivity, while a compound with wide energy gap portrays higher stability and less chemical reactivity (Tao *et al.,* 2016).

For chlorpyrifos, the most suitable sites for electrophilic attack are oxygen and sulfur atoms, while hydrogen atoms on the pyridine ring are the most ideal sites for nucleophile attack. This active site may be crucial in adsorption onto zeolite. The band gap of imidacloprid and chlorpyrifos are relatively lower (4.19 eV and 4.83 eV, respectively) compared to diuron (5.30 eV). This high band-gap energy shows that diuron molecule is stable among the three pesticides. However, when the band gap of imidacloprid and chlorpyrifos are compared then the latter is more stable. The imidacloprid lower or moderate chemical hardness value 4.19 eV confirms that it is highly reactive compared to diuron and chlorpyrifos. Polarizability of molecules depends on the complexity of the structure and on the distortion of electron cloud by the incoming charges (Morad *et al.,* 2023). It is important to note that chlorpyrifos being large sized molecule compared to imidacloprid and diuron it is more polarizable, which is consisted with the values recorded in Table 4.9. Dipole moment accelerates the chemical bond formation, various non-bonding

interaction and binding energy affinity. The dipole moment of the compound results from non-uniform distribution of charges on the atoms in the molecule. Mostly it is used to examine the intermolecular interactions. In this study, diuron has highest dipole moment (5.77 μ) while chlorpyrifos recorded the lowest dipole moment (2.06 μ). The high dipole moments represent the binding position within a specific structure and stronger the intermolecular interactions (Morad *et al.,* 2023). This therefore, show that chlorpyrifos and imidacloprid have weak interactions compared to diuron.

4.4.1.1 Molecular Electrostatic Potential (MEP)

The molecular electrostatic potential is a critical factor in determining the reactivity of a chemical. MEP is a derivative of total charge density created by displaying distinct sets of electron density magnitudes using color codes. It is therefore, a map or graphic representation of the potential difference between electron donating, electron accepting, and neutral zones (Refaat, *et al.,* 2023). Green represents neutral character, red represents electron rich zone, and blue represents electron deficient zone (Rezaei-Sameti & Zarei, 2018). It is used in determining the reactivity of molecules to electrophilic and nucleophilic attacks. Figure 4.29 shows the molecular electron potential of the three pesticides.

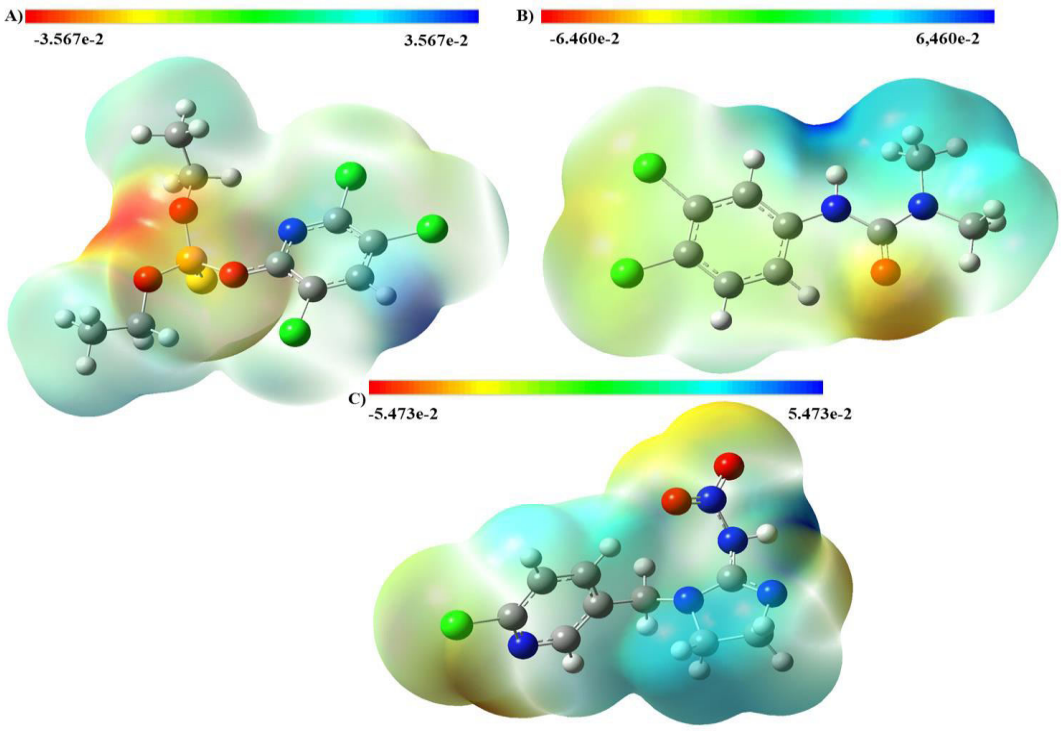

Figure 4. 29: Molecular electrostatic potential of (a) chlorpyrifos (b) diuron and (c) imidacloprid

The results demonstrate that pesticide oxygenated groups have a significant negative electron density and are delocalized on these functional groups (red color). This suggests that these groups could serve as nucleophilic attack sites for the pesticides. On the other hand, the amine groups are the electrophilic attack sites. As a result, this location will attract electrophiles, whereas the regions indicated in blue will have the opposite effect. From these results, the H atoms indicate the strongest attraction and O atom indicates the strongest repulsion. Charge density distribution near oxygen atom of the carboxyl group shows regions of large negative electrostatic potential. These images show that the carboxyl-end of the molecule is electron rich relative to the phenyl end.

4..4.1.2 The IR Spectrum the Pesticides

The simulated spectra of diuron, chlorpyrifos, and imidacloprid molecules are depicted in Figure 4.30-4.32, indicating that the presence of unique functional groups results in different bands, resulting in spectral disparities between the IR spectra of different compounds. In the case of imidacloprid (Figure 4.30), the bands at 1572 and 1548 cm^{-1} clearly show the pyridine group's =CH- stretching. The $-NO_2$ symmetric stretching band is detected between 1300 and 1250 cm^{-1}, while the bands between 1420 and 1500 cm^{-1} and 1109 cm^{-1} are most likely due to aromatic =CH- and aryl-Cl stretching, respectively.

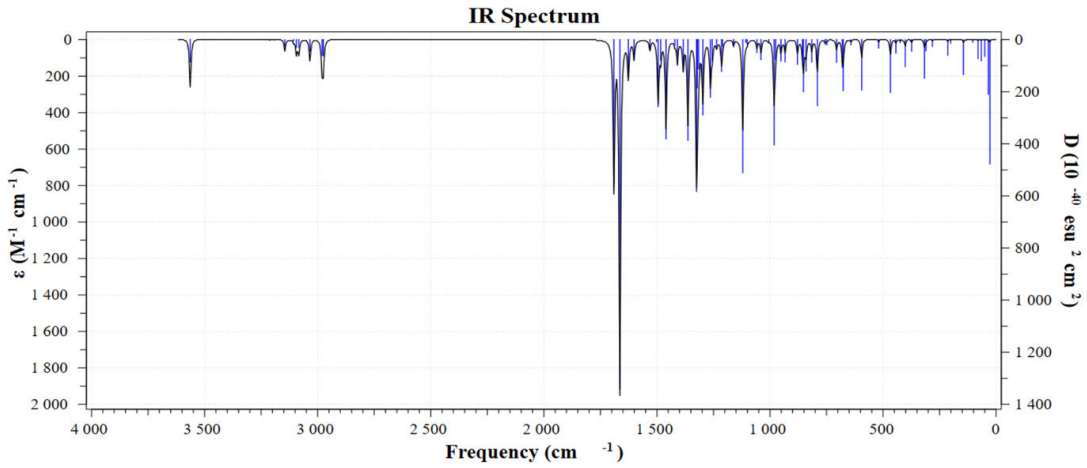

Figure 4. 30: Simulated IR Spectra of Imidacloprid

The infrared spectra of chlorpyrifos (Figure 4.31) exhibited bands at 3,444 and 1,627 cm^{-1}, which correspond to the N-H and C=O, respectively. C=C features can be discovered at peak locations of 1,415, 1,050, 845, and 670 cm^{-1}. The peak at 634.59 cm^{-1} is caused by P=S stretching, which is typical of chlorpyrifos, and the peak at 537.12 cm^{-1} is caused by P-O stretching, which is also typical of chlorpyrifos. Armenta *et al.,* (2005) reported C-N stretching, C-Cl stretching, and P-S stretching absorption bands for chlorpyriphos.

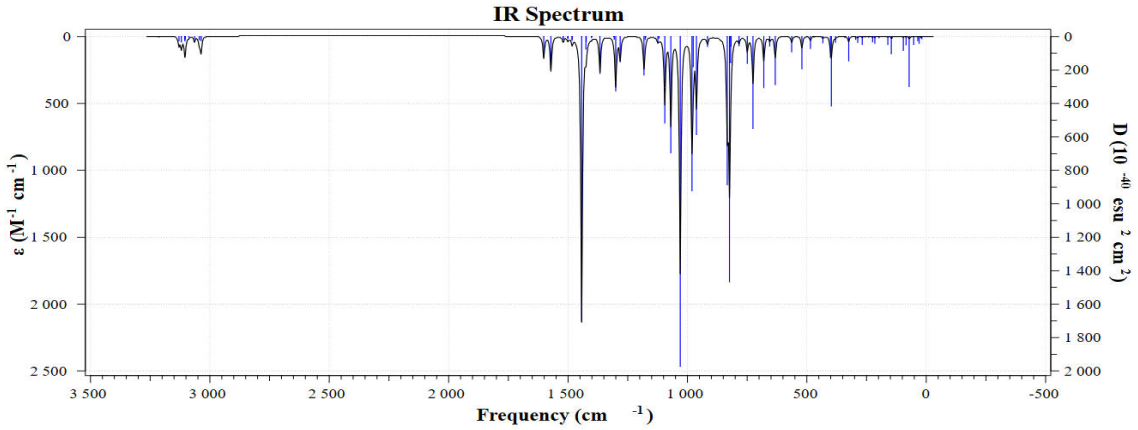

Figure 4. 31: IR Simulated IR Spectra of Chlorpyrifos

Figure 4.32 shows the IR spectrum of diuron.

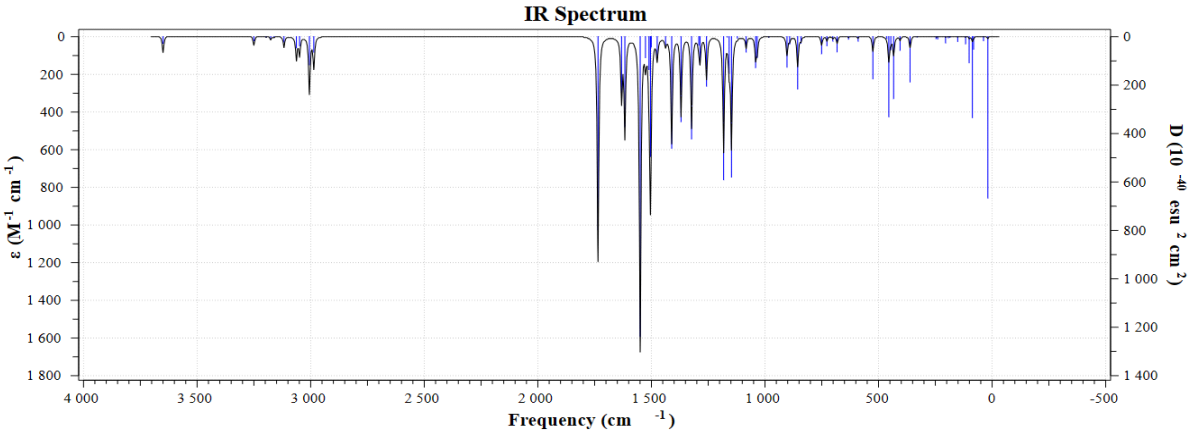

Figure 4. 32: Simulated IR Spectra of Diuron

The peaks at 3320 cm^{-1} and 1620 cm^{-1} represent the vibrational adsorption peaks of N-H symmetric stretching and the most intense carbonyl bands, respectively. In addition, the benzene ring stretched at 1525, 1476, and 1394 cm^{-1}. Other absorption bands of the benzene ring are located at 1586 cm^{-1} (due to C-C stretching vibration) and 1189 cm^{-1} (due to C-H in-plane bending vibration). Peaks at 816, 866, and 755 cm^{-1} are attributed to benzene ring C-H out-of-plane bending vibration, as well as C-Cl stretching vibration. The peaks at 3243 cm^{-1} and 1620 cm^{-1} could be interpreted as N-H and O-H vibration absorption peaks, respectively.

4.4.1.3 Loading Capacity of Pesticides

Different force fields were evaluated and it was found that universal force field was the best for the three halogenated pesticides as shown in Figure 4.33

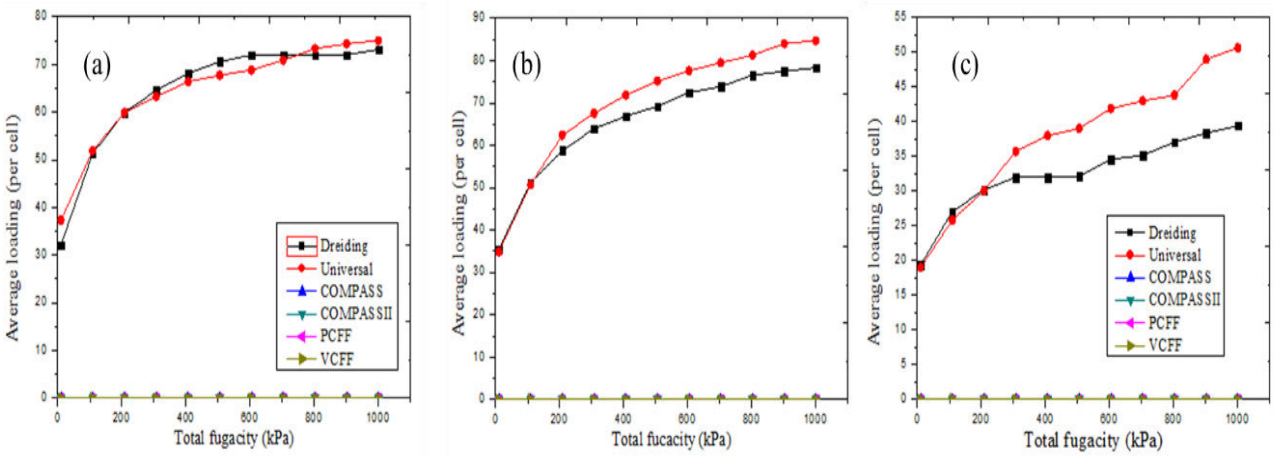

Figure 4. 33: Loading of a) imidacloprid, b) diuron and c) chlorpyrifos on CLO using various force fields.

Based on this force field, the adsorption of the three pesticides on the different zeolites was studied. The results are tabulated in Table 4.10. Several structural parameters of zeolites' porous domains such as the mass (M), density (D), helium void fraction (HVF), accessible pore volume (APV), gravimetric surface area (GSA), and dimensionality of the pore system (Di) are important in determining the loading of the molecules.

As shown in Table 4.10, CLO showed the highest loading of the pesticides per cell. These were 90, 89 and 51 molecules per cell for imidacloprid, diuron and chlorpyrifos, respectively. This can be due to the fact that CLO has the lowest mass and density among the 23 studied zeolites, with a higher helium vacancy percentage (HVF), larger ring pore system, diameter pore volume, and volumetric surface area. Conversely, the loading onto the other zeolites was relatively low.

Table 4. 10: The structural characteristics and loading capacity of imidacloprid, diuron and chlorpyrifos on the best performing zeolites.

CODE	M	D	HVF	APV	VSA	GSA	DPS	Di	Loading of Imidacloprid	TE	Loading of Diuron	TE	Loading of Chlorpyrifos	TE
CLO	11728.18	1128.76	0.55	0.49	2069.69	1833.61	3	15.33	75	5439.94	84	2486.59	51	7132.11
LTN	46144.74	1695.18	0.31	0.18	1181.64	697.06	0	0	6	348.27	8	146.35	1	61.24
TSC	23072.37	1318.71	0.49	0.37	1472.61	1116.72	3	15.87	16	1343.48	19	332.33	12	1263.89
ITV	11792.17	1075.18	0.55	0.51	2110.04	1962.51	3	8.54	17	1189.87	21	435.65	10	1120.31
PAU	40376.65	1585.70	0.36	0.23	1639.21	1033.75	3	10.08	1	62.57	0	0.00	0	0.00
FAU	11536.19	1327.65	0.49	0.37	1615.92	1217.14	3	10.69	11	712.15	14	206.48	8	618.86
DFO	7931.13	1485.63	0.43	0.29	1625.72	1094.30	3	10.89	10	602.62	9	120.57	2	208.14
LTA	1442.02	1414.17	0.47	0.33	1674.58	1184.14	3	10.24	8	488.57	0	0.00	0	0.00
SBT	8652.14	1368.16	0.47	0.34	1585.49	1158.84	3	10.41	6	382.30	9	123.31	3	312.31
SBE	7690.79	1370.15	0.46	0.34	1514.00	1104.99	3	12.09	6	379.69	8	108.18	3	308.93
IRY	4598.41	1115.15	0.60	0.44	1701.51	1525.79	3	10.69	8	547.23	8	136.21	5	537.05
JSR	5768.09	1225.53	0.52	0.42	2271.20	1853.23	3	7.43	4	242.22	3	41.19	1	34.57
EMT	5768.09	1328.95	0.49	0.37	1618.80	1218.11	3	11.00	6	388.72	7	101.08	3	312.57

IMF	17304.28	1744.41	0.30	0.17	1261.47	723.15	2	6.70	5	156.31	0	0.00	0	0.00
IWV	9132.81	1498.62	0.41	0.27	1455.32	971.11	2	8.14	4	254.12	6	73.92	0	0.00
SBS	5768.09	1368.86	0.47	0.34	1585.68	1158.39	3	10.97	4	261.75	6	81.98	2	200.39
BOG	5768.09	1602.00	0.38	0.24	1486.24	927.74	3	7.49	2	115.37	2	18.06	0	0.00
BOZ	5527.76	1290.63	0.46	0.36	2017.67	1563.33	3	8.31	2	129.42	0	0.00	0	0.00
KFI	5768.09	1493.77	0.41	0.28	1638.56	1096.93	3	10.16	2	122.08	0	0.00	0	0.00
HEU	2163.04	1748.00	0.29	0.17	1335.49	764.01	2	5.22	1	121.11	2	28.24	0	0.00

Table key; D=density [kg/m^3], M=mass [g/mol]; HVF=helium void fraction; APV=accessible pore volume [cm^3/g]; VSA=volumetric surface area [m^2/cm^3]; GSA=gravimetric surface area [m^2/g]; DPS=dimensionality of the pore system; Di=largest overall cavity diameter [A]; L= loading is given in molecules per cell Average total energy =ATE

For example, ITV, is in second place in terms of loading of imidacloprid and diuron molecules with 17 and 21molecules per cell, respectively. This is a significant difference between CLO and ITV loading can be attributed to differences in their mass, density, helium vacancy percentage. ITV is closely followed by TSC for the adsorption of imidacloprid and diuron, this is because ITV has a larger cavity width than TSC (8.54 vs. 15.87 m^2/cm^3). On the other hand, despite having a higher Di than ITV, FAU has a lower loading capacity (11 molecules per cell). This could be attributable to FAU's larger bulk and density. FAU and DFO have about identical loads (11 vs. 10 molecules per cell for imidacloprid). This could be due to a similarity in their Di (10.69 vs.10.89 m^2/cm^3). LTA and IRY have similar loading (8 molecules per cell), whereas LTN, SBT, SBE, and EMT have lower loading (6 molecules per cell), which may be due to similarities in their HVF and Di. JSR and SBS exhibit similar loading (4 molecules per cell). This may be attributed to having almost similar densities and their negligible differences in HVF, APV and Di

In the case of chlorpyrifos, CLO is still the best candidate for its adsorption with an uptake capacity of 51 molecules per cell. This is equivalent to 50% weight percentage adsorption capacity of chlorpyrifos. The trend of adsorption of chlorpyrifos is generally similar to those of imidacloprid and diuron.

4.4.1.4 DFT Adsorption Isotherms

It is observed that CLO exhibited the L-shape isotherm for imidacloprid, chlorpyrifos and diuron with a maximum loading of 75, 51 and 84 for per unit cell, respectively (Figure 4.34). This shows that the molecules experience stepwise multilayer adsorption onto the CLO zeolite, that occurs only when the surface has various adsorption sites types with energetically diverse properties. The low loading of chlorpyrifos compared to the rest is

due to it has high molecular weight of 350.60 g/mol. Imidacloprid and diuron exhibited close loading onto CLO, due to their close molecular weight of 255.66 and 233.09 g/mol, respectively. The lower molecular mass allows more packing of the pesticides in the CLO structure cavities/pores.

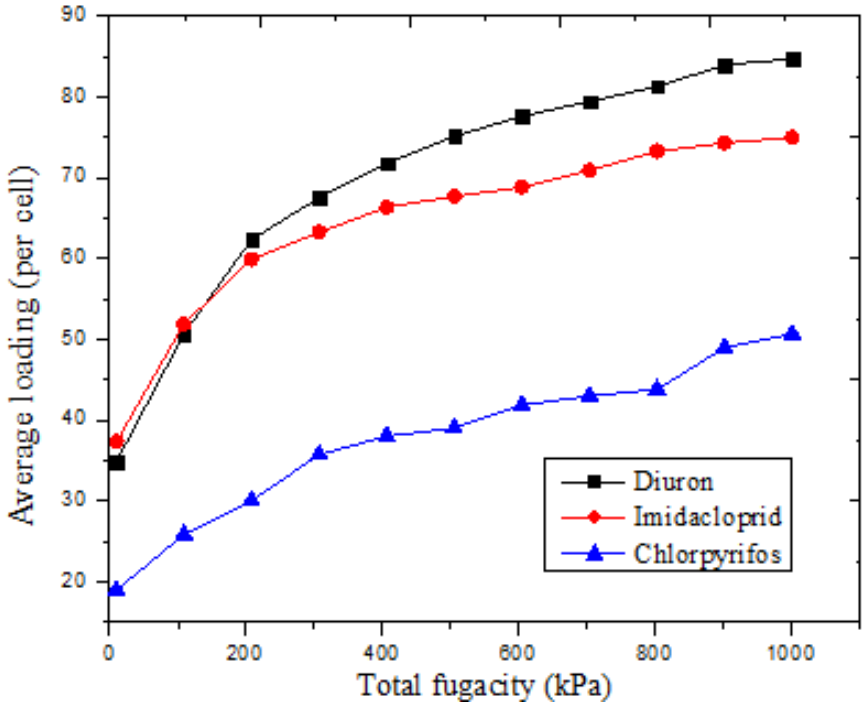

Figure 4. 34: Adsorption isotherms of diuron, imidacloprid and chlorpyrifos loading onto CLO at 298 K

As expected, when compared with other zeolites (TSC, ITV and FAU) (Figure 4.35), CLO showed the highest loading. The loading of TSC, ITV and FAU were relatively low with nearly a horizontal plateau isotherm. This is attributed to the limited surface-active sites for the pesticides (Amutova *et al.,* 2023).

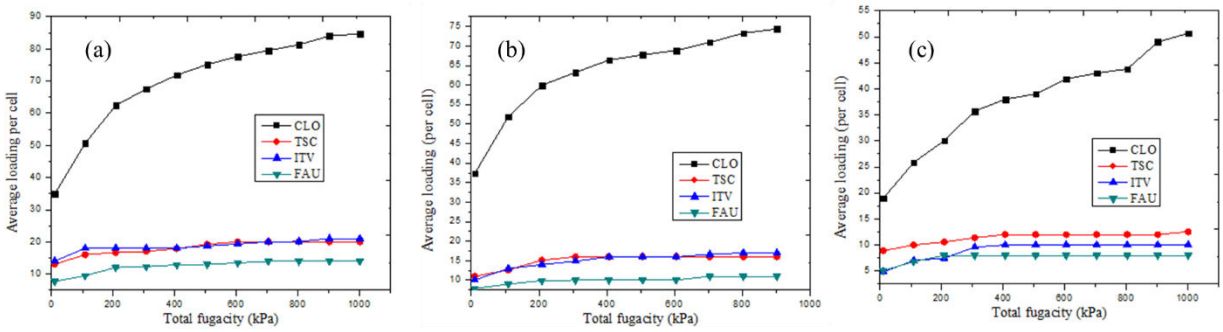

Figure 4. 35: Adsorption isotherms showing the adsorption of a) diuron, b) imidacloprid and c) chlorpyrifos on the selected best performing zeolites

4.4.1.5 Stable Configurations of Diuron, Imidacloprid and Chlorpyrifos on CLO

. In the most stable conformation, the chlorpyrifos molecule is adsorbed at almost the center of 20- ring window of CLO, while diuron is located in the extreme upper left in 20-ring window connecting super cages and the two oxide moieties. The imidacloprid molecule is located in the to the extreme left of 8-ring window. After the sorption of the pesticides on CLO zeolites, the binding energy, was computed. Binding energy influences the structural stability of molecules, with a negative value indicating that the structure is stable (Liu et al., 2020). Figure 4.36, shows structures of the most stable configuration of diuron, imidacloprid and chlorpyrifos adsorbed onto CLO

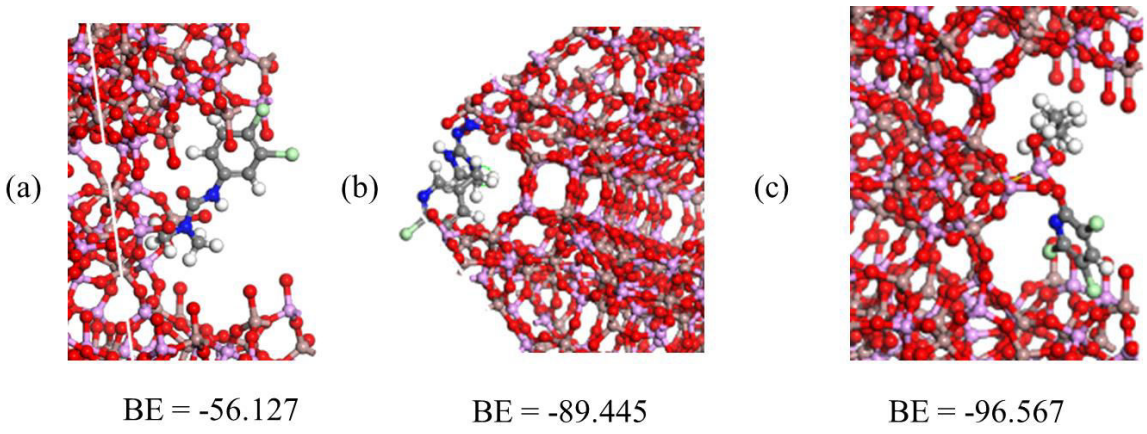

Figure 4. 36: Structures of the most stable configuration of a) diuron, b) imidacloprid and c) chlorpyrifos as adsorbed on the CLO

Consequently, the highest negative value observed for chlorpyrifos on CLO structure was -96.57 kcal/mol while lowest negative value was observed for diuron at -56.127 kcal/mol. Binding energy for Imidacloprid was -89.45 kcal/mol. It can be concluded from binding energy results that sorption of chlorpyrifos and imidacloprid were the most favorable on the CLO zeolite with more stable and lowest energy value. This argument can be justified from previous studies in which higher negative values were measured for bond length imposes significant effects on adsorption process (Mo *et al.,* 2021). The strong bonds possess smaller bond lengths than weaker bonds. The more negative values of adsorption and enthalpy energies show that the pesticides have strong chemical interaction with CLO, thus the stable adsorbed structures are formed.

Conclusion

In conclusion, CLO zeolite was the most suitable for the adsorption of diuron, imidacloprid and chlorpyrifos compared to other zeolite structures. Chlorpyrifos forms the most stable configuration with CLO compared to the other two pesticides. Diuron had the highest

stability, with an energy gap of 5.30 eV, followed by imidacloprid (4.83 eV) and chlorpyrifos (4.19 eV). This implies that it will be more persistent in the environment. Also, sorption of chlorpyrifos and imidacloprid were the most favorable on the CLO zeolite with more stable and lowest energy value compared to diuron based on the binding energy.

Objective 3; To determine the kinetics and mechanisms of the adsorption of the selected pollutants onto the HEU zeolite: Experimental Study

4.5. Characterization of the HEU Zeolite

4.5.1 Chemical Composition

Elemental data results obtained from the EDX analysis showed that SiO_2 is the most abundant compound in the zeolite followed by Al_2O_3 (Table 4.11).

Table 4. 11: Chemical composition of the HEU zeolite

Oxide	SiO_2	Al_2O_3	MgO	K_2O	CaO
Weight %	76.35	11.66	4.59	3.39	1.61

The Si/Al ratio in the zeolite was 3.7. This affirmed that the zeolite used in this study is a heulandite zeolite since the ratio is less than 4 (Diale *et al.,* 2011)**.** Since the Si/Al ratio in the zeolite is less than 5, it can be said that, this is low silica zeolite and therefore more acidic making it ideal for ion-exchange reactions (Auerbach *et al.,* 2003; Nair *et al.,* 2013). In addition, the zeolite contained little amounts of K, Ca and Mg. However, there were no traces of lead, cadmium, nitrogen and phosphorous in the zeolite structure.

4.5.2 Crystallinity of the HEU zeolite

The XRD patterns of the zeolite are shown in Figure 4.37 and 4.38. The structure of the zeolite was analyzed in $4° \leq 2\theta \leq 90°$ range. The zeolite mainly composed of heulandite-K, heulandite-Ca, clinoptilolite-Ca, orthoclase, and SO_2. The peaks from K-type heulandite (DB card No. 9012215), Ca-type heulandite (DB card No. 9000150), Ca-type clinoptilolite (DB card No. 9009578), orthoclase (DB card No. 9006347), and SiO_2 (DB card No. 9006291).

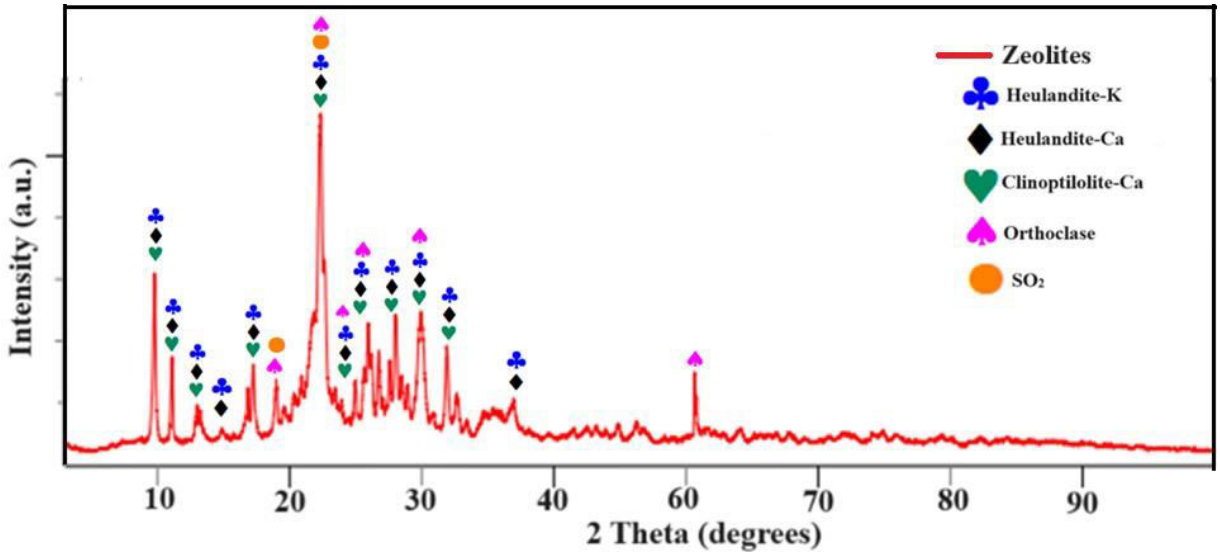

Figure 4. 37: X-ray diffraction patterns for zeolite

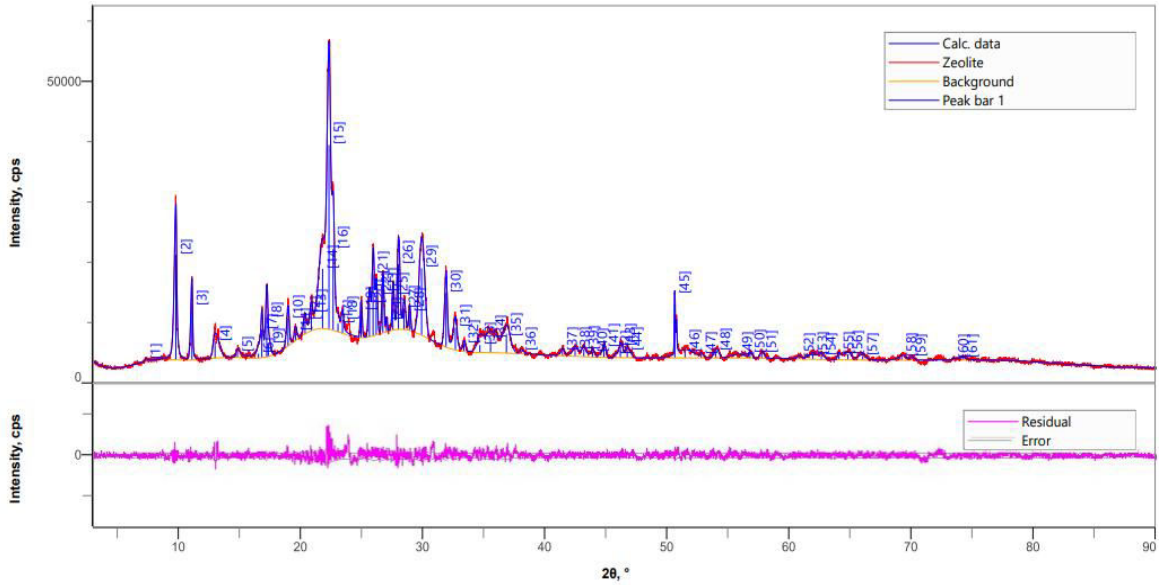

Figure 4. 38: X-ray diffraction peak profile for the zeolite

Distinct peaks of the zeolite were observed at 2θ = 9.8, 11.1, 13, 22.3, 22.6, 25.9 and 30°. This agrees with work done by Treacy, (1996). The peaks observed at 2θ = 22.3° and 9.8° corresponds non-amorphous SiO_2 and Al_2O_3, respectively (Barlokova, 2008; Galli *et al.,* 1983; Treacy *et al.,* 1996). The recorded pattern coincides with the reported simulated patterns for the HEU with peaks at 9.85, 11.07, and 22.22º, with heulandite (Si/Al=3.88) (Treacy *et al.,* 1996). The results reveal that the zeolite sample was crystalline given the symmetrical peaks that were sharp and of high intensity. Due to the high crystalline behavior of the HEU its active sites can easily attract the heavy metals (Pb^{2+} and Cd^{2+} ions), anions ($PO_4^{3-}$and NO_3^-) and selected halogenated pesticides and pharmaceuticals (Sihombing *et al.,* 2018). Figure 4.39 shows the PXRD zeolite profile view or pattern of the zeolite with most observed peaks being highly intensive and sharp; an indication of its high crystallinity and porous nature and therefore stable for the adsorption studies (Sihombing *et al.*, 2018)

4.5.3 Functional Groups Analysis

FT-IR analysis was used to provide information regarding functional groups on the surface of the zeolite adsorbent over a spectra range of 4000–400 cm^{-1} (Figure 4.39).

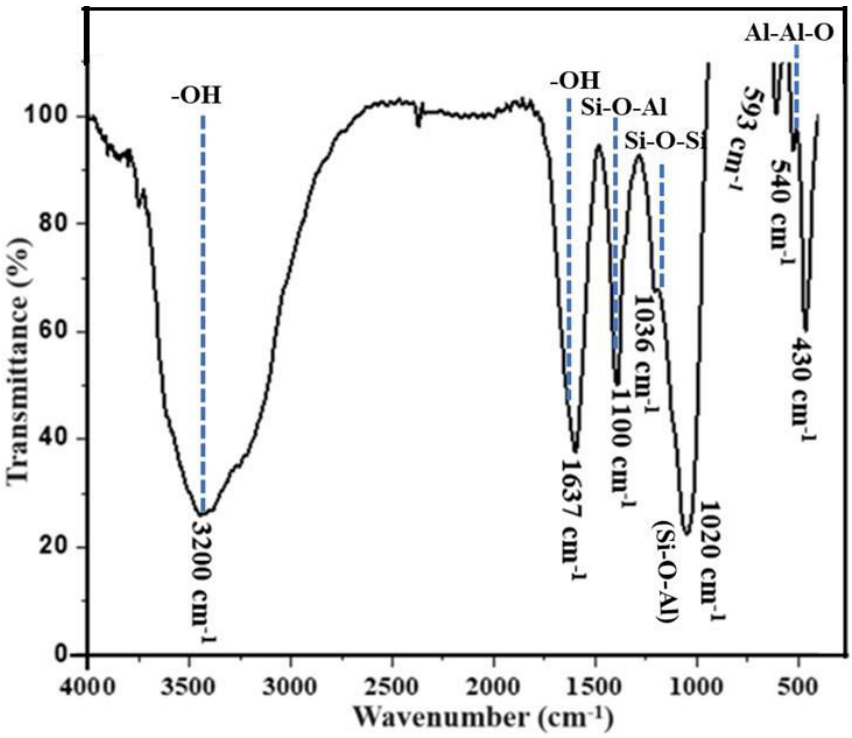

Figure 4. 39: FT-IR spectrum of the HEU zeolite

The broad band at 3000-3600 cm^{-1} is attributed to the stretching vibration of hydroxyl groups on the surface of the zeolite and adsorbed water molecules, which possess the bending vibration mode at 1637 cm^{-1} The strong absorption band at 1036 cm^{-1} is attributable to silicate oxygen bond (Si-O-Si) while the bands at 540 and 1000 cm^{-1} are due to bending vibration for Al-Al-O (Mir, 2020). The existence of the heulandite phase is confirmed by the appearance of 593 cm^{-1} band (Christidis *et al.*, 2003). The existence of 593 cm^{-1} shows the presence of heulandite type -II"(Perraki & Orfanoudaki, 2004). Furthermore, the most intensive vibration frequency is between 1100 and 1020 cm^{-1}; a

result of the structural units of the Si-O-Al of the natural zeolite confirming the main composition of the material used in this study. The bands located at about 500 – 430 cm^{-1} is assigned to a T-O bending mode where (T =AI or Si).

4.5.4 Scanning Electron Microscopy (SEM) Analysis

Scanning electron microscopy (SEM) is a valuable tool for precise measurement and analysis of extremely small features and morphology of the sample. Figure 4.40 shows the SEM micrograph of HEU zeolite before adsorption.

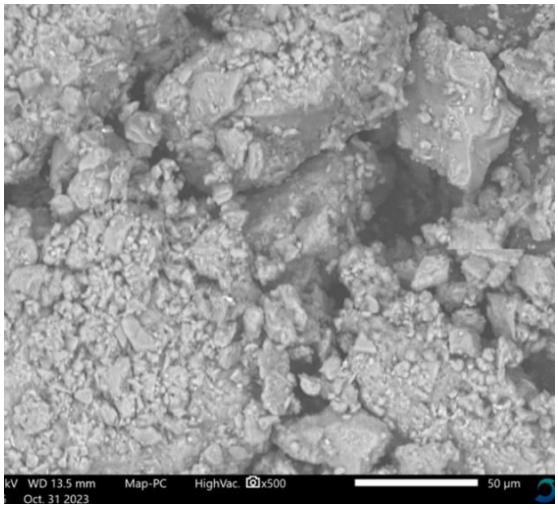

Figure 4. 40: Natural heulandite before adsorption pollutants

It is evident from Figure 4.41 that SEM image of natural heulandite zeolite exhibits a highly heterogeneous and rough surface with large number of micropores. It is clear that the zeolite has pores that provides high surface area for potential adsorption of pollutants. This roughness is due to the presence of Al_2O_3 and SiO_2 in the zeolite matrix as shown in the XRD and EDX (Figure 4.38 and Table 4.11).

4.6 Experimental Studies

4.7 Removal of Pb^{2+} and Cd^{2+} from Water Using South African Heulandite Zeolite: Experimental and Computational Study

In this study the efficacy of HEU zeolites in removing Pb^{2+} and Cd^{2+} from aqueous solution was investigated through batch experiments and molecular simulations. Monte Carlo simulations computed the adsorption isotherms in the Grand Canonical Ensemble (GCMC), which were used in evaluating the performance of the undoped and doped HEU. Therefore, this study provides valuable insights into the use of HEU zeolite as an efficacious adsorbent for the removal of Pb^{2+} and Cd^{2+} from water to alleviate water pollution.

4.7.1 Results

The effects of several physical factors on the adsorption of the selected heavy metals onto the HEU zeolite was investigated.

4.7.1.1 Effect of Contact Time on Pb^{2+} and Cd^{2+} Adsorption on Heulandite

Figure 4.41 shows the efficiency of Pb^{2+} and Cd^{2+} removal by the zeolite as a function of contact time. The initial $Pb^{2+}$and Cd^{2+} were 10 and 1.5 ppm, respectively.Adsorbent mass of 1.0 g and 0.1 g, volume of 100 and 10 mL, respectively and temperature 25 ^{o}C.

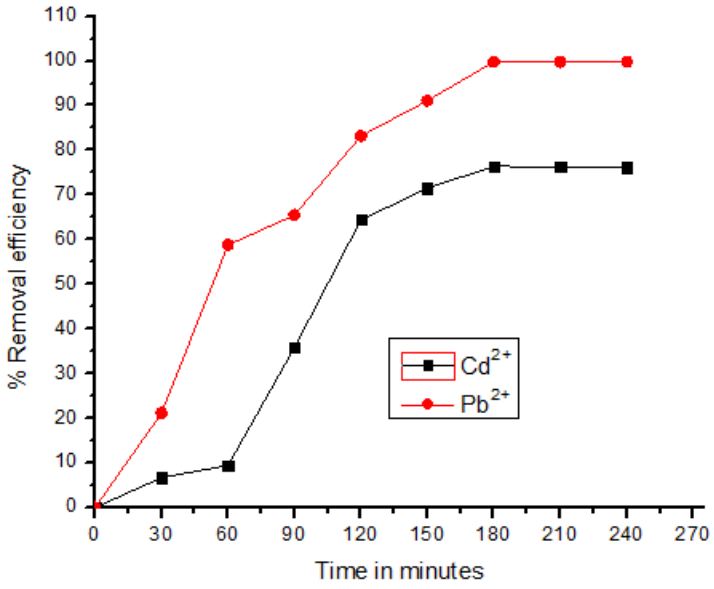

Figure 4. 41: Effect of contact time on the adsorption of Pb^{2+} and Cd^{2+} onto zeolite

The maximum adsorption capacity for Pb^{2+} and Cd^{2+} was reached after 3 hours. A sharp and rapid adsorption of Pb^{2+} onto the adsorbent was observed in the first 60 min. On the other hand, adsorption of Cd^{2+} was slow in the first 60 min. However, the adsorption rate increases rapidly between 60 and 120 min. Thereafter, in both cases, the adsorption rates gradually slowed down reaching an equilibrium after 180 min. The adsorption behavior of the two metal ions can be explained by the fact that there were more active sites and a larger surface area for adsorption at the start of the experiment, which increased mass transfer. The subsequent slow adsorption is due to the decrease in driving force caused by a decrease in active sites, up until maximum capacity is attained (El-Araby *et al.,* 2019; Matei *et al.,* 2019). The percent adsorption increased gradually as the contact time was extended to 4 hours, recording 99.7% and 76.7% removal for Pb^{2+} and Cd^{2+}, respectively. The higher removal rate of Pb^{2+} compared to Cd^{2+} is due to its higher electronegativity (2.33) compared to that of Cd^{2+} (1.69) hence readily adsorbed onto the HEU zeolite. This

is because a high electronegativity is responsible for the strong covalent formation between the metal ion and oxygen atoms on the zeolite surfaces (Zhao *et al.,* 2020). These results compare favorably with published results whereby most zeolites have a higher cation exchange capacity for Pb^{2+} than Cd^{2+} (Velarde *et al.,* 2023).

4.7.1.2 The Adsorption Kinetics Model

To study the kinetics of adsorption of $Pb^{2+}$and Cd^{2+} onto the HEU zeolite, the *pseudo* first-order and *pseudo* second-order models were used. Figure 4.42 and Table 4.12 show the kinetic model fits and results of adsorption for Pb^{2+} and Cd^{2+}.

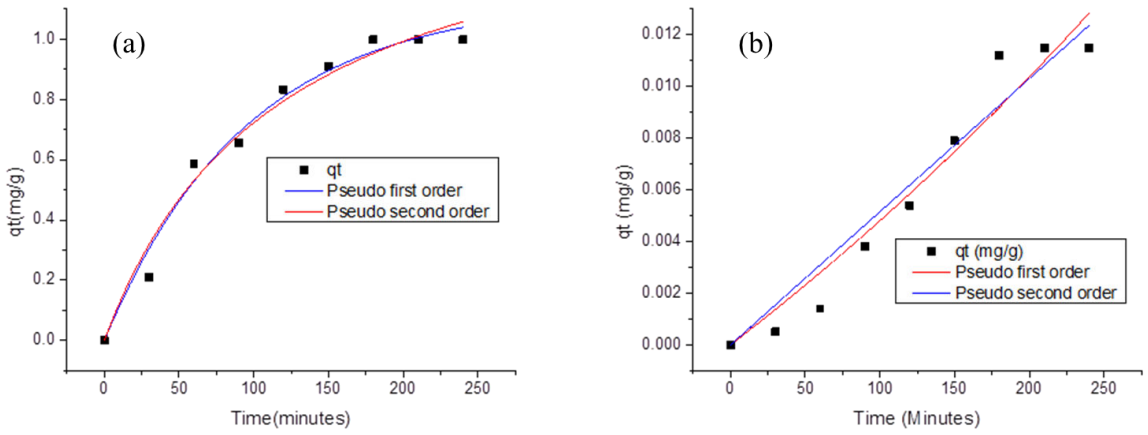

Figure 4. 42: Kinetic models of adsorption for (a) Pb^{2+} and (b) Cd^{2+} *pseudo*-first-order and *pseudo*-second-order

Table 4. 12**:** Kinetic model parameters for $Pb^{2+}$and Cd^{2+} uptake by HEU

Models	***Pseudo*-first-order model**				***Pseudo*-second-order model**			
Parameters	Qe	k_1	R^2	($\chi 2$)	Qe	k_2	R^2	($\chi 2$)
Pb^{2+}	1.1288	1.05×10^{-2}	0.9811	2.53×10^{-3}	1.583	1.5×10^{-3}	0.9748	3.37×10^{-3}
Cd^{2+}	0.0304	5.31×10^{-3}	0.9414	1.35×10^{-6}	9.9418	5.22×10^{-7}	0.9364	1.46×10^{-6}

For Pb^{2+} and Cd^{2+} from Table 4.12 the *pseudo* first-order kinetic model best fit the adsorption process of Pb^{2+} and Cd^{2+} due to superior R^2 values compared to *pseudo*- second order. This indicates that physisorption was primarily responsible for the adsorption of both ions onto the HEU zeolite (Wan *et al.,* 2021). Besides the q_e obtained from this model for *pseudo*- first order were consistent with the experimental values of adsorption capacity.

From *pseudo* first-order rate constants, it is clear that the adsorption of Pb^{2+} onto the zeolites was faster than that of the Cd^{2+}. Furthermore, the pseudo-first order was found to have a lower chi-squared (χ^2) value (0.00253) for Pb^{2+} than the *pseudo*-second order. For Cd^{2+} having a lower chi-squared (χ^2) value (1.35×10^{-6}) in the *pseudo*-first order compared to *pseudo*-second order, indicating that the pseudo-first order is more accurately represents the data.

4.7.1.3 Effect of Initial Concentration of Lead and Cadmium ion on Adsorption onto HEU Zeolite

The initial concentration of adsorbate in the solution determines the number of heavy metal ions in the bulk solution which may be available for binding to active sites of the adsorbent. The effect of the initial metal ion concentration on the adsorption of the selected metal ions onto the HEU zeolite was investigated by varying Pb^{2+} and Cd^{2+} initial concentration from

5 to 30 ppm and 1 to 3 ppm, respectively, adsorbent mass 1.0 0.1 g, respectively and reaction temperature 25 °C (Figure 4.43).

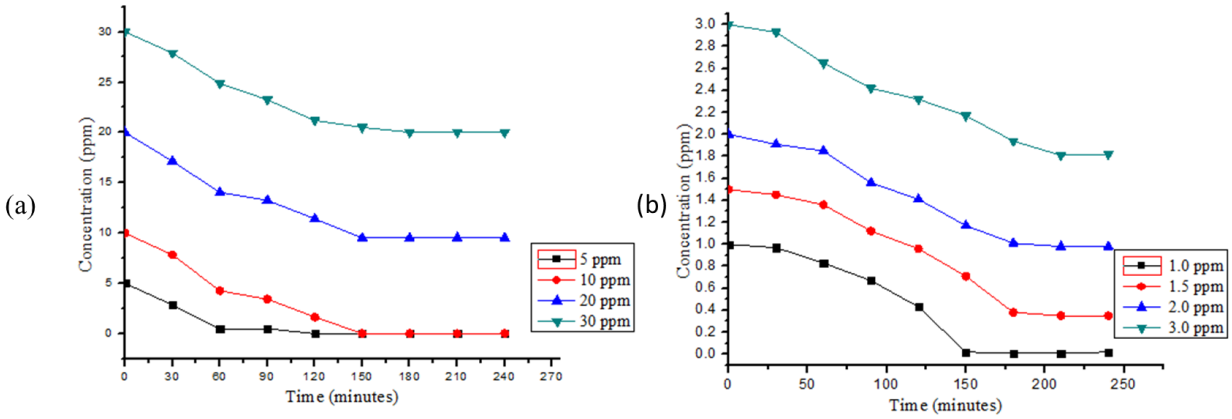

Figure 4. 43: Effect of concentration of (a) Pb^{2+} and (b) Cd^{2+} removal by zeolite

It was observed that the 5 ppm Pb^{2+} attained equilibrium after 60 min while the other concentrations reached equilibrium after 150 min. Thereafter, no appreciable changes in adsorption occurred after 150 min.

In the case of Cd^{2+}, the adsorption followed the same trend as Pb^{2+} with lower concentrations reaching equilibrium faster than the higher concentrations. For example, the 1 ppm reached equilibrium after 150 min, while the 2 ppm reached equilibrium after 175 min.

From Figure 4.47, 20 and 30 ppm of Pb^{2+} show high adsorption compared to 5 and 10 ppm h show same trend with Cd^{2+}.This is so because by increasing the number of metal ions there is increase in the competition for the limited surface-active binding sites of the adsorbent, thereby resulting in increased adsorption capacity because the active sites become saturated (El-Araby *et al.,* 2019). Researchers have carried out several studies on the effect of initial concentration on metal removal by different adsorbents. For example,

Kumar *et al.,* (2012) reported that an increase in Cd^{2+} concentration from 80.1 to 66.6 %, resulted in a decrease in percent removal. Also, Nurain *et al.,* (2021) reported a similar trend in the removal of Pb^{2+} by banana peel where at high Pb^{2+} concentration (100 ppm), the removal efficiency was lower 89.5%, while at low concentration (50 ppm) the percentage removal was 87.65% (Nurain *et al.,* 2021)

4.7.1.4 Effect of Adsorbent Dosage.

By varying the zeolite dose from 0.3 to 2.0 g at initial concentrations of 10 and 1.5 ppm of Pb^{2+} and Cd^{2+} ions, respectively, it was possible to determine the impact of adsorbent dosage on the removal of Pb^{2+} and Cd^{2+} from water. This was carried out for 60 minutes and reaction temperature of 25 ^{o}C. The percent removal of Pb^{2+} and Cd^{2+} from water at different zeolite quantities is depicted in Figure 4.44.

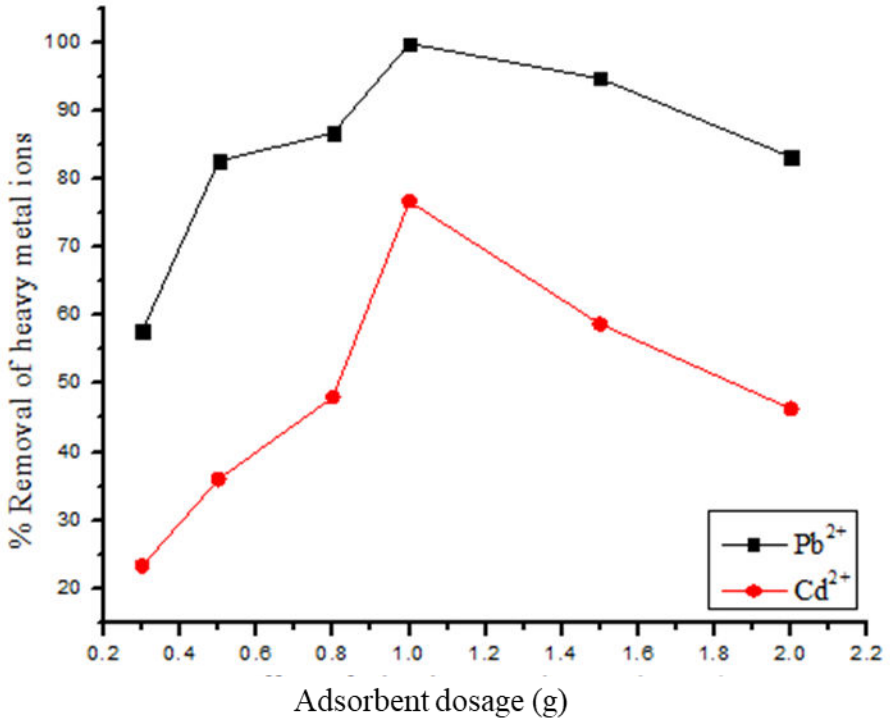

Figure 4. 44: Effect of adsorbent dose on adsorption of Pb^{2+} and Cd^{2+}ions on zeolite

An increase in the amount of zeolite increases the removal percent of Pb^{2+} and Cd^{2+} ions up to a maximum amount of 1.0 g. This is attributed to increased adsorption active sites as the adsorbent mass increases. The findings are comparable with previous report for adsorption of Pb^{2+} and Cd^{2+}, respectively (Bao *et al.,* 2013; Sayed & Khater, 2013). Further increase in the amount of HEU zeolite beyond 1.0 g led to decrease in the adsorption. This can be attributed to reduced mass transfer due to increased viscosity (Yousefi *et al.,* 2018).

4.7.1.5 Adsorption Isotherms Studies for Pb^{2+} and Cd^{2+} Adsorption onto HEU

Adsorption models can be used as the reference in evaluating the characteristic performance of an adsorbent. In order to determine the uptake capacity of the Pb^{2+} and Cd^{2+} ions adsorption onto the HEU zeolite, non-linear Langmuir, Freundlich, Redlich-Peterson and Sips isotherms models were employed. The best-fitted model was then decided from the comparison of the R^2 values from the fitted models as shown in Figure 4.45 and 4.46.

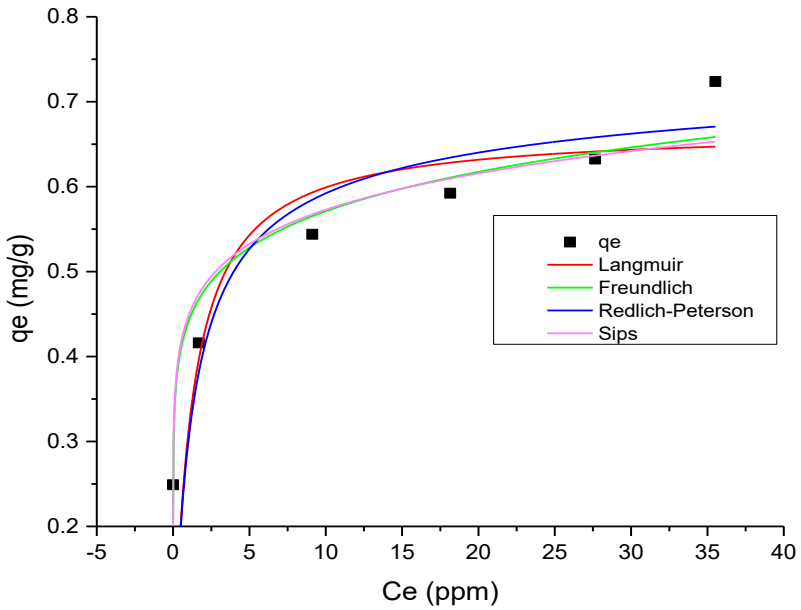

Figure 4. 45: Non-linearized (a) Langmuir, Freundlich, Redlich-Peterson and Sips isotherms for Pb^{2+} adsorption by HEU zeolite

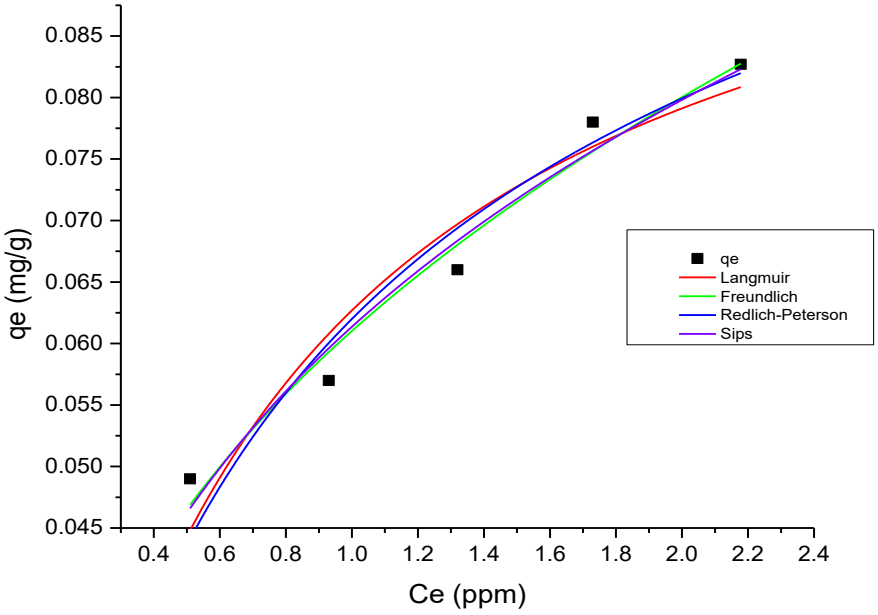

Figure 4. 46: Non-linearized (a) Langmuir, Freundlich, Redlich-Peterson and Sips isotherms for Cd^{2+} adsorption by HEU zeolite

The Langmuir, Freundlich, Redlich-Peterson and Sips isotherms parameters and coefficients obtained for the adsorption of the two heavy metal ions onto the HEU zeolite are collected in Table 4.13.

Table 4. 13: Isotherm parameters for the adsorption of Pb^{2+} and Cd^{2+} onto HEU zeolite

Langmuir Isotherm				
Ion	**q_{max}**	**$K_{L.}$**	**$R_{L.}$**	**R^2**
Pb^{2+}	0.6681	0.8676	0.920	0.3771
Cd^{2+}	0.1072	1.4079	0.516	0.9106
Freundlich Isotherm				
Ions	**K_F**	**1/n**		**R^2**
Pb^{2+}	0.4408	0.1124		0.9142
Cd^{2+}	0.0610	0.3914		0.9671
Redlich-Peterson				
Ions	A	B	G	**R^2**
Pb^{2+}	0.6058	1.0168	0.9579	0.1921
Cd^{2+}	0.1588	1.5608	0.9295	0.8795
Sips				
	Qms	As	Bs	**R^2**
Pb^{2+}	3.3437	0.1545	0.1266	0.8687
Cd^{2+}	0.2848	0.2747	0.5037	0.9401

From the non-linear regression correlation coefficient (R^2) values obtained, the adsorption of the two metal ions fits best in the Freundlich isotherm. The Freundlich isotherm model describes the adsorption of Pb^{2+} and Cd^{2+} onto zeolite as nonuniform type of adsorption on the outer surface of the adsorbent and each site has different affinity. This means that adsorption of the two heavy metal ions is multilayer on the heterogeneous surface of heulandite zeolite. Freundlich's 1/n value is related to adsorption strength. The values of 1/n obtained for the adsorption of Pb^{2+} and Cd^{2+} was 0.1124 and 0.3914, respectively. This indicates that adsorption of the two ions was spontaneous and when more adsorbates are present in the adsobent free energies is enhanced for futher adsorption (Shukuku *et al.,* 2015). The K_F values in Freundlich model, shows that the sorption capacity of Pb^{2+} was higher than that of Cd^{2+}.

Table 4.14 compares these results with results obtained in previous studies on the adsorption of Pb^{2+} and Cd^{2+}onto different zeolites (Gupta *et al.,* 2021; Tare *et al.,* 1992). The results obtained in this study are comparable with those reported in other studies.

Table 4. 14: Reported adsorption capacities (mgg^{-1}) of natural zeolite for heavy metal ions

Type of zeolite	**Cd^{2+}**	**Pb^{2+}**	**References**
.	Adsorption capacity (mg/g)	Adsorption capacity (mg/g)	
Greek Natural zeolite	1.4	1.2	(Malliou *et al.*, 1994)
Bulgaria Clinoptilolite	1.6	2.4	(Babel *et al.,* 2003)
Synthetic zeolite SZM-5	30.6	24.4	(Mukti, 2016)
Ukraine Clinoptilolite	13.0	4.2	(Sprynskyy *et al.,* 2006)
Turkey Clinoptilolite	27.7	-	(Karatas, 2012)
Iranian Natural zeolite	52.6	29.4	(Ghahfarokhi *et al.,* 2014)]
Iranian sepiolite zeolite	50.0	19.2	(Ghahfarokhi et al., 2014)
Bulgaria Clinoptilolite	1.6	2.4	(Shaheen *et al.,* 2012; Zamzow *et al.,* 1990)
Na-A zeolite	224.7	118.3	(Ba*o et al.,* 2013)
Iranian Modified clinoptilolite zeolite	91.3	78.3	(Mirbaloochzehi *et al.,* 2020)
South African Haundatite	0.5	0.29	*This study (Experimental)*
Activated biocarbon	2.9	2.8	(Singanan, 2011)
p-type zeolite	3.9	-	(Mingyue *et al.,* 2020)
Cow manure	102.77	38.11	(Zhu *et al.,* 2017)
Extracellular polymeric substance (EPS)	31.55	23.42	(Cui *et al.,* 2020)
Carbon nanotubes	23.4	10.5	(Šolić et al., 2021)
Iron phosphate-modified pollen microspheres as adsorbents	6.13	4.62	(X. Zhang *et al.,* 2021)

4.7.1.6 Computational Adsorption Isotherms of Pb^{2+} and Cd^{2+}onto Heulandite

The structure of the HEU zeolite was obtained from the Zeolite database (Baerlocher *et al.,* 2007). Material Studio 17.0 software was used for the molecular simulations. First-principles DMol3 method was applied for the geometry optimizations of the of Pb^{2+} and Cd^{2+} (Delley, 2000). Natural bond orbital (NBO) population calculations were conducted using NBO 3.1 program embedded in the Gaussian 09 program (Frisch *et al.,* 2010). The quantum theory of atoms-in-molecules (QTAIM) investigation was done using Multiwfn 3.7 software (Lu and Chen, 2012b).

The adsorption isotherm at a given temperature, T and the number of adsorbed ions per cell as a function of the pressure of the fluid in contact with the porous material was determined.

The percent weight capacity was calculated using as follows,

$$\text{Percent weight } (\%wt) = \frac{Mass\ of\ the\ adsorbed\ heavy\ metal\ ion}{Mass\ of\ the\ zeolite\ used + mass\ of\ adsorbed\ heavy\ metal\ ion} \times 100\%$$

Adsorption capacity depends on the initial conditions of the adsorbent, the fluid-phase concentration and the temperature within the adsorbent. It is observed that Pb^{2+} exhibited a linear- H-shaped isotherm with a pronounced inflexion at a maximum loading of 8 ions per unit cell giving a weight capacity of 43.36%. The H-type isotherm implies a progressive saturation of the adsorbent, by achieving high adsorption properties at low adsorbate concentrations due to the very strong adsorbate−adsorbent affinity (Bonilla-Petriciolet *et al.,* 2017; de Vargas *et al.,* 2021).

Cd^{2+} exhibited a C-shaped isotherm adsorption capacities on HEU with loading of 7 ions per unit cell loading, giving a lower weight percentage capacity of 26.60%. In this study,

adsorption increased sharply because HEU was not saturated with ions. The adsorption of Cd^{2+} is not yet at equilibrium due to the availability of more sites to accommodate ions packing, as shown in Figure 4.47. The loading of Pb^{2+} is higher than that of Cd^{2+} since the Pb^{2+} ions are smaller in size than Cd^{2+}; hence it can enter the pores easily.

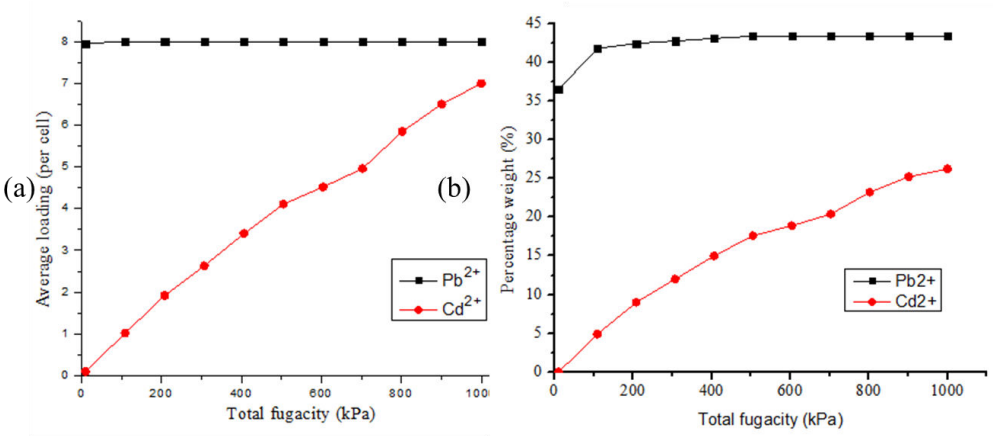

Figure 4. 47: Adsorption isotherms for Pb^{2+} and Cd^{2+} ions (a) loading capacity and (b) percentage

For both Cd^{2+} and Pb^{2+}, the maximum weight capacity was below 50% due to the small interlinked /unintercalated pores of the zeolite. This makes HEU adsorb less heavy metal ions as it cannot trap more ions in its structure. Interestingly, the percent weight and loading obtained from this computational study follow the experimental trend of 50% and 29.2% for Pb^{2+} and Cd^{2+}, respectively. The small variation between the experimental and computational results might be due to amorphous and crystalline impurities that are inevitably present in natural HEU zeolites that are not considered intrinsic constituents, as well as the high rate of water sorption capacity and the hydration of the metal ions during the experiment.

The adsorption data obtained from the Morte Carlo simulations fitted well to the Freundlich adsorption isotherm model, as depicted in Figure 4.47, which shows the variation in the

average loading of Pb^{2+} and Cd^{2+} adsorbed by unity mass of HEU zeolite with the pressure of the system from 10 kPa to 1000 kPa at 298 K.

4.7.1.7 The effect of temperature on adsorption of pb^{2+} and cd^{2+} (Computational study)

The adsorption isotherms of Pb^{2+} and Cd^{2+} ions at different temperatures and pressures were studied ranging from 10 to 1000 kPa and temperatures ranging from 298 to 398K, as shown in Figure. 4.48.

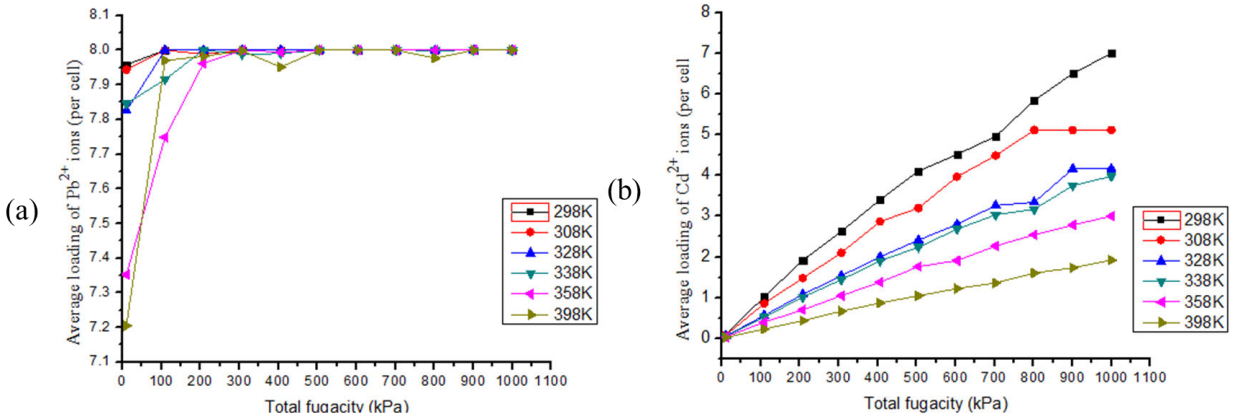

Figure 4. 48: Averaging loading of (a) Pb^{2+} and (b) Cd^{2+} onto HEU zeolite as a function of pressure at different temperatures

From the results obtained, the adsorption of Pb^{2+} ions exhibit no significant effect with temperature increase. The loading of Pb^{2+} per cell remains at 8 ions across all the temperatures studied. On the other hand, the adsorption of Cd^{2+} ions per cell onto HEU zeolite decreased as the temperature was increased. This can be due to the breaking of hydrogen bonds between the adsorbent and the Cd^{2+} at high temperature. The loading of Cd^{2+} per cell decreases, recording 7, 5, 4, 4, 3 and 2 ions per cell observed at temperatures of 298,308, 328, 338, 358 and 398 K, respectively. The adsorption difference of Pb^{2+} and

Cd^{2+} ions regarding temperature dependence is due to differences in the nature of the interactions between the HEU zeolite and the metal ions.

4.7.1.8 The Most Stable Configuration of Pb^{2+} and Cd^{2+} Adsorbed on the HEU Adsorbent

Figure 4.49 displays the most stable structural configurations of Pb^{2+} and Cd^{2+} adsorbed onto the HEU zeolite.

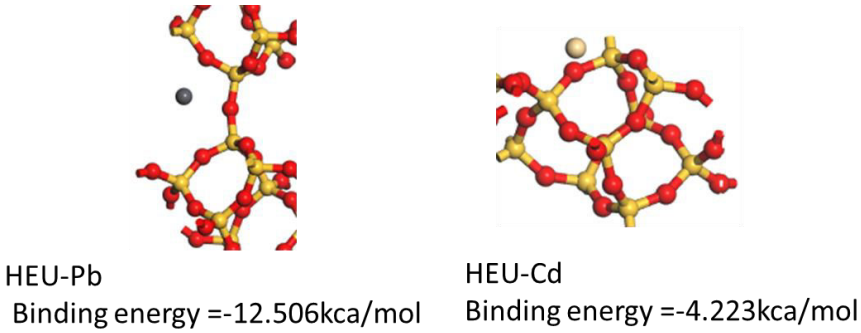

Figure 4. 49: Most stable configuration of Pb^{2+} and Cd^{2+} onto the HEU zeolite

In the case of Pb^{2+}, the ions are adsorbed at the window of HEU zeolite, equidistant from two adjacent oxygen atoms on the structure. This suggests that Pb^{2+} ions form stable bonds with the oxygen atoms in the zeolite framework structure. In contrast, the Cd^{2+} ions are adsorbed on the upper left side of the 8-ring HEU window connecting super cages, and the two oxide moieties located in the upper right segment of the 8-ring. The adsorption energy of Pb^{2+} and Cd^{2+} on the HEU zeolite structure was -12.51 and - 4.22 kcal/mol, respectively. The adsorption process is exothermic as indicated by the negative energy. Based on the binding energy results, it can be inferred that Pb^{2+} sorption onto the HEU zeolite is preferable to Cd^{2+} sorption. The more negative adsorption energy observed for

Pb^{2+}suggests stronger interactions between the Pb^{2+} ions and the zeolite structure framework, indicating a more stable adsorption for Pb^{2+} on the HEU zeolite structure.

4.7.1.9 Natural Bond Orbital (NBO) Analysis

Information on charge density transfer and molecular stabilization due to electronic delocalization is the key aspect that provides valuable insights into chemical bonding and reactivity. This allows for the evaluation of the extent to which electronic delocalization or charge density transfer contributes to molecular stabilization. Natural bond orbitals are a useful tool in scrutinizing the chemical characteristics of a given compound. It can provide information on the basicity, stability, intra- and intermolecular charge transfer. In addition, it provides information on the link between donor and acceptor molecular orbitals (Louis *et al.,* 2022). In this study, NBO analyses were conducted to gain insights on the charge delocalization and molecular stabilization in Pb-HEU and Cd-HEU complexes. The second-order perturbation energies and the various sites of contribution from different excitation types for the Pb-HEU and Cd-HEU complexes were analyzed and are recorded in Table 4.15.

Table 4. 15: The Pb-HEU and Cd-HEU complexes Second order perturbation energy at ώB97XD with def2svp basis set

Donor NBO (i)	Acceptor NBO (j)	E^2 Kcal/mol	E(j) – E(i) a.u	F(i,j) a.u.
		Pb-HEU complex		
σ*Si3-O16	σ*O1-Si3	10.11	0.02	0.060
LP (3) O1	LP (1) Al2	30.30	0.74	0.191
LP (3) O1	LP*(2) Al2	15.09	0.68	0.127
LP (3) O5	LP(4) Al10	19.50	0.82	0.161
LP (2) O13	LP* Al2	13.20	0.51	0.107
		Cd-HEU complex		
LP (3) O1	LP*(1) Al2	36.99	0.80	0.220
LP (3) O1	LP*(3) Al2	18.54	0.88	0.162
LP(3) O4	LP*(1) Al2	34.28	0.84	0.217
LP(3) O4	LP*(3) Al2	24.99	0.92	0.192

Thus, the total stabilization interaction for the charge transfer (LP→LP*, LP→LP, σ*→ σ*) was reported with respect to Mohammadi and coworkers, (2022). The results presented in table 4.17 elucidate that the stabilization energies of Pb-HEU complex ranged from 10.11 to 30.30 kcal/mol, with σ→ σ) interaction having the lowest $E^{(2)}$ contribution of 10.11 kcal/mol. In comparison, the stabilization energy is between 18.54 to 36.99 kcal/mol for the Cd-HEU complex, with the LP→LP* molecular orbital contributing the highest stabilization energy of 114.8 kcal/mol. The high stabilization energy values demonstrate the system's stability as a result of a robust donor-to-acceptor intermolecular connection. As a result, the Cd-HEU complex system with the highest $E^{(2)}$ value is the most stable. Nevertheless, the total change in charge density transfer for the Pb-HEU complex was 49.80 kcal/mol for (**ΔETLP** → L.P.) and 28.29 kcal/mol for (**ΔETLP** → L.P*), which contributed to the stability of the Pb-HEU complex.

The delocalization of charge density in molecules is crucial for predicting an isolated system's conformation character and reactivity. Delocalization and Mulliken charge analysis play a crucial role in charge transformative process, electronegativity equalization, and potential energy surface (Hussain *et al.,* 2020; Louis *et al.,* 2022).

Mulliken analysis is calculated at the ωBb97XD/def2svp theoretical level to compare and analyze the total charge density distribution and delocalization over the whole complex (Mohammadi *et al.,* 2022). This analysis can help in understanding how the electron density is distributed and transferred during chemical reactions, as well as in identifying the most reactive sites in a molecule Figure 4.50 shows Mulliken population charge analysis of the Pb-HEU and Cd-HEU complexes. It was observed that the two complexes have higher negative density due to the presence of negatively charged oxygen between two hydroxyl groups (O.H.—O—O.H.) and linked to Silicon (Si—O). This clearly shows that these immensely negatively charged oxygens attract a higher electronic distribution than other charged atoms in the complexes.

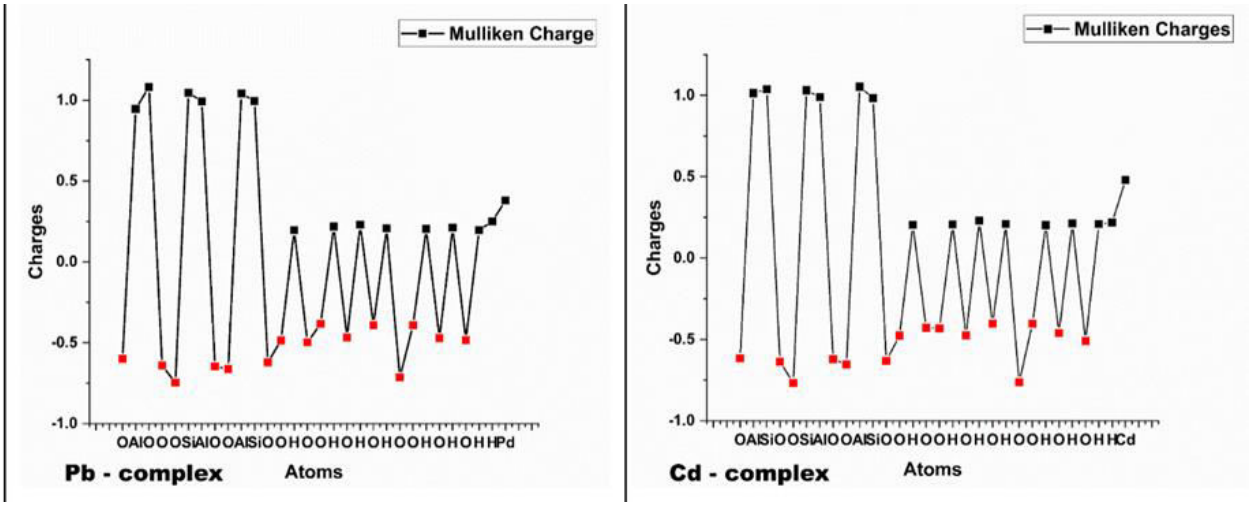

Figure 4. 50: Mulliken population Charge analysis of the Pb-HEU and Cd-HEU complexes

Remarkably, the presence of positively charged aluminum in both complexes results in a shift in the electronic charge delocalization, with the Pb- HEU complex shifting from -0.75 to 1.33 eV and from -0.80 to 1.0 eV for the Cd-HEU complex**.**

4.7.1.10 Quantum Theory of Atoms in Molecule (QTAIM) Analysis

Quantum Theory of Atoms in Molecules (QTAIM) which is a theoretical framework was utilized extensively to understand better the behavior of inter- or intramolecular hydrogen bonding interaction molecular and atomic levels using electronic charge density. Furthermore, it provides insights into chemical reactivity and molecular recognition. The QTAIM theory partitions a molecule into atoms using its electronic charge density, which could be obtained computationally or experimentally (Wilson *et al.,* 2021). Various critical points are identified by evaluating the first and second derivatives of the electron density, which are used to characterize a number of non-covalent interactions such as intermolecular hydrogen bonding within atoms in the molecule. QTAIM can also be used to identify and characterize molecules which possess non-covalent bonds. Therefore, information on the electron density at different bond critical points (bcps) of an intra- or intermolecular hydrogen bond interaction can be utilized to determine the strength of the hydrogen bond (Shiroudi *et al.,*2024). Hence, the concept of QTAIM formulated by Malloum and coworker was used to study Pb-HEU and Cd-HEU complexes to characterize the features of the intermolecular hydrogen bonds present (Malloum & Conradie, 2022). Figure 4.51 illustrates the critical point (C.P.) between each intramolecular interaction, providing insights into the strength of hydrogen bonding within Pb-HEU and Cd-HEU complexes. Hence, the concept of QTAIM formulated by Richard F.W was used to

characterize the features of the intermolecular hydrogen bonds present in the studied Pb-HEU and Cd-HEU complexes (Bader, 1991).

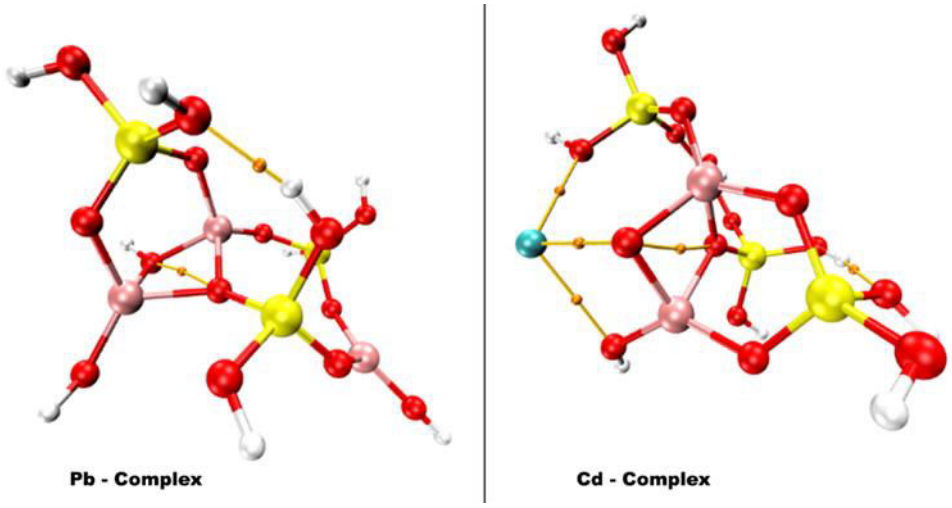

Figure 4. 51: The critical point (C.P.) between each intramolecular interaction in the Pb-HEU and Cd-HEU complexes

Table 4.16 provides additional information on the nature and strength of the bonding interactions within the studied Pb-HEU and Cd-HEU complexes. The Laplacian of electron density ($\nabla^2\rho$BCP), ellipticity (Ɛ), kinetic energy density G(r), potential energy density V(r), total energy H(r), binding energy at each critical point and the ratio of G(r)/V(r) ratio are all given in Table 4.16. Thus, the binding energy at the bond critical points (BCPs) [$E_{O5\text{-}O15}$, $E_{O22\text{-}H26}$] for the Pb-HEU and Cd-HEU complexes was -188.88 and -23.79 kcal/mol, respectively. It is worth noting that no critical point of interaction exists between Pb and other atoms detected, indicating weak or no interaction. In contrast, a significant chemisorption interaction for O_{22}-Cd_{30} and Cd_{30}-O_{27} bond critical points, with a binding energy (B.E.) of -148.72 and 72.87 kcal/mol, respectively. This suggests a strong interaction between Cd and the oxygen atoms, which can have significant implications for

the properties and behavior of the complex. The higher binding energy observed for the Cd and O interaction indicates stronger stability of Cd-HEU complexes, which is the complex's second-order perturbation energy $E^{(2).}$ This is because BE is directly proportional to stability of a complex (Louis *et al.,* 2022; Chandrasekaran & Betouras, 2022). The positive Laplacian electron density observed in Pb HEU and Cd-HEU complexes show that the most prominent interactions in the two complexes is electrostatic in nature (Table 4.18). The concept of ellipticity (Ɛ), which is calculated using the negative Hessian of the electron density at Bond Critical Points (BCPs), is expressed as $\varepsilon = \lambda1/\lambda2 - 1$, where $\lambda1$ and $\lambda2$ represent the eigenvalues of the negative Hessian of electron density at BCPs. As a result, the parallel expansion $\lambda1/\lambda2$ and ellipticity values for the Pb-HEU complex and Cd HEU complex systems are less than one, indicating a highly strong intermolecular interaction between the HEU zeolite and the heavy metal ions. The investigated compounds have high stability, with the Cd-HEU combination having the most stable chemisorption bonds with an oxygen atom at the aromatic ring.

Table 4. 16: QTAIM parameters for Pb-HEU and Cd-HEU complex systems

QTAIM parameters for Pb-HEU and Cd-HEU complex systems

Systems	Parameters	Bond	p(r)	∇^2 p(r)	G(r)	K(r)	V(r)	H(r)	G(r)/V(r)	ELF	Ɛ	λ_1	λ_2	λ_3
Pb-HEU complex	BCPs	O_5-O_{15}	0.85	0.76	0.18	-0.52	-0.17	-0.52	-1.06	0.61	0.04	-0.15	-0.16	0.10
	BE($E_{O—O}$)	-188.88												
	BCPs	O_{18}-H_{26}	0.11	0.91	0.24	0.13	-0.25	-0.13	-0.96	0.91	0.01	0.13	-0.20	-0.21
	BE($E_{O—H}$)	-23.79												
Cd-HEU complex	BCPs	O_{22}-Cd_{30}	0.67	0.36	0.98	0.72	-0.10	-0.72	-9.80	0.94	0.01	0.52	-0.77	-0.78
	BE($E_{O—Cd}$)	-148.72												
	BCPs	Cd_{30}-O_{27}	0.33	0.14	0.36	0.14	-0.36	-0.14	-1.00	0.73	0.05	0.20	-0.32	-0.31
	BE($E_{Cd—O}$)	-72.87												
	BCPs	Cd_{30}-O_{18}	0.24	0.92	0.22	-0.60	-0.21	0.60	-1.05	0.65	0.05	0.13	-0.19	-0.20
	BE($E_{Cd—O}$)	-52.79												
	BCPs	O_{22}-O_{22}	0.32	0.14	0.33	-0.19	-0.31	0.19	-1.06	0.77	5.28	-0.28	0.17	-0.45
	BE($E_{O—O}$)	-70.64												
	BCPs	O_{25}-H_{29}	0.35	0.13	0.33	-0.55	-0.32	0.55	-1.03	0.10	0.03	0.26	-0.63	-0.61
	BE($E_{O—H}$)	-77.33												

Conclusion

In conclusion the experimental and computational studies revealed that the percent weight capacity of the zeolite for the two ions followed the decreasing order of $Pb^{2+} > Cd^{2+}$. This trend suggests that the zeolite had a higher adsorption capacity for Pb^{2+} ions compared to Cd2+. Furthermore, the BE at the BCPs for the Pb-HEU complex was -188.88 kcal/mol and -148.72 kcal/mol for the Cd-HUE complex. The stronger binding energy of the interaction between Pb and HEU provides a rationale for Pb's greater percent weight capacity on the zeolite compared to Cd, as shown by the experimental results. The results suggest that different excitation types contribute differently to the stabilization energy and charge transfer in these complexes, with the Cd-HEU complex showing a higher degree of stabilization than the Pb-HEU complex. These findings could have implications for understanding the properties and behavior of these complexes in environmental remediation. Meanwhile, being locally available, and freely abundant with a considerably high adsorption capacity, natural zeolite is an attractive choice for removing metal ions from water.

4.8 Removal of PO_4^{3-} and NO_3^- from Wastewater using Heulandite Zeolite

The study herein aims to exploit HEU zeolite as a cost-efficient and highly potent adsorbent for PO_4^{3-} and NO_3^- ions in synthetic wastewater, employing a batch mode. Optimization was conducted for parameters including contact time, initial concentration, adsorbent dosage, and temperature in the removal of PO_4^{3-} and NO_3^- by the HEU zeolite. Additionally, the investigation encompassed the examination of adsorption isotherms, kinetics, and thermodynamics concerning the adsorption of the two anions onto HEU zeolites

4.8.1 Characterization

The morphology of HEU zeolite before and after adsorption of two anions is displayed in Figure 4.52.

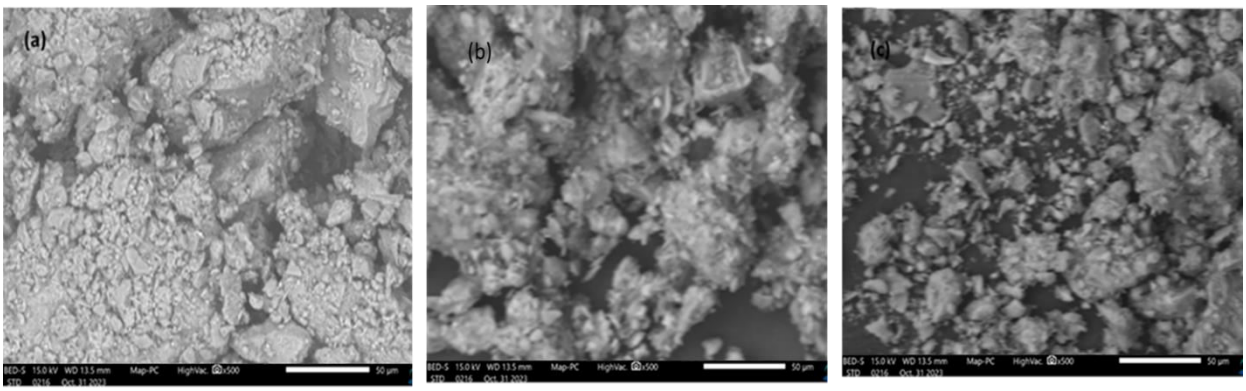

Figure 4. 52: SEM micrographs of the natural heulandite zeolite (a) before adsorption and after adsorption for (b) NO_3^- and c) PO_4^{3-}

As it can be seen, the zeolite before adsorption has a rough texture surface with irregular particles with different sizes with cavities distinguished as dark areas. After adsorption, the surface of the anion-loaded adsorbent shows that the surface was covered with anions (NO_3^- and PO_4^{3-}). The surface of HEU zeolite became smooth after the adsorption of anions and the pores appear to be smooth due to the adsorption of anions onto the pores of the adsorbent.

4.8.2 Adsorption Studies

The effects of different physical factors on the adsorption of the PO_4^{3-} and NO_3^- onto the natural zeolite was investigated.

4.8.2.1 Effect of Contact Time on PO_4^{3-} and NO_3^- Removal from Aqueous Solution using HEU Zeolite

Contact time influence adsorption of the selected anions onto the HEU adsorbent. The effect of contact time on adsorption capacity is given in Figure 4.53. Figure 4.53 shows efficiency of PO_4^{3-} and NO_3^- removal by the zeolite as a function of contact time (0 to 120 min). The initial PO_4^{3-} and NO_3^- concentrations were both 4 ppm the adsorbent dose was 1.0 g and volume of the solution was 100 mL at 25 °C.

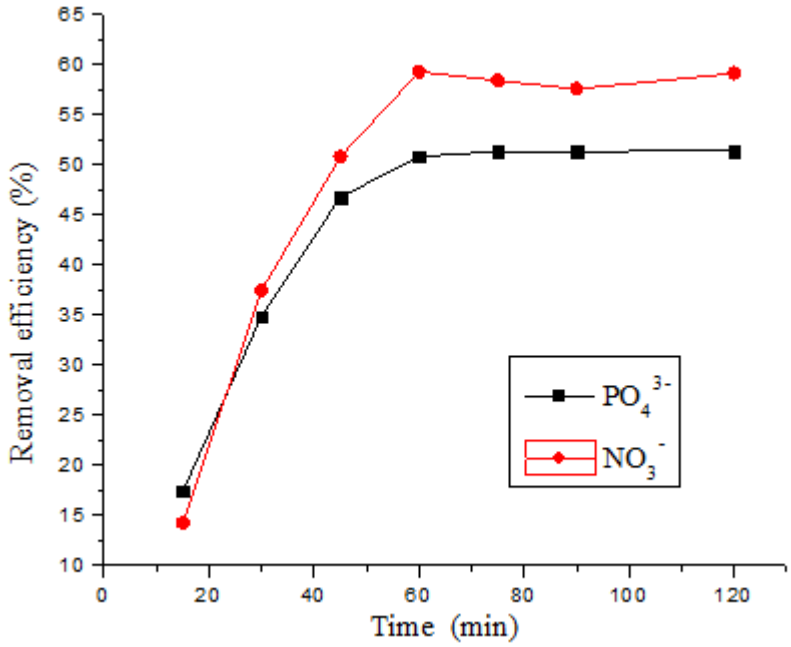

Figure 4. 53: Effect of contact time on the adsorption of PO_4^{2-} and NO_3^- onto HEU zeolite

The results in Figure 4.53 show that HEU has a strong selectivity for the selected anions. The adsorption of the two anions removal occurred in two stages; a rapid and a slow phase. For the first 45 min adsorption was rapid which was followed by slow removal then it reached equilibrium after 60 min. At initial stage, adsorption was fast due to presence of

more binding sites. As the contact time progressed, available effective surface for binding has reached its maximum capacity within the first 60 min for two the anions. The data also shows that the adsorption of NO_3^- was higher compared to PO_4^{3-}. This could be because PO_4^{3-} is larger size and weight (94.97.03g/mol) than the NO_3^- whose molar mass is 62.03 g/mol, since a lower mass and ionic size allows for more packing in the zeolite structure but less mobility within the structure. Furthermore, the charge of the ions is important. Nitrate is a monovalent negatively charged ion, whereas phosphate is a trivalent negatively charged ion. The higher phosphate charge leads to repulsion between the phosphate ion and the negatively charged zeolite framework, lowering the phosphate's overall adsorption capacity (Capa-Cobos *et al.,* 2021).

4.8.2.2 Adsorption Kinetics

Adsorption kinetics describes the rate of adsorption. The *pseudo* first-order and *pseudo*-second-order kinetic models were used to evaluate adsorption of PO_4^{3-} and NO_3^- ion onto HEU-zeolite.

Figure 4.54 and 4.55 show kinetic models of adsorption for PO_4^{3-} and NO_3^- onto the HEU zeolite. pseudo-first-order and pseudo-second-order at the concentration of 4 ppm, adsorbent dose of 1.0 g and at reaction temperature of 25 ^oC.

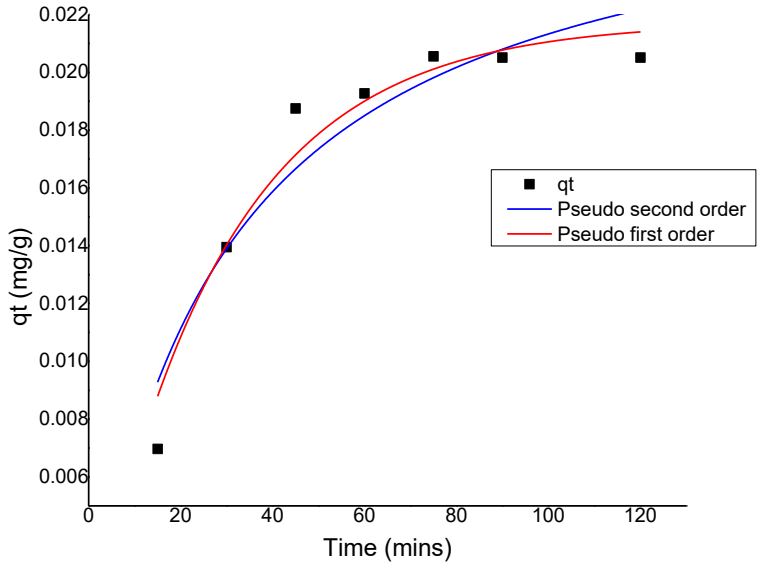

Figure 4. 54: Kinetic models for the adsorption for PO_4^{3-} onto the HEU zeolite

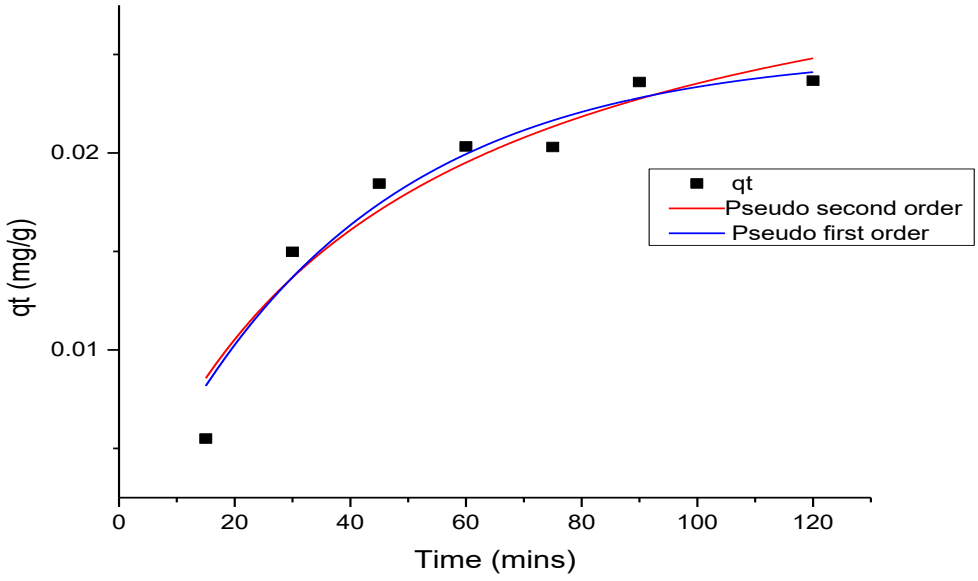

Figure 4. 55: Kinetic models of adsorption for NO_3^- onto the HEU zeolite

Table 4.17 shows compared parameters of kinetic model constants of NO_3^- than PO_4^{3-} adsorption onto HEU zeolite. The best-fit kinetic model was then selected based on the coefficient of determination (R^2) as shown in Table 4.17

Table 4. 17: Compared parameters of kinetic model constants of NO_3^- and PO_4^{3-} adsorption onto HEU zeolite

Pseudo-First order						
Adsorbate	q_e (exp)	q_e (cal)	k_1	S (rate)	t 1/2	R^2
NO_3^-	0.0236	0.0252	0.0262	0.0007	26.54	0.9368
PO_4^{3-}	0.0206	0.0217	0.0345	0.0008	20.08	0.9457
Pseudo-Second order						
Adsorbent	q_e (exp)	q_e (cal)	k_2	S (rate)	t 1/2	R^2
NO_3^-	0.0236	0.0340	0.6579	0.0008	44.66	0.9167
PO_4^{3-}	0.0206	0.0278	1.2159	0.0009	29.72	0.8941

It is clear from Table 4.17 that the *pseudo*-first-order model describe the adsorption of PO_4^{3-} and NO_3^- onto HEU-zeolite more precisely. It can be concluded that adsorption of PO_4^{3-} and NO_3^- may be affected by many factors, but physisorption interactions between the HEU zeolite and the anions play a significant role. Previous studies on adsorption of nitrate and phosphate ions adsorption on zeolite also demonstrated that *pseudo*-first order kinetic model provided a better description of the adsorption data kinetics (Revellame *et al.,* 2020; Onyango *et al.,* 2010).

The adsorption kinetics fitted the *pseudo*-first order kinetic model, suggesting that adsorption is primarily controlled by adsorbate diffusion rather than surface control. In this case, the calculated q_e values for the anions are almost the same as the experimental value. The higher values obtained for NO_3^- indicate that the HEU is more energetically suitable adsorption for NO_3^- than PO_4^{3-}.

4.8.2.3 Intraparticle Diffusion

The diffusion that occurs within the adsorbents pores is described by intraparticle diffusion. Furthermore, as the regression lines fortwo anions in Figure 4.56 do not pass through the origin, the intraparticle diffusion is not the rate-determining (Kimosop *et al.,* 2016)

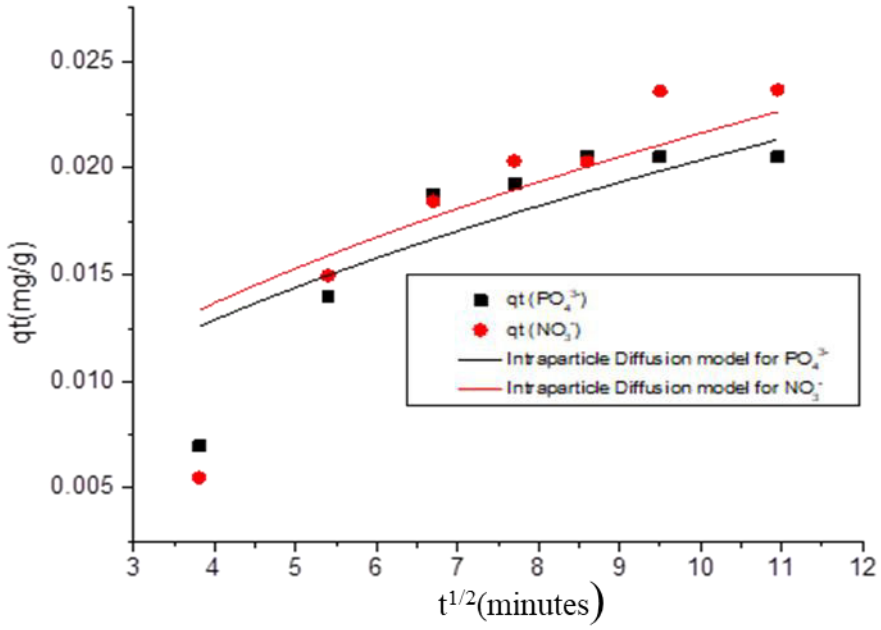

Figure 4. 56: The intraparticle diffusion plot for the removal of NO_3^- and PO_4^{3-}

When the intraparticle diffusion is the rate determining step the plot of qt verses $t^{1/2}$ passes through the origin, which is not the case in the adsorption of selected anions. Hence it can

be concluded that other multiple processes, bulk, and film diffusion could be rate determining step for adsorption of anions onto HEU zeolite surface. From Figure 4.56, the two anions were adsorbed in two phases, where at first there were a rapid diffusion of NO_3^- and PO_4^{3-} on the external surface of the adsorbent and later an intraparticle diffusion occurs. On the other hand, the second phase is an indicative of complete utilization of all binding sites since the ions migrated from the outside of the adsorbents into their pores where adsorption took place (Liu *et al.,* 2014).

4.8.3 Adsorption Isotherm

The adsorption isotherm is the ratio between the quantity adsorbed to what remains in the solution at a fixed temperature. This explains how the adsorbent's adsorption capacity is determined since it describes the relationship between the adsorbent and adsorbate interaction. In the present study, the data obtained was fitted to Langmuir, Freundlich, Sips and Redlich-Peterson isotherms models. The adsorption equilibria data were studied and feasibility of the models were evaluated using the coefficient of determination (R^2). The non-linear adsorption isotherms are presented in Figure 4.57and 4.58. The isotherm constants are presented in Table 4.20.

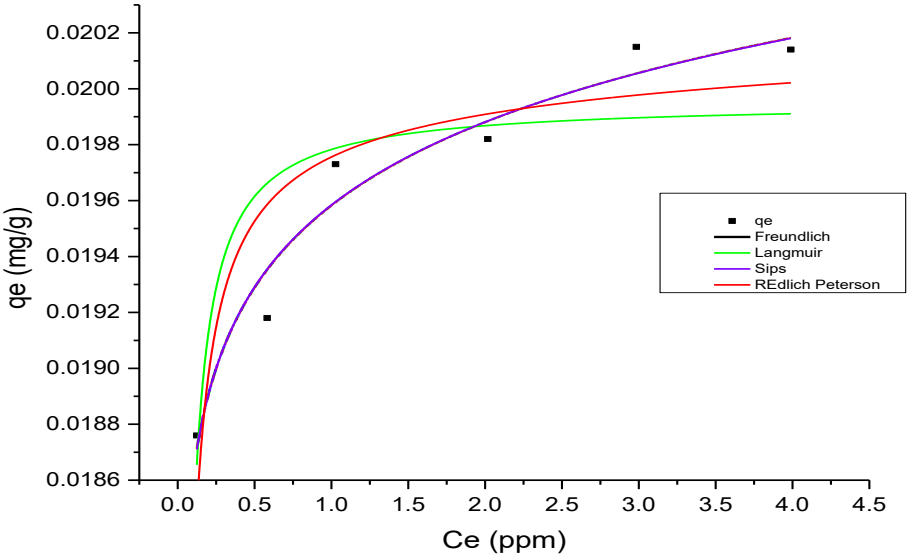

Figure 4. 57: Adsorption of NO_3^- onto HEU zeolites

The non-linearized Langmuir, Freundlich, Sips and Redlich-Peterson adsorption isotherms for PO_4^{3-} sorption onto HEU adsorbent are presented in Figure 4.58 below.

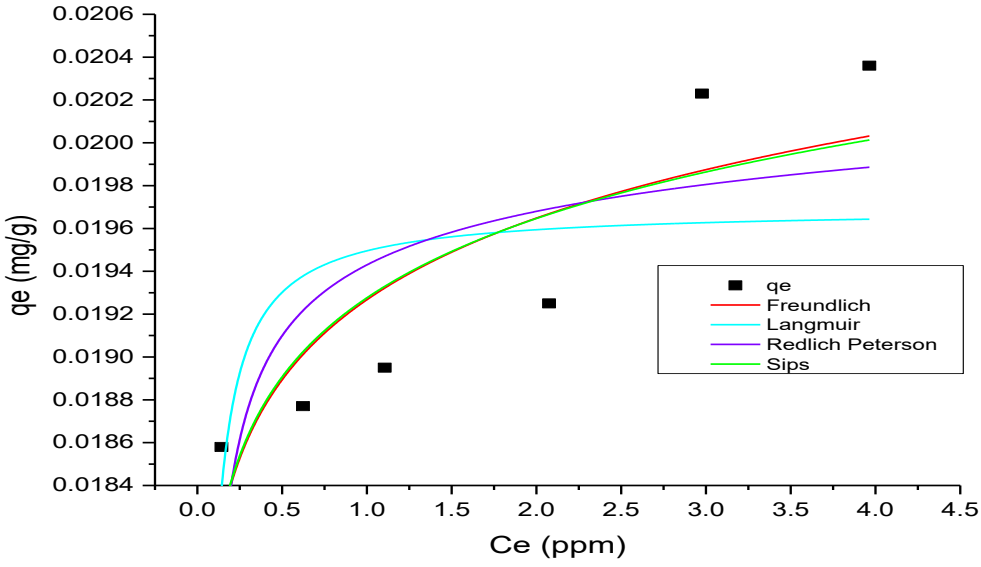

Figure 4. 58: Adsorption of PO_4^{3-} onto HEU zeolite

From the parameters determined in Table 4.18, it can be concluded that the Langmuir isotherm equation is not suitable to describe the adsorption of the two anions due to lower R^2 values and theoretical maximum adsorption which is 0.02.

Table 4. 18: Isotherm parameters for the adsorption NO_3^- and PO_4^{3-}onto zeolite

Langmuir isotherm					
Ion	q_{max}	K_L	R_L	R^2	Chi-sqr
NO_3^-	0.01995	115.829	0.9261	0.70204	9.15×10^{-8}
PO_4^{3-}	0.01969	98.4776	0.9270	0.65409	4.32×10^{-7}
Freundlich isotherm					
	K_F	1/n	R^2		Chi-sqr
NO_3^-	0.01958	45.87	0.94649		1.64×10^{-8}
PO_4^{3-}	0.01927	35.41	0.85409		1.82×10^{-7}
Sips isotherm					
	q_{ms}	a_s	Bs	R^2	Chi-sqr
NO_3^-	0.09677	0.25372	0.02727	0.9283	2.52×10^{-8}
PO_4^{3-}	0.0416	0.8637	0.05163	0.5647	2.52×10^{-7}
Redlich-Peterson isotherm					
	g	a_R	Kr	R^2	Chi-sqr
NO_3^-	0.9948	121.26	2.41534	0.6826	9.75×10^{-8}
PO_4^{3-}	0.9881	108.79	2.13335	0.20113	4.62×10^{-7}

The Langmuir isotherm profile can be used to evaluate the nature of the adsorption based on the values of R_L which can be irreversible ($R_L = 0$), favorable ($0 < R_L < 1$), linear ($R_L = 1$),

or unfavorable $R_L > 1$) (Worch, 2021). From Table 4.18, the R_L values of PO_4^{3-} and NO_3^- samples were found to be between 0 and 1, implying the adsorption of NO_3^- and PO_4^{3-} ions is favorable. The values of K_L are higher than 1 for the two anions, implying that the ions interacted more strongly with surface functionalities on the HEU. Furthermore, the high K_L indicate that the binding forces are weak, which could imply the presence of physio-sorption (Shikuku *et al.,* 2020).

The Freundlich isotherm model is most ideal for NO_3^- and PO_4^{3-} since it has highest R^2 value of 0.94649 and 0.85409, respectively and least error function (1.64×10^{-8} and 1.82×10^{-7}, respectively). Also, the 1/n values obtained are higher than 1, suggesting favorable physisorption of NO_3^- and PO_4^{3-} onto HEU zeolite surface.

The constant K_F has a linear dependence on the adsorption capacity of the adsorbent, i.e., the lower k_F values, the lower the adsorption capacity. The Freundlich intensity capacity parameter also shows the surface heterogeneity, where it becomes more heterogeneous as its value gets closer to zero (Shikuku *et al.,* 2020). Thus, while the adsorption isotherm validates that the adsorption is spontaneous, the question remaining is the type of molecular mechanism that plays a role in this process.

The equilibrium data for NO_3^- was suitably fitted to Sips isotherm due to high coefficient of determination R^2 = 0.9283) For the adsorption of PO_4^{3-} the R^2 value of 0.525 was observed. Additionally, the differences between Langmuir and Freundlich isotherm models were identified using heterogeneity index (Bs) values. The lower heterogeneity values obtained in this study indicate a heterogenous system (Shukuku *et al.,* 2020). Lastly, the low Redlich-Peterson isotherm R^2 values of 0.2011 for NO_3^- compared to PO_4^{3-} (0.6826) shows its inapplicability to account for the sorption of NO_3^- onto HEU zeolite.

4.8.4 The effect of adsorbent dose on the adsorption of PO_4^{3-} and NO_3^- onto HEU zeolite

The effect of adsorbent dose on the elimination of PO_4^{3-} and NO_3^- from aqueous solution is an important descriptor that establishes the HEU zeolite's capacity. Figure 4.62 shows the effect of adsorbent dosage on the removal efficiency of PO_4^{3-} and NO_3^- ions from aqueous solution under the condition of concentration 4 ppm, contact time of 60 min and temperature of 25 ℃.

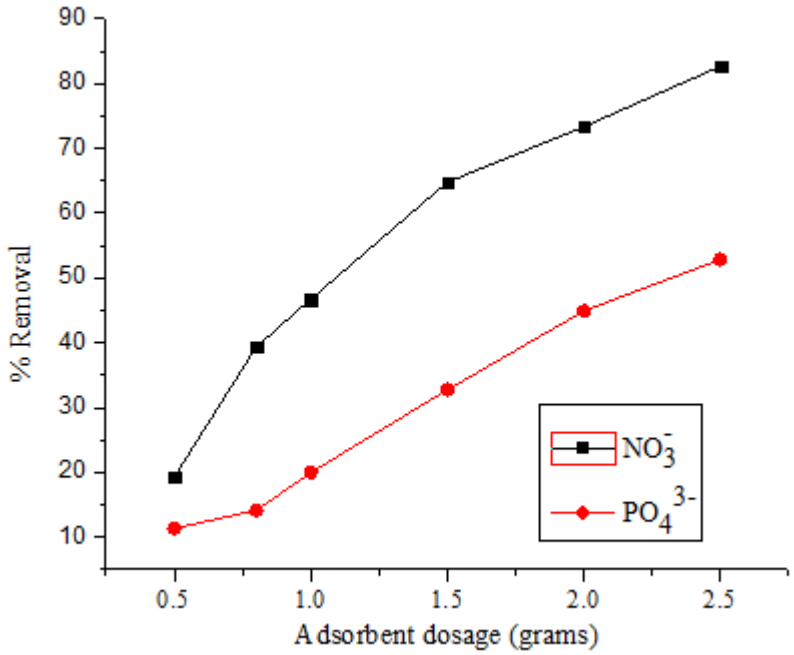

Figure 4. 59: Effect of adsorbent dosage on the adsorption of PO_4^{3-} and NO_3^- onto HEU zeolite

It is reasonable to assume that the rise in natural zeolite quantity is responsible for the increased number of active adsorption sites for PO_4^{3-} and NO_3^- at higher dosages, which in turn leads to an improvement in removal efficiency. Consequently, the zeolite adsorbent studied in this work can be an ideal and potential material for treating effluents that contain traces of PO_4^{3-} and NO_3^- (El Ouardi *et al.,* 2015).

4.8.5 Effect of Temperature on Adsorption of PO_4^{3-} and NO_3^- onto HEU Zeolite

Temperature presents an important role in PO_4^{3-} and NO_3^- adsorption onto HEU zeolite; hence temperature studies were carried out at 25, 30, 60 and 75°C, as shown in Figure 4.60.

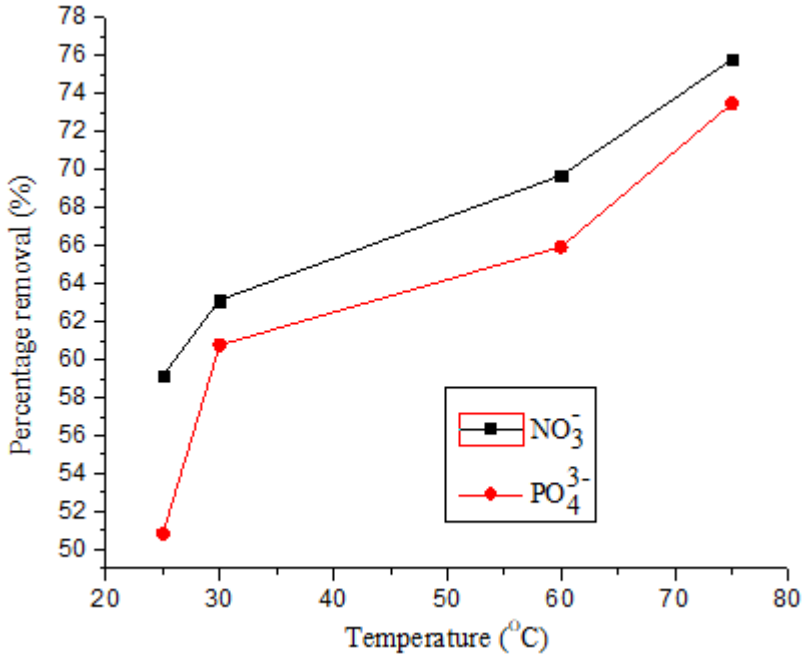

Figure 4. 60: Effect of temperature on the removal efficiency of PO_4^{3-} and NO_3^- onto HEU zeolite

The results show that increase in temperature increases anions sorption. This could be because of a higher frequency of collisions, that increases the ions mobility between the ions and HEU zeolite. It may also be attributed to the enlargement of pore size and activation of the adsorbent surface when temperature increases (Masukume *et al.*, 2013; Wang & Zhu, 2006). The increase in temperature positively affects the adsorption capacity, implying an exothermic process.

The thermodynamic parameters of anions (PO_4^{3-} and NO_3^-) adsorption onto the HEU zeolite structure were calculated and the results are shown in Table 4.19. The slope and the intercept as displayed in Figure 4.61, were used to calculate the values of ΔH and ΔS.

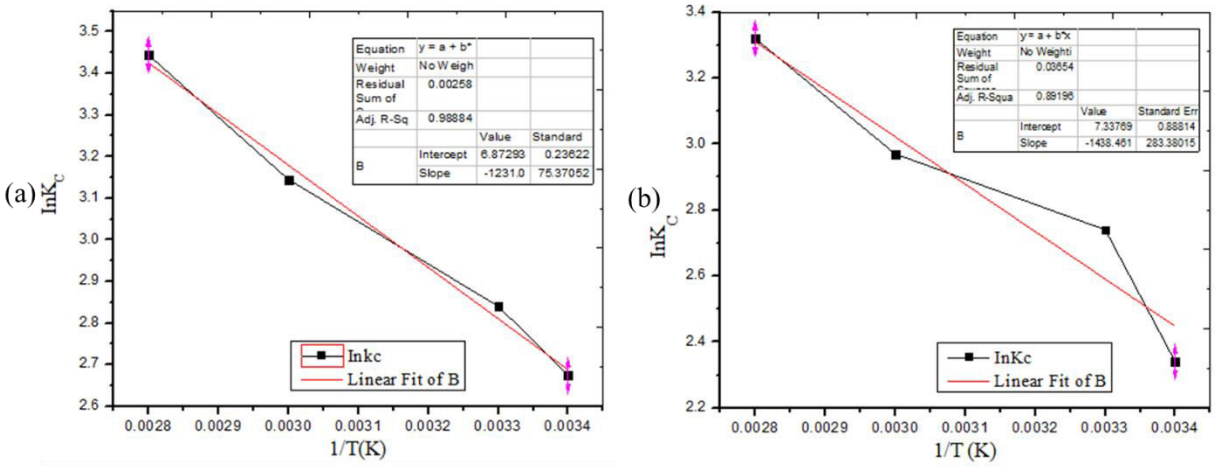

Figure 4. 61: The relationship between In K_c with 1/T for (a) NO_3^- and (b) PO_4^{3-}

Table 4. 19: The thermodynamic parameters for $NO_3^-$and PO_4^{3-}adsorption onto HEU.

Adsorbate	**Temperature (K)**	**Gibb's free energy ΔG (kJmol^{-1})**	**Enthalpy(kJmol^{-1})**	**Entropy (JK^{-1}mol^{-1})**
	298	-6.63		
	303	-7.15		
NO_3^-	333	-8.71	-10.235	57.14
	348	-9.68		
	298	-5.80		
	303	-6.91		
PO_4^{3-}	333	-8.21	-11.958	61.01
	348	-9.62		

The sorption process was found to be favorable and spontaneous as shown by the negative ΔG values (Alagha *et al.,* 2020). The results indicate that increase in temperature leads to enhanced adsorption of PO_4^{3-} and NO_3^- onto the HEU. It's important to note that the values of ΔG which are in a range between 0 and -20kJ/mol show the process is physical adsorption (Hu *et al.,* 2018). The enthalpy change (ΔH) values were negative for both PO_4^{3-} and NO_3^- adsorption indicating that the process was exothermic. The sorption process at the adsorbent and solution interface shows an increase in randomness, as indicated by the positive value of entropy change. In conclusion, the negative Gibbs free energy and positive entropy values revealed that the PO_4^{3-} and NO_3^- adsorption was favorable.

4.8.6 Comparison of Experimental Results of Adsorption of PO_4^{3-} and NO_3^- onto HEU zeolite

The NO_3^- and PO_4^{3-} removal values obtained in this study are comparable with those reported in other studies are shown in Table 4.20. In this study, values of 0.024 and 0.020 mg/g^{-1} removal for NO_3^- and PO_4^3-, respectively were obtained.

Table 4. 20: The PO_4^{3-} and NO_3^- adsorption capacities of HEU zeolite.

Zeolite adsorbent	**Adsorbate**	**Adsorption Capacity (mg/g)**	**Reference**
Clinoptilolite	PO_4^{3-}	20	(Hamdi & Srasra, 2012)
Natural clinoptilolite	NO_3^-	1.3	(Murkani et al., 2015)
Chinese clinoptilolite	NO_3^-	0.016	(Du *et al.,* 2005)
Iran clinoptilolite	NO_3^-	2.03	Sepehri *et al.,* 2014
Heulandite	NO_3^-	0.0231	This study
Heulandite	PO_4^{3-}	0.0194	This study

4.8.7 Computational Study Results

Computational simulation modeling was performed to generate adsorption isotherms, which are useful in developing and optimizing adsorption processes, understand the sorption behavior of the anions on the HEU zeolite. Grand canonical Monte Carlo (GCMC) simulations were used to investigate the capability of HEU zeolite for the adsorption of PO_4^{3-} and NO_3^-. Figure 4.62 show adsorption isotherms for PO_4^{3-} and NO_3^- adsorption onto the HEU zeolite. In both cases, it gave favorable isotherms that have convex shapes which represent a large amount of adsorption at a lower partial pressure. Irreversible adsorption is the favorable isotherm, with maximum adsorption occurring at extremely low partial pressures. Figure 4.62 shows that the loading of NO_3^- ion is higher than that of PO_4^{3-} since the NO_3^- is smaller in size than PO_4^{3-} hence it can easily enter and move in the pores easily and gets attached even within the HEU structure. Furthermore, it was found that the adsorption of NO_3- and PO_4^{3-} was exothermic due to negative values of adsorption energy of -962.25 and -12099.04 kcal/mol.

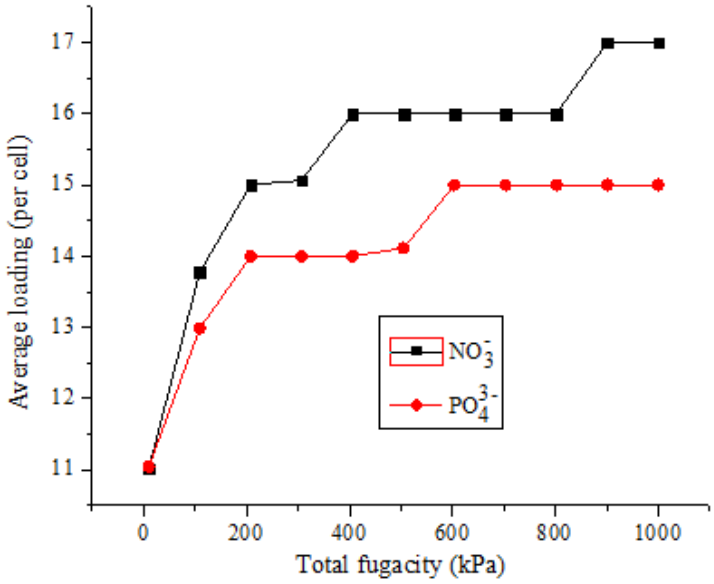

Figure 4. 62: Adsorption isotherms for PO_4^{3-} and NO_3^- on the HEU zeolite

The most stable adsorbed configurations of the PO_4^{3-} and NO_3^- ion onto the HEU zeolite using the simulated annealing approach (Kirkpatrick, 1983) was explored. Figure 4.63, shows the structure of the most stable configuration of PO_4^{3-} and NO_3^- adsorbed on the HEU zeolite.

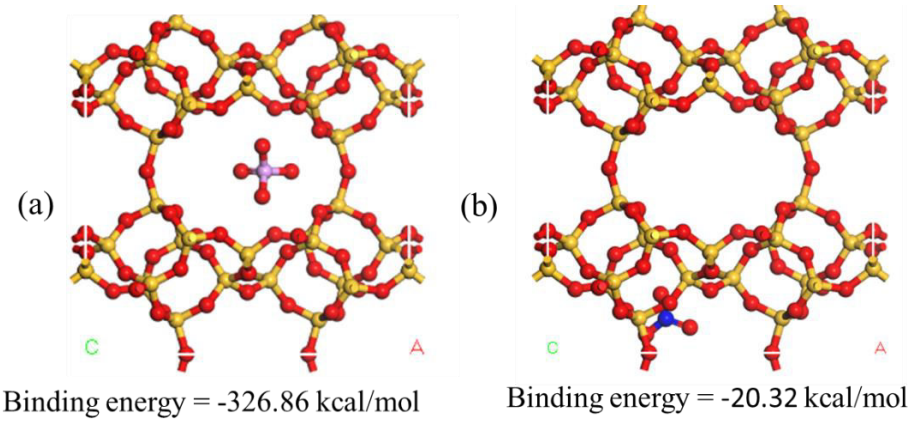

Figure 4. 63: Structures of the most stable configuration of the (a) PO_4^{2-} and (b) NO_3^- ion HEU zeolite

The most stable configuration of the adsorbed PO_4^{3-} is located equidistance at the center of 10-ring window of HEU. On the other hand, the NO_3^- is located at the lower left side of the HEU structure. From Figure 4.63, PO_4^{3-} has a higher binding energy (-326.86 kcal/mol) compared to NO_3^- (-20.32. kcal/mol). Hence, PO_4^{3-} is more stable than the NO_3^- in the HEU zeolite. This suggests that the PO_4^{3-} ions are more strongly interacted with the surface functionalities of the HEU zeolite than NO_3^-.

The effect of temperature on adsorption of the PO_4^{3-} and NO_3^- ion onto the HEU zeolite using the sorption simulation program was investigated. Figure 4.64, shows the isotherms of PO_4^{3-} and NO_3^- adsorbed on the HEU zeolite.

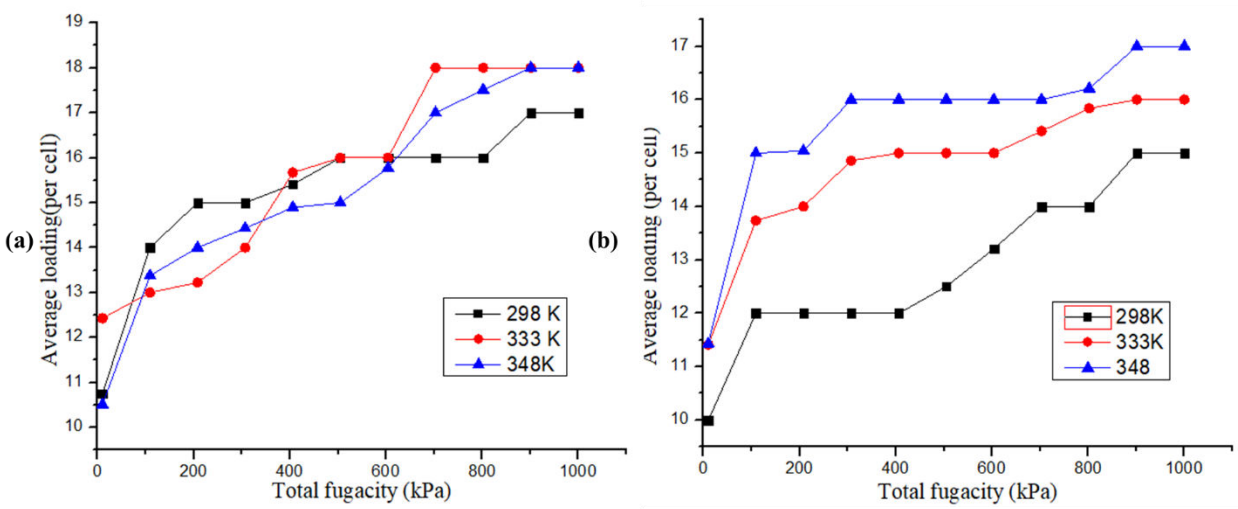

Figure 4. 64: Effect of temperature for adsorption (a) NO_3^- and (b) PO_4^{3-} ions using HEU zeolite

Adsorption of PO_4^{3-} and NO_3^- onto HEU was conducted at several reaction temperatures (298, 333 and 348 K). It was found that NO_3^- adsorption increased before reaching equilibrium with varying loading capacity, with the loading increasing from 17 to 18 ions for temperature (348K). The PO_4^{3-}, on the other hand, increased from 15 to 16 ions per cell due to an increase in entropy caused by an increase in temperature.

In conclusion, heulandite adsorption equilibrium was achieved after 60 minutes for NO_3^- and PO_4^{3-} ions. The loading capacity of NO_3 was greater than PO_4^{3-} onto HEU zeolite. The kinetics fitted the *pseudo*-first order model, indicating a physisorption mediated rate determining step. The sorption of NO_3^- and PO_4^{3-} of ions gave a negative average total energy which shows that the sorption is an exothermic process. Therefore, the adsorption process was multi-mechanistic. The adsorption thermodynamic functions, namely ΔG values, enthalpy (ΔH = -10.23 and -11.96 $kJmol^{-1}$) and positive entropy (ΔS = 57.14 and 61.01 $JK^{-1}mol^{-1}$) respectively, indicated that adsorption exothermic and spontaneous with the increased disorder at the solid-liquid interphase. It was observed that interactions,

binding energy, and operational conditions all affect the adsorption capacity. These factors are made clear by molecular simulations, which aid in understanding the anion adsorption process.

4.9 Removal of selected pesticides (Chlorpyrifos and Imidacloprid) from water onto Heulandite Zeolite; Experimental Study

This study aimed to evaluate the removal of chlorpyrifos and imidacloprid from water using HEU zeolite. The two halogenated pesticides were used because of their extensive use and their detection in the environment

4.9.1 Characterization

From the SEM images it can be observed that the HEU zeolite before adsorption has rough texture surface with irregular particles with different sizes and cavities distinguished as dark areas. SEM images of adsorbent before and after adsorption with imidacloprid and chlorpyrifos are shown in Figure 4.68.

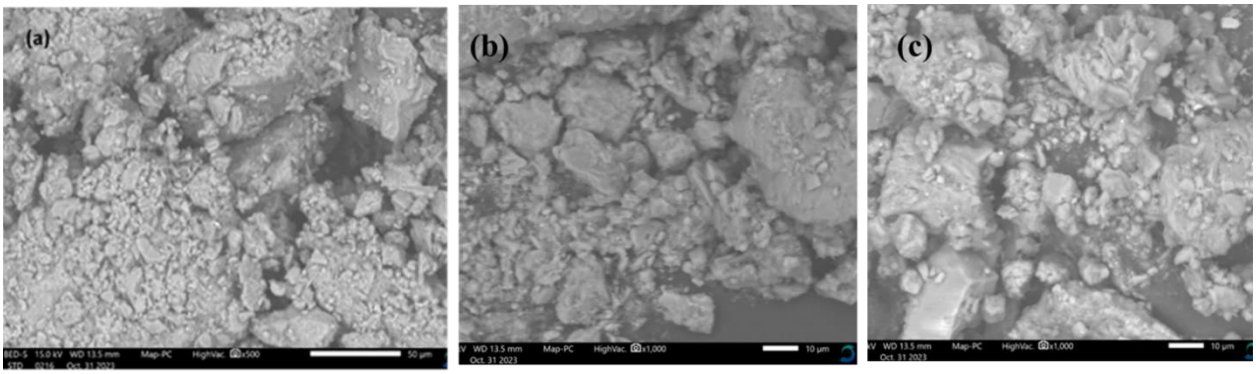

Figure 4. 65: The SEM images of HEU zeolite before (a) after adsorption of (b) chlorpyrifos and (c) imidacloprid

It can be observed that the surface of HEU zeolite after adsorption changed. The cavities of the surface of the HEU zeolite have smoothened due to being filled up by the pesticides. It is evident from SEM images of the two selected pesticides loaded HEU zeolite (Figure 4.65) that their surfaces have become smooth and shiny with less cavities due to the attachment of pesticides after adsorption.

4.9.2 Effects of contact time on adsorption of the selected pesticides onto HEU zeolite

Contact time is one of the most important parameters for practical application. The effect of contact time was studied at 25 ^{0}C. Initial chlorpyrifos and imidacloprid concentration of 4 ppm, and 100 mg adsorbent dosage. Figure 4.66 illustrates how contact time of up to 120 min affects the HEU zeolite's ability to removal chlorpyrifos and imidacloprid from water.

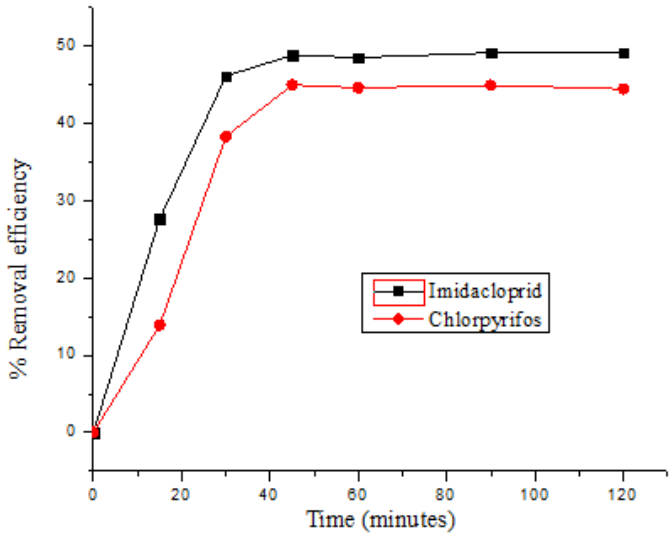

Figure 4. 66: Effect of contact time on the adsorption of imidacloprid and chlorpyrifos onto HEU zeolite

There are a lot of active surface sites available for adsorption at the initial stage. During the first 30 min, there is a rapid accumulation of adsorbates on the zeolite. Then, after 45 min the zeolite attained maximum adsorption capacity for the two pesticides. In both cases, it took 45 minutes to reach equilibrium, suggesting that this was enough time to reach the adsorption equilibrium. Similar results were obtained by Dehghani *et al.,* (2019), who observed that the amount of adsorption is nearly constant and reaches equilibrium after 15 minutes. They also found that the removal efficacy of diazinon by carbon nanotubes improves with a commensurate increase in contact time. Furthermore, similar findings were reported for the removal of trichloroethylene on multiwall carbon nanotubes (Naghizadeh *et al.,* 2011).

4.9.3 Adsorption Kinetics

The mechanism of sorption and potential rate-controlling steps have been studied using kinetic models, which is useful in selecting the optimum operating conditions for the full-scale batch process. Figure 4.67 and Table 4.21 shows that the *pseudo*-first-order and *pseudo*-second order model adequately describes the adsorption kinetics of imidacloprid and chlorpyrifos onto HEU-zeolite.

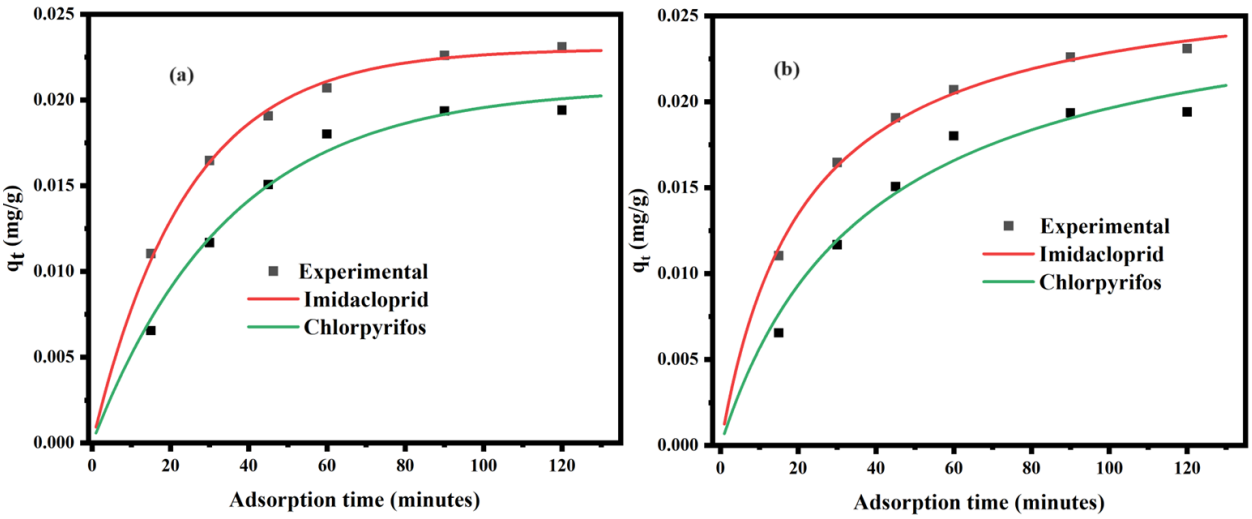

Figure 4. 67: *Pseudo* -first order and b) Pseudo-second order for imidacloprid and chlorpyrifos adsorption onto the HEU zeolite

It may be concluded that the adsorption of imidacloprid and chlorpyrifos is influenced by a variety of parameters, but that interactions between the HEU and these pesticides during physio sorption play a major effect. The greater the k value, the faster the attainment of the equilibrium. Table 4.21 displays the correlation coefficients for the *pseudo*-first and *pseudo*-second orders along with the best fit values of $q_{e,}$ k_1, and k_2. The linear regression correlation coefficient (R^2) was then used to choose the kinetic model that fit the data the best. Regression coefficients R^2 of the *pseudo*-first order kinetic model for imidacloprid and chlorpyrifos, respectively, were found to be 0.9950 and 0.9898, indicating the best fit. For the two pesticides also, pseudo-second order kinetics showed higher R^2 values, suggesting that the removal of the pesticides follow *pseudo*-second order kinetics. The $q_{e,}$ experimental (0.0231 and 0.0194 mg/g) for imidacloprid and chlorpyrifos was closer to the calculated values q_e, (0.0230 and 0.0207mg/g) in the *pseudo*-first order.

Table 4. 21: Calculated kinetic parameters for Imidacloprid and Chlorpyrifos adsorption onto HEU

Model	Parameter	Imidacloprid	Chlorpyrifos
Pseudo first order	$q_{e,}$, exp (mg/g)	0.0231	0.01941
	$q_{e,}$, cal (mg/g)	0.0230	0.0207
	k_1 (min^{-1})	0.0416	0.0286
	R^2	0.9950	0.9898
	χ^2	3.2861 x 10^{-5}	1.5505 x 10^{-4}
	SSE	5.3940 x 10^{-7}	2.0360 x 10^{-6}
Pseudo second order	$q_{e,}$ cal (mg/g)	0.0277	0.0271
	k_2 (g/mg min)	1.7108	0.9716
	R^2	0.9941	0.9749
	χ^2	3.5680 x 10^{-5}	3.7400 x 10^{-4}
	SSE	5.8181 x 10^{-7}	4.9789 x 10^{-6}

Its worthy to note that the R^2 values from the two models sufficiently describe the adsorption of the two pesticides, a higher R^2 and lower χ^2 and SSE values, confirm that adsorption process of these pesticides follow the *pseudo*-first order. This demonstrates that the adsorption of the pesticides is facilitated by both physisorption and chemisorption. Similar finding was reported for simazine, 2, 4-dichlorophenoxyacetic acid and 1, 1'-dimethyl-4, 4'-bipyridinium ion adsorption onto zeolite carbon composites (Andrunik *et al.,* 2023; Pukcothanung *et al.,* 2018)

4.9.4 Intraparticle Diffusion

Figure 4.68 and Table 4.22 show the intraparticle diffusion plot and parameters of imidacloprid and chlorpyrifos removal, respectively.

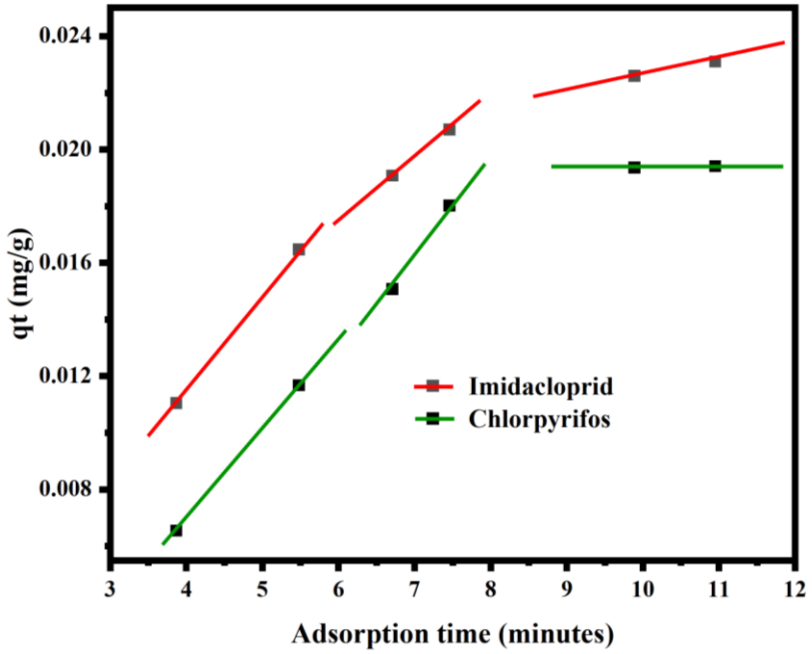

Figure 4. 68: The intraparticle diffusion plot for the removal of imidacloprid and chlorpyrifos by HEU zeolite

Table 4. 22: Intraparticle diffusion parameters of Imidacloprid and Chlorpyrifos onto HEU zeolite.

Model	Parameter	Imidacloprid	Chlorpyrifos
Intraparticle diffusion	K_{id} (mg/g $min^{1/2}$)	0.001594	0.001774
	C_i	0.007051	0.001903
	R^2	0.8659	0.9069
	χ^2	7.3200×10^{-4}	1.4000×10^{-3}
	SSE	1.2064×10^{-5}	1.8520×10^{-5}

From Figure 4.68 and Table 4.22 the initial phase shows a rapid adsorption which is characteristic of boundary or surface adsorption. The second phase exhibit decreased adsorption attributed to attempts of imidacloprid and chlorpyrifos molecules to enter through the smaller pores and channels of the HEU zeolite. While the final step is a plateau region which indicate dynamic equilibrium has been established. Conversely, $Ci \neq 0$ for imidacloprid (0.007051) and chlorpyrifos (0.001903) (Table 4.22) indicates the existence of some degree of boundary layer control, depicting that intraparticle diffusion does not solely govern the rate-limiting step.

The regression lines for the pesticides in Figure 4.68 do not pass through the origin, implying that intraparticle diffusion is not the rate determining step. It was also observed that the adsorption plots were not linear indicating a multi-step mechanism of the adsorption process. Therefore, it can be concluded that the mass transfer of pesticides from the aqueous solution to the HEU surface by bulk and film diffusion could be rate determining step (Bruzzoniti *et al.,* 2016). Similar multi-mechanistic stages have been reported before by Shikuku *et al.,* (2015) during the removal of tebuconazole from aqueous solution using zeolite (Shikuku *et al.,* 2015).

4.9.5 Effect of initial concentration on Pesticide Removal by Adsorption

The effect of initial pesticide concentration on the removal of imidacloprid and chlorpyrifos by HEU zeolite was investigated by varying initial concentrations (2, 2.5, 3.4, 5 and 6 ppm), at an adsorbent dose of 0.1 g and temperature of 25 °C. Figure 4.69 show the effect of initial pesticide concentration of imidacloprid and chlorpyrifos on their adsorption onto HEU zeolite

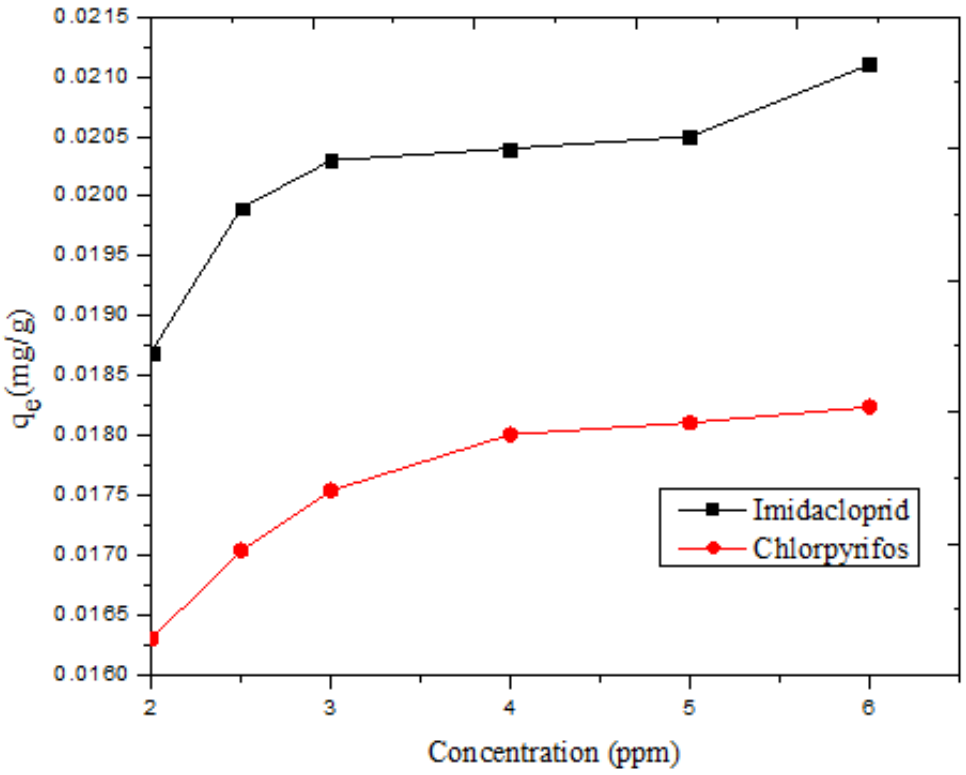

Figure 4. 69: Removal capacity as function of initial concentrations of imidacloprid and chlorpyrifos adsorption onto HEU zeolite

Figure 4.69 show that when the initial concentration is varied from 2 to 6 ppm, imidacloprid removal capacity increased from 0.0187 to 0.0211 mg/g while chlorpyrifos increased from 0.0163 to 0.01824 mg/g. Increase in initial concentration of the two pesticides led to increase in adsorption capacity which slowed down at high concentration. This was due to the reduction in the ratio of the available surface binding sites to the number of the pesticide's molecules in solution since a constant mass of adsorbent has a fixed adsorption site. Furthermore, at higher concentrations the surface attachment sites which had higher affinity for pesticides were fully saturated. Adsorption capacities were found to increase with increased initial pesticides concentration and were fitted in the adsorption isotherms.

The removal of imidacloprid was higher than chlorpyrifos due to its lower molecular mass (255.7 g/mol) compared to chlorpyrifos (350.6 g/mol). This can be credited to the chemical structure of the pesticides and their geometrical fit within the shape of the pores of the adsorbent (Chen *et al.,* 2020)

4.9.6 Adsorption Isotherms

Various adsorption isotherms were used to describe the equilibrium created between the adsorbed pesticides on the HEU's surface and pesticides in solution. The pesticides equilibrium concentration with the quantity of pesticides adsorbed at constant temperature gives the sorption isotherms. To determine the potential adsorption capacity of HEU zeolite toward the investigated pesticides, the experimental data were fitted with Langmuir, Freundlich, Sips and Redlich-Peterson models. The accuracy of the adsorption isotherms was estimated by the correlation coefficient R^2 value. The adsorption isotherms and their parameters are presented in Figure 4.70 and Table 4.24, respectively.

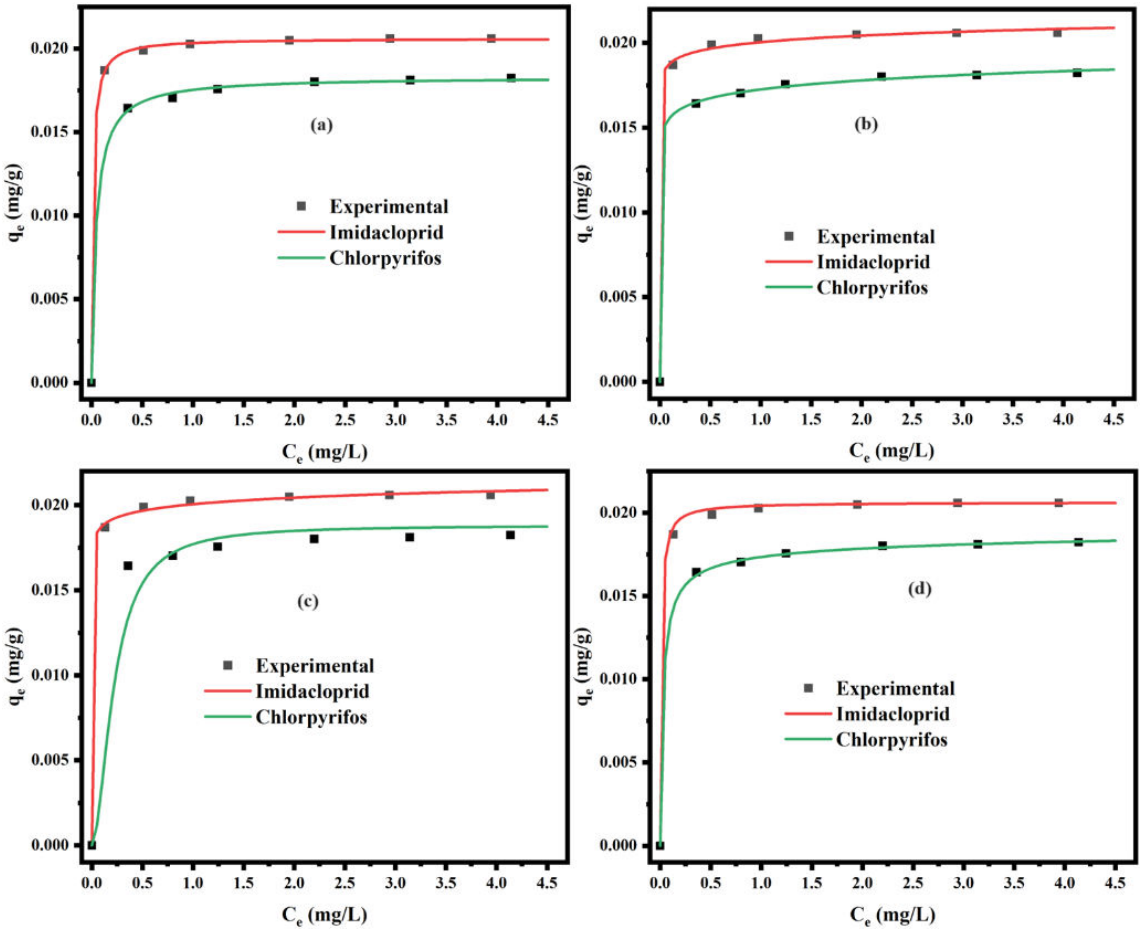

Figure 4. 70: Langmuir isotherm b) Freundlich isotherm, c) Sips isotherm, and d) Redlich-Peterson isotherm models for imidacloprid and chlorpyrifos adsorption over zeolites

Table 4. 23: Parameter and error function data for sorption isotherm models of imidacloprid and chlorpyrifos onto zeolites.

Model	Parameter	Imidacloprid	Chlorpyrifos
Langmuir isotherm	$q_{max\ exp}$ (mg/g)	0.0206	0.0183
	K_L (L mg^{-1})	73.1810	22.4242
	R_L	0.0032	0.0112
	R^2	0.9819	0.9379
	χ^2	2.3869×10^{-6}	8.6478×10^{-6}
	SSE	4.8021×10^{-8}	1.500×10^{-7}
	$q_{max\ cal}$ (mg/g)	0.0206	0.0183
Freundlich isotherm	K_F (mg/g)	0.0201	0.0176
	1/n	0.0277	0.0437
	R^2	0.9081	0.9715
	χ^2	1.1338×10^{-5}	3.9339×10^{-6}
	SSE	2.2490×10^{-7}	6.9670×10^{-8}
	K_F (mg/g)	0.0201	0.0173
Sips isotherm	q_S (mg g^{-1})	0.0414	0.0188
	K_S (L mg^{-1})	0.3230	4.5748
	B_S	0.0538	1.8264
	R^2	0.9171	0.9305
	χ^2	1.0367×10^{-5}	0.000764
	SSE	2.0589×10^{-7}	1.0511×10^{-5}
Redlich-Peterson isotherm	A (Lg^{-1}),	2.0593	0.6966
	B (Lmg^{-1})	100.68	39.15
	B	1	0.9766
	R^2	0.9974	0.9769
	χ^2	3.5031×10^{-7}	3.9597×10^{-6}
	SSE	7.1098×10^{-9}	6.6420×10^{-8}

The Freundlich and Langmuir models are the most widely used adsorption models (Majd *et al.,* 2022). From the linear regression coefficient of determination (R^2) values obtained, the adsorption of Imidacloprid fits best in the Langmuir isotherm. This means that the adsorption of the Imidacloprid onto HEU zeolite forms a mono-layer on the surface of the adsorbent with finite number of identical binding sites. On the other hand, chlorpyrifos fitted on Freundlich model based on having higher R^2 (0.9715) compared to imidacloprid (0.9081). Using HEU zeolite, the maximum adsorption capacity of imidacloprid was greater than chlorpyrifos. From the parameters determined it can be concluded that Langmuir and Freundlich isotherm model are suitable to describe the adsorption mechanism of imidacloprid and chlorpyrifos, respectively. The adsorption of imidacloprid and chlorpyrifos is suitable for monolayer and multilayer process, respectively.

The Langmuir K_L which is used for the quantification of the interaction between adsorbent and adsorbate also had higher values for imidacloprid (73.18) than for chlorpyrifos (22.42). This implies that interaction of imidacloprid and HEU zeolite are more stable compared to the interactions between chlorpyrifos same zeolite. Regarding the separation factor range which were found to be in the range $0 < R_L < 1$, indicating a favorable adsorption process. The regression results shows that Redlich-Peterson isotherm fitted the experimental data better than the others. Since, imidacloprid, the highest R^2 of 0.9974 and the lowest SSE and χ^2 values of 7.1098×10^{-9} and 3.5031×10^{-7}, respectively. For, chlorpyrifos, also correlated the most like for imidacloprid with the highest R^2 of 0.9769 and the lowest SSE and χ^2 values of 6.6420×10^{-8} and 3.9597×10^{-6}, respectively. From the Freundlich parameters, the magnitude of 1/n values of imidacloprid and chlorpyrifos samples were found to be between 0 and 1, this indicates that the interaction between HEU zeolite and

imidacloprid and chlorpyrifos corresponds to physisorption and the interactions were weak.

Based on Giles *et al.* (1974) classification the adsorption of imidacloprid and chlorpyrifos displayed L-type curves where L-shaped stands for Langmuir which in essence is consistent with data in this study fitting more onto Langmuir model. The overall, the equilibrium were described by the isotherms in the order Redlich-Peterson, Langmuir, Freundlich and Sips. All the isotherms give an R^2 of more than 0.90 implying that the adsorption of the two pesticides is multi-mechanistic.

4.9.7 Effect of Adsorbent Dosage on Removal by Adsorption of Chlorpyrifos and Imidacloprid

The adsorbent dosage is also a paramount factor since it indicates the adsorption capacity of an adsorbent in a given initial concentration. Figure 4.71 shows the effect of adsorbent dosage on the removal efficiency of imidacloprid and chlorpyrifos from aqueous solution under the condition of concentration 4 ppm, contact time of 60 min and temperature of 25 °C.

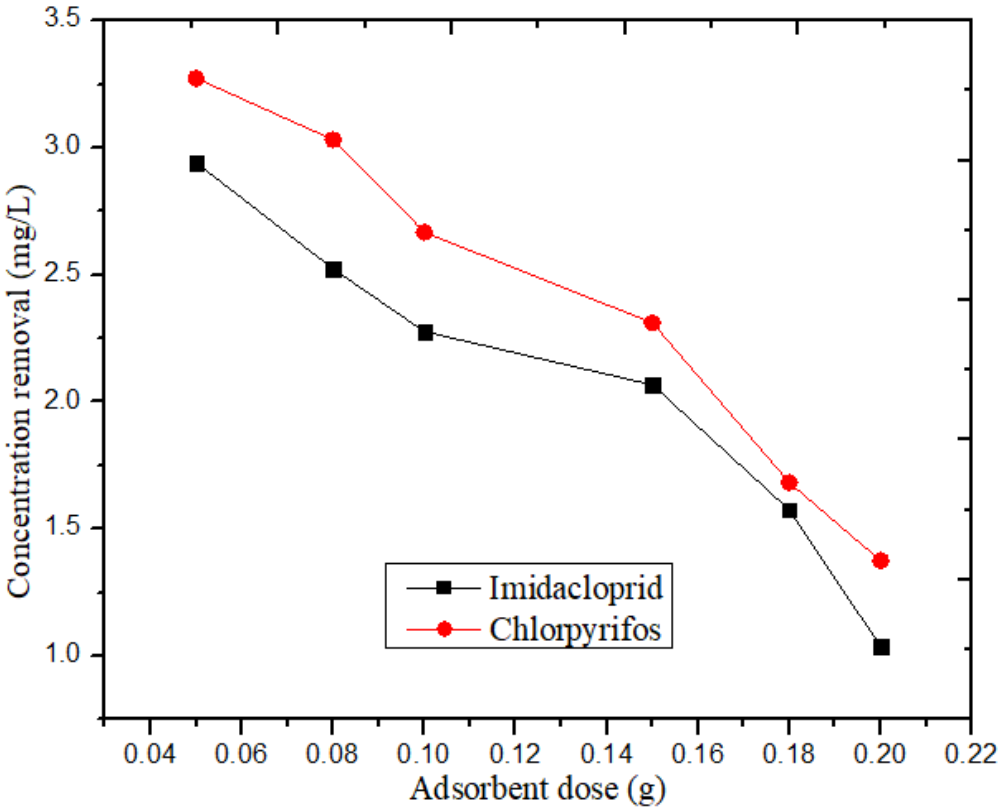

Figure 4. 71: Effect of adsorbent dosage for adsorption of Imidacloprid and Chlorpyrifos using HEU zeolite.

Figure 4.71 shows that the removal of imidacloprid and chlorpyrifos by the zeolite increases with increase in the adsorbent dosage. The removal of imidacloprid is higher than that of chlorpyrifos since molecular weight of imidacloprid (255.66) is lower compared to chlorpyrifos (350.60). The lower molecular mass allows more packing of the pesticides in the HEU zeolite cavities. This can be attributable to increased availability of adsorption active sites and surface area as the adsorbent mass increases for adsorption. This agrees with the findings given by Sou *et al.,* (2019) who reported pesticide removal by activated carbon increased with increase in adsorbent dosage due to availability of surface area for adsorption.

4.9.8 Effect of temperature on the adsorption of selected pesticides

The effect of temperature on the adsorption capacity of imidacloprid and chlorpyrifos were conducted at 298, 313, 333 and 348 K with constant pesticides concentration (4 ppm), adsorbent dosage (100 mg) and contact time (60 min). From the results sorption efficiency of pesticides increased with increase in temperature from 25 to 75 ℃ and results are presented in Figure 4.72.

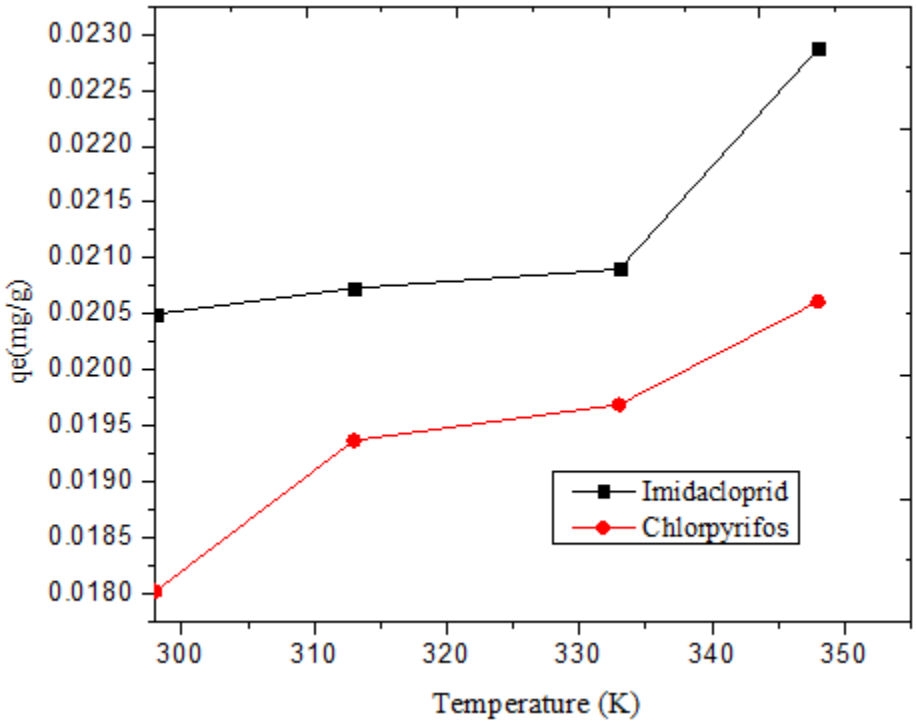

Figure 4. 72: Effect of different temperatures on adsorption capacity of imidacloprid and chlorpyrifos solution

The results show that increase in temperature increases pesticides sorption capacity. It can be due to the increase in collision frequency which increase the pesticides molecules mobility between the molecule and HEU zeolite. The imidacloprid molecules move more quickly in the solution, increasing their efficiency in the adsorption when the temperature

was varied from 25 to 75°C, demonstrating the endothermic character of the process. High temperature increases pesticide mobility and improves the penetration of adsorbed molecules into the internal pores of adsorbent by decreasing solution viscosity, thus promoting adsorption. Similar observation was reported in the study on sorption of glyphosate on natural clay and porous clay heterostructure (Besghaier *et al.,* 2021).

Figure 4.73 show plots of InKc and 1/T of imidacloprid and chlorpyrifos adsorption onto HEU zeolite.

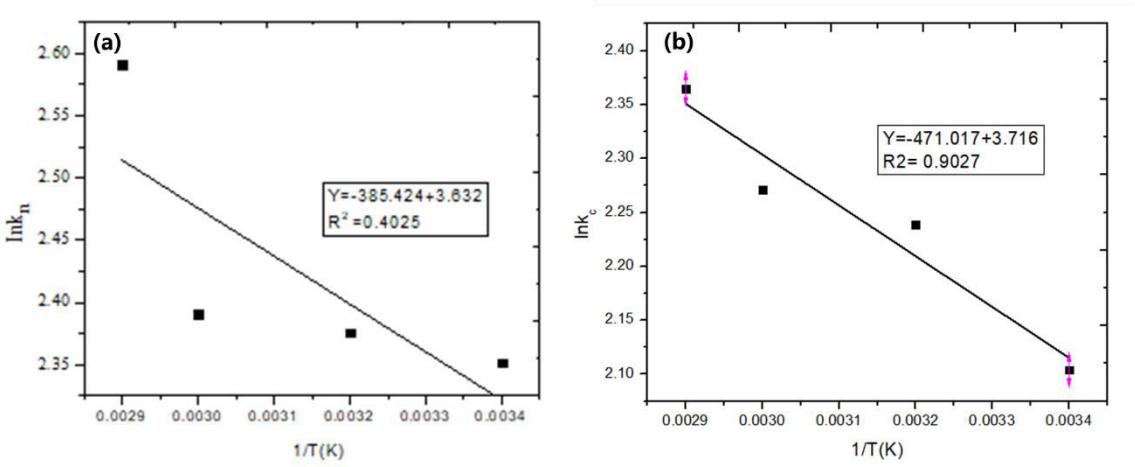

Figure 4. 73: InK_n and 1/T of imidacloprid and chlorpyrifos adsorption onto HEU zeolite.

Table 4. 24: Thermodynamic parameters for imidacloprid and chlorpyrifos adsorption onto HEU

Adsorbate	Temperature (K)	ΔG ($kJmol^{-1}$)	ΔH ($kJmol^{-1}$)	ΔS ($JK^{-1}mol^{-1}$)	Absorbate	Temperature (K)	ΔG ($kJmol^{-1}$)	ΔH ($kJmol^{-1}$)	ΔS ($JK^{-1}mol^{-1}$)
	298	-5.53				298	-5.21		
	313	-6.18				313	-6.09		
Imidacloprid	333	-6.62	3.038	30.196	Chlorpyrifos	333	-6.54	3.916	30.86
	348	-7.50				348	-6.84		

The plot of ln K_c versus 1/T for pesticides provide regression lines that are used to calculate the thermodynamic parameter values. Table 4.24 displays the thermodynamic parameters for adsorption of the two pesticides. Depending on the magnitude of the enthalpy change, the adsorption process can be divided into two categories: chemisorption and physical adsorption. An adsorption process is considered physical if the enthalpy change magnitude is within the range of 5–10 $kJmol^{-1}$, and belongs to chemisorption if it is within the 30-80 $kJmol^{-1}$ range (Besghaier *et al.,* 2021). From the results the ΔH is positive for the two pesticides indicating that adsorption is an endothermic process while the negative ΔG°, indicates that adsorption is a spontaneous process. Furthermore, the low values of ΔG° demonstrates that the adsorption was a spontaneous and a physisorption process, respectively. The decrease in the value of ΔG with increase in temperature indicates that the adsorption process of the pesticides on zeolite is more favorable at high temperatures (Yan *et al.,* 2008). The presence of degree of freedom at the solid-liquid interface during the adsorption process of imidacloprid and chlorpyrifos was indicated by a positive value

of ΔS°. This study aligns with other research reported prior which observed the adsorption process to be spontaneous (Balarak *et al.,* 2015; Tran *et al.,* 2022).

In conclusion the equilibrium data for imidacloprid and chlorpyrifos adsorption were best described by the Freundlich isotherm models with a maximum multi-layer adsorption capacity of 0.0231 and 0.0194 mg/g. The percent removal of imidacloprid and chlorpyrifos by HEU zeolite were 50.25 and 48.43 %, respectively. The adsorption kinetics followed both *pseudo*-first order model indicating both physisorption and chemisorption. The reaction was spontaneous and exothermic.

4.10 Application of Zeolites as Adsorbents for the Removal of pharmaceutical Pollutants from water

The study aimed to investigate the adsorption capacity and performance of natural HEU zeolite in removing diclofenac, ciprofloxacin, and chloramphenicol from water.

4.10.1 Characterization

Figure 4.74 shows the SEM images of HEU zeolites before and after 2 hours contact with pharmaceuticals.

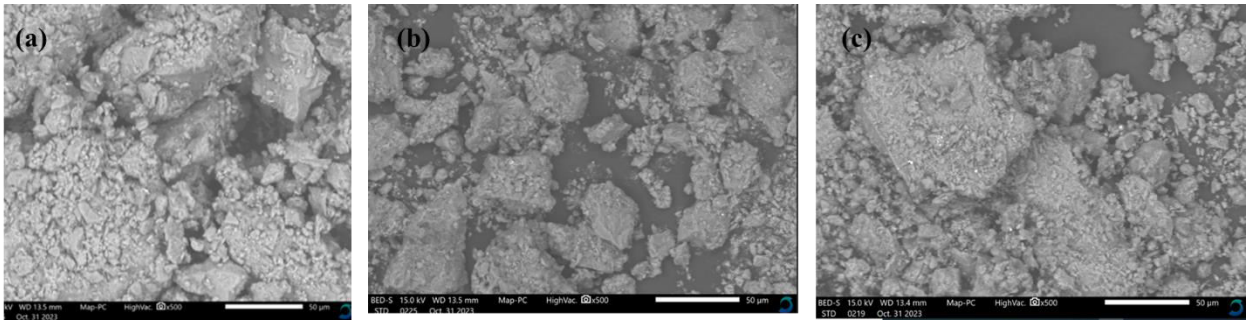

Figure 4. 74: The SEM-micrograph of HEU zeolite before and after adsorption of (a) ciprofloxacin and (b) chloramphenicol

The mineral sample had a fairly uneven structure, with sporadic appearances of macropores all of which had roughened surfaces and some cracks with white spots that might have been caused by pharmaceutical adsorption. Because of the rough surface, the zeolite sticks together and becomes uneven, forming cavities that allow the pharmaceuticals to attach and cause adsorption.

4.10.2 Effects of contact time on adsorption of selected pharmaceuticals by adsorption

Figure 4.75 shows the effect of contact time on removal of diclofenac, ciprofloxacin and chloramphenicol by HEU adsorbent at initial concentration 10 ppm and adsorbent dose of 1 g at the temperature of 25 °C

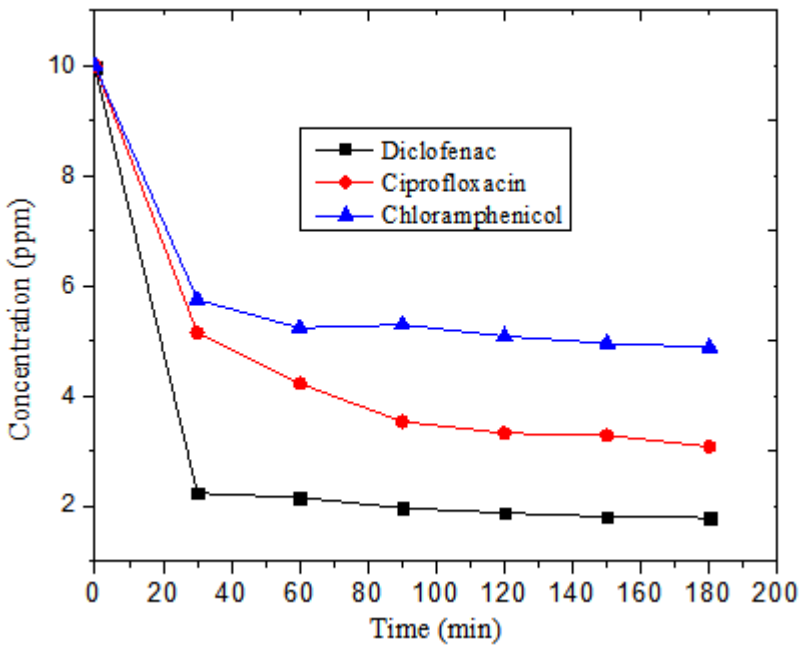

Figure 4.75: The effect of contact time on removal of pharmaceuticals by HEU adsorbent

From Figure 4.75 it was observed that removal of diclofenac, ciprofloxacin and chloramphenicol was high at the initial step within the first 30 minutes of adsorption process. Thereafter, the rate of adsorption slowed down (Wang *et al.,* 2017). In terms of percent removal, diclofenac recorded highest removal (82.3 %), followed by ciprofloxacin (69.2 %) then lastly chloramphenicol (51.2 %) after 180 minutes. Diclofenac has more packing on the surface of the adsorbent because it is a smaller molecule (296.1 g/mol) than ciprofloxacin 331.34 g/mol, which is even smaller than chloramphenicol 323.13 g/mol. Chloramphenicol recorded lower percent removal since it has neutral charge and its more hydrophilic compared to diclofenac and ciprofloxacin which reduces its interaction with the HEU zeolite. It should be noted that the removal rate of adsorbate is rapid initially , but gradually decreases with the contact time until it attains equilibrium due to diminished available active sites onto the adsorbent Also the adsorption sites become exhausted, the rate of removal is controlled by the rate of transport from the exterior to interior sites adsorbent (Liu *et al.,* 2013; Wang *et al.,* 2018).

4.10.3 Kinetics of Adsorption of the Pharmaceuticals and Model Fittings

The kinetic dynamics data for diclofenac, ciprofloxacin and chloramphenicol onto heulandite was analyzed using two nonlinear kinetic models, *pseudo*-first-order model, *pseudo*-second-order model and intraparticle diffusion model. At the onset, when all the adsorption sites are vacant, HEU zeolite had the highest initial adsorption rate due to the highest number of accessible sites. With time, however, the equilibrium was attained as all the binding sites were saturated, and their after, the equilibrium shifted towards desorption. The results of the kinetic modeling are displayed in Figures 4.76 and the kinetics constants are shown in Table 4.25,

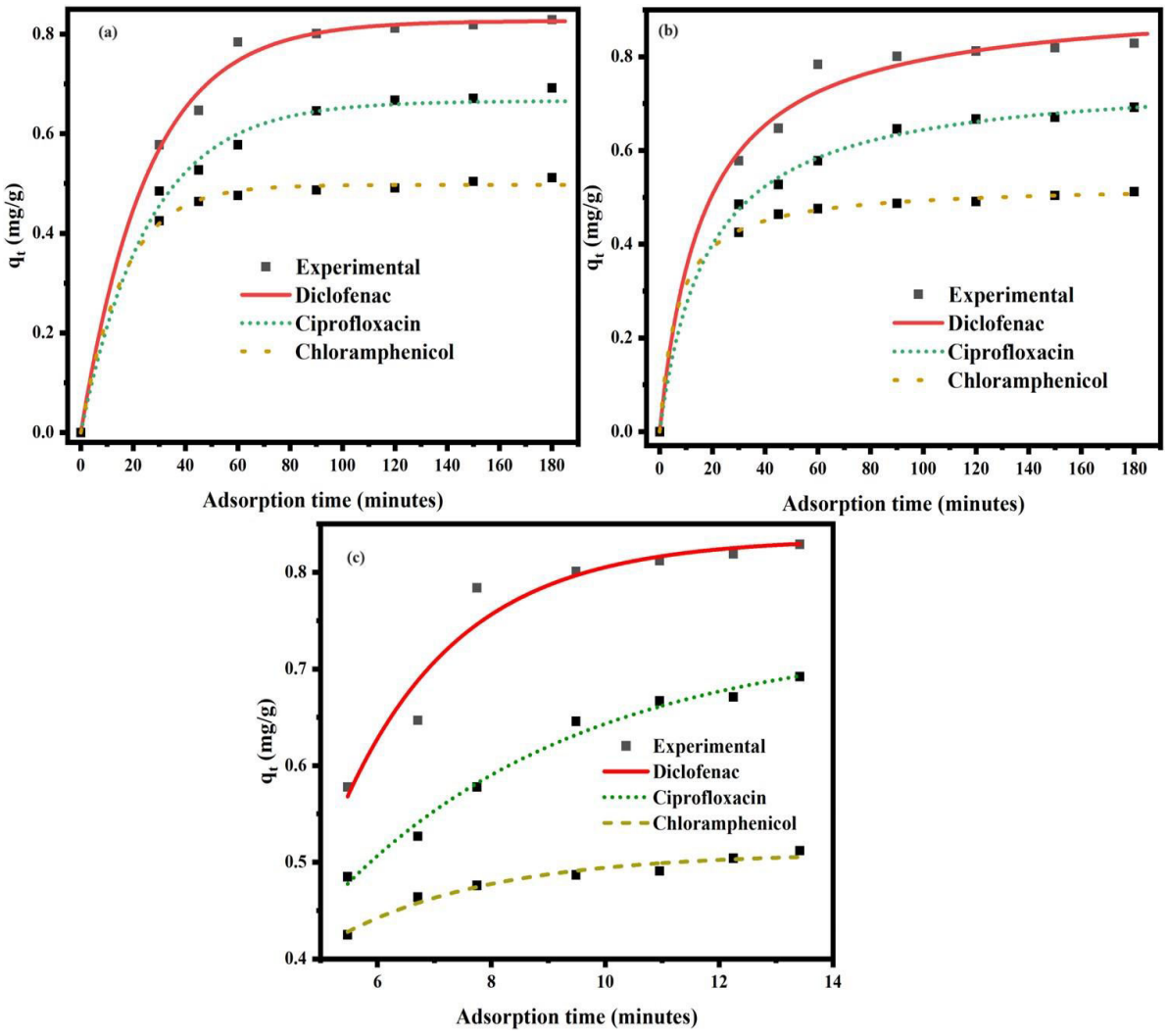

Figure 4. 76: Nonlinear plots of experimental data for the selected pharmaceutical adsorption onto HEU zeolite, (a) *Pseudo* first order, (b) *Pseudo* second order, and (c) Intraparticle diffusion models.

The applicability of the model to describe the kinetics was decided based on the closeness between experimental $q_{e,}$, exp and model calculated ($q_{e,}$, cal) equilibrium adsorption capacities using the R^2, χ^2 and SSE.

Table 4. 25: The calculated parameters for the *Pseudo*-first-order, *Pseudo*-second- order and intraparticle kinetic models for adsorption of pharmaceuticals onto 1.0 g heulandite zeolite adsorbent.

Model	**Parameter**	**Diclofenac**	**Ciprofloxacin**	**Chloramphenicol**
Pseudo-first order	$q_{e,}$, exp (mg/g)	0.8291	0.6923	0.5121
	$q_{e,}$, cal (mg/g)	0.8265	0.6657	0.4973
	k_1 (min^{-1})	0.0389	0.0375	0.0619
	R^2	0.9485	0.9902	0.9461
	χ^2	4.0191×10^{-3}	4.7095×10^{-3}	9.9731×10^{-4}
	SSE	2.864×10^{-3}	1.8676×10^{-3}	4.8815×10^{-4}
Pseudo-second order	$q_{e,}$ cal (mg/g)	0.9251	0.7612	0.5267
	k_2 (g/mg min)	0.0653	0.0723	0.2788
	R^2	0.8906	0.9830	0.9698
	χ^2	7.7377×10^{-3}	1.1470×10^{-3}	3.1895×10^{-4}
	SSE	5.5795×10^{-3}	6.5011×10^{-4}	1.5210×10^{-4}
Intraparticle diffusion	K_d (mg/g $min^{1/2}$)	0.0290	0.02917	0.0092
	C_d	0.4791	0.3398	0.3928
	R^2	0.6592	0.8552	0.85608
	χ^2	2.1073×10^{-2}	5.4000×10^{-3}	1.4020×10^{-3}
	SSE	1.4933×10^{-2}	1.9825×10^{-3}	6.3700×10^{-4}

The kinetic results showed that the *pseudo*-first order model was suitable for describing the diclofenac and ciprofloxacin adsorption onto heulandite adsorbent, since they have higher correlation coefficient, R^2 (0.9485 and 0.9902, respectively). In addition, the *pseudo*- first order model calculated and experimental qe values are almost the same for diclofenac and ciprofloxacin. Chloramphenicol fitted best on *pseudo* second order recording R^2 value of 0.9698. The adsorption of diclofenac and ciprofloxacin onto HEU zeolite implied that adsorption is physical process. On the other hand, since the adsorption of chloramphenicol onto the HEU zeolite can be described by *pseudo*-second order kinetics, it implies the adsorption process is a chemical process. The results were in accordance with results presented in the literature regarding adsorption of pharmaceutical onto the adsorbent (Tran *et al.,* 2022). Therefore, the *pseudo*-first order was suitable for describing diclofenac and ciprofloxacin while *pseudo*-second order described chloramphenicol adsorption onto HEU zeolite. The coefficient of determination of intraparticle diffusion model was lower compared to *pseudo* first and second models. Also, none of intraparticle diffusion plots passed through the origin, indicating that this mechanism is not the rate limiting step of adsorption process (Shikuku *et al.,* 2015).

4.10.4 Effect of Initial Concentration of Pharmaceuticals Removal onto Heulandite

In the current study, the experiments were done at different initial concentration (5, 10. 15, 20, 30 and 40 mg/L) to determine the effect of initial diclofenac, ciprofloxacin and chloramphenicol concentrations on percent removal efficiency. Figure 4.77 shows effect of initial concentration on the adsorption of the selected pharmaceuticals onto the HEU zeolite.

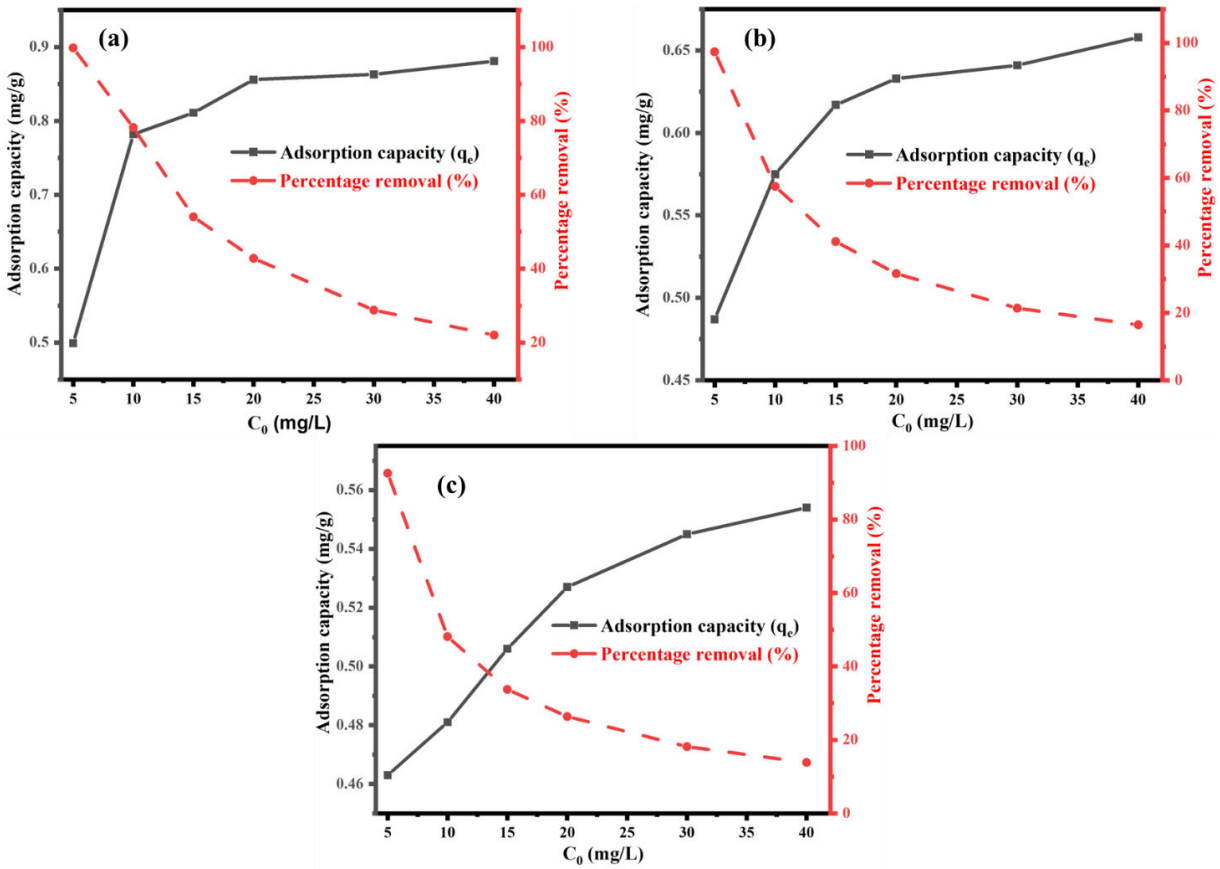

Figure 4. 77: Adsorption capacity and percentage removal for adsorption of (a) Diclofenac, (b) Ciprofloxacin, (c) Chloramphenicol by HEU zeolite

The adsorption of diclofenac, ciprofloxacin and chloramphenicol decreases from 99.8, 97.4 and 94.6% to 22.03, 16.45 and 13.85 % on increasing the initial pharmaceutical concentration from 5 to 40 ppm. From the Figure 4.85 the percent removal efficiency of diclofenac, ciprofloxacin and chloramphenicol decreased from 5 to 40 mg/L, while the adsorption capacity increased with increase in initial concentration. According to Figure 4.77, there is a high adsorption removal at low concentrations because the active sites and surface area is substantial, and the pharmaceutical molecules were easily adsorbed and removed. On the other hand, at high initial concentration, the removal percentage efficiency decreases since the total available adsorption binding sites are limited, thus

resulting in a decrease in percentage removal of the pharmaceuticals. Moreover, higher force to overcome the various mass transfer resistances of the pharmaceuticals from the aqueous solution to the solid phase resulting in higher probability of collision between the pharmaceuticals and the active sites (Avcu *et al.,* 2021). According to Abbas *et al.,* (2017), the observed that there is an increase in adsorption capacity onto activated onion skin by increasing initial concentration of diclofenac and (Abbas *et al.,* 2017). Besides, Fernandez *et al.,* (2015) reported that that at an initial concentration of 40 mg/L, there were more pollutants adsorbed onto activated carbon from orange peels than there were at 5 mg/L. Therefore, the higher the initial concentration of pollutants, the higher amounts of pharmaceuticals adsorbed onto the adsorbent (Fernandez *et al.,* 2015).

4.10.5 Adsorption Isotherm

The adsorption of diclofenac, ciprofloxacin and chloramphenicol onto HEU adsorbent in batch experiment were conducted with initial concentrations in a range (5 to 40 mg/L) with adsorbent dose (1.0 g) at 298 K in order to determine the isotherms constants for the non-linearized Langmuir, Freundlich, Sips and Redlich-Peterson models. Plotting the solute adsorbed (qe) against the solute's equilibrium concentration (Ce) yielded the adsorption isotherms. The data on adsorption equilibria were examined, and the coefficient of determination (R^2) was used to evaluate the models' feasibility (Table 4.28). The non-linearized Langmuir, Freundlich, Sips and Redlich-Peterson adsorption isotherms for diclofenac, ciprofloxacin and chloramphenicol sorption onto HEU adsorbent are presented in Figures 4.78.

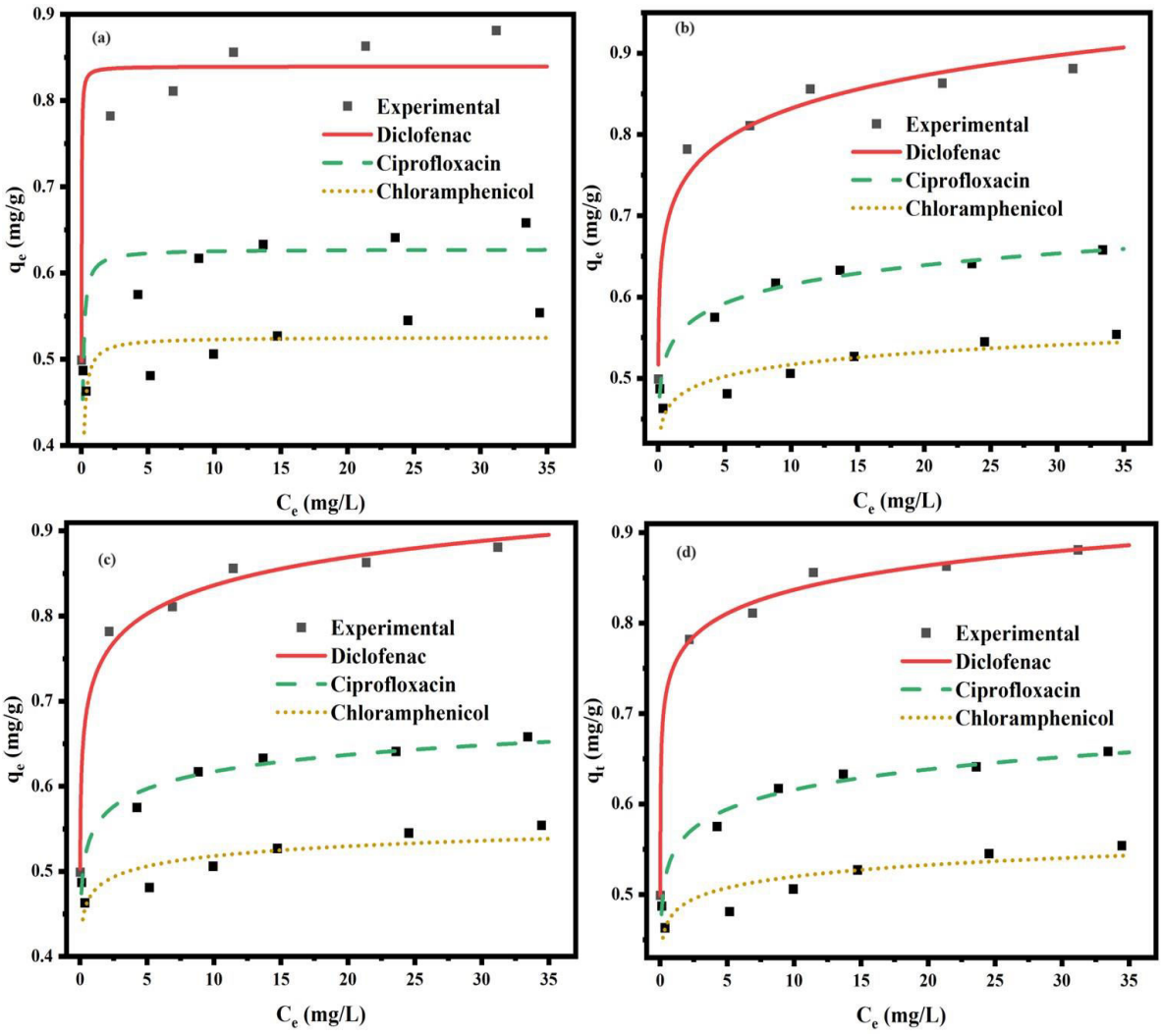

Figure 4. 78: a) Langmuir isotherm b) Freundlich isotherm, c) Sips isotherm, and d) Redlich-Peterson isotherm models for diclofenac, ciprofloxacin and chloramphenicol adsorption onto HEU zeolite

Table 4. 26: Parameter and error function data for sorption isotherm models of diclofenac, ciprofloxacin and chloramphenicol onto the HEU zeolite

Model	Parameter	diclofenac	Ciprofloxacin	Chloramphenicol
Langmuir isotherm	q_{max} (mg/g)	0.8396	0.6276	0.5257
	K_L (L mg^{-1})	145.9896	26.1453	18.7648
	R_L	0.0068	0.0038	0.0053
	R^2	0.9341	0.7867	0.9389
	χ^2	7.596 x 10^{-3}	5.6187 x 10^{-3}	5.98 x 10^{-3}
	SSE	6.368 x 10^{-3}	3.503 x 10^{-3}	3.0122 x 10^{-3}
	q_{max} (mg/g)	0.7819	0.6018	0.5127
Freundlich isotherm	K_F (mg/g)	0.7099	0.5421	0.4696
	1/n	0.0689	0.0549	0.04158
	R^2	0.9775	0.9872	0.9827
	χ^2	2.9881 x 10^{-3}	4.4956 x 10^{-4}	2.8381 x 10^{-3}
	SSE	2.2093 x 10^{-3}	2.5097 x 10^{-4}	9.22x 10^{-4}
	K_F (mg/g)	0.7822	0.6018	0.5127
Sips isotherm	q_S (mg g^{-1})	1.4442	0.9263	0.6882
	K_S (L mg^{-1})	1.0273	14.1048	44.2159
	n_S	0.1367	0.1399	0.1326
	R^2	0.9919	0.9779	0.9757
	χ^2	1.0367 x 10^{-3}	7.02 x 10^{-4}	2.431 x 10^{-3}
	SSE	2.0589 x 10^{-4}	4.1888 x 10^{-4}	1.252 x 10^{-3}
Redlich-Peterson isotherm	A (Lg^{-1}),	270.9731	308.1909	896.7064
	B (Lmg^{-1})	235.4325	563.461	1869.7951
	B	0.9546	0.9484	0.9651
	R^2	0.9966	0.9846	0.9771
	χ^2	4.1656 x 10^{-4}	4.8355 x 10^{-4}	2.1609 x 10^{-3}
	SSE	3.4757 x 10^{-4}	2.902 x 10^{-4}	1.114 x 10^{-3}

From the nonlinear fits of the applied isotherm models and parameters in Table 4.26, it can be observed that the adsorption of diclofenac, ciprofloxacin and chloramphenicol onto HEU zeolite is better described by Freundlich isotherm model since the value of the coefficient (R^2) were high (0.9775, 0.9872 and 0.9827, respectively), compared to Langmuir. This may be due to the fact that the HEU zeolite has heterogenous surfaces and

thus the pharmaceutical molecules have multiple adsorption sites. Also, the exponent β (from Redlich Peterson isotherm) is not equal to 1 indicating that the adsorption of the three pharmaceuticals are likely to follow the Freundlich model than Langmuir model. However, in relation to error functions it was observed that the experimental data fitted well Freundlich model. From the Freundlich model parameters, the magnitude of (n) for diclofenac, ciprofloxacin and chloramphenicol demonstrates the favourability of adsorption process. Further 1/n (0.0689, 0.0549 and 0.0416) is less than 1 for diclofenac, ciprofloxacin and chloramphenicol adsorption onto HEU zeolite, respectively, indicating weak adsorbate-adsorbent forces corresponding to an overall physisorption (Shikuku *et al.,* 2020). Furthermore, the adsorbent surface's heterogeneity is indicated by the value of ns; the closer the value is to zero or value lower than 1, the more heterogeneous the surface hence its heterogeneous adsorption. The calculated values of R_L for diclofenac, ciprofloxacin and chloramphenicol are 6.8 x 10^{-4}, 3.8 x $10^{-3}$and 5.3 x 10^{-3}, respectively. This show that in all the cases, R_L values fall between 0 and 1, indicating favourable adsorption (Mouni *et al.,* 2018).

4.10.6 Effect of adsorbent dose on pharmaceuticals removal onto HEU zeolite

The amount of adsorbent in the adsorption system determines the number of available binding sites and exchanging molecules for the adsorption. As a result, by increasing the adsorbent dose, the adsorption capacity of an adsorbent at a given initial concentration demonstrated an increase of sorption percentage. Figure 4.79 illustrates the removal efficiency of diclofenac, ciprofloxacin, and chloramphenicol molecules from an aqueous solution having fixed initial concentration of 10 mg/L at varying HEU zeolite amounts (0.2– 2 g) at a constant temperature of 25℃.

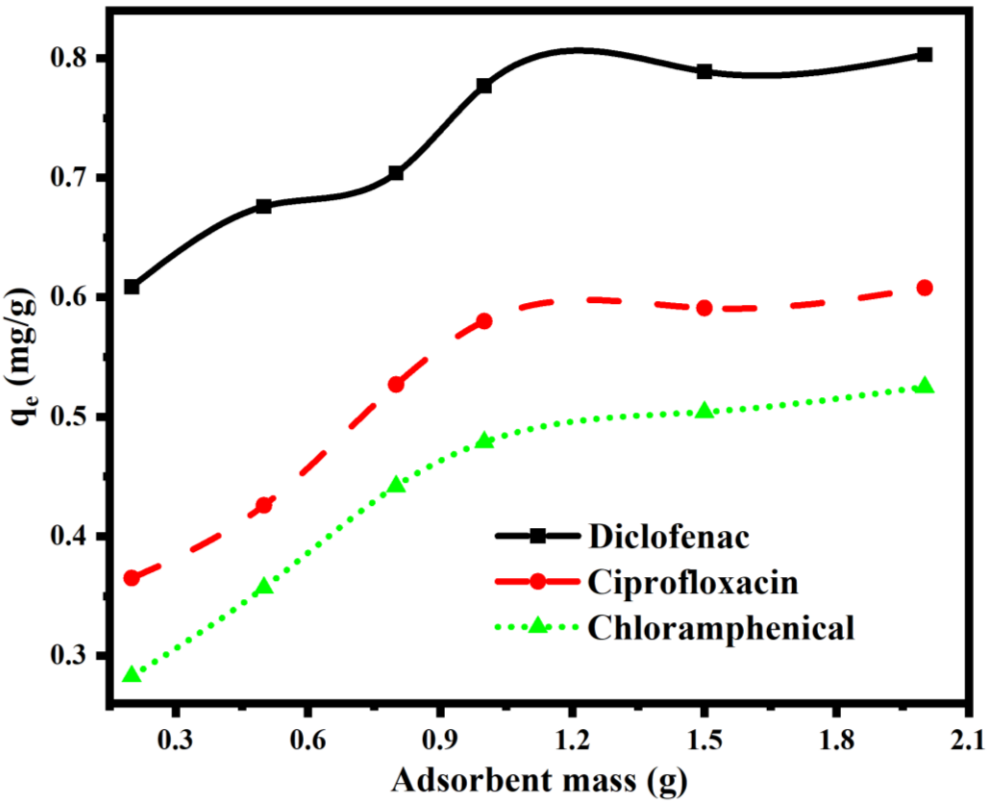

Figure 4.79: Effect of adsorbent dose on diclofenac, ciprofloxacin and chloramphenicol adsorption capacity.

It was observed that the percent removal of the three pharmaceuticals by the heulandite zeolite increases with an increase in the adsorbent dose up to 1.2 g. This can be attributable to increased availability of adsorption binding active sites and surface area as the adsorbent mass increases (Derikvand *et al.,* 2019; Zeng *et al.,* 2021). Further increase in adsorbent dose (beyond 1.2 g) reduced adsorption capacity due to aggregation of the adsorbent thus reducing the surface area available for adsorption This result agrees with the report given by Ngeno and coworkers (2019) who reported removal of caffeine and ciprofloxacin by zeolite which increase with increase in adsorbent dosage due to availability of surface area for adsorption (Ngeno *et al.,* 2019).

4.11 Removal of selected pharmaceutical from environmental wastewater sample

To apply the obtained optimal conditions for the removal of selected pollutants by the HEU zeolite from environmental wastewater samples.

4.11.1 Selectivity of the Method

The selectivity of the method refers to the extent to which a particular analyte can be determined in a complex mixture without interference from other matrix components (Sahoo *et al.,* 2018; Vessman *et al.,* 2001). This was done for the pesticides and pharmaceutical compounds studied. This was verified by comparison of the chromatograms obtained from samples with known concentration of the standard and those samples free from pollutants. Blanks samples did not present any peak at the retention time of the pharmaceuticals and pesticides standards. Moreover, the chromatograms of the pharmaceuticals and pesticides standards and sample extracts presented satisfactory chromatographic resolution. Chromatograms of some of the studied pollutants are shown in Figure 4.80 and 4.81. The peaks for ciprofloxacin and chloramphenicol at retention time of 1.3 and 2.7 minutes, respectively. The peaks for chlorpyrifos and imidacloprid occurred at retention time 7.97 and 2.7 respectively

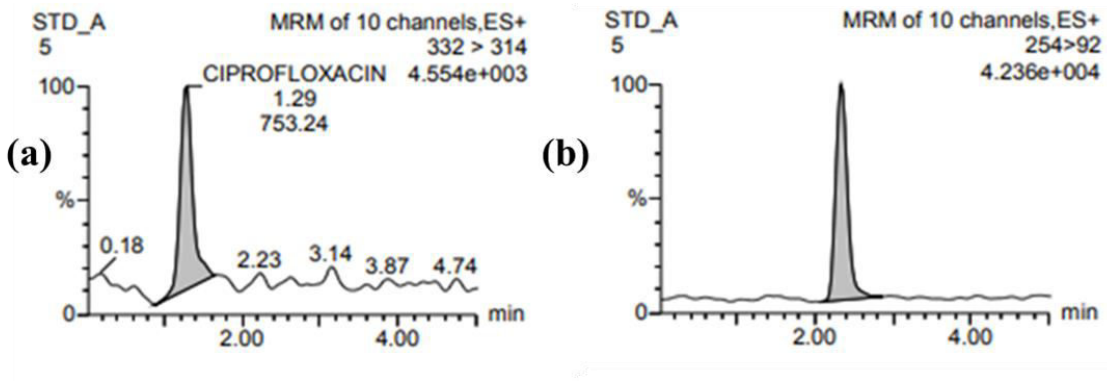

Figure 4. 80: The LC chromatogram of (a) ciprofloxacin, (b) chloramphenicol standards.

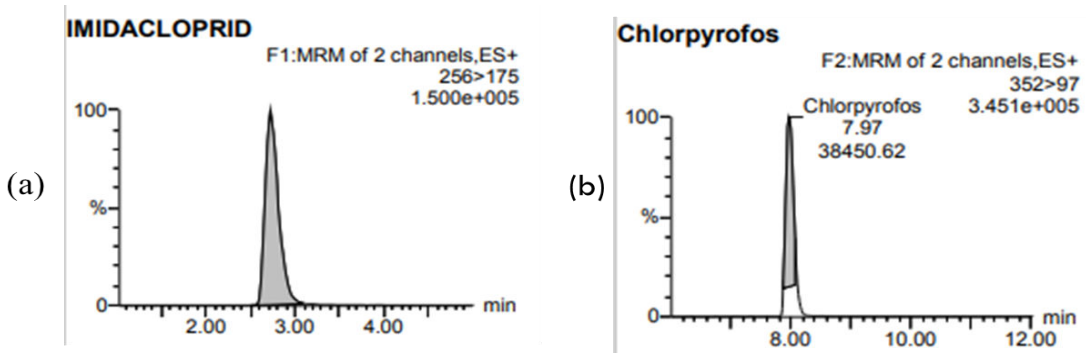

Figure 4. 81: The LC chromatogram of (a) Imidacloprid and (b) Chlorpyrifos standards.

These standards peaks were used to identify the peaks of the analytes in the extracted samples.

For real water analysis the standard solutions of selected pesticides (imidacloprid and chlorpyrifos) were 20, 50, 100, 200, 300, 400, 600 ppb, were prepared by serial dilution from the 4 ppm standard stock solution of imidacloprid and chlorpyrifos into 25 mL volumetric flasks and diluting to the mark with water solution. The linear equations and regression coefficients of the pesticides are shown below in Table 4.27.

Table 4. 27: Linear equations and regression coefficients (R^2) obtained for Imidacloprid and chlorpyrifos

Pesticides	Regression equation (Y)	Regression coefficient (R^2)	LOD ppb
Imidacloprid	y=42.5601x+ 246.172	0.999	<0.1
Chlorpyrifos	y = 65.4198x -649.065	0.997	<0.1

Regression coefficient (R^2) ranged between 0.997 and 0.999 with most analyte giving a regression coefficient of determination ($R^2 \geq 0.99$) which were adequate for residues analysis as reported by Ouma *et al.* (2021). All the limit of detection values were 0.1 which were below the maximum residue limits (MRLs) of the respective pesticides. For real water samples, the correlation coefficients (R^2) obtained was above 0.99 (R^2>0.99) and the equations of the lines y=163.377x + 49.1311 and y= 1705x + 1732.21 for ciprofloxacin and diclofenac respectively, were used for quantification of the compounds in the real water samples. The correlation coefficients (R^2) obtained was above 0.99 which showed a good linearity of the detector response within the specified ranges making the calibration curve useful for quantification.

4.11.2 Detection and quantification limits

Limit of detection (LOD) and limit of quantification (LOQ) are the two important performance characteristics used in method validation for this work. Method detection limit was set at a signal-to-noise ratio of the sample in the sample chromatograms. In this study, the limit of detection was the injected amount in terms of volume that resulted in a peak with a height at least three times as high as the baseline noise level. The Quantification limit of the target chemicals was evaluated for each sample based on the average blank concentrations plus five times the standard deviation of the blanks.

Also, the detection and quantification limits of the two pharmaceuticals analyzed are shown Table 4.28.

Table 4. 28: Detection and quantification limits of pharmaceuticals analyzed.

Pharmaceuticals	limit of detection µg/mL	Limit of Quantification µg/mL
Ciprofloxacin	0.05 ± 0.001	0.01 ± 0.002
Diclofenac	0.02 ± 0.001	0.01 ± 0.001
Chloramphenicol	0.01 ± 0.001	0.01 ± 0.001

4.11.3 Analysis of Environmental Wastewater Samples for Pharmaceuticals

The samples were collected from Kisumu wastewater treatment plant at Kisat. The residue levels of the pharmaceutical of interest was determined by LC-MS/MS. Out of the three pharmaceuticals, only ciprofloxacin was found at a concentration of 2771.4µg/L. The high concentrations of this antibiotics in the raw wastewater are likely to be present due to the high levels of pharmaceuticals consumption rate. The findings of this study are consistent with other studies where high concentrations of pharmaceuticals have been found in wastewater. Higher ciprofloxacin concentrations were reported in Italy (630 ng L^{-1}) (10) and Spain (2200 ng L^{-1}). The study by Gracia-Lor and coworkers, (2012) detected pharmaceuticals in the influents of urban wastewater sample with salicylic acid having the highest concentration (276.7 ng mL^{-1}) (Gracia-Lor et al*.,* 2012). The greatest concern is the antibiotics which is not surprising, may be due more intense use of antibiotics. The health risks associated with exposure to a large number of pharmaceuticals, even at low concentrations, cannot be ignored. Hence the effluents are a big concern because are they are point sources of pollutants to the receiving waters that act as habitants for aquatic organisms and may find their way into drinking waters. This clearly indicates that the current wastewater treatment plants are ineffective in removing pollutants.

4.11.4 Removal of pharmaceuticals from wastewater by the HEU zeolite

Adsorption of ciprofloxacin was studied at a constant heulandite zeolite dose of (1.0 gram). Table 4.29 presents the results obtained from the study of pharmaceuticals removal before and after 120 minutes time.

Table 4. 29: Percentage removal of ciprofloxacin by HEU zeolite

Initial concentration (µg/L)	Concentration of remaining in solution(µg/L) after 120 min	Ciprofloxacin percent removal (%)
2771.4	27.32	99.01

The concentration of ciprofloxacin decreased from 2771.4 µg/L to 552.6 µg/L within the first 30 min then further decreased to 27.32 µg/L after 120 min. This translates to 99.01 % removal after 120 minutes. The LC-MS/MS results indicate that the HEU zeolite has a high adsorption capacity for ciprofloxacin.

4.12 Removal of Selected Pesticides from Wastewater

It is important to note that contamination of water due to a wide range of toxic heterocyclic molecules is a serious environmental problem owing to their organisms' toxicity. Hence, there is urgent need to improve on technologies that can remove such toxic pollutants from wastewaters. Recently, adsorption on heulandite adsorbent is becoming more popular method for the removal of pollutants from the wastewater.

The initial concentration of imidacloprid and chlorpyrifos in the water samples were 75.6 and 600 ppb, respectively. The 0.1 g HEU zeolite reduced imidacloprid from its initial

concentration of 75.6 ppb to 10.1 ppb after 60 minutes at 25 °C representing a 86.6 % removal. After 60 min, the concentration of chlorpyrifos reduced from 600 to 180 ppb representing a percent removal of 70%. This implies that the adsorbent surface has higher affinity for the pesticides, which makes it good material for removal of pesticides. The results are satisfactory and therefore the method was reliable and can be used to remove pesticides in environmental water samples.

CHAPTER FIVE

CONCLUSION AND RECOMMENDATIONS

5.1 Conclusions

- According to the molecular simulation results, only the zeolites with high diameter pores exhibited appreciable loading of the Pb^{2+} and Cd^{2+} these were CLO, FAU, PAU, TSC, LTA LTN, and MWF. CLO exhibited the L-shape isotherm with maximum loading and a pronounced inflection at a maximum loading of 728 lead (II) ions per unit cell. On the other hand, MWF exhibited the highest loading of 440 cadmium (II) ions. Machine learning showed that, total energy is most important parameter which is in agreement with molecular simulation results for the best performing zeolite structures showed negative values, thus an exothermic process. It is seen that the adsorption energy of the cations on the zeolite framework is directly related to the loading capacity, whereby a trend of $Pb^{2+} > Cd^{2+}$. Experimental results indicate that the maximum adsorption for the two ions onto Heulandite (HEU) zeolite occur at pH 6 and after 240 minutes of contact time. The percentage removal of Pb^{2+} and Cd^{2+} ions were 97.7 % and 76.6 %, respectively. The adsorption of the two cations Freundlich and Sips isotherm models and the *pseudo*-first order predicting physisorption.
- Furthermore, the BE at the BCPs for the Pb-HEU complex was -188.88 kcal/mol and -148.72 kcal/mol for the Cd-HUE complex. The stronger binding energy of the interaction between Pb and HEU provides a rationale for Pb's greater percent weight capacity on the zeolite compared to Cd, as shown by the experimental results. The results suggest that different excitation types contribute differently to the stabilization energy and charge transfer in these complexes, with the Cd-HEU complex showing

a higher degree of stabilization than the Pb-HEU complex. These findings could have implications for understanding the properties and behavior of these complexes in environmental remediation. This study shows that the doped or modified HEU zeolite shows high sorption ability toward all cations studied. This suggests that the modified zeolite has the potential to effectively adsorb different cations. Meanwhile, being locally available, and freely abundant with a considerably high adsorption capacity, natural zeolite is an attractive choice for removing metal ions from wastewater

- A screening process involving an initial selection of zeolites based on the pore-limiting diameter was done and it was found that. CLO, LTN, MWF, TSC, ITV, PAU, FAU and DFO zeolites are the best performing in terms of loading. Overall cavity diameter, mass and accessible pore volume are the three most important parameters in the removal of nitrates and phosphates from water.
- Using experimental techniques, the potential of heulandite (HEU) zeolite for the removal of PO_4^{3-} and NO_3^- ions from wastewater in batch mode was explored. The adsorption of PO_4^{3-} and NO_3^- onto the HEU zeolite follows the Freundlich isotherm model. The percentage removal of PO_4^{3-} and NO_3^- was 59.15 and 51.39 %, respectively, whereas the corresponding maximum adsorption capacity of the adsorbent was 0.0236 and 0.0206 mg/g. The adsorption kinetics of both anions by HEU fitted well in the *pseudo*-first order (PFO) kinetics model indicating a physisorption-mediated rate-determining step. It was revealed that the adsorption process was multi-mechanistic spontaneous and exothermic.

- The CLO zeolite was the most suitable for the adsorption of diuron, imidacloprid and chlorpyrifos compared to other zeolite structures. Diuron had the highest stability, with an energy gap of 5.30 eV, followed by imidacloprid (4.83 eV) and chlorpyrifos (4.19 eV). Also, sorption of chlorpyrifos and imidacloprid were the most favorable on the CLO zeolite with more stable and lowest energy value compared to diuron based on the binding energy.
- Furthermore, the adsorption of imidacloprid and chlorpyrifos adsorption were best described by the Freundlich and Langmuir isotherms with a maximum multi-layer adsorption capacity of 0.0231 and 0.0194 mg/g ie. percentage removal of 50.25 and 48.43 %, respectively. The adsorption kinetics followed both pseudo- *first* order and *second* order kinetic models indicating both physisorption and chemisorption. The reaction was spontaneous
- According to the molecular simulation results, CLO zeolite has proved to be the satisfactory zeolite suited for adsorption of diclofenac, ciprofloxacin and chloramphenicol, since its structure has more adsorption sites. The most stable adsorbed configurations of the adsorbed pollutants on the CLO zeolite showed that diclofenac, ciprofloxacin and chloramphenicol molecules get adsorbed at the pores with reasonably high adsorption energies (−78.23, −173.68 and − 84.46 kcal/mol for diclofenac, chloramphenicol and ciprofloxacin, respectively). The larger adsorption energy at the pores appears due to the strong electrostatic interactions between the symmetric, electron-rich pore. Thus, these simulations have proven to be very useful for the initial screening of adsorbents, prior to experimental work. This screening has

considerable potential that can lead to the development of new remediation techniques for wastewater treatment.

- Onto the HEU zeolite, the maximum adsorption capacity of diclofenac, ciprofloxacin and chloramphenicol was 0.7099, 0.5421and 0.4696 mg/g with corresponding percentage removal of 82.3, 69.2 and 51.2 %, respectively. The equilibrium data of diclofenac, ciprofloxacin and chloramphenicol were best described by Freundlich and Sips isotherm models. The kinetics followed *pseudo*-first order for diclofenac and ciprofloxacin, while *pseudo*-second order for chloramphenicol predicting physisorption and chemisorption, respectively.
- The HEU zeolite recorded 99.02 % removal of ciprofloxacin from real water. It was also effective in removing imidacloprid and chlorpyrifos from environmental water samples with percent removal of 86.6 and 70.13 %, respectively.

5.2 Recommendations

- The simulations in this study have proven to be very useful for the initial screening of adsorbents, prior to experimental work. Further experimental work on the synthesis and application of CLO, FAU, TSC, MWF and PAU as adsorbents in environmental remediation is recommended.
- Zeolite shows a potential for use in water treatment due to its capability on removing the pollutants. Therefore, it is recommended that a gadget or zeolite based water filter for water purification and/or treatment for portable water and wastewater be developed.
- Modification of zeolite using nanoparticles of elements should be exploited and its effect on removal of the investigated and other pollutants.

- Based on the findings of this study, further work should be carried out to continue the scientific development and generation of knowledge about environmental remediation; Other groups of compounds should be simulated in order to classify them with their associated adsorbents.
- Remediation measures for collecting, storage and recycling surface water runoff and wastewater from agricultural farms and industrial establishments should be instituted before water is discharged to the river.

REFERENCES

Abbas, G., Javed, I., Iqbal, M., Haider, R., Hussain, F., & Qureshi, N. (2017). Adsorption of non-steroidal anti-inflammatory drugs (diclofenac and ibuprofen) from aqueous medium onto activated onion skin. *Desalination. Water Treatment*, **95,** 274-285

Abdallah, M. A. E., Nguyen, K. H., Ebele, A. J., Atia, N. N., Ali, H. R. H., & Harrad, S. (2019). A single run, rapid polarity switching method for determination of 30 pharmaceuticals and personal care products in waste water using Q-Exactive Orbitrap high resolution accurate mass spectrometry. *Journal of Chromatography A*, **1588**, 68-76.

Abdelwahab, O., & Thabet, W. M. J. T. E. J. O. A. R. (2023). Natural zeolites and zeolite composites for heavy metal removal from contaminated water and their applications in aquaculture Systems: A review.

Adeli, M., Yamini, Y., & Faraji, M. (2017). Removal of copper, nickel and zinc by sodium dodecyl sulphate coated magnetite nanoparticles from water and wastewater samples. *Arabian Journal of Chemistry,* **10,** S514-S521.

Afzaal, M., Hameed, S., Liaqat, I., Ali Khan, A. A., Abdul Manan, H., Shahid, R. (2022). Heavy metals contamination in water, sediments and fish of freshwater ecosystems in Pakistan. **17**(5), 1253-1272.

Agrafioti, E., Kalderis, D., & Diamadopoulos, E. (2014). Arsenic and chromium removal from water using biochars derived from rice husk, organic solid wastes and sewage sludge. *Journal of environmental management,* **133,** 309-314.

Aguilar Romero, I. M. (2021). Biobed biopurification systems with agroindustrial wastes to remove organic contaminants from water: *microbiological and molecular aspects*

Akawa, M. N., Dimpe, K. M., & Nomngongo, P. N. J. A. J. O. C. (2021). Ultrasonic assisted magnetic solid phase extraction based on the use of magnetic waste-tyre derived activated carbon modified with methyltrioctylammonium chloride adsorbent for the preconcentration and analysis of non-steroidal anti-inflammatory drugs in wastewater. **14** (9), 103329.

Akhtar, J., Amin, N. A. S., & Shahzad, K. (2016). A review on removal of pharmaceuticals from water by adsorption. *Desalination and Water Treatment**, 57*** (27), 12842-12860.

Aktar, W., Sengupta, D., & Chowdhury, A. (2009). Impact of pesticides use in agriculture: their benefits and hazards. *Interdisciplinary toxicology*, **2**(1), 1-12.

Al-Asheh, S., Aidan, A. J. P. T. f. W. T., & Assessment, W. Q. (2020). A comprehensive method of ion exchange resins regeneration and its optimization for water treatment. *Promising techniques for wastewater treatment and water quality assessment* 163-176.

Al-Ghouti, M. A., & Da'ana, D. A. (2020). Guidelines for the use and interpretation of adsorption isotherm models: A review. *Journal of hazardous materials,* **393,** 122383..

Al-Sehemi, A. G., Irfan, A., Alrumman, S. A., & Hesham, A. (2016). Antibacterial activities, DFT and QSAR studies of quinazolinone compounds. *Bulletin of the Chemical Society of Ethiopia, **30***(2), 307-316.

Al-Shaalan, N. H., Ali, I., ALOthman, Z. A., Al-Wahaibi, L. H., & Alabdulmonem, H. (2019). High performance removal and simulation studies of diuron pesticide in water on MWCNTs. *Journal of Molecular Liquids,* ***289*****,** 111039

Al-Wabel, M. I., Ahmad, M., Usman, A. R., Sallam, A. S., Hussain, Q., Binyameen, R. B., Ok, Y. S. (2020). Evaluating the efficiency of different natural clay sediments for the removal of chlortetracycline from aqueous solutions. J*ournal of hazardous materials*, ***384***, 121500.

Alagha, O., Manzar, M. S., Zubair, M., Anil, I., Mu'azu, N. D., & Qureshi, A. (2020). Comparative adsorptive removal of phosphate and nitrate from wastewater using biochar-MgAl LDH nanocomposites: coexisting anions effect and mechanistic studies. *Nanomaterials*, **10**(2), 336.6.

Ali, H., Khan, E., & Ilahi, I. (2019). Environmental chemistry and ecotoxicology of hazardous heavy metals: environmental persistence, toxicity, and bioaccumulation. J*ournal of chemistry*, 2019.

Ali, J. K., Abi Jaoude, M., & Alhseinat, E. (2021). Polyimide ultrafiltration membrane embedded with reline-functionalized nanosilica for the remediation of pharmaceuticals in water. *Separation and Purification Technology*, **266,** 118585.

Aliyu, U. M., Rathilal, S., Isa, Y. M. J. W. P., & Technology. (2018). Membrane desalination technologies in water treatment: A review. ***13***(4), 738-752.

Almasri, D. A., Rhadfi, T., Atieh, M. A., McKay, G., & Ahzi, S. (2018). High performance hydroxyiron modified montmorillonite nanoclay adsorbent for arsenite removal. *Chemical Engineering Journal,* ***335*****,** 1-12.

Alnajrani, M. N., & Alsager, O. A. (2020). Removal of antibiotics from water by polymer of intrinsic microporosity: Isotherms, kinetics, thermodynamics, and adsorption mechanism. *Scientific reports, **10*** (1), 1-14.

Aly, F. (2023). Removal of Diclofenac Pharmaceutical Residues from Wastewater (Master's thesis, *The American University in Cairo* (Egypt).

Amalina, F., Abd Razak, A. S., Krishnan, S., Zularisam, A. W., & Nasrullah, M. (2022). The effects of chemical modification on adsorbent performance on water and wastewater treatment-A review. *Bioresource Technology Reports*, *20*, 101-259.

Ambaye, T. G., Vaccari, M., van Hullebusch, E. D., Amrane, A., & Rtimi, O. E. (2021). Mechanisms and adsorption capacities of biochar for the removal of organic and inorganic pollutants from industrial wastewater. *International Journal of Environmental Science and Technology*, **18 (**10), 3273-3294

Amutova, F., Jurjanz, S., Akhmetsadykov, N., Kazankapova, M., Razafitianamaharavo, A., Renard, A., Delannoy, M. (2023). Adsorption of organochlorinated pesticides: adsorption kinetic and adsorption isotherm study. *Results in Engineering, **17***, 100823.

Andrunik, M., Skalny, M., Gajewska, M., Marzec, M., & Bajda, T. (2023). Comparison of pesticide adsorption efficiencies of zeolites and zeolite-carbon composites and their regeneration possibilities. *Heliyon,* **9**(10).

Ang, W. L., & Mohammad, A. W. (2020). State of the art and sustainability of natural coagulants in water and wastewater treatment. *Journal of Cleaner production*, **262**, 121267

Angosto, J. M., Roca, M. J., Fernández-López, J. A. (2020). Removal of diclofenac in wastewater using biosorption and advanced oxidation techniques: Comparative results. *Wate*r, **12**(12), 3567.

Anju, A., Ravi S, P., & Bechan, S. (2010). Water pollution with special reference to pesticide contamination in India. *Journal of Water Resource and Protection, 2010*.

Wani AL, Ara A, Usmani JA. Lead toxicity: a review. *Interdiscipline Toxicology* **8** (2): 55–64.

Arnnok, P., & Burakham, R. (2014). Retention of carbamate pesticides by different surfactant-modified sorbents: a comparative study. *Journal of the Brazilian Chemical Society*, **25,** 1720-1729.

Ashraf, S., Ali, Q., Zahir, Z. A., Ashraf, S., & Asghar, H. N. (2019). Phytoremediation: Environmentally sustainable way for reclamation of heavy metal polluted soils. *Ecotoxicology and environmental safety,* **174,** 714-727.

Asiedu, O. (2016). Removal of Fluoride from Water Using Surfactant Modified Synthetic Zeolites (*Doctoral dissertation).*

Auerbach, S. M., Carrado, K. A., & Dutta, P. K. (2003). *Handbook of zeolite science and technology*: CRC press.

Avcu, T., Üner, O., Geçgel, Ü. (2021). Adsorptive removal of diclofenac sodium from aqueous solution onto sycamore ball activated carbon-isotherms, kinetics, and thermodynamic study. *Surfaces and Interfaces*, **24**, 101097.

Awad, A. M., Jalab, R., Benamor, A., Nasser, M. S., Ba-Abbad, M. M., El-Naas, M., & Mohammad, A. W. J. J. o. M. L. (2020). Adsorption of organic pollutants by nanomaterial-based adsorbents: *An overview*. ***301***, 112335.

Aydin, S., Aydin, M. E., Beduk, F., Ulvi, A. (2019). Removal of antibiotics from aqueous solution by using magnetic Fe_3O_4/red mud-nanoparticles. *Science of the total environment*, **670**, 539-546.

Azanu, D., Styrishave, B., Darko, G., Weisser, J. J., Abaidoo, R. C. (2018). Occurrence and risk assessment of antibiotics in water and lettuce in Ghana. *Science of the Total Environment,* **622**, 293-305.

Babel, S., & Kurniawan, T. A. (2003). Low-cost adsorbents for heavy metals uptake from contaminated water: a review. *Journal of Hazardous Materials,* ***97***(1-3), 219-243.

Baerlocher, C. (2008). Database of zeolite structures. *http://www. iza-structure. org/databases/*.

Baerlocher, C., McCusker, L. B., & Olson, D. H. (2007). *Atlas of zeolite framework types*: Elsevier.

Babeker, T. M. A., & Chen, Q. (2021). Heavy metal removal from wastewater by adsorption with hydrochar derived from biomass: current applications and research trends. *Current Pollution Reports,* **7**, 54-71.

Balarak, D., Jaafari, J., Hassani, G., Mahdavi, Y., Tyagi, I., Agarwal, S., & Gupta, V. K. (2015). The use of low-cost adsorbent (Canola Residues) for the adsorption of methylene blue from aqueous solution: isotherm, kinetic and thermodynamic studies. *Colloids and Interface Science Communications*, **7**, 16-199.

Baig, N. (2023). Two-dimensional nanomaterials: A critical review of recent progress, properties, applications, and future directions. Composites Part A: *Applied Science and Manufacturing*, **165**, 107362.

Bao, W. W., Zou, H. F., Gan, S. C., Xu, X. C., Ji, G. J., Zheng, K. Y. (2013). Adsorption of heavy metal ions from aqueous solutions by zeolite based on oil shale ash: Kinetic and equilibrium studies. *Chemical Research in Chinese Universities,* **29**, 126-131.

Barczyk, K., Mozgawa, W., Król, M. (2014). Studies of anions sorption on natural zeolites. *Spectrochimica Acta Part A: Molecular and Biomolecular Spectroscopy,* ***133*****,** 876-882.

Barlokova, D. (2008). Natural zeolites in the water treatment process. *Slovak Journal. Civil. Engeeniring*, **2**, 8-12.

Baste, I. A., Watson, R. T., Brauman, K. I., Samper, C.,Walzer, C. (2021). Making peace with nature: a scientific blueprint to tackle the climate, biodiversity and pollution emergencies.

Becke, A. D. (1988). Density-functional exchange-energy approximation with correct asymptotic behavior. *Physical review A,* ***38***(6), 3098.

Becke, A. D. (1992). Density-functional thermochemistry. I. The effect of the exchange-only gradient correction. *The Journal of chemical physics,* ***96***(3), 2155-2160.

Berkessa, Y. W., Mereta, S. T., Feyisa, F. F. (2019). Simultaneous removal of nitrate and phosphate from wastewater using solid waste from factory. *Applied Water Science,* **9**, 1-10.

Besghaier, S., Cecilia, J. A., Chouikhi, N., Vilarrasa-García, E., Rodríguez-Castellón, E., Chlendi, M., Bagane, M. (2021). Glyphosate adsorption onto porous clay heterostructure (PCH): kinetic and thermodynamic studies. *Brazilian Journal of Chemical Engineering*, 1-15.

Bezerra, C. D. O., Cusioli, L. F., Quesada, H. B., Nishi, L., Mantovani, D., Vieira, M. F., Bergamasco, R. (2018). Assessment of the use of Moringa oleifera seed husks for removal of pesticide diuron from contaminated water. *Environmental technology.*

Bhatnagar, A., Sillanpää, M., Witek-Krowiak, A. (2015). Agricultural waste peels as versatile biomass for water purification–A review. *Chemical engineering journal, **270***, 244-271.

Biovia, D. S. (2017). BIOVIA pipeline pilot. *Dassault Systèmes: San Diego, BW, Release*.

Bocșa, M., Pintea, S., Lung, I., Opriș, O., Stegarescu, A., Humayun, M., Bellucci, S. J. S. (2023). Biochar-Based Adsorbents for Pesticides, Drugs, Phosphorus, and Heavy Metal Removal from Polluted Water. *Separations **10***(10), 533.

Bolisetty, S., Peydayesh, M., Mezzenga, R. (2019). Sustainable technologies for water purification from heavy metals: review and analysis. *Chemical Society Reviews, **48***(2), 463-487.

Bonilla-Petriciolet, A., Mendoza-Castillo, D. I., Reynel-Ávila, H. E. (Eds.). (2017). Adsorption processes for water treatment and purification (Vol. 256). *Berlin: Springer*.

Borah, P., Kumar, M., Devi, P. (2020). Types of inorganic pollutants: metals/metalloids, acids, and organic forms. *Inorganic pollutants in water* (pp. 17-31): *Elsevier.*

Briceño, G., Fuentes, M. S., Palma, G., Jorquera, M. A., Amoroso, M. J., Diez, M. C. (2012). Chlorpyrifos biodegradation and 3, 5, 6-trichloro-2-pyridinol production by actinobacteria isolated from soil. *International Biodeterioration & Biodegradation*, ***73,*** 1-7.

Bruzzoniti, M. C., De Carlo, R. M., Rivoira, L., Del Bubba, M., Pavani, M., Riatti, M., Onida, B. (2016). Adsorption of bentazone herbicide onto mesoporous silica: application to environmental water purification. *Environmental Science and Pollution Research*, **23,** 5399-5409.

Buaisha, M., Balku, S., & Özalp-Yaman, S. (2020). Heavy metal removal investigation in conventional activated sludge systems. *Civil Engineering Journal,* ***6***(3), 470-477.

Bukowski, B. C., Keil, F. J., Ravikovitch, P. I., Sastre, G., Snurr, R. Q., Coppens, M. O. (2021). Connecting theory and simulation with experiment for the study of diffusion in nanoporous solids. *Adsorption*, **27**(5), 683-760.

Buser, H. R., Poiger, T., & Müller, M. D. (1998). Occurrence and fate of the pharmaceutical drug diclofenac in surface waters: rapid photodegradation in a lake. *Environmental science & technology*, **32**(22), 3449-3456.

Giles, C. H., Smith, D., & Huitson, A. (1974). A general treatment and classification of the solute adsorption isotherm. Theoretical. *Journal of colloid and interface science*, ***47***(3), 755-765.

Cabrera-Lafaurie, W. A., Román, F. R., Hernández-Maldonado, A. J. (2014). Removal of salicylic acid and carbamazepine from aqueous solution with Y-zeolites modified with extraframework transition metal and surfactant cations: Equilibrium and fixed-bed adsorption. *Journal of Environmental Chemical Engineering,* ***2*****(**2), 899-906.

Cantu, Y., Remes, A., Reyna, A., Martinez, D., Villarreal, J., Ramos, H., Eubanks, T. (2014). Thermodynamics, kinetics, and activation energy studies of the sorption of

chromium (III) and chromium (VI) to a Mn_3O_4 nanomaterial. *Chemical Engineering Journal,* ***254***, 374-383.

Cao, C., Xuan, W., Yan, S., Wang, Q. (2023). Zeolites synthesized from industrial and agricultural solid waste and their applications: A review. *Journal of Environmental Chemical Engineering,* 110898.

Cao, Z., Iskhakova, L., Sun, X., Anjikar, N. D., Yang, S., Dong, J. J. M., Materials, M. (2022). Self-seeded growth of very large open-structured zeolite nanosheet assemblies with extraordinary micropore accessibility.*Microporous and Mesoporous Materials*, ***336*****,** 111854.

Cao, Z., Iskhakova, L., Sun, X., Anjikar, N. D., Yang, S., & Dong, J. (2022). Self-seeded growth of very large open-structured zeolite nanosheet assemblies with extraordinary micropore accessibility. *Microporous and Mesoporous Materials,* **336,** 111854.

Carazo-Rojas, E., Pérez-Rojas, G., Pérez-Villanueva, M., Chinchilla-Soto, C., Chin-Pampillo, J. S., Aguilar-Mora, P., Vryzas, Z. (2018). Pesticide monitoring and ecotoxicological risk assessment in surface water bodies and sediments of a tropical agro-ecosystem. *Environmental pollution*, **241**, 800-809.

Cevallos-Mendoza, J., Amorim, C. G., Rodríguez-Díaz, J. M., & Montenegro, M. D. C. B. (2022). Removal of contaminants from water by membrane filtration: *a review. Membranes*, **12**(6), 570.

Chadwick, S. S. (1988). Ullmann's encyclopedia of industrial chemistry. R*eference Services Review*, **16**(4), 31-34.

Chai, W. S., Cheun, J. Y., Kumar, P. S., Mubashir, M., Majeed, Z., Banat, F., Show, P. L. (2021). A review on conventional and novel materials towards heavy metal adsorption in wastewater treatment application. *Journal of Cleaner Production*, **296**, 126589.

Chaka, B., Osano, A. M., Wesley, O. N., Forbes, P. B. (2023). Seasonal variation in pesticide residue occurrences in surface waters found in Narok and Bomet Counties, Kenya. *Environmental Monitoring and Assessment*, **195**(9), 1050.

Chakraborty, R., Verma, R., Asthana, A., Vidya, S. S., & Singh, A. K. (2021). Adsorption of hazardous chromium (VI) ions from aqueous solutions using modified sawdust: kinetics, isotherm and thermodynamic modelling. *International Journal of Environmental Analytical Chemistry, **101***(7), 911-928.

Chandrasekaran, A., Betouras, J. J. (2022). Effect of disorder on density of states and conductivity in higher-order Van Hove singularities in two-dimensional bands. *Physical review B, **105***(7), 075-144.

Chavoshani, A., Hashemi, M., Amin, M. M., & Ameta, S. C. (2020). Pharmaceuticals as emerging micropollutants in. Micropollutants and Challenges: *Emerging in the Aquatic Environments and Treatment Processes*, **35**.

Chebet, E. B., Kibet, J. K., & Mbui, D. (2020). The assessment of water quality in river Molo water basin, Kenya. *Applied Water Science,* **10,** 1-10.

Chellaiah, E. R. (2018). Cadmium (heavy metals) bioremediation by Pseudomonas aeruginosa: a minireview. *Applied water science*, **8(**6), 154.

Chen, B., Chen, Z., & Lv, S. (2011). A novel magnetic biochar efficiently sorbs organic pollutants and phosphate. *Bioresource technology,* **102**(2), 716-723.

Chen, J. L., Gao, L., Jiang, Q., Hou, Q., Hong, Y., Shen, W. J.,Zhu, J. H. (2020). Fabricating efficient porous sorbents to capture organophosphorus pesticide in solution. *Microporous and Mesoporous Materials,* **294,** 109911.

Cheng, D., Ngo, H. H., Guo, W., Lee, D., Nghiem, D. L., Zhang, J., & Wang, J. (2020). Performance of microbial fuel cell for treating swine wastewater containing sulfonamide antibiotics. *Bioresource technology,* **311**, 123588.

Cheng, H., & Hu, Y. (2010). Lead (Pb) isotopic fingerprinting and its applications in lead pollution studies in China: a review. *Environmental pollution,* **158**(5), 1134-1146.

Chepkorir, L. (2022). Assessment of zinc, lead and cadmium contributions to diabetes and hypertension: a case study of marakwet east and marakwet west sub counties (*Doctoral dissertation, University of Eldoret)*.

Chirikona, F., Filipovic, M., Ooko, S., & Orata, F. (2015). Perfluoroalkyl acids in selected wastewater treatment plants and their discharge load within the Lake Victoria basin in Kenya. *Environmental monitoring and assessment,* **187**, 1-12.

Chowdhary, P., Bharagava, R. N., Mishra, S., & Khan, N. (2020). Role of industries in water scarcity and its adverse effects on environment and human health. Environmental Concerns and Sustainable Development. *Air, Water and Energy Resources,* **1** 235-256.

Chowdhury, I. R., Chowdhury, S., Mazumder, M. A. J., & Al-Ahmed, A. (2022). Removal of lead ions (Pb^{2+}) from water and wastewater: a review on the low-cost adsorbents. *Applied Water Science,* **12**(8), 185.

Chowdhury, K. F., Hall, R. J., McNally, A., & Carter, L. J. (2023). Phytoremediation as a Tool to Remove Drivers of Antimicrobial Resistance in the Aquatic Environment. *Reviews of Environmental Contamination and Toxicology*, **261**(1), 16.

Choy, K. K., Porter, J. F., & Mckay, G. (2004). Intraparticle diffusion in single and multicomponent acid dye adsorption from wastewater onto carbon. *Chemical Engineering Journal, **103***(1-3), 133-145.

Christidis, G. E., Moraetis, D., Keheyan, E., Akhalbedashvili, L., Kekelidze, N., Gevorkyan, R., & Sargsyan, H. (2003). Chemical and thermal modification of natural HEU-type zeolitic materials from Armenia, Georgia and Greece. *Applied Clay Science,* **24**(1-2), 79-91.

Chutia, P., Kato, S., Kojima, T., & Satokawa, S. (2009). Adsorption of As (V) on surfactant-modified natural zeolites. *Journal of Hazardous materials, **162*(**1), 204-211.

Cimirro, N. F., Lima, E. C., Cunha, M. R., Dias, S. L., Thue, P. S., Mazzocato, A. C., & Pavan, F. A. (2020). Removal of pharmaceutical compounds from aqueous solution by novel activated carbon synthesized from lovegrass (Poaceae). *Environmental Science and Pollution Research,* **27**, 21442-21454.

Collin, M. S., Venkatraman, S. K., Vijayakumar, N., Kanimozhi, V., Arbaaz, S. M., Stacey, R. S., ... & Swamiappan, S. (2022). Bioaccumulation of lead (Pb) and its effects on human: A review. *Journal of Hazardous Materials Advances*, **7,** 100094.

Craswell, E. (2021). Fertilizers and nitrate pollution of surface and ground water: an increasingly pervasive global problem. *SN Applied Sciences*, **3**(4), 518.

Cui, D., Tan, C., Deng, H., Gu, X., Pi, S., Chen, T., Li, A. J. A. (2020). Biosorption mechanism of aqueous Pb^{2+}, Cd $^{2+}$, and Ni^{2+} ions on extracellular polymeric substances (EPS). *2020*.

Das, S. K., Bhowal, J., Das, A. R., & Guha, A. K. (2006). Adsorption behavior of rhodamine B on rhizopus o ryzae biomass. *Langmuir, **22***(17), 7265-7272.

De Araujo, B. R. S., Onrubia-Calvo, J. A., Stambouli, I., Pétaud, G., Hidalgo-Carrillo, J., Nieto-Marquéz, A., Gil, S. (2022). Towards the development of advanced hierarchical chabazite materials: Novel micro-mesoporous silicoaluminophosphate SAPO-34 zeolites. *Materials Today Communications, **31***, 103580.

de Oliveira, D. M., Agostinetto, L., & Siegloch, A. E. (2023). Comparison of the drinking water standard for pesticides of the Brazil with other countries. *Heliyon*, **9**(3).

de Vargas Brião, G., da Silva, M. G., & Vieira, M. G. A. (2021). Expanded vermiculite as an alternative adsorbent for the dysprosium recovery. *Journal of the Taiwan Institute of Chemical Engineers, **127*,** 228-235.

Dehbi, A., Dehmani, Y., Omari, H., Lammini, A., Elazhari, K., & Abdallaoui, A. J. J. O. E. C. E. (2020). Hematite iron oxide nanoparticles (α-Fe_2O_3): synthesis and modelling adsorption of malachite green. *Journal of Environmental Chemical Engineering,* **8**(1), 103394 *8*(1), 103394.

Dehmani, Y., Mohammed, B. B., Oukhrib, R., Dehbi, A., Lamhasni, T., Brahmi, Y., & Abouarnadasse, S. (2023). Adsorption of various inorganic and organic pollutants by natural and synthetic zeolites: A critical review. *Arabian Journal of Chemistry*, 105474.

Delley, B. (1990). An all-electron numerical method for solving the local density functional for polyatomic molecules. *The Journal of chemical physics,* ***92***(1), 508-517.

Delgado-Montiel, T., Baldenebro-López, J., Soto-Rojo, R., & Glossman-Mitnik, D. (2020). Theoretical study of the effect of π-bridge on optical and electronic properties of carbazole-based sensitizers for DSSCs. *Molecules*, *25*(16), 3670.

Derikvand, Z., Akbari, S., Kouchakzadeh, G., Azadbakht, A., & Nemati, C. A. (2019). High performance removal of azo and cationic dyes pollutants with Mn-aluminophosphate particles: kinetics, thermodynamics, and adsorption equilibrium studies. *Russian Journal of Physical Chemistry A,* **93**(13), 2604-2612.

Diale, P., Mkhize, S., Muzenda, E., & Zimba, J. (2011). The sequestration of heavy metals contaminating the wonderfonteinspruit catchment area using natural zeolite. *World Academy of Science, Engineering and Technology,* ***74***, 766-772.

Dias, J. M., Alvim-Ferraz, M. C., Almeida, M. F., Rivera-Utrilla, J., & Sánchez-Polo, M. (2007). Waste materials for activated carbon preparation and its use in aqueous-phase treatment: a review. *Journal of environmental management*, **85(**4), 833-846.

Douterelo, I., Dutilh, B. E., Calero, C., Rosales, E., Martin, K., & Husband, S. (2020). Impact of phosphate dosing on the microbial ecology of drinking water distribution systems: Fieldwork studies in chlorinated networks. *Water Research,* **187,** 116416.

Du, Q., Liu, S., Cao, Z., & Wang, Y. (2005). Ammonia removal from aqueous solution using natural Chinese clinoptilolite. *Separation and purification technology,* **44 (**3), 229-234.

Duchet, C., Kraft, A., & Stark, J. D. (2018). Effects of environmentally realistic concentrations of neonicotinoid insecticides on an aquatic invertebrate community.

Ebelegi, A. N., Godwin, J., Ayawei, N., & Wankasi, D. (2019). Facile uptake of cadmium (II) from aqueous solution using polyamidoamine functionalized silica. *Journal of Environmental Analytical Chemistry*, **6,** 2380-2391.

Edet, U. A., & Ifelebuegu, A. O. (2020). Kinetics, isotherms, and thermodynamic modeling of the adsorption of phosphates from model wastewater using recycled brick waste. *Processes,* ***8***(6), 665.

Eid, E. M., Galal, T. M., Sewelam, N. A., Talha, N. I., Abdallah, S. M. J. E. S., & Research, P. (2020). Phytoremediation of heavy metals by four aquatic macrophytes and their potential use as contamination indicators: A comparative assessment. *Environmental Science and Pollution Research*, **27,** 12138-12151..

El-Araby, H., Ahmed Ibrahim, A., & Mangood, A. (2019). Removal of copper (II) and cadmium (II) ions from aqueous solution by adsorption on modified almond shells. *International Journal of Engineering & Technology*, **19**(5), 1-39.

El Ouardi, M., Qourzal, S., Alahiane, S., Assabbane, A., & Douch, J. (2015). Effective removal of nitrates ions from aqueous solution using new clay as potential low-cost adsorbent. *Journal of Encapsulation and Adsorption Sciences,* **5**(4), 178-190.

Elbehiry, F., Elbasiouny, H., Ali, R., & Brevik, E. C. (2020). Enhanced immobilization and phytoremediation of heavy metals in landfill contaminated soils. *Water, Air, & Soil Pollution,* ***23***(5), 1-20.

Fainerman, V. B., Lylyk, S. V., Aksenenko, E. V., Kovalchuk, N. M., Kovalchuk, V. I., Petkov, J. T., & Miller, R. (2012). Effect of water hardness on surface tension and dilational visco-elasticity of sodium dodecyl sulphate solutions. *Journal of colloid and interface science,* **377**(1), 1-6.

Fallah, Z., Isfahani, H. N., & Tajbakhsh, M. (2019). Cyclodextrin-triazole-titanium based nanocomposite: Preparation, characterization and adsorption behavior investigation. Process Safety and Environmental Protection, **124**, 251-265.

Fallah, Z., Zare, E. N., Ghomi, M., Ahmadijokani, F., Amini, M., Tajbakhsh, M., & Varma, R. S. (2021). Toxicity and remediation of pharmaceuticals and pesticides using metal oxides and carbon nanomaterials. Chemosphere, **275**, 130055.

Fernandez, M. E., Ledesma, B., Román, S., Bonelli, P. R., & Cukierman, A. L. (2015). Development and characterization of activated hydrochars from orange peels as potential adsorbents for emerging organic contaminants. *Bioresource technology,* **183**, 221-228.

Foo, K. Y., & Hameed, B. H. (2011). The environmental applications of activated carbon/zeolite composite materials. *Advances in colloid and interface science,* **162(**1-2), 22-28.

Frisch, M. J. E. A., Trucks, G. W., Schlegel, H., Scuseria, G. E., Robb, M. A., Cheeseman, J. R., & Pople, J. A. (2004). Gaussian 03, revision c. 02, Gaussian. Inc., Wallingford, CT, 4.

Galli, E., Gottardi, G., Mayer, H., Preisinger, A., & Passaglia, E. (1983). The structure of potassium-exchanged heulandite at 293, 373 and 593 K. Acta Crystallographica Section B: *Structural Science*, **39**(2), 189-197.

Gawad, D. A., Elnaggar, M. M., & Belal, T. S. J. C. (2022). Multi-Analyte HPLC–DAD Method for Concurrent Analysis of Six Antimicrobials and Three Proton Pump Inhibitors Frequently Used in Management of Helicobacter Pylori Infection: *Application to Simulated Intestinal Fluid Samples*. ***85***(7), 617-628.

Gao, Z. R., Balestra, S. R., Li, J., & Camblor, M. A. (2021). Synthesis of Extra-Large Pore, Large Pore and Medium Pore Zeolites Using a Small Imidazolium Cation as the Organic Structure-Directing Agent. *Chemistry–A European Journal*, *27*(72), 18109-18117.

Ge, A., Peng, Q., Wu, H., Liu, H., Tong, Y., Nishida, T., & Ye, S. (2013). Effect of functional group on the monolayer structures of biodegradable quaternary ammonium surfactants. *Langmuir*, **29(**47), 14411-14420.

George, J., & Shukla, Y. (2011). Pesticides and cancer: insights into toxicoproteomic-based findings. *Journal of proteomics, **74***(12), 2713-2722.

G Hashemian Ghahfarokhi, S. S., Landi, A., Khademi, H., & Hojati, S. (2014). Removal of Cd2+ and Pb^{2+} ions from aqueous solutions using Iranian natural zeolite and sepiolite. *Journal of Environmental Studies*, **40**(1), 189-198.

Ghosh, S., Pourebrahimi, S., Malloum, A., Ajala, O. J., AlKafaas, S. S., Onyeaka, H., ... & Wani, M. Y. (2023). A review on ciprofloxacin removal from wastewater as a pharmaceutical contaminant: Covering adsorption to advanced oxidation processes to computational studies. *Materials Today Communications*, 107500.

Giesy, J. P., Solomon, K. R., Mackay, D., & Anderson, J. (2014). Evaluation of evidence that the organophosphorus insecticide chlorpyrifos is a potential persistent organic pollutant (POP) or persistent, bioaccumulative, and toxic (PBT). *Environmental Sciences Europe*, **26,** 1-20.

Gilbert, N. (2012). Drug-pollution law all washed up: EU initiative to clean up waterways faces tough opposition. *Nature,* **491**(7425), 503-505.

Gizaw, A., Zewge, F., Kumar, A., Mekonnen, A., & Tesfaye, M. (2021). A comprehensive review on nitrate and phosphate removal and recovery from aqueous solutions by adsorption. AQUA—*Water Infrastructure, Ecosystems and Society,* **70**(7), 921-947.

Glibert, P. M. (2020). Harmful algae at the complex nexus of eutrophication and climate change. *Harmful algae*, **91**, 101583.

Golchoobi, A., & Pahlavanzadeh, H. (2017). Extra-framework charge and impurities effect, Grand Canonical Monte Carlo and volumetric measurements of $CO_2/CH_4/N_2$ uptake on NaX molecular sieve. *Separation Science and Technology,* ***52***(16), 2499-2512.

Gonzalez-Olmos, R., Kopinke, F.-D., Mackenzie, K., & Georgi, A. (2013). Hydrophobic Fe-zeolites for removal of MTBE from water by combination of adsorption and oxidation. *Environmental science & technology,* ***47*****(**5), 2353-2360.

Gracia-Lor, E., Sancho, J. V., Serrano, R., & Hernández, F. (2012). Occurrence and removal of pharmaceuticals in wastewater treatment plants at the Spanish Mediterranean area of Valencia. *Chemosphere,* **87**(5), 453-462.

Grassi, M., Kaykioglu, G., Belgiorno, V., & Lofrano, G. (2012). Removal of emerging contaminants from water and wastewater by adsorption process. Emerging compounds removal from wastewater: *Natural and solar based treatments,* 15-37.

Grela, A., Kuc, J., & Bajda, T. (2021). A Review on the Application of Zeolites and Mesoporous Silica Materials in the Removal of Non-Steroidal Anti-Inflammatory Drugs and Antibiotics from Water. *Materials,* ***14***(17), 4994.

Gupta, A., Sharma, V., Sharma, K., Kumar, V., Choudhary, S., Mankotia, P., Ekielski, A. J. M. (2021). A review of adsorbents for heavy metal decontamination: Growing approach to wastewater treatment. *Materials* **14**(16), 4702.

Gusain, R., Kumar, N., & Ray, S. S. (2020). Recent advances in carbon nanomaterial-based adsorbents for water purification. *Coordination Chemistry Reviews,* **405**, 213111.

Guzzella, L., Capri, E., Di Corcia, A., Barra Caracciolo, A., & Giuliano, G. (2006). Fate of diuron and linuron in a field lysimeter experiment. *Journal of environmental quality,* **35**(1), 312-323.

Gyesi, J. N., Nyaaba, B. A., Darko, G., Mills-Robertson, F. C., Miezah, K., Acheampong, N. A., ... & Borquaye, L. S. (2022). Occurrence of pharmaceutical residues and antibiotic-resistant bacteria in water and sediments from major reservoirs (owabi and barekese dams) in Ghana. *Journal of Chemistry*, **2022**, 1-14..

Haider, F. U., Liqun, C., Coulter, J. A., Cheema, S. A., Wu, J., Zhang, R., Farooq, M. (2021). Cadmium toxicity in plants: Impacts and remediation strategies. *Ecotoxicology and Environmental Safety*, *211*, 111887.

Hamdi, N., & Srasra, E. (2012). Removal of phosphate ions from aqueous solution using Tunisian clays minerals and synthetic zeolite. *Journal of Environmental Sciences,* **24(**4), 617-623.

Han, P., Hu, K., Li, L., Zhao, Y., Yang, C., Liu, X., & Huang, Y. (2022). Preparation of Hypercrosslinked Polymer-Based Sponge and its Application for the Removal of Non-Steroidal Anti-Inflammatory Drugs in Water Samples. *Water, Air, & Soil Pollution,* **233**(11), 456.

Hernandez Tamargo, C. E. (2017). *Computational Study of Layered Zeolite MFI and Titanium-substituted Zeolite LTA and their Applications in Catalysis.* UCL (University College London),

Hira, N. e., Lock, S. S. M., Shoparwe, N. F., Lock, I. S. M., Lim, L. G., Yiin, C. L., Hassam, M. J. S. (2023). Review of Adsorption Studies for Contaminant Removal from Wastewater Using Molecular Simulation. *Sustainability* ***15*****(**2), 1510.

Hu, X., Xue, Y., Long, L., & Zhang, K. (2018). Characteristics and batch experiments of acid-and alkali-modified corncob biomass for nitrate removal from aqueous solution. *Environmental Science and Pollution Research,* **25,** 19932-19940.

Hussain, A., Khan, M. U., Ibrahim, M., Khalid, M., Ali, A., Hussain, S., Al-Sehemi, A. G. (2020). Structural parameters, electronic, linear and nonlinear optical exploration of thiopyrimidine derivatives: A comparison between DFT/TDDFT and experimental study. *Journal of Molecular Structure****, 1201*****,** 127183.

Ibigbami, T. B., Dawodu, F. A., & Akinyeye, O. J. (2016). Removal of heavy metals from pharmaceutical industrial wastewater effluent by combination of adsorption and chemical precipitation methods. *American Journal of Applied Chemistry,* **4**(1), 24-32.

Idrees, N., Tabassum, B., Abd_Allah, E. F., Hashem, A., Sarah, R., & Hashim, M. (2018). Groundwater contamination with cadmium concentrations in some West UP Regions, India. *Saudi journal of biological sciences,* **25**(7), 1365-1368.

Igberase, E., & Osifo, P. (2015). Equilibrium, kinetic, thermodynamic and desorption studies of cadmium and lead by polyaniline grafted cross-linked chitosan beads

from aqueous solution. *Journal of Industrial and Engineering Chemistry*, **26**, 340-347.

Inglezakis, V. J., Poulopoulos, S. G., & Kazemian, H. (2018). Insights into the S-shaped sorption isotherms and their dimensionless forms. *Microporous and Mesoporous Materials,* **272,** 166-176

Iyer, S., Sinkar, P., Kallathiyan, K., & Sengupta, C. (2020). Prevalence of High Cadmium Levels in Major Metro Cities of India. *Asian Journal of Biological and Life Sciences,* **9(**1), 27.

Jayaraj, R., Megha, P., & Sreedev, P. (2016). Organochlorine pesticides, their toxic effects on living organisms and their fate in the environment. *Interdisciplinary toxicology*, **9(**3-4), 90-100.

Jeele, M. O. O., Hussein, A. A., Mohamud, M. A., Adani, A. A., & Mohamud, M. F. Y. (2023). Spectrum and prevalence of renal dysfunction among heart failure patients attending tertiary care hospital: first report from Somalia. *The Egyptian Journal of Internal Medicine,* **35**(1), 70.

Jiménez, V. A. P., Hernández-Montoya, V., Ramírez-Montoya, L. A., Castillo-Borja, F., Tovar-Gómez, R., & Montes-Morán, M. A. (2021). Adsorption of impurities from nickel-plating baths using commercial sorbents to reduce wastewater discharges. *Journal of environmental management,* **284**, 112024.

Jiang, L., Tu, Y., Li, X., & Li, H. (2018). Application of reverse osmosis in purifying drinking water. In *E3S web of conferences* (Vol. 38, p. 01037). EDP Sciences.

John, Y., David, V. E., & Mmereki, D. (2018). A comparative study on removal of hazardous anions from water by adsorption: a review. *International Journal of Chemical Engineering, 2018*.

K'oreje, K. O., Kandie, F. J., Vergeynst, L., Abira, M. A., Van Langenhove, H., Okoth, M., & Demeestere, K. (2018). Occurrence, fate and removal of pharmaceuticals, personal care products and pesticides in wastewater stabilization ponds and receiving rivers in the Nzoia Basin, Kenya. *Science of the Total Environment*, **637**, 336-348.

Kairigo, P., Ngumba, E., Sundberg, L. R., Gachanja, A., & Tuhkanen, T. (2020). Occurrence of antibiotics and risk of antibiotic resistance evolution in selected Kenyan wastewaters, surface waters and sediments. *Science of the Total Environment,* **720**, 137580.

Kairigo, P., Ngumba, E., Sundberg, L. R., Gachanja, A., & Tuhkanen, T. (2020). Contamination of surface water and river sediments by antibiotic and antiretroviral drug cocktails in low and middle-income countries: occurrence, risk and mitigation strategies. *Water*, **12**(5), 1376.

Kalam, S., Abu-Khamsin, S. A., Kamal, M. S., & Patil, S. (2021). Surfactant adsorption isotherms: A review. *ACS omega,* **6**(48), 32342-32348.

Kandie, F. J., Krauss, M., Massei, R., Ganatra, A., Fillinger, U., Becker, J., ... & Brack, W. (2020). Multi-compartment chemical characterization and risk assessment of chemicals of emerging concern in freshwater systems of western Kenya. *Environmental Sciences Europe,* **32**, 1-12.

Kaonga, C. C., Takeda, K., & Sakugawa, H. (2015). Diuron, Irgarol 1051 and Fenitrothion contamination for a river passing through an agricultural and urban area in Higashi Hiroshima City, Japan. *Science of the Total Environment,* **518**, 450-458.

Karatas, M. (2012). Removal of Pb (II) from water by natural zeolitic tuff: kinetics and thermodynamics. Journal of hazardous materials, **199,** 383-389.

Khan, M. A., & Ghouri, A. M. (2011). Environmental pollution: its effects on life and its remedies. *Researcher World: Journal of Arts, Science & Commerce, **2***(2), 276-285.

Khatoon, N., Khan, A. H., Pathak, V., Agnihotri, N., & Rehman, M. (2013). Removal of hexavalent chromium from synthetic waste water using synthetic nano zero valent iron (NZVI) as adsorbent. *International Journal of Innovative Research in Science, Engineering and Technology, **2***(11), 2319-8753.

Kihampa, C., Mato, R. R., & Mohamed, H. (2010). Levels of pesticide residues in irrigation effluent from tomato fields in Owiro Estate, Tanzania. *International Journal of Biological and Chemical Sciences*, **4**(3).

Kim, K. J., & Ahn, H. G. (2012). The effect of pore structure of zeolite on the adsorption of VOCs and their desorption properties by microwave heating. *Microporous and Mesoporous Materials,* **152**, 78-83.

Kim, S., Chen, J., Cheng, T., Gindulyte, A., He, J., He, S., ... & Bolton, E. E. (2019). PubChem 2019 update: improved access to chemical data. Nucleic acids research, **47**(1), 1102-1109.

Kimosop, S. J., Getenga, Z., Orata, F., Okello, V., & Cheruiyot, J. (2016). Residue levels and discharge loads of antibiotics in wastewater treatment plants (WWTPs),

hospital lagoons, and rivers within Lake Victoria Basin, Kenya. *Environmental monitoring and assessment,* ***188***(9), 532.

King, J. F., Szczuka, A., Zhang, Z., & Mitch, W. A. (2020). Efficacy of ozone for removal of pesticides, metals and indicator virus from reverse osmosis concentrates generated during potable reuse of municipal wastewaters. *Water research*, **176**, 115744.

Kinoti, I. K., Karanja, E. M., Nthiga, E. W., M'thiruaine, C. M., & Marangu, J. M. (2022). Review of clay-based nanocomposites as adsorbents for the removal of heavy metals. *Journal of Chemistry,* 2022.

Kinuthia, G. K., Ngure, V., Beti, D., Lugalia, R., Wangila, A., & Kamau, L. J. S. R. (2020). Levels of heavy metals in wastewater and soil samples from open drainage channels in Nairobi, Kenya: *Community health implication*. ***10***(1), 8434.

Kirkpatrick Jr, S., CDG, and Vecchi, M. P. (1983). Optimization by simulated annealing. *Science,* ***220***(4598), 671-680.

Kithinji Kinoti, I., Ogunah, J., Muturia M'Thiruaine, C., & Marangu, J. M. (2022). Adsorption of heavy metals in contaminated water using zeolite derived from agro-wastes and clays: A review. *Journal of Chemistry,* 2022.

Kong, L., Huang, M., Chen, J., & Lin, M. (2020). Fabrication of sensitive silver-decorated cotton swabs for SERS quantitative detection of mixed pesticide residues in bitter gourds. *New Journal of Chemistry,* **44**(29), 12779-12784.

Kooijman, G., De Kreuk, M., Houtman, C., & Van Lier, J. J. J. O. W. P. E. (2020). Perspectives of coagulation/flocculation for the removal of pharmaceuticals from domestic wastewater: *A critical view at experimental procedures*. **34**, 101161.

Kordbacheh, F., & Heidari, G. (2023). Water pollutants and approaches for their removal. *Materials Chemistry Horizons*, **2**(2), 139-153.

Kostraba, J. N., Gay, E. C., Rewers, M., & Hamman, R. F. (1992). Nitrate levels in community drinking waters and risk of IDDM: an ecological analysis. *Diabetes care*, **15**(11), 1505-1508.

Kouakou, L. P. M.-S., Kouyate, A., Sanou, A., Koffi, A., Tigori, M., Meite, N., Research, E. (2022). Evaluation of the physico-chemical quality of drinking water in the city of Daloa (Mid-West of Côte d'Ivoire) *Effects on human health*. ***8***(3), 186-196.

Kubier, A., Hamer, K., & Pichler, T. (2020). Cadmium background levels in groundwater in an area dominated by agriculture. *Integrated Environmental Assessment and Management,* **16**(1), 103-113.

Kuehl, V. A. (2021). Substituent Modified Covalent Organic Frameworks for Applications in Selective Separations: *University of Wyoming.*

Kumar, M., Goswami, L., Singh, A. K., & Sikandar, M. (2019). Valorization of coal fired-fly ash for potential heavy metal removal from the single and multi-contaminated system. *Heliyon,* ***5***(10), 02562.

Kumar, P. S., Ramalingam, S., Sathyaselvabala, V., Kirupha, S. D., Murugesan, A., & Sivanesan, S. (2012). Removal of cadmium (II) from aqueous solution by agricultural waste cashew nut shell. *Korean Journal of Chemical Engineering*, **29**, 756-768.

Kumari, N., & Mohan, C. (2021). Basics of clay minerals and their characteristic properties. *clay Clay Miner*, **24**(1).

Kursa, M. B., Jankowski, A., & Rudnicki, W. R. (2010). Boruta–a system for feature selection. *Fundamenta Informaticae,* ***101***(4), 271-285.

Kursa, M. B., & Rudnicki, W. R. (2010). Feature selection with the Boruta package. *Journal of statistical software,* **36**, 1-13.

Lagunas-Basave, B., Brito-Hernández, A., Saldarriaga-Noreña, H. A., Romero-Aguilar, M., Vergara-Sánchez, J., Moeller-Chávez, G. E., Murillo-Tovar, M. A. J. W. (2022). Occurrence and Risk Assessment of Atrazine and Diuron in Well and Surface Water of a Cornfield Rural Region. *Water* **14**(22), 3790.

Langmuir, I. (1918). The adsorption of gases on plane surfaces of glass, mica and platinum. *Journal of the American Chemical society,* ***40***(9), 1361-1403.

Lee, C., Yang, W., & Parr, R. G. (1988). Development of the Colle-Salvetti correlation-energy formula into a functional of the electron density. *Physical review B,* ***37***(2), 785.

Lee, H. J., Lee, E., Yoon, S. H., Chang, H. R., Kim, K., & Kwon, J. H. (2012). Enzymatic and microbial transformation assays for the evaluation of the environmental fate of diclofenac and its metabolites. *Chemosphere***, 87(**8), 969-974..

Lee, H. C., Kim, K. M., Choi, S. I., Kim, Y. H., Woo, H. C., & Won, Y. S. (2018). A Computational Study on the Adsorption Characteristics of Hydrocarbons (Propylene, n-Butane and Toluene) by uing Cation-exchanged ZSM-5 Zeolites. *Korean Chemical Engineering Research,* ***56***(6), 909-913.

Lee, S. J., Mamun, M., Atique, U., & An, K. G. (2023). Fish Tissue Contamination with Organic Pollutants and Heavy Metals: Link between Land Use and Ecological Health. *Water*, **15**(10), 1845.

Letsoalo, M. R., Sithole, T., Mufamadi, S., Mazhandu, Z., Sillanpaa, M., Kaushik, A., & Mashifana, T. (2023). Efficient detection and treatment of pharmaceutical contaminants to produce clean water for better health and environmental. *Journal of Cleaner Production,* **387,** 135798.

Li, J., Zhang, W., Lin, Z., Huang, Y., Bhatt, P., & Chen, S. (2021). Emerging strategies for the bioremediation of the phenylurea herbicide diuron. *Frontiers in Microbiology*, **12**, 686509.

Li, W. C. (2014). Occurrence, sources, and fate of pharmaceuticals in aquatic environment and soil. *Environmental pollution,* **187**, 193-201.

Lin, Y. C., Hsiao, K. W., & Lin, A. Y. C. (2018). Photolytic degradation of ciprofloxacin in solid and aqueous environments: kinetics, phototransformation pathways, and byproducts. *Environmental Science and Pollution Research,* **25**, 2303-2312.

Lin, L., Yang, H., & Xu, X. (2022). Effects of water pollution on human health and disease heterogeneity: a review. *Frontiers in environmental science,* **10**, 880246.

Lin, W., Jing, L., & Zhang, B. (2020). Micellar-enhanced ultrafiltration to remove nickel ions: a response surface method and artificial neural network optimization. *Water,* ***12***(5), 1269.

Lisouza, F. A., Owuor, O. P., & Lalah, J. O. (2011). Variation in indoor levels of polycyclic aromatic hydrocarbons from burning various biomass types in the traditional grass-roofed households in Western Kenya. *Environmental Pollution,* **159**(7), 1810-1815.

Liu, C., Huang, X., Meng, Z., Qian, H., Liu, X., Lu, R., & Xu, D. (2020). Study on the adsorption mechanism of benzoylurea insecticides onto modified hyperbranched polysilicon materials. *RSC advances*, **10**(48), 28664-28673.

Liu, M., Hou, L. A., Yu, S., Xi, B., Zhao, Y., & Xia, X. (2013). MCM-41 impregnated with A zeolite precursor: Synthesis, characterization and tetracycline antibiotics removal from aqueous solution. *Chemical engineering journal*, **223**, 678-687.

Liu, Y., Zhu, X., Qian, F., Zhang, S., & Chen, J. (2014). Magnetic activated carbon prepared from rice straw-derived hydrochar for triclosan removal. RSC Advances, **4**(109), 63620-63626.

Lonappan, L., Brar, S. K., Das, R. K., Verma, M., & Surampalli, R. Y. (2016). Diclofenac and its transformation products: environmental occurrence and toxicity-a review. *Environment International*, **96,** 127-138.

Lonappan, L., Rouissi, T., Brar, S. K., Verma, M., & Surampalli, R. Y. (2018). An insight into the adsorption of diclofenac on different biochars: Mechanisms, surface chemistry, and thermodynamics. *Bioresource technology,* **249,** 386-394.

Louis, H., Mathias, G. E., Unimuke, T. O., Emori, W., Ling, L., Owen, A. E., Cheng, C.-R. (2022). Isolation, characterization, molecular electronic structure investigation, and in-silico modeling of the anti-inflammatory potency of trihydroxystilbene. *Journal of Molecular Structure*, 133418.

Lu, C., Yang, Z., Liu, J., Liao, Q., Ling, W., Waigi, M. G., & Odinga, E. S. (2020). Chlorpyrifos inhibits nitrogen fixation in rice-vegetated soil containing Pseudomonas stutzeri A1501. *Chemosphere*, **256**, 127098.

Lu, T., & Chen, F. (2012). Multiwfn: a multifunctional wavefunction analyzer. *Journal of computational chemistry,* ***33***(5), 580-592.

Ma, X., Qi, M., Li, Z., Zhao, Y., Yan, P., Liang, B., & Wang, A. (2019). Characterization of an efficient chloramphenicol-mineralizing bacterial consortium. *Chemosphere*, **222**, 149-155.

Madikizela, L. M., & Chimuka, L. (2017). Simultaneous determination of naproxen, ibuprofen and diclofenac in wastewater using solid-phase extraction with high performance liquid chromatography. *Water Sa*, **43**(2), 264-274.

Maged, A., Iqbal, J., Kharbish, S., Ismael, I. S., & Bhatnagar, A. (2020). Tuning tetracycline removal from aqueous solution onto activated 2: 1 layered clay mineral: Characterization, sorption and mechanistic studies. *Journal of Hazardous Materials*, **384**, 121320.

Maheshwari, U., Mathesan, B., & Gupta, S. (2015). Efficient adsorbent for simultaneous removal of Cu (II), Zn (II) and Cr (VI): Kinetic, thermodynamics and mass transfer mechanism. *Process Safety and Environmental Protection*, **98,** 198-210.

Mahmood, T., Momin, S., Ali, R., Naeem, A., & Khan, A. (2022). Technologies for removal of emerging contaminants from wastewater. *Wastewater treatment*.

Mahmoodi, N. M., Hayati, B., Arami, M., & Lan, C. (2011). Adsorption of textile dyes on Pine Cone from colored wastewater: Kinetic, equilibrium and thermodynamic studies. *Desalination, **268***(1-3), 117-125.

Majd, M. M., Kordzadeh-Kermani, V., Ghalandari, V., Askari, A., & Sillanpää, M. J. S. o. T. T. E. (2021). Adsorption isotherm models: A comprehensive and systematic review (2010− 2020). 151334.

Malliou, E., Loizidou, M., & Spyrellis, N. (1994). Uptake of lead and cadmium by clinoptilolite. *Science of the Total Environment,* **149**(3), 139-144.

Malloum, A., & Conradie, J. (2022). QTAIM analysis dataset for non-covalent interactions in furan clusters. *Data in Brief*, **40,** 107766.

Manjunatha, R., Usharani, K., Naik, D. J. J. O. P., & Phytochemistry. (2019). Synthesis and characterization of ZnO nanoparticles: A review. ***8***(3), 1095-1101.

Martucci, A., Pasti, L., Marchetti, N., Cavazzini, A., Dondi, F., & Alberti, A. (2012). Adsorption of pharmaceuticals from aqueous solutions on synthetic zeolites. *Microporous and Mesoporous Materials,* **148**(1), 174-183.

Massobrio, C., & Blandin, P. (1996). Classical and First Principles Molecular Dynamics Simulations in Material Science: Application to Structural and Dynamical Properties of Free and Supported Clusters. *In Stability of Materials* (pp. 295-324). Boston, MA: Springer US.

Masukume, M., Onyango, M. S., Aoyi, O., & Otieno, F. (2013). Nitrate removal from groundwater using modified natural zeolite. *Water Institute of Southern Africa*, **26**.

Matei, E., Predescu, A. M., Râpă, M., Tarcea, C., Pantilimon, C. M., Favier, L., ... & Predescu, C. (2019). Removal of Chromium (VI) from aqueous solution using a novel green magnetic nanoparticle–chitosan adsorbent. *Analytical Letters,* **52**(15), 2416-2438.

Mayo, S. L., Olafson, B. D., & Goddard, W. A. (1990). DREIDING: a generic force field for molecular simulations. *Journal of Physical chemistry,* ***94***(26), 8897-8909.

McCusker, L., & Baerlocher, C. (2019). Zeolites.

Meena, A. K., Mishra, G., Rai, P., Rajagopal, C., & Nagar, P. (2005). Removal of heavy metal ions from aqueous solutions using carbon aerogel as an adsorbent. *Journal of Hazardous materials,* ***122***(1-2), 161-170.

Mehta, M. J., & Chorawala, K. K. (2014). Adsorptive removal of dye from industrial dye effluents using low-cost adsorbents: a review. *Journal. Engineering. Research. Applied,* **4**(12), 40-44..

Mehta, R., Brahmbhatt, H., Saha, N. K., & Bhattacharya, A. (2015). Removal of substituted phenyl urea pesticides by reverse osmosis membranes: laboratory scale study for field water application. *Desalination,* **358**, 69-75.

Mhadhbi, L., Beiras, R. J. W., Air,, & Pollution, S. (2012). Acute toxicity of seven selected pesticides (alachlor, atrazine, dieldrin, diuron, pirimiphos-methyl, chlorpyrifos, diazinon) to the marine fish (turbot, Psetta maxima). *Water, Air, & Soil Pollution,* ***223*****(**9), 5917-5930.

Mingyue, C., Shuying, N., Yantao, Z., Muhammad, S. R., Yi, X., Molokeev, M. S., & Fuqiang, H. (2020). Renewable P-type zeolite for superior absorption of heavy metals: Isotherms, kinetics, and mechanism.

Mir, J. M. (2020). Molecular electron density and nitrate-phosphate sorption efficiency of zeolite-A: Physico-chemical and DFT analyses. *Indian Journal of Chemistry-Section A (IJCA*), **59**(7), 939-947.

Mirbaloochzehi, M. R., Rezvani, A., Samimi, A., & Shayesteh, M. (2020). Application of a novel surfactant-modified natural nano-zeolite for removal of heavy metals from drinking water. Advanced Journal of Chemistry-Section A, **3**(5), 612-620.

Mirenga, E. O. a. (2018). Biodegradation kinetics of chlorpyrifos and diuron degrading bacterial isolates from the nzoia river drainage basin, kenya. MMUST,

Mo, Q., Yang, X., Wang, J., Xu, H., Li, W., Fan, Q., & Zhang, Y. (2021). Adsorption mechanism of two pesticides on polyethylene and polypropylene microplastics: DFT calculations and particle size effects. *Environmental Pollution*, **291**, 118120.

Mohamed Noor, M. H., Wong, S., Ngadi, N., Mohammed Inuwa, I., & Opotu, L. A. (2022). Assessing the effectiveness of magnetic nanoparticles coagulation/flocculation in water treatment: a systematic literature review. *International Journal of Environmental Science and Technology,* **19**(7), 6935-6956.

Mohammadi, M. D., Abbas, F., Louis, H., Mathias, G. E., & Unimuke, T. O. (2022). Trapping of CO, CO_2, H_2S, NH_3, NO, NO_2, and SO_2 by polyoxometalate compound. *Computational and Theoretical Chemistry, **1215**,* 113826.

Mohod, C. V., & Dhote, J. (2013). Review of heavy metals in drinking water and their effect on human health. *International Journal of Innovative Research in Science, Engineering and Technology,* **2**(7), 2992-2996.

Morad, R., Akbari, M., & Maaza, M. (2023). Theoretical study of chemical reactivity descriptors of some repurposed drugs for COVID-19. *Mrs Advances*, **8**(11), 656-660.

Moosavi, S., Lai, C. W., Gan, S., Zamiri, G., Akbarzadeh Pivehzhani, O., & Johan, M. R. (2020). Application of efficient magnetic particles and activated carbon for dye removal from wastewater. *ACS omega*, *5*(33), 20684-20697.

Moretto, J. A. S., Furlan, J. P. R., Fernandes, A. F. T., Bauermeister, A., Lopes, N. P., & Stehling, E. G. (2019). Alternative biodegradation pathway of the herbicide diuron. *International biodeterioration & biodegradation,* **143**, 104716.

Moshoeshoe, M., Nadiye-Tabbiruka, M. S., & Obuseng, V. (2017). A review of the chemistry, structure, properties and applications of zeolites. *Am. J. Mater. Sci*, **7**(5), 196-221.

Mouni, L., Belkhiri, L., Bollinger, J. C., Bouzaza, A., Assadi, A., Tirri, A., Remini, H. (2018). Removal of Methylene Blue from aqueous solutions by adsorption on Kaolin: Kinetic and equilibrium studies. *Applied Clay Science*, **153**, 38-45.

Mukherjee, A., Mehta, R., Saha, S., Bhattacharya, A., Biswas, P. K., & Kole, R. K. (2020). Removal of multiple pesticide residues from water by low-pressure thin-film composite membrane. *Applied Water Science,* **10**, 1-8.

Mukti, R. R. (2016). Characteristics of heavy metals adsorption Cu, Pb and Cd using synthetics zeolite Zsm-5. *Journal of Tropical Soils,* **20**(2), 77-83.

Munene, M. J. (2019). Sequestering Of Selected Heavy Metal Ions In Wastewater From Industrial Area In Nairobi Using Water Hyacinth As A Low Cost Adsorbent (Doctoral dissertation, *University of Nairobi).*

Murkani, M., Nasrollahi, M., Ravanbakhsh, M., Bahrami, P., & Jaafarzadeh Haghighi Fard, N. (2015). Evaluation of natural zeolite clinoptilolite efficiency for the removal of ammonium and nitrate from aquatic solutions. *Environmental Health Engineering and Management Journal,* **2**(1), 17-22.

Musa, F. S., Abdelrahim, A. I., & Abd El aziz Elnasri, H. (2020). Determination of Lead and Cadmium concentration in water used by food providers in Bahri Locality-Sudan. EAS J *Nutrition Food Science*, **2**(2), 33-38.

Mutavi, F., Aarts, N., Van Paassen, A., Heitkönig, I., & Wieland, B. (2018). Techne meets Metis: Knowledge and practices for tick control in Laikipia County, Kenya. *NJAS-Wageningen Journal of Life Sciences*, **86**, 136-145.

Mutua, F. N., Njogu, P., & Kanali, C. (2021). Distribution and Concentrations of Heavy Metals in Tropospheric Suspended Particulate Matter (PM10) In Nairobi City, Kenya. *Open Journal of Applied Sciences,* **11**(8), 899-907.

Mwatsahu, S. H., Wanjau, R., Tole, M., & Munga, D. (2020). Heavy metal contamination in water, sediments, and fauna of selected areas along the Kenyan coastline. *Indo Pacific Journal of Ocean Life*, **4**(1).

Mwove, J., Imathiu, S., Orina, I., & Karanja, P. (2023). Environmental exposure assessment of lead and cadmium in street vended foods sold in selected locations in Kenya. *Food science & nutrition,* **11**(6), 2610-2619.

Naghizadeh, A., Nasseri, S., & Nazmara, S. (2011). Removal of trichloroethylene from water by adsorption on to multiwall carbon nanotubes.

Nagpal, M., & Kakkar, R. (2019). Use of metal oxides for the adsorptive removal of toxic organic pollutants. *Separation and Purification Technology*, **211**, 522-539.

Nair, S., Hussain, A. H. M. S., & Tatarchuk, B. J. (2013). The role of surface acidity in adsorption of aromatic sulfur heterocycles from fuels. *Fuel, **105**,* 695-704.

Nakhli, A., Bergaoui, M., Toumi, K. H., Khalfaoui, M., Benguerba, Y., Balsamo, M., ... & Erto, A. (2020). Molecular insights through computational modeling of methylene blue adsorption onto low-cost adsorbents derived from natural materials: A multi-model's approach. *Computers & Chemical Engineering*, **140**, 106965.

Nandi, N. K., Vyas, A., Akhtar, M. J., & Kumar, B. (2022). The growing concern of chlorpyrifos exposures on human and environmental health. *Pesticide biochemistry and physiology,* **185**, 105138.

Nantaba, F., Wasswa, J., Kylin, H., Palm, W. U., Bouwman, H., & Kümmerer, K. (2020). Occurrence, distribution, and ecotoxicological risk assessment of selected pharmaceutical compounds in water from Lake Victoria, Uganda. *Chemosphere,* **239,** 124642.

Narayanan, N., Gupta, S., & Gajbhiye, V. T. (2020). Decontamination of pesticide industrial effluent by adsorption–coagulation–flocculation process using biopolymer-nanoorganoclay composite. International *Journal of Environmental Science and Technology*, **17**, 4775-4786.

Nasseri Maleki, G., Bayati Khatibi, M., Khamnian, Z., Jalali, Z., Dastgiri, S., & Ghodrati Aroogh, H. J. I. J. o. E. H. R. (2022). Association between nitrate concentration in drinking water and rate of colorectal cancer: *A case study in northwestern Iran.* **32**(8), 1791-1800.

Ngeno, E. C., Orata, F., Lilechi, D., Shikuku, V. O., & Kimosop, S. J. J. C. C. E. (2016). Adsorption of caffeine and ciprofloxacin onto pyrolitically derived water hyacinth biochar: isothermal, kinetic and thermodynamic studies. ***10*****,** 185-194.

Ngeno, E. C., Shikuku, V. O., Orata, F., Baraza, L. D., & Kimosop, S. J. (2019). Caffeine and ciprofloxacin adsorption from water onto clinoptilolite: Linear isotherms, kinetics, thermodynamic and mechanistic studies. *South African Journal of Chemistry*, **72**, 136-142.

Nie, J., Sun, Y., Zhou, Y., Kumar, M., Usman, M., Li, J., & Tsang, D. C. (2020). Bioremediation of water containing pesticides by microalgae: Mechanisms, methods, and prospects for future research. *Science of the Total Environment*, **707,** 136080.

Nurain, A., Sarker, P., Rahaman, M. S., Rahman, M. M., & Uddin, M. K. (2021). Utilization of banana (Musa sapientum) peel for removal of pb^{2+} from aqueous solution. Journal of Multidisciplinary Applied Natural Science.

Nyabiba, A. M. (2022). Microbial Degradation Of Chlorpyrifos Residues And Their Effects On Calcium Levels In Fresh And Processed Milk In Nakuru County, Kenya. *KENYATTA UNIVERSITY,*

Obasi, P. N., & Akudinobi, B. B. (2020). Potential health risk and levels of heavy metals in water resources of lead–zinc mining communities of Abakaliki, southeast Nigeria. *Applied Water Science,* **10**(7), 1-23.

Obotey Ezugbe, E., & Rathilal, S. (2020). Membrane technologies in wastewater treatment: a review. *Membranes*, **10**(5), 89.

Odoemelam, S. A., Onwu, F. K., Uchechukwu, S. C., & Chinedu, M. A. (2015). Adsorption isotherm studies of Cd (ll) and Pb (ll) ions from aqueous solutions by bamboo-based activated charcoal and bamboo dust. *American Chemical Science Journal,* ***5***(3), 253-269.

Ojha, A. (2020). Materials in electrochemical detection of water pollutants. In *Sensors in Water Pollutants Monitoring: Role of Material* (pp. 161-185): Springer.

Okello, V. A., Kimosop, S. J., Getenga, Z. M., Orata, F., & Shikuku, V. O. (2017). Green remediation of carbamazepine from water using novel magnetic iron modified carbonized baggasse: kinetics, equilibrium and mechanistic studies.

Onyango, M. S., Masukume, M., Ochieng, A., & Otieno, F. (2010). Functionalised natural zeolite and its potential for treating drinking water containing excess amount of nitrate. *Water South Africa,* ***36***(5).

Orata, F. (2020). Chemicals of emerging concern in surface and wastewater: a perspective of their fate within the lake victoria catchment area of Kenya. In *Effects of Emerging Chemical Contaminants on Water Resources and Environmental Health* (pp. 1-16): IGI Global.

Oremo, J., Orata, F., Owino, J., & Shivoga, W. (2020). Assessment of available phosphates and nitrates levels in water and sediments of River Isiukhu, Kenya. *Applied ecology and environmental journal*

Othmani, A., Magdouli, S., Kumar, P. S., Kapoor, A., Chellam, P. V., & Gökkuş, Ö. (2022). Agricultural waste materials for adsorptive removal of phenols, chromium (VI) and cadmium (II) from wastewater: A review. *Environmental Research*, **204,** 111916.

Otieno, P., Okinda Owuor, P., Lalah, J. O., Pfister, G., & Schramm, K. W. (2015). Monitoring the occurrence and distribution of selected organophosphates and carbamate pesticide residues in the ecosystem of Lake Naivasha, Kenya. *Toxicological & Environmental Chemistry,* **97**(1), 51-61.

Ouki, S. K., & Kavannagh, M. (1997). Performance of natural zeolites for the treatment of mixed metal-contaminated effluents. *Waste Management & Research,* ***15***(4), 383-394.

Ouma, I. L., Naidoo, E. B., & Ofomaja, A. E. (2018). Thermodynamic, kinetic and spectroscopic investigation of arsenite adsorption mechanism on pine cone-magnetite composite. *Journal of Environmental Chemical Engineering,* **6**(4), 5409-5419.

Ouma, J., Gachanja, A., Mugo, S., & Gikunju, J. (2021). Antibiotic residues in milk from Juja and Githurai markets in Kenya by liquid chromatography-tandem mass spectrometry. *Chemistry Africa,* **4(**4), 769-775.

Outa, J. O., Kowenje, C. O., Plessl, C., & Jirsa, F. (2020). Distribution of arsenic, silver, cadmium, lead and other trace elements in water, sediment and macrophytes in the Kenyan part of Lake Victoria: spatial, temporal and bioindicative aspects. *Environmental Science and Pollution Research,* **27**, 1485-1498.

Pan, S., Shen, H., Xu, Q., Luo, J., & Hu, M. (2012). Surface mercapto engineered magnetic Fe3O4 nanoadsorbent for the removal of mercury from aqueous solutions. *Journal of colloid and interface science,* ***365***(1), 204-212.

Pan, S., Shen, H., Xu, Q., Luo, J., & Hu, M. (2012). Surface mercapto engineered magnetic Fe3O4 nanoadsorbent for the removal of mercury from aqueous solutions. *Journal of colloid and interface science,* **365**(1), 204-212..

Panda, L., & Dash, S. (2020). Characterization and utilization of coal fly ash: a review. *Emerging Materials Research*, **9**(3), 921-934.

Pandey, G., & Madhuri, S. (2014). Heavy metals causing toxicity in animals and fishes. *Research Journal of Animal, Veterinary and Fishery Sciences, **2***(2), 17-23.

Pandey, S. (2017). A comprehensive review on recent developments in bentonite-based materials used as adsorbents for wastewater treatment. *Journal of Molecular Liquids,* **241,** 1091-1113.

Pandiyan, J., Mahboob, S., Govindarajan, M., Al-Ghanim, K. A., Ahmed, Z., Al-Mulhm, N., & Krishnappa, K. (2021). An assessment of level of heavy metals pollution in the water, sediment and aquatic organisms: A perspective of tackling environmental threats for food security. *Saudi Journal of Biological Sciences*, **28**(2), 1218-1225.

Patel, M., Kumar, R., Kishor, K., Mlsna, T., Pittman Jr, C. U., & Mohan, D. (2019). Pharmaceuticals of emerging concern in aquatic systems: chemistry, occurrence, effects, and removal methods. *Chemical reviews*, **119**(6), 3510-3673.

Pembere, A. M. (2014). Investigation of heavy metals in cowpeas, kales and sweet potatoes grown in bungoma and kakamega counties, western kenya. University of Nairobi,

Pérez-Botella, E., Valencia, S., & Rey, F. (2022). Zeolites in adsorption processes: State of the art and future prospects. *Chemical Reviews,* **122**(24), 17647-17695.

Perraki, T., & Orfanoudaki, A. (2004). Mineralogical study of zeolites from Pentalofos area, Thrace, Greece. *Applied Clay Science,* **25**(1-2), 9-16.

Perry, J., Cotton, J., Rahman, M. A., & Brumby, S. A. (2020). Organophosphate exposure and the chronic effects on farmers: a narrative review. *Rural and Remote Health,* **20**(1), 206-222.

Pham, T.-H., Lee, B.-K., Kim, J., & Lee, C. H. (2016). Enhancement of CO_2 capture by using synthesized nano-zeolite. *Journal of the Taiwan Institute of Chemical Engineers,* ***64*****,** 220-226.

Praveena, S. M., Shaifuddin, S. N. M., Sukiman, S., Nasir, F. A. M., Hanafi, Z., Kamarudin, N., ... & Aris, A. Z. (2018). Pharmaceuticals residues in selected tropical surface water bodies from Selangor (Malaysia): Occurrence and potential risk assessments. *Science of the total environment,* **642**, 230-240.

Praveenkumarreddy, Y., Vimalkumar, K., Ramaswamy, B. R., Kumar, V., Singhal, R. K., Basu, H., ... & Balakrishna, K. (2021). Assessment of non-steroidal anti-inflammatory drugs from selected wastewater treatment plants of Southwestern Indi*a. Emerging Contaminants*, **7**, 43-51.

Pukcothanung, Y., Siritanon, T., & Rangsriwatananon, K. (2018). The efficiency of zeolite Y and surfactant-modified zeolite Y for removal of 2, 4-dichlorophenoxyacetic acid and 1, 1′-dimethyl-4, 4′-bipyridinium ion. *Microporous and Mesoporous Materials,* **258**, 131-140.

Qalyoubi, L., Al-Othman, A., & Al-Asheh, S. J. E. R. (2022). Removal of ciprofloxacin antibiotic pollutants from wastewater using nano-composite adsorptive membranes. **215**, 114182.

Qasim, S. R., & Zhu, G. (2017). Wastewater Treatment and Reuse Theory and Design Examples, Volume 2:: Post-Treatment, Reuse, and Disposal: CRC press.

Qayoom, I., & Jaies, I. (2023). Phytoremediation potential of macrophytes against heavy metals, nitrates and phosphates: A review. *Environment Conservation Journal,* **24**(1), 273-280.

Qu, J., Tian, X., Jiang, Z., Cao, B., Akindolie, M. S., Hu, Q., Zhang, Y. (2020). Multi-component adsorption of Pb (II), Cd (II) and Ni (II) onto microwave-functionalized cellulose: Kinetics, isotherms, thermodynamics, mechanisms and application for electroplating wastewater purification. *Journal of Hazardous materials,* ***387***, 121718.

Rad, L. R., & Anbia, M. (2021). Zeolite-based composites for the adsorption of toxic matters from water: A review. *Journal of Environmental Chemical Engineering,* **9**(5), 106088.

Rahimzadeh, M. R., Rahimzadeh, M. R., Kazemi, S., & Moghadamnia, A. A. (2017). Cadmium toxicity and treatment: An update. *Caspian journal of internal medicine,* **8**(3), 135.

Rahman, Z., & Singh, V. P. (2019). The relative impact of toxic heavy metals (THMs)(arsenic (As), cadmium (Cd), chromium (Cr)(VI), mercury (Hg), and lead (Pb)) on the total environment: an overview. *Environmental monitoring and assessment,* **191**, 1-21.

Ramalingam, S., Panneerselvam, B., & Kaliappan, S. P. (2022). Effect of high nitrate contamination of groundwater on human health and water quality index in semi-arid region, South India. *Arabian Journal of Geosciences,* **15**(3), 242.

Rathi, B. S., & Kumar, P. S. (2021). Application of adsorption process for effective removal of emerging contaminants from water and wastewater. *Environmental Pollution*, **280**, 116995.

Raza, H., Yildiz, I., Yasmeen, F., Munawar, K. S., Ashfaq, M., Abbas, M., & Ahmad, N. (2021). Synthesis of a 2D copper (II)-carboxylate framework having ultrafast adsorption of organic dyes. *Journal of Colloid and Interface Science*, **602**, 43-54.

Refaat, A., Elhaes, H., & Ibrahim, M. A. (2023). Effect of alkali metals on physical and spectroscopic properties of cellulose. *Scientific Reports,* **13**(1), 21649.

Ren, L., Xu, J., Zhang, Y., Zhou, J., Chen, D., & Chang, Z. (2019). Preparation and characterization of porous chitosan microspheres and adsorption performance for hexavalent chromium. *International journal of biological macromolecules, **135***, 898-906.

Revellame, E. D., Fortela, D. L., Sharp, W., Hernandez, R., & Zappi, M. E. (2020). Adsorption kinetic modeling using pseudo-first order and pseudo-second order rate laws: A review. *Cleaner Engineering and Technology,* **1**, 100032..

Rezaei-Sameti, M., & Zarei, P. N. B. O. (2018). NBO, AIM, HOMO–LUMO and thermodynamic investigation of the nitrate ion adsorption on the surface of pristine, Al and Ga doped BNNTs: A DFT study. *Adsorption*, **24(**8), 757-767.

Ritschl, F., Fait, M., Fiedler, K., Köhler, J. E., Kubias, B., & Meisel, M. (2002). An Extension of the Consistent Valence Force Field (CVFF) with the Aim to Simulate the Structures of Vanadium Phosphorus Oxides and the Adsorption of n-Butane and of 1-Butene on their Crystal Planes. *Zeitschrift für anorganische und allgemeine Chemie, **628(***6), 1385-1396.

Safi, J., Awad, Y., & El-Nahhal, Y. (2014). Bioremediation of diuron in soil environment: influence of cyanobacterial mat. *American Journal of Plant Sciences*, 2014.

Sahoo, T. R., & Prelot, B. (2020). Adsorption processes for the removal of contaminants from wastewater: the perspective role of nanomaterials and nanotechnology. In *Nanomaterials for the detection and removal of wastewater pollutants* (pp. 161-222): Elsevier.

Salahshoori, I., Jorabchi, M. N., Ghasemi, S., Golriz, M., Wohlrab, S., & Khonakdar, H. A. (2023). Advancements in wastewater Treatment: A computational analysis of adsorption characteristics of cationic dyes pollutants on amide Functionalized-MOF nanostructure MIL-53 (Al) surfaces. *Separation and Purification Technology*, **319,** 124081.

Sathishkumar, P., Meena, R. A. A., Palanisami, T., Ashokkumar, V., Palvannan, T., & Gu, F. L. (2020). Occurrence, interactive effects and ecological risk of diclofenac in environmental compartments and biota-a review. *Science of the total environment,* **698,** 134057.

Sawyer, C. N., McCarty, P. L., & Parkin, G. F. (2003). Chemistry for environmental engineering and science (Vol. 5): *McGraw-Hill* New York.

Sayed, M. A., & Khater, M. S. (2013). Removing cadmium and lead from wastewater using natural zeolite isotherm models. *Middle East Journal of Applied Sciences,* **3**(3), 98-104.

Sayo, S., Kiratu, J. M., & Nyamato, G. S. (2020). Heavy metal concentrations in soil and vegetables irrigated with sewage effluent: A case study of Embu sewage treatment plant, Kenya. *Scientific African,* **8,** 00337

Sepehri, S., Heidarpour, M., & Abedi-Koupai, J. (2014). Nitrate removal from aqueous solution using natural zeolite-supported zero-valent iron nanoparticles. *Soil & Water Research*, **9**(4)

Schulman, E., Wu, W., & Liu, D. (2020). Two-dimensional zeolite materials: structural and acidity properties. *Materials,* **13**(8), 1822.

Schullehner, J., Hansen, B., Thygesen, M., Pedersen, C. B., & Sigsgaard, T. (2018). Nitrate in drinking water and colorectal cancer risk: A nationwide population-based cohort study. *International journal of cancer,* **143**(1), 73-79.

Shafique, U., Ijaz, A., Salman, M., uz Zaman, W., Jamil, N., Rehman, R., & Javaid, A. (2012). Removal of arsenic from water using pine leaves. J*ournal of the Taiwan Institute of Chemical Engineers*, **43**(2), 256-263.

Shaheen, S. M., Derbalah, A. S., & Moghanm, F. S. (2012). Removal of heavy metals from aqueous solution by zeolite in competitive sorption system. *International Journal of Environmental Science and Development,* **3**(4), 362-367.

Shalaby, S. E., El-Saadany, S. S., Abo-Eyta, A. M., Abdel-Satar, A. M., Al-Afify, A. D. G., & Abd El-Gleel, W. M. M. (2018). Levels of pesticide residues in water, sediment, and fish samples collected from Nile River in Cairo, Egypt. *Environmental Forensics,* **19**(4), 228-238.

Sharma, A., Kapoor, D., Wang, J., Shahzad, B., Kumar, V., Bali, A. S.,Yan, D. J. P. (2020). Chromium bioaccumulation and its impacts on plants: an overview. *plants* ***9***(1), 100.

Sharma, J. K., Srivastava, P., Ameen, S., Akhtar, M. S., Singh, G., & Yadava, S. (2016). Azadirachta indica plant-assisted green synthesis of Mn_3O_4 nanoparticles:

Excellent thermal catalytic performance and chemical sensing behavior. *Journal of colloid and interface science,* **472**, 220-228.

Sharma, S., & Singh, B. (2014). Metabolism and persistence of imidacloprid in different types of soils under laboratory conditions. I*nternational Journal of Environmental Analytical Chemistry*, **94**(11), 1100-1112.

Sheikhi, M., & Rezaei, H. (2021). Adsorption of hexavalent chromium ions from aqueous solutions using nano-chitin: kinetic, isotherms and thermodynamic studies. *Water Practice & Technology,* **16**(2), 436-451.

Shi, W., & Maginn, E. J. (2007). Continuous fractional component Monte Carlo: an adaptive biasing method for open system atomistic simulations. *Journal of chemical theory and computation,* **3**(4), 1451-1463.

Shikuku, V. O., & Jemutai-Kimosop, S. (2020). Efficient removal of sulfamethoxazole onto sugarcane bagasse-derived biochar: Two and three-parameter isotherms, kinetics and thermodynamics. *South African Journal of Chemistry,* **73**(1), 111-119.

Shikuku, V. O., Kowenje, C. O., Donato, F. F., Zanella, R., & Prestes, O. D. (2015). A comparison of adsorption equilibrium, kinetics and thermodynamics of aqueous phase clomazone between faujasite X and a natural zeolite from Kenya. *South African Journal of Chemistry,* **68**(1), 245-252.

Shikuku, V. O., Zanella, R., Kowenje, C. O., Donato, F. F., Bandeira, N., & Prestes, D. (2017). Single and competitive removal of sulfachloropyridazine and sulfadimethoxine onto natural kaolinite clay: kinetics, isotherms and thermodynamics studies. *South African Journal of Chemistry* ***70*****(**1), 120-126.

Shiroudi, A., Śmiechowski, M., Czub, J., & Abdel-Rahman, M. A. (2024). Computational analysis of substituent effects on proton affinity and gas-phase basicity of TEMPO derivatives and their hydrogen bonding interactions with water molecules. *Scientific Reports*, **14**(1), 8434.

Sholl, D. S. (2006). Understanding macroscopic diffusion of adsorbed molecules in crystalline nanoporous materials via atomistic simulations. *Accounts of Chemical Research,* **39(**6), 403-411.

Shraim, A. M. (2017). Rice is a potential dietary source of not only arsenic but also other toxic elements like lead and chromium. *Arabian Journal of Chemistry*, **10**, 3434-3443.

Shrestha, J., Kandel, M., Subedi, S., & Shah, K. K. (2020). Role of nutrients in rice (Oryza sativa L.): A review. *Agrica*, **9**(1), 53-62.

Shultana, S., & Khan, R. A. (2022). Water quality assessment, reasons of river water pollution, impact on human health and remediation of polluted river water. *GSC Advanced Research and Reviews,* **10**(2), 107-115.

Sihombing, J. L., Gea, S., Pulungan, A. N., Agusnar, H., Wirjosentono, B., & Hutapea, Y. A. (2018, December). The characterization of Sarulla natural zeolite crystal and its morphological structure. *In AIP Conference Proceedings (Vol. 2049, No. 1). AIP Publishing.*

Singanan, M. (2011). Removal of lead (II) and cadmium (II) ions from wastewater using activated biocarbon. *Science Asia,* **37**(2), 115-119.

Singh, G., Kim, I. Y., Lakhi, K. S., Srivastava, P., Naidu, R., & Vinu, A. (2017). Single step synthesis of activated bio-carbons with a high surface area and their excellent CO2 adsorption capacity. *Carbon,* **116**, 448-455.

Singh, N. B. (2016). Removal of arsenic from aqueous solution by an adsorbent nickel ferrite-polyaniline nanocomposite. *Indian Journal of Chemical Technology (IJCT),* **23**(5), 374-383.

Singh, V., Patra, S., Murugan, N. A., Toncu, D.-C., & Tiwari, A. J. M. A. (2022). Recent trends in computational tools and data-driven modeling for advanced materials. *Materials Advances, **3**(10), 4069-4087*.

Singh, S., Wasewar, K. L., & Kansal, S. K. (2020). Low-cost adsorbents for removal of inorganic impurities from wastewater. In *Inorganic pollutants in water* (pp. 173-203). Elsevier.

Singh, B. M., Singh, D., & Dhal, N. K. (2022). Enhanced phytoremediation strategy for sustainable management of heavy metals and radionuclides. *Case Studies in Chemical and Environmental Engineering*, *5*, 100176.

Singhal, M., Agrawal, M., Bhavna, K., Sethiya, N. K., Bhargava, S., Gondkar, K. S., Arora, M. K. (2023). Chloramphenicol and tetracycline (broad spectrum antibiotics). In *Antibiotics-Therapeutic Spectrum and Limitations* (pp. 155-165): Elsevier.

Š Šolić, M., Maletić, S., Isakovski, M. K., Nikić, J., Watson, M., Kónya, Z., & Rončević, S. (2021). Removing low levels of Cd (II) and Pb (II) by adsorption on two types of oxidized multiwalled carbon nanotubes. *Journal of Environmental Chemical Engineering*, **9**(4), 105402.

Somashekara, D., & Mulky, L. (2023). Sequestration of contaminants from wastewater: a review of adsorption processes. *ChemBioEng Reviews,* **10**(4), 491-509.

Soufan, M., Deborde, M., & Legube, B. (2012). Aqueous chlorination of diclofenac: kinetic study and transformation products identification. *Water research,* **46**(10), 3377-3386.

Sprynskyy, M., Buszewski, B., Terzyk, A. P., & Namieśnik, J. (2006). Study of the selection mechanism of heavy metal (Pb^{2+}, Cu^{2+}, $Ni^{2+,}$ and Cd^{2+}) adsorption on clinoptilolite. *Journal of colloid and interface science,* ***304***(1), 21-28.

S Srikhaow, A., Chaengsawang, W., Kiatsiriroat, T., Kajitvichyanukul, P., & Smith, S. M. (2022). Adsorption kinetics of imidacloprid, acetamiprid and methomyl pesticides in aqueous solution onto eucalyptus woodchip derived biochar. *Minerals,* **12**(5), 528.

Steinmaus, C., Miller, M. D., & Smith, A. H. (2010). Perchlorate in drinking water during pregnancy and neonatal thyroid hormone levels in California. *Journal of Occupational and Environmental Medicine*, 1217-1224.

S Stork, P. R., Bennett, F. R., & Bell, M. J. (2008). The environmental fate of diuron under a conventional production regime in a sugarcane farm during the plant cane phase. *Pest Management Science: Formerly Pesticide Science,* **64**(9), 954-963.

Syafrudin, M., Kristanti, R. A., Yuniarto, A., Hadibarata, T., Rhee, J., Al-Onazi, W. A., ... & Al-Mohaimeed, A. M. (2021). Pesticides in drinking water a review. *International journal of environmental research and public health*, **18**(2), 468.

Syam Babu, D., Anantha Singh, T. S., Nidheesh, P. V., & Suresh Kumar, M. (2020). Industrial wastewater treatment by electrocoagulation process. *Separation Science and Technology*, **55**(17), 3195-3227.

Tambosi, J. L., Yamanaka, L. Y., José, H. J., Moreira, R. d. F. P. M., & Schröder, H. F. (2010). Recent research data on the removal of pharmaceuticals from sewage treatment plants (STP). *Química Nova, **33**(*2), 411-420.

Tan, Z., Yang, X., Chen, L., Liu, Y., Xu, H.-J., Li, Y., & Gong, B. J. B. T. (2022). Biodegradation mechanism of chloramphenicol by Aeromonas media SZW3 and genome analysis. **344**, 126-280.

Tang, L., Ma, X. Y., Wang, Y., Zhang, S., Zheng, K., Wang, X. C., & Lin, Y. (2020). Removal of trace organic pollutants (pharmaceuticals and pesticides) and reduction of biological effects from secondary effluent by typical granular activated carbon. *Science of the Total Environment*, **749**, 141611.

Tao, Y., Han, L., Li, X., Han, Y., & Liu, Z. (2016). Molecular structure, spectroscopy (FT-IR, FT-Raman), thermodynamic parameters, molecular electrostatic potential and HOMO-LUMO analysis of 2, 6-dichlorobenzamide. *Journal of Molecular Structure*, **1108**, 307-314.

Tarannum, N., & Khan, R. (2020). Cost-effective green materials for the removal of pesticides from aqueous medium. In *Green Materials for Wastewater Treatment* (pp. 99-130): Springer.

Tare, V., Chaudhari, S., & Jawed, M. (1992). Comparative evaluation of soluble and insoluble xanthate process for heavy metal removal from wastewaters. *Water Science and Technology*, **26**(1-2), 237-246.

Tekin, Z., Er, E. Ö., Günkara, Ö. T., & Bakırdere, S. (2020). A novel determination method for diuron in seaweed samples: combination of quadruple isotope dilution strategy with liquid chromatography-quadrupole time of flight-tandem mass spectrometry for superior accuracy and precision. *Journal of Chromatography A*, **1611**, 460612.

Thakur, M., & Pathania, D. (2020). Environmental fate of organic pollutants and effect on human health. In *Abatement of Environmental Pollutants* (pp. 245-262): Elsevier.

Thommes, M., Kaneko, K., Neimark, A. V., Olivier, J. P., Rodriguez-Reinoso, F., Rouquerol, J., & Sing, K. S. (2015). Physisorption of gases, with special reference to the evaluation of surface area and pore size distribution (IUPAC Technical Report). *Pure and applied chemistry,* **87(**9-10), 1051-1069.

Thommes, M., Kaneko, K., Neimark, A. V., Olivier, J. P., Rodriguez-Reinoso, F., Rouquerol, J., & Sing, K. S. (2015). Physisorption of gases, with special reference to the evaluation of surface area and pore size distribution (IUPAC Technical Report). *Pure and applied chemistry*, **87**(9-10), 1051-1069.

Tibugari, H., Mafere, G., Dube, S., Chakavarika, M., Mandumbu, R., Musara, J. P., ... & Mpofu, N. (2020). Worrying cadmium and lead levels in a commonly cultivated vegetable irrigated with river water in Zimbabwe. *Cogent Biology*, **6**(1), 1802814.

Tinkov, A. A., Filippini, T., Ajsuvakova, O. P., Skalnaya, M. G., Aaseth, J., Bjørklund, G., ... & Skalny, A. V. (2018). Cadmium and atherosclerosis: A review of toxicological mechanisms and a meta-analysis of epidemiologic studies. *Environmental research,* **162**, 240-260.

Tran, N. H., Reinhard, M., & Gin, K. Y. H. (2018). Occurrence and fate of emerging contaminants in municipal wastewater treatment plants from different geographical regions-a review. *Water research,* **133**, 182-207.

Tran, Q. T., Do, T. H., Ha, X. L., Nguyen, H. P., Nguyen, A. T., Ngo, T. C. Q., & Chau, H. D. (2022). Study of the ciprofloxacin adsorption of activated carbon prepared from mangosteen peel. Applied Sciences, **12**(17), 8770.

Treacy, M. M., Higgins, J. B., & von Ballmoos, R. (1996). Collection of simulated XRD powder patterns for zeolites (Vol. 552): Elsevier New York.

Tyagi, B., & Kumar, N. (2021). Bioremediation: Principles and applications in environmental management. *In Bioremediation for environmental sustainability* (pp. 3-28): Elsevier.

Uzunova, E. L., & Mikosch, H. (2016). Adsorption of phosphates and phosphoric acid in zeolite clinoptilolite: electronic structure study. *Microporous and Mesoporous Materials,* ***232*****,** 119-125.

Vane, C. H., Kim, A. W., dos Santos, R. A. L., Gill, J. C., Moss-Hayes, V., Mulu, J. K., ... & Olaka, L. A. (2022). Impact of organic pollutants from urban slum informal settlements on sustainable development goals and river sediment quality, Nairobi, Kenya, Africa. *Applied Geochemistry,* **146,** 105468.

Vardhan, K. H., Kumar, P. S., & Panda, R. C. (2019). A review on heavy metal pollution, toxicity and remedial measures: Current trends and future perspectives. *Journal of Molecular Liquids,* **290,** 111-197.

Vela, N., Fenoll, J., Garrido, I., Pérez-Lucas, G., Flores, P., Hellín, P., & Navarro, S. (2019). Reclamation of agro-wastewater polluted with pesticide residues using

sunlight activated persulfate for agricultural reuse. *Science of the Total Environment,* **660**, 923-930.

Vessman, J., Stefan, R. I., Van Staden, J. F., Danzer, K., Lindner, W., Burns, D. T., Müller, H. (2001). Selectivity in analytical chemistry (IUPAC Recommendations 2001). *Pure and Applied Chemistry,* **73**(8), 1381-1386.

Von-Kiti, E. (2012). Synthesis of zeolites and their application to the desalination of seawater (Doctoral dissertation).

Wakil, W., Schmitt, T., & Kavallieratos, N. G. (2021). Performance of diatomaceous earth and imidacloprid as wheat, rice and maize protectants against four stored-grain insect pests. J*ournal of stored products research*, **91,** 101759.

Wan, J., Zhang, F., Han, Z., Song, L., Zhang, C., & Zhang, J. (2021). Adsorption of Cd^{2+} and Pb^{2+} by biofuel ash-based geopolymer synthesized by one-step hydrothermal method. *Arabian Journal of Chemistry*, **14(**8), 103234.

Wan, Y., Han, Q., Wang, Y., & He, Z. (2020). Five degradates of imidacloprid in source water, treated water, and tap water in Wuhan, central China. *Science of The Total Environment*, **741**, 140-227.

Wang, C., Wang, H., & Gu, G. (2018). Ultrasound-assisted xanthation of cellulose from lignocellulosic biomass optimized by response surface methodology for Pb (II) sorption. *Carbohydrate polymers*, **182**, 21-28.

Wang, L., Liu, S., Li, J., & Li, S. (2022). Effects of several organic fertilizers on heavy metal passivation in Cd-contaminated gray-purple soil. *Frontiers in Environmental Science*, **10,** 895646.

Wang, M., Li, G., Huang, L., Xue, J., Liu, Q., Bao, N., & Huang, J. (2017). Study of ciprofloxacin adsorption and regeneration of activated carbon prepared from Enteromorpha prolifera impregnated with H_3PO_4 and sodium benzenesulfonate. *Ecotoxicology and environmental safety,* **139**, 36-42.

Wang, S., & Zhu, Z. J. J. O. H. M. (2006). Characterisation and environmental application of an Australian natural zeolite for basic dye removal from aqueous solution. **136**(3), 946-952.

Wang, Y., Li, H., Feng, G., Du, L., & Zeng, D. (2017). Biodegradation of diuron by an endophytic fungus Neurospora intermedia DP8-1 isolated from sugarcane and its potential for remediating diuron-contaminated soils. *PLoS One*, **12**(8), 0182556.

Wanyonyi, F. S., Fidelis, T. T., Mutua, G. K., Orata, F., & Pembere, A. M. (2021). Role of pore chemistry and topology in the heavy metal sorption by zeolites: From molecular simulation to machine learning. *Computational Materials Science, **195***, 110519.

Wasike, P. W., Nawiri, M. P., & Wanyonyi, A. A. (2019). Levels of heavy metals (Pb, Mn, Cu and Cd) in water from river Kuywa and the adjacent wells. *Environment and Ecology Research* **7**(3), 135-138.

Weber Jr, W. J., & Morris, J. C. (1963). Kinetics of adsorption on carbon from solution. *Journal of the sanitary engineering division,* **89**(2), 31-59.

Wasike, P. W. (2015). Analysis of Selected Heavy Metals in Water from River Kuywa and Adjacent Wells in Bungoma Central Sub County-Kenya.*School of Pure and Applied Sciences, Kenyatta University,*

Wilson, M. M., Michieka, R. W., & Mwendwa, S. M. (2021). Assessing the influence of horticultural farming on selected water quality parameters in Maumau stream, a tributary of Nairobi River, Kenya. *Heliyon,* **7**(12).

Wilson, T. R., Alexandrova, A. N., & Eberhart, M. E. (2021). Electron density geometry and the quantum theory of atoms in molecules. *The Journal of Physical Chemistry A*, ***125*****(**50), 10622-10631.

Wołejko, E., Łozowicka, B., Jabłońska-Trypuć, A., Pietruszyńska, M., & Wydro, U. (2022). Chlorpyrifos occurrence and toxicological risk assessment: a review. *International journal of environmental research and public health,* **19**(19), 12209.

Wolfe, A. H., & Patz, J. A. (2002). Reactive nitrogen and human health: acute and long-term implications. Ambio: *A journal of the human environment,* **31**(2), 120-125.

Wong, S., Ngadi, N., Inuwa, I. M., & Hassan, O. (2018). Recent advances in applications of activated carbon from biowaste for wastewater treatment: a short review. *Journal of Cleaner Production,* **175**, 361-375.

Yan, L., Min, Y. A. N. G., & Hong-bin, W. A. N. G. (2008). Study on thermodynamics of soil adsorbing glyphosate. J*ournal Anhui Agricultral Science*, **23**.

Yang, Y., Tian, C., & Zhao, X. (2011). Adsorption kinetics of methylene blue onto Fe-doped sulfated titania. Colloids and Surfaces A: *Physicochemical and Engineering Aspects*, **389**(1-3), 12-17.

Yousefi, T., Mohsen, M. A., Mahmudian, H. R., Torab-Mostaeidi, M., Moosavian, M. A., & Aghayan, H. (2018). Removal of Pb (II) by modified natural adsorbent; thermodynamics and kinetics studies. *Journal of Water and Environmental Nanotechnology*, **3**(3), 265-272.

Yuna, Z. (2016). Review of the natural, modified, and synthetic zeolites for heavy metals removal from wastewater. *Environmental Engineering Science,* ***33***(7), 443-454.

Zamzow, M., Eichbaum, B., Sandgren, K., & Shanks, D. (1990). Removal of heavy metals and other cations from wastewater using zeolites. *Separation science and technology,* ***25***(13-15), 1555-1569.

Zeng, K., Hachem, K., Kuznetsova, M., Chupradit, S., Su, C. H., Nguyen, H. C., & El-Shafay, A. S. (2022). Molecular dynamic simulation and artificial inte/lligence of lead ions removal from aqueous solution using magnetic-ash-graphene oxide nanocomposite. *Journal of Molecular Liquids*, **347**, 118290.

Zeng, S., & Kan, E. (2021). Adsorption and regeneration on iron-activated biochar for removal of microcystin-LR. *Chemosphere,* **273,** 129649.

Zhang, B., Chen, M., Zhang, C., & He, H. J. C. (2019). Electrochemical oxidation of gaseous benzene on a Sb-SnO2/foam Ti nano-coating electrode in all-solid cell. *Chemosphere,* ***217*****,** 780-789.

Zhang, X., Liu, H., Yang, J., Zhang, L., Cao, B., Liu, L., & Gong, W. (2021). Removal of cadmium and lead from aqueous solutions using iron phosphate-modified pollen microspheres as adsorbents. *Reviews on advanced materials science,* **60**(1), 365-376.

Zhao, G., Wu, X., Tan, X., & Wang, X. (2010). Sorption of heavy metal ions from aqueous solutions: a review. *The open colloid science journal,* ***4***(1). '

Zhao, X., Gu, F., Wang, Y., Peng, Z., & Liu, J. (2020). Surface electronegativity as an activity descriptor to screen oxygen evolution reaction catalysts of Li–O_2 battery. *ACS applied materials & interfaces,* ***12***(24), 27166-27175.

Zheng, W., & Liu, W. (1999). Kinetics and mechanism of the hydrolysis of imidacloprid. *Pesticide science,* **55**(4), 482-485.

Zhou, L. J., Li, J., Zhang, Y., Kong, L., Jin, M., Yang, X., & Wu, Q. L. (2019). Trends in the occurrence and risk assessment of antibiotics in shallow lakes in the lower-middle reaches of the Yangtze River basin, China. *Ecotoxicology and Environmental Safety,* **183**, 109511.

Zhu, W., Du, W., Shen, X., Zhang, H., & Ding, Y. (2017). Comparative adsorption of Pb^{2+} and Cd^{2+} by cow manure and its vermicompost. *Environmental Pollution,* 227, 89-97.

APPENDICES

Appendix 1: List of 242 zeolites, in terms of loading of Pb^{2+} ions on the zeolites, as [determined from the Monte Carlo simulations

CODE	Structure	Total density	Pore size (Å)	Average Volume%	Total VolumeÅ^3	Loading Pb^{2+}	Total Energy (kcal/mol)	CPU of time in minutes
ABW	Orthorhombic	0.70370	4.24	5.19%	454.9	2	-15.226	1.33
ACO	Cubic	0.666	4.5	8.68	971.8	6	-72.516	2.43
AEI	Orthorhombic	0.58308	7.33	17.31	3189.4	20	-216.301	4.21
AEL	Orthorhombic	0.76697	5.64	6.77	2084.8	5	-51.079	2.43
AEN	Orthorhombic	0.85777	4.43	4.02	2384.7	8	-98.832	2.52
AET	Orthorhombic	0.69792	8.41	12.88	3953.2	16	-143.248	3.47
AFG	Hexagonal	0.69333	6.37	0	2834.8	12	-153.781	3.35
AF1	Hexagonal	0.7022	8.3	14.07	2834.8	6	-56.583	2.41
AFN	Monoclinic	0.66111	5.25	7.82	1420.6	6	-68.292	2.43
AFO	Orthorhombic	0.76968	5.43	7.23	2082.5	5	-49.94	3.10
AFR	Orthorhombic	0.59923	8.36	19.62	2109.8	12	-124.408	3.14
AFS	Hexagonal	0.56875	9.51	21.6	3827.8	26	-240.262	2.21
AFT	Hexagonal	0.58571	7.75	17.28	4780.6	31	-514.902	5.48
AFV	Trigonal	0.60952	7.08	15.29	1906.4	10	-103.325	3.24
AFX	Hexagonal	0.58571	7.76	17.28	1389.2	20	-207.366	4:22
AFY	Trigonal	0.48889	7.82	21.88	1136.2	9	-74.456	3.30
AHT	Orthorhombic	0.72916	3.95	0	1248.8	4	-41.116	1.43
ANA	Cubic	0.8011	4.21	0	2497.2	16	-202.539	3.28
APC	Orthorhombic	0.69629	4.23	4.8	1808.7	8	-85.822	2.30
APD	Orthorhombic	0.75901	4.93	5.73	1779.1	0	0	2.59
AST	Cubic	0.625	7.94	0	2528.8	8	-83.768	2.54
ASV	Tetragonal	0.66667	5.43	6.98	1047.2	3	37.971	3.32
ATN	Tetragonal	0.70374	5.91	7.3	898	2	-26.513	2.44
ATO	Trigonal	0.7601	5.74	6.93	1917.1	3	-34.75	2.49
ATS	Orthorhombic	0.6400	7.3	15.64	1493.1	6	-52.614	2.50
ATT	Orthorhombic	0.64762	5.42	9.18	702.6	8	-96.289	3.09
ATV	Orthorhombic	0.81666	6.86	3.92	1269	4	-57.909	1.10
AVE	Trigonal	0.65541	6.86	12.39	8707.7	31	-331.65	6.59
AVL	Trigonal	0.61718	7.14	14.36	2653.3	16	-151.309	

								4.28
AWO	Orthorhombic	0.70884	5.16	5.36	2632.8	8	-111.212	3.07
AWW	Tetragonal	0.65608	7.48	12.04	1417.8	12	-128.303	3.14
BCT	Tetragonal	0.81481	3.8	0.45	421.9	0	0	0.26
BEC	Tetragonal	0.65664	6.95	21.18	2115.9	10	-75.666	3.54
BIK	Orthorhombic	0.90740	4.17	3.98	642.9	2	-23.224	2.10
BOF	Orthorhombic	0.76190	5.58	9.06	1313.6	4	-51.745	3.14
BOG	Orthorhombic	0.6599	8.05	18.13	5978.9	40	-385.525	2.52
BOZ	Orthorhombic	0.64761	8.71	22.27	7112.1	52	-512.205	10.28
BPH	Hexagonal	0.56875	9.51	21.65	1914.8	2	-11.414	2.10
BRE	Monoclinic	0.77803	5.29	6.84	874	4	-36.722	2.27
BSV	Cubic	0.71948	5.17	6.59	5134.7	26	-333.14	5.30
CAN	Hexagonal	0.69333	6.27	8.41	710.3	4	-42.975	2.34
CAS	Orthorhombic	0.89595	5.05	3.95	1279.6	4	-61.692	2.58
CDO	Orthorhombic	0.93023	5.89	7.82	1993.9	6	-66.98	3.32
CFI	Orthorhombic	0.76515	7.47	13.38	1908.3	8	-68.416	3.28
CGF	Monoclinic	695238	5.76	2.95	1894.5	6	-77.416	3.26
CGS	Orthorhombic	0.61333	5.86	10.62	1894.2	12	-134.24	3.54
CHA	Trigonal	0.56667	7.37	17.27	2391.6	6	-59.98	3.06
CHI	Orthorhombic	0.83344	3.93	2.39	1410.2	0	0	0.32
CLO	Cubic	0.4432	15.72	33.76	17253.	728	-4807.16	25hrs
CON	Monoclinic	0.67022	7.45	19.18	3566.3	18	-174.604	4.59
CSV	Triclinic	0.65541	7.56	18.01	1231.6	13	-143.89	3.18
CZP	Hexagonal	0.8123	4.26	3.97	1167.8	5	-61.415	2.43
DAC	Monoclinic	0.84119	5.28	9.5	1375.2	6	-71.879	3.12
DDR	Trigonal	0.85080	7.66	9.26	6716	32	-397.225	7.00
DFO	Hexagonal	0.57604	11.29	22.01	8865.1	111	-974.254	9.50
DFT	Tetragonal	0.71111	5.1	6.58	451.7	2	-28.093	3.00
DOH	Hexagonal	0.88219	7.85	0	2005.2	8	-117.802	3.32
DON	Orthorhombic	0.72892	8.79	15.59	3737.9	16	-148.983	4.40
EAB	Hexagonal	0.62859	7.14	14.32	2256.7	12	-131.223	4:19
EDI	Tetragonal	0.66667	5.72	9.52	307.5	2	-27.863	3.01
EEI	Orthorhombic	0.87359	6.96	9.36	11153.	46	-474.891	8.49
EMT	Hexagonal	0.49309	11.54	27.39	7207.5	51	-448.838	11.38
EON	Orthorhombic	0.76967	7.83	12.48	3563	16	-174.653	1.37
EPI	Monoclinic	0.84506	5.47	9.04	1357.2	6	-69.724	3.22
ERI	Hexagonal	0.62857	7.04	15.1	2239.5	12	-118.645	3.44
ESV	Orthorhombic	0.75499	6.22	8.36	2704.3	16	-179.661	4.16
ETL	Orthorhombic	0.87099	6.37	7.27	3989.4	17	-185.056	4.46

ETR	Hexagonal	0.5767	10.05	18.97	3107	18	-184.635	4.46
ETV	Triclinic	0.69696	5.85	9.78	808.2	3	-32.842	3.07
EUO	Orthorhombic	0.87297	7	12.24	6540	28	-296.18	2.12
EWO	Orthorhombic	0.87532	5.41	3.55	1258.7	4	-54.484	3.10
EWS	Orthorhombic	0.80519	6.12	12.64	5547.7	24	-259.151	4.45
EZT	Orthorhombic	0.639	6.57	13.14	2790.8	10	-97.224	1.21
FAR	Hexagonal	0.633	6.36	0	4915.6	18	217.322	1.52
FAU	Cubic	0.47619	11.24	27.42	14428	128	-1062.16	10.12
FER	Orthorhombic	0.88763	6.31	10.01	2051.3	8	-94.837	1.28
FRA	Trigonal	0.68398	6.67	0	350.7	12	-147.251	1.38
GIS	Tetragonal	0.61111	4.97	9.38	975.8	4	-50.195	1.05
GIU	Hexagonal	0.69333	6.32	0	5604.6	24	-276.918	1.58
GME	Hexagonal	0.58571	7.76	17.29	1594.6	9	-90.797	1.19
GON	Orthorhombic	0.78737	6.32	8.12	1811.8	4	-45.509	1.08
GOO	Orthorhombic	0.71675	4.51	4.83	1687.6	2	-24.325	1.00
HEU	Monoclinic	0.77825	5.97	9.42	2054.8	8	-94.717	1.16
IFO	Orthorhombic	0.66320	7.76	16.89	1852.1	8	-72.263	1.13
IFR	Monoclinic	0.67822	7.24	15.54	1865.5	8	-79.292	1.20
IFT	Orthorhombic	0.48311	10.44	33.37	12525.	100	-760.043	17.39
IFU	Orthorhombic	0.4857	10.99	33.08	10543.	76	-572.817	5.11
IFW	Monoclinic	0.71617	7.7	17.99	4052.2	20	180.245	1.42
IFY	Tetragonal	0.6580	6.94	10.62	2717.8	14	171.733	1.26
IHW	Orthorhombic	0.89896	6.67	9.7	6064.6	17	-182.814	1.44
IMF	Orthorhombic	0.846	7.34	12.12	16472.6	62	-703.874	4.54
IRN	Orthorhombic	0.65283	9.17	17.71	6005.4	35	-376.829	2.30
IRR	Hexagonal	0.47792	14.46	37.79	4423.1	36	-269.383	2.37
IRY	Hexagonal	0.45194	11.33	40.9	6847.5	67	-511.989	4.13
ISV	Tetragonal	0.69453	7.01	21.34	4255.6	22	-180.452	1.48
ITE	Orthorhombic	0.71180	8.3	16.45	4071.1	23	-244.03	1.54
ITG	Monoclinic	0.72034	7	15.72	3377.2	15	-150.61	1.30
ITH	Orthorhombic	0.79954	6.72	11.59	3213.5	13	-145.4	1.27
ITR	Orthorhombic	0.78528	6.36	11.79	6454	28	-311.757	5.26

ITT	Hexagonal	0.54112	11.74	25.1	3556.6	27	-127.889	5.09
ITV	Cubic	0.28138	9.32	37.82	18212	146	-987.131	15.09
ITW	Monoclinic	0.76916	4.32	7.83	1354	8	-101.72	3.28
IWR	Orthorhombic	0.651	7.48	19.35	3580.2	18	-167.418	4.37
IWS	Tetragonal	0.6389	8.25	23.19	9194.1	56	-504.419	10.52
IWV	Orthorhombic	0.71241	8.54	22.28	10119.6	11	-25.858	5.30
IWW	Orthorhombic	0.75665	7.07	15.3	6339	27	-258.98	2.28
JBW	Orthorhombic	0.75333	4.29	4.18	319.5	4	-50.094	1.02
JNT	Monoclinic	0.77316	4.72	0	1559	4	-56.171	1.07
JOZ	Orthorhombic	0.74978	4.92	7.5	1222.1	4	-49.289	1.04
JRY	Orthorhombic	0.78095	4.59	6.76	1299.1	6	-68.97	1.05
JSN	Monoclinic	0.67965	5.12	8.04	895.3	4	-51.14	1.03
JSR	Cubic	0.57229	7.83	28.09	7815.4	60	-563.174	4.17
JST	Cubic	0.64675	5.35	14.39	3354.8	28	-312.718	2.02
JSW	Orthorhombic	0.73766	5.38	0	2606.2	8	-100.347	1.15
KFI	Cubic	0.57142	10.67	17.91	6412.1	46	-466.011	3.12
LAU	Monoclinic	0.65820	6.04	9.57	1333.6	4	-50.229	3.14
LEU	Trigonal	0.60571	7.1	14.32	3390.1	18	-184.723	4.59
LIO	Hexagonal	0.69333	6.05	0	2041.8	9	-111.935	3.52
LIT	Orthorhombic	0.69555	3.24	0	1248.2	0	0	0.35
LOS	Hexagonal	0.69333	6.36	0	1423.3	6	-72.958	3.22
LOV	Tetragonal	754446	5.15	7.57	1071.1	4	43.284	3.00
LTA	Cubic	0.53333	11.05	21.43	1693.2	102	-1005.41	8.58
LTF	Hexagonal	0.71428	8.16	11.21	6394.5	34	-336.397	6.09
LTJ	Tetragonal	0.77662	4.1	3.56	862.7	4	-49.967	3.12
LTL	Hexagonal	0.61904	10.01	15.37	2153.1	9	-83.267	3.49
LTN	Cubic	0.69845	10.13	0	45201.7	170	-3047.35	56.42
MAR	Hexagonal	0.69332	6.35	0	4085.2	8	-92.275	5.06
MAZ	Hexagonal	0.69703	8.09	12.72	2161.9	12	-125.564	4.17
MEI	Hexagonal	0.63068	8.06	21.11	2317.9	16	139.612	4.19
MEL	Tetragonal	0.80863	7.72	12.61	5529.9	21	-229.498	5.29
MEP	Cubic	0.95539	0	0	2574.2	8	-129.85	3.59
MER	Tetragonal	622222	6.65	10.37	1954.3	12	-133.65	4.06

MFI	Orthorhombic	0.82	6.36	9.81	5311.3	20	-229.149	5.15
MFS	Orthorhombic	0.86632	6.81	10.96	2063	8	-94.596	3.36
MON	Tetragonal	0.88580	4.24	5.98	906.4	4	-45.614	2.49
MOR	Orthorhombic	0.80234	6.7	12.27	2827.3	16	-175.605	4.23
MOZ	Hexagonal	0.64285	10.03	13.12	6366.6	26	-264.4	5.15
MRT	Orthorhombic	0.68917	5.97	9.17	1400.2	8	-94.323	3.22
MSE	Tetragonal	0.753	7.09	16.4	6843.8	25	-245.993	5.05
MSO	Trigonal	0.69444	7.23	0	5048.5	24	-259.583	5.27
MTF	Monoclinic	0.94211	6.25	6.66	2121.5	6	-68.886	3.28
MTN	Cubic	0.92759	7.44	0	7919.9	24	-384.352	6.28
MTT	Orthorhombic	0.88318	6.19	7.98	1318	2	-29.252	3.06
MTW	Monoclinic	0.7760	6.08	9.42	1535.8	9	-95.66	3.58
MVY	Orthorhombic	0.81039	3.76	1	572.1	0	0	0.33
MWF	Cubic	0.63636	10.64	11.44	89581	463	-1518.98	6.03h
MWW	Hexagonal	0.75212	9.09	17.43	4518.8	22	-2333.12	6.03
NAB	Tetragonal	0.74074	4.31	7.05	621.4	3	-23.338	2.25
NAT	Tetragonal	0.74074	4.52	9.06	1231.5	16	175.163	2.57
NES	Orthorhombic	0.81868	7.04	14.91	8271.1	18	-182.102	4.11
NON	Orthorhombic	0.91532	6.5	0	4987.7	8	-100.406	4.04
NPO	Hexagonal	0.75	4.23	2.8	377.3	1	-7.04	1.53
NPT	Cubic	0.67013	10.28	19.05	2675.5	17	-172.208	4.41
NSI	Monoclinic	0.86921	4.16	3.48	639.3	2	-19.394	2.31
OBW	Tetragonal	0.68989	9.26	22.73	5971.7	39	-37.4756	7.39
OFF	Hexagonal	0.62857	7	15.09	1118	7	-67.528	3.16
OKO	Monoclinic	0.8216	6.7	14.34	3884.6	15	-152.5	4.33
OSI	Tetragonal	0.7777	6.66	9.6	1804.1	8	-88.87	3.35
OSO	Hexagonal	0.645	6.07	19.95	675.7	5	-50.739	2.56
OWE	Orthorhombic	0.68571	5.78	10.35	934	5	-58.78	3.06
PAR	Monoclinic	0.66491	4.21	3.67	1643.2	6	-70.152	1.05
PAU	Cubic	0.62337	10.48	12.39	42282.4	247	-2897.13	36.37
PCR	Monoclinic	0.1029	6.03	6.89	3199.9	10	-126.453	2.12
PHI	Orthorhombic	0.63555	5.49	9.89	1953.7	12	-129.161	1.05
PON	Orthorhombic	0.725	4.93	7.04	1320.6	4	-52.258	1.04
POR	Tetragonal	0.70389	6.14	10.34	3643.2	20	-222.4	1.43
POS	Tetragonal	0.69783	7.27	19.86	4118.2	22	-199.963	1.44

PSI	Orthorhombic	0.81298	5.79	3.84	6971	8	-126.365	3.55
PTT	Trigonal	0.63982	6.87	10.38	1453.9	5	-90.173	1.01
PTY	Triclinic		5.11	12.04	588.4	3	-36.847	2.58
PUN	Orthorhombic	0.63290	5.51	14.97	2405.3	19	-193.77	4.10
PWN	Cubic	0.61126	10.47	14.12	15377	94	-1092.77	20.31
PWW	Monoclinic	0.7740	5.23	11.66	2347.1	12	-141.981	4.05
PWO	Monoclinic	0.77922	5.22	11.9	1165.3	6	-72.711	3.27
RHO	Cubic	0.53333	10.43	20.63	3320.6	24	-253.09	5.30
RON	Tetragonal	0.68898	5.74	7.39	2938.4	0	0	0.41
RRO	Monoclinic	0.80146	4.56	6.92	1007.8	6	-59.431	2.18
RSN	Orthorhombic	0.78695	5.15	7.03	2147.5	9	-81.882	3.15
RTE	Monoclinic	0.71587	7.06	11.68	1398.6	7	-70.622	3.14
RTH	Monoclinic	0.69576	8.18	16.03	1988.9	12	-124.448	4.04
RUT	Monoclinic	0.76749	5.96	0	1985.7	4	-54079	3.30
RWR	Tetragonal	0.91965	4.42	4.37	1666.3	8	-114.648	2.30
RWY	Cubic	0.3333	14.4	45.53	6333.4	56	-418.281	3.35
SAF	Orthorhombic	0.76277	6.66	9.86	3368.7	8	-83.206	1.21
SAO	Tetragonal	0.54546	8.64	25.69	3948.1	26	-224.472	1.57
SAS	Tetragonal	0.58667	8.99	18.09	2140.9	12	-111.629	1.21
SAT	Trigonal	0.64444	6.84	13.02	4386.9	14	-134.779	1.40
SAV	Tetragonal	0.58730	8.82	17.85	3284.9	20	-202.483	1.41
SBE	Tetragonal	0.51432	12.54	26.41	9320.8	69	-619.48	13.50
SBN	Hexagonal	0.70399	5.06	8.89	619.3	4	-56.861	1.03
SBS	Hexagonal	0.53409	11.45	27.23	6997.3	51	-422.910	10.09
SBT	Trigonal	0.52234	11.17	27.25	10501.3	77	-676.296	15.15
SEW	Orthorhombic	0.72381	7.35	16.6	3878.1	10	-112.723	5.21
SFE	Monoclinic	0.76736	6.66	12.61	827.2	4	-48.863	3.03
SFF	Monoclinic	0.76507	7.59	13.99	1793.2	8	-98.711	1.31
SFG	Orthorhombic	0.85044	6.96	11.12	4194.9	16	-171.422	4.22
SFH	Orthorhombic	0.72419	7.63	14.85	3880.5	16	-146.147	4.53
SFN	Monoclinic	0.96283	7.94	1569	1933.2	8	-76.374	4.48
SFO	Monoclinic	0.57508	7.92	19.57	2109.7	13	-124.33	4.10
SFS	Monoclinic	0.75930	7.52	15.96	33.67	16	-168.733	4.42

SFW	Trigonal	0.59740	7.78	17.2	7157.8	40	-432.134	2.55
SGT	Tetragonal	0.86290	7.74	0	3666	16	-171.422	4.42
SIV	Orthorhombic	0.636	5.38	9.74	3910.8	20	-242.989	1.43
SOD	Cubic	0.66667	6.32	0	718.4	2	-29.753	1.02
SOF	Orthorhombic	0.70736	5.14	12.57	2435.8	16	-180.051	1.27
SOR	Orthorhombic	0.72381	7.06	13.29	2811.1	8	-77.48	1.21
SOS	Orthorhombic	0.63175	4.82	9.36	1414.4	8	-86.014	4.17
SOV	Orthorhombic	0.67878	7.25	20.6	8354.3	44	-388.068	2.54
SSF	Hexagonal	0.71082	7.66	15.63	3281.2	16	-149.658	3.56
STF	Monoclinic	0.74895	7.63	15.39	1896.3	10	-112.706	1.16
STI	Orthorhombic	0.72034	6.29	13.27	4312.6	12	-120.997	4.03
STT	Monoclinic	0.76071	7.04	13.9	3773	20	-214.297	4.36
STW	Hexagonal	0.70303	5.43	13.93	3660.8	20	-2235.71	1.46
SVR	Monoclinic	0.75671	5.85	10.75	5349	20	-222.681	5.20
SVV	Monoclinic	0.73766	6.41	0	3106.6	8	-94.1	4.06
SWY	Hexagonal	0.63723	7.06	15.07	4478.3	22	-214.331	5.33
SYT	Tetragonal	0.42424	8.29	27.95	10455	18	-691.186	17.02
SZR	Orthorhombic	0.78	6.27	9.33	2041.8	6	-70.712	3.46
TER	Orthorhombic	0.73932	6.94	12.77	4694.1	18	-201.272	1.47
THO	Orthorhombic	0.66667	5.15	9.94	635.2	11	-120.502	1.11
TOL	Trigonal	0.693	6.37	0	4031.1	18	-228.125	4.36
TON	Orthorhombic	0.86711	5.71	8.04	1322.7	4	-50.864	1.06
TSC	Cubic	0.48254	16.45	27.85	29053	231	-2000.62	2Hrs
TUN	Monoclinic	0.803	8.46	12.93	10904.	44	-490.704	9.39
UEI	Orthorhombic	0.78844	5.6	6.53	2748.9	8	-103.603	3.27
UFI	Tetragonal	0.64132	10.09	19.74	4210	28	-290.115	6.01
UOS	Orthorhombic	0.75584	5.85	9.02	1362.1	6	-70.227	3.33
UOV	Orthorhombic	0.70216	6.98	17.13	10840	51	-416.808	10.58
UOZ	Tetragonal	0.65844	5.43	0	2047.0	6	-83.127	3.41
USI	Monoclinic	0.59038	6.76	17.46	2514.7	15	-144.935	4.23
UTL	Monoclinic	0.71371	9.3	12.88	4872.5	31	-293.415	6.41
UWY	Orthorhombic	0.72554	8.78	16.18	3680.0	17	-173.645	4.52

VET	Tetragonal	0.91374	6.39	7.82	842.4	2	-28.215	2.40
VFI	Hexagonal	0.5625	12.03	25.4	2486.7	14	-114.724	4.28
VNI	Tetragonal	0.89660	4.8	4.66	3415.5	12	-143.613	4.22
VSV	Tetragonal	0.818	4.31	6.43	2142.7	10	-109.305	3.35
WEI	Orthorhombic	0.65586	4.19	7.82	1211.8	0	0	0.33
WEN	Hexagonal	0.64069	5.53	11.58	1208.2	3	-42.519	3.16
YFI	Orthorhombic	0.74199	7.97	15.37	7317.5	36	-401.795	7.24
YUG	Monoclinic	0.79788	4.49	5.7	891.4	4	-39.55	2.40
ZON	Orthorhombic	0.67909	5.83	8.07	1773.1	5	-54.421	3.14

Appendix 2: Zeolite characterization FT-IR

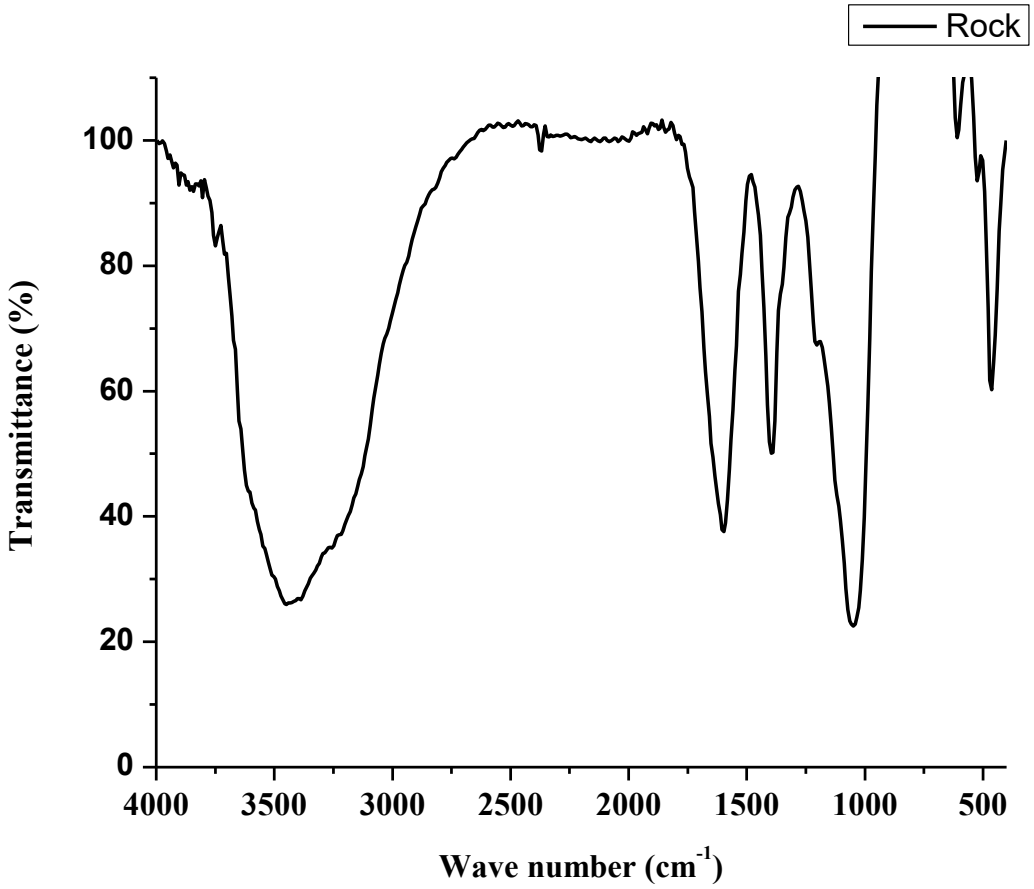

Appendix 3 Zeolite characterization XRD

Zeolite-Evaluation report (Zeolite)

General information

Analysis date	2022-09-16 13:53:34	Measurement start time	07/25/2022 11:44:20
Analyst	Administrator	Operator	Administrator
Sample name	Zeolite	Comment	
Measured data name	C:\Users\Rigaku\Desktop\Rigaku MiniFlex600\OneDrive - University of K...	Memo	

Measurement Conditions

X-Ray generator	40 kV, 15 mA	Scan mode	1D(scan)
Incident primary	No unit	Scan speed/Duration time	10.00 °/min
Goniometer	MiniFlex 300/600	Step width	0.01 °
Attachment	ASC-8	Scan axis	θ/2θ
Filter	None	Scan range	3 ~ 90 °
Selection slit	None	DS	1.25deg
Diffracted beam mono	None	IHS	10 mm
Detector	D/teX Ultra2	SS	Open
Optics attribute	None	RS	Open

Measured profile view

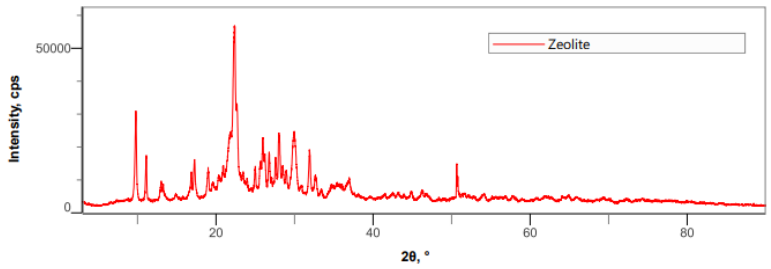

No.	2θ, °	d, Å	Height, cps	FWHM, °	Int. I., cps°	Int. W., °	Asymmetry	Decay(ηL/mL)	Decay(ηH/mH)	
1	7.325(16)	12.06(3)	327(21)	0.21(6)	109(19)	0.33(8)	0.5(6)	0.1(12)	1.3(4)	
2	9.801(3)	9.017(2)	17433(402)	0.227(2)	5205(34)	0.299(9)	2.20(14)	0.40(3)	0.92(5)	
3	11.118(4)	7.952(3)	9060(278)	0.170(3)	1891(25)	0.209(9)	2.2(2)	0.20(5)	0.79(10)	
4	13.006(4)	6.802(2)	2788(116)	0.561(12)	1664(48)	0.60(4)	0.50(5)	0.00(14)	0.00(11)	
5	14.84(3)	5.965(11)	953(53)	0.37(4)	556(30)	0.58(6)	0.51(18)	0.3(4)	1.2(2)	
6	16.560(15)	5.349(5)	730(38)	0.28(4)	269(51)	0.37(9)	1.36(12)	0.96(8)	0.01(10)	
7	16.837(4)	5.2616(12)	4704(174)	0.178(8)	1122(40)	0.238(17)	1.36(12)	0.96(8)	0.01(10)	
8	17.236(5)	5.1406(14)	6555(211)	0.193(5)	1692(65)	0.258(18)	1.36(12)	0.96(8)	0.01(10)	
9	17.37(7)	5.10(2)	2121(87)	0.43(2)	1229(76)	0.58(6)	1.36(12)	0.96(8)	0.01(10)	
10	18.985(6)	4.6709(15)	4549(162)	0.242(8)	1265(31)	0.278(17)	1.50(14)	0.00(6)	0.52(8)	
11	19.609(10)	4.524(2)	1532(64)	0.24(2)	423(31)	0.28(3)	1.50(14)	0.00(6)	0.52(8)	
12	20.379(8)	4.3544(17)	2321(89)	0.270(18)	720(44)	0.31(3)	1.50(14)	0.00(6)	0.52(8)	
13	20.888(9)	4.2494(18)	2982(104)	0.317(18)	1087(56)	0.36(3)	1.50(14)	0.00(6)	0.52(8)	
14	21.812(11)	4.071(2)	9874(256)	0.67(3)	7634(347)	0.77(6)	1.50(14)	0.00(6)	0.52(8)	
15	22.331(3)	3.9780(5)	30523(519)	0.315(7)	11051(369)	0.362(18)	1.50(14)	0.00(6)	0.52(8)	
16	22.671(4)	3.9190(7)	13447(299)	0.261(18)	4039(321)	0.30(3)	1.50(14)	0.00(6)	0.52(8)	
17	23.069(16)	3.852(3)	1375(51)	0.24(5)	377(89)	0.27(7)	1.50(14)	0.00(6)	0.52(8)	
18	23.441(8)	3.7919(12)	2262(82)	0.21(2)	558(45)	0.25(3)	1.50(14)	0.00(6)	0.52(8)	
19	24.958(15)	3.565(2)	4501(159)	0.151(10)	725(51)	0.161(17)	1.1(4)	0.0(3)	0.0(4)	
20	25.643(5)	3.4711(7)	5527(181)	0.218(11)	1308(59)	0.237(19)	1.25(15)	0.00(8)	0.12(10)	
21	25.942(3)	3.4318(5)	10201(276)	0.192(8)	2127(90)	0.209(14)	1.25(15)	0.00(8)	0.12(10)	
22	26.200(5)	3.3986(6)	6521(196)	0.193(14)	1364(82)	0.209(19)	1.25(15)	0.00(8)	0.12(10)	
23	26.743(6)	3.3308(8)	6867(210)	0.189(5)	1407(28)	0.205(10)	1.25(15)	0.00(8)	0.12(10)	
24	27.042(6)	3.2947(7)	1923(76)	0.100(17)	209(21)	0.109(15)	1.25(15)	0.00(8)	0.12(10)	
25	27.568(3)	3.2330(4)	5753(180)	0.184(7)	1130(31)	0.196(11)	0.99(5)	0.00(7)	0.00(5)	
26	28.016(3)	3.1823(4)	10806(282)	0.243(4)	2793(41)	0.258(11)	0.99(5)	0.00(7)	0.00(5)	

Appendix 4: Zeolite characterization SEM

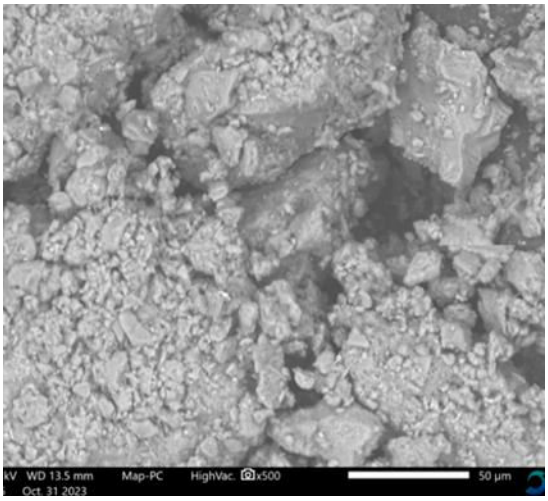

Appendix 5: Loading data for the Heulandite

Loading of Pb^{2+} and Cd^{2+}ions on the zeolites, as determined from the Monte Carlo simulations

CODE	Structure	Total density	Pore size (Å)	Average Volume%	Total Volume $Å^3$	Loading Pb^{2+}	Loading of Cd^{2+}	Total Energy (kcal/mol)
HEU	Monoclinic	0.7783	5.97	9.42	2054.81	8	7	-94.717

Appendix 6: Heulandite zeolite alongside the respective adsorption isotherm for Pb2+ and Cd^{2+} ions

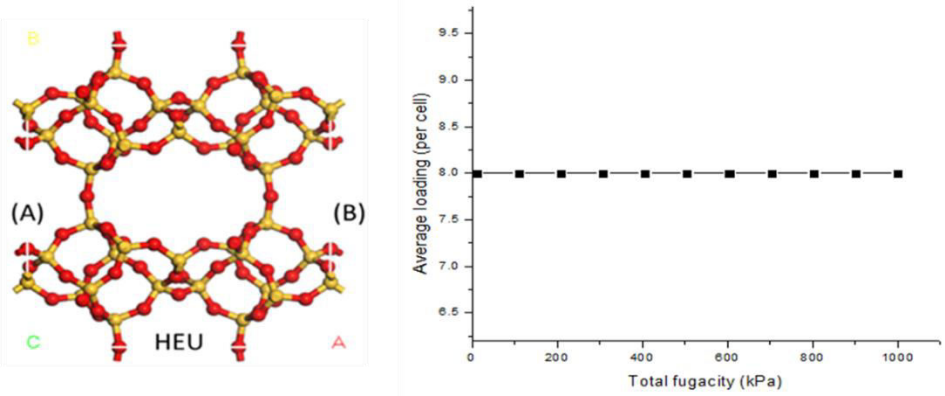

Figure S1, (A) HEU Zeolite, (B) Adsorption isotherm of lead (II) ion on HEU Zeolite

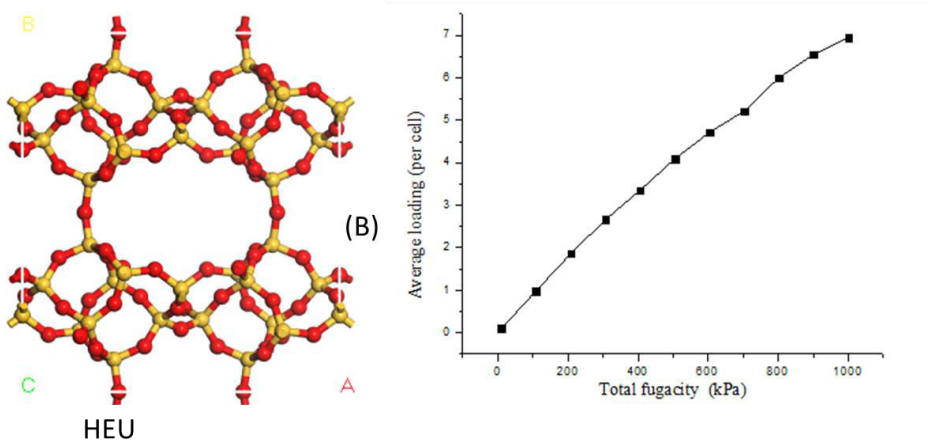

Figure S2 (A) HEU Zeolite, (B) Adsorption isotherm of Cadmium (II) ion on ATO Zeolite

Appendix 7: Average loading Cd^{2+} ions onto HEU zeolite as a function of pressure at different temperatures

Total fugacity (kPa)	298 K	308 K	328 K	338 K	358 K	398 K
10	0.09392	0.07617	0.05262	0.0504	0.03348	0.02209
109	1.01709	0.85569	0.56325	0.52083	0.39718	0.22726
208	1.91772	1.48047	1.07812	1.01241	0.69841	0.43475
307	2.62638	2.09976	1.53632	1.44143	1.04763	0.6649
406	3.40036	2.86582	1.9987	1.90114	1.37693	0.86673
505	4.10705	3.1998	2.41301	2.2382	1.76251	1.04661
604	4.5164	3.96892	2.79891	2.68289	1.90946	1.22232
703	4.95909	4.48907	3.26418	3.03295	2.26702	1.35949
802	5.84283	5.112	3.34305	3.16829	2.54368	1.60472
901	6.50393	5.112	4.163	3.7504	2.783	1.73422
1000	6.99452	5.112	4.163	3.97732	2.9993	1.92025

Appendix 8: Average loading Pb^{2+} ions onto HEU zeolite as a function of pressure at different temperatures

Total fugacity (kPa)	298 K	308 K	328 K	338 K	358 K	398 K
10	7.95774	7.9432	7.82495	7.84513	7.35255	6.45129
109	8	8	8	7.91585	7.74851	7.72772
208	8	7.98844	8	8	7.96144	7.97875
307	8	8	8	7.98794	8	7.94099
406	8	8	8	7.99035	7.99355	7.94123
505	8	8	8	8	8	7.95972
604	8	8	8	8	8	7.89387
703	8	8	8	8	8	7.86688
802	8	8	8	7.99899	8	7.93963
901	8	8	8	8	8	8
1000	8	8	8	8	8	8

Appendix 9: Molecular simulation percent weight removal capacity of Pb^{2+} onto HEU

HEU Total fugacity (kPa)	Average loading Pb^{2+} (per cell)	Percent weight capacity (%wt)
10	6.5	36.48
109	7.49	41.78
208	7.76	42.42
307	7.89	42.74
406	7.99	43.05
505	8	43.36
604	8	43.36
703	8	43.36
802	8	43.36
901	8	43.36
1000	8	43.36

Appendix 10: Molecular simulation percent weight removal capacity of Cd^{2+} onto HEU

HEU Total fugacity (kPa)	Average loading Cd^{2+} (per cell)	Percent weight capacity (%wt)
10	0.09392	0
109	1.01709	4.9
208	1.91772	9.I
307	2.62638	12.3
406	3.40036	15.11
505	4.10705	17.6
604	4.5164	18.9
703	4.95909	20.4
802	5.84283	23.21
901	6.50393	25.2
1000	6.99452	26.22

Appendix 11: Table S1. The structural characteristics and loading capacity of phosphate on zeolites

CODE	M [g/mol]	D [kg/m^3]	HVF [-]	APV [cm^3/g]	VSA [m^2/cm^3]	GSA [m^2/g]	DPS [-]	Di [A]	L	Total energy	isoletric heats
CLO	11728.2	1128.76	0.55	0.49	2069.69	1833.61	3	15.33	420	32592.6	10.82
LTN	46144.7	1695.18	0.31	0.18	1181.64	697.06	0	0	103	7419.18	16.48
MWF	86521.4	1603.83	0.35	0.22	1593.89	993.81	3	10.06	99	7086.69	15.84
TSC	23072.4	1318.71	0.49	0.37	1472.61	1116.72	3	15.87	89	6797.43	12.51
ITV	11792.2	1075.18	0.55	0.51	2110.04	1962.51	3	8.54	70	5732.67	10.74
PAU	40376.7	1585.7	0.36	0.23	1639.21	1033.75	3	10.08	61	4455.79	15.22
FAU	11536.2	1327.65	0.49	0.37	1615.92	1217.14	3	10.69	60	4496.42	13.85
DFO	7931.13	1485.63	0.43	0.29	1625.72	1094.3	3	10.89	49	3717.5	13.25
LTA	1442.02	1414.17	0.47	0.33	1674.58	1184.14	3	10.24	48	3583.79	14.65
SBT	8652.14	1368.16	0.47	0.34	1585.49	1158.84	3	10.41	37	2926.27	13.67
SBE	7690.79	1370.15	0.46	0.34	1514	1104.99	3	12.09	31	2450.22	13.57
IRY	4598.41	1115.15	0.6	0.54	1701.51	1525.79	3	10.69	30	2444.57	11.75
JSR	5768.09	1225.53	0.52	0.42	2271.2	1853.23	3	7.43	29	2286.25	13.65
EMT	5768.09	1328.95	0.49	0.37	1618.8	1218.11	3	11	28	2220.58	13.49
IMF	17304.3	1744.41	0.3	0.17	1261.47	723.15	2	6.7	28	2125.03	15.68
IWV	9132.81	1498.62	0.41	0.27	1455.32	971.11	2	8.14	26	2054.62	13.3
SBS	5768.09	1368.86	0.47	0.34	1585.68	1158.39	3	10.97	24	1898.87	13.53
BOG	5768.09	1602	0.38	0.24	1486.24	927.74	3	7.49	16	1244.11	14.26
BOZ	5527.76	1290.63	0.46	0.36	2017.67	1563.33	3	8.31	16	1265.97	12.7
KFI	5768.09	1493.77	0.41	0.28	1638.56	1096.93	3	10.16	16	1232.11	14.47
EEI	12016.9	1789.07	0.25	0.14	921.42	515.03	0		0	1097.42	15.47
IRN	5527.76	1528.47	0.41	0.27	1503.19	983.46	2	8.62	15	1091.47	14.92
ISV	3845.39	1500.62	0.43	0.28	1637.06	1090.93	3	6.37	12	938.53	14.07
SAO	3364.72	1415.19	0.48	0.34	1736.16	1226.8	3	8.21	12	949.95	13.25
ITR	6729.44	1731.23	0.3	0.17	1341.02	774.61	3	5.96	12	912.46	15.69
LTF	6489.1	1685.17	0.29	0.18	1210.73	718.47	1	7.76	10	752.03	16.03
RHO	2884.05	1442.22	0.45	0.31	1710.52	1186.03	3	10.03	10	776	14.65
EUO	6729.44	1708.43	0.29	0.17	1169.65	684.64	1	6.26	9	684.03	15.31
MFI	5768.09	1837.96	0.27	0.14	1216.85	662.07	3	5.94	9	680.03	15.86
SAT	4326.07	1637.54	0.32	0.2	1295.92	791.38	3	6.18	9	656.61	15.73
MWW	4326.07	1589.73	0.39	0.25	1542.13	970.06	2	9.29	9	701.18	15.04
MSO	5407.59	1778.68	0.26	0.15	1001.81	563.23	0	0	9	682.46	15.99
CON	3364.72	1566.66	0.4	0.26	1599.49	1020.96	3	6.77	8	618.6	14.45

MTN	8171.46	1713.29	0.34	0.2	1222.69	713.65	0	0	8	576.56	18.89
TER	4806.74	1700.41	0.32	0.19	1406.58	827.2	2	6.18	8	612.56	14.99
AEI	2884.05	1501.58	0.4	0.27	1735.45	1155.78	3	6.9	8	576.79	15.06
SIV	3845.39	1632.79	0.32	0.19	1639.92	1004.37	3	4.98	7	513.61	17.85
DDR	7210.12	1782.75	0.3	0.17	1174.34	658.73	2	7.07	7	513.24	14.95
STW	3605.06	3605.06	0.37	0.22	3605.06	1051.52	3	4.91	7	530.89	15.59
AFX	2884.05	1501.67	0.4	0.27	1732.89	1153.98	3	7.12	7	538.33	15.06
DON	3845.4	1708.28	0.29	0.17	955.59	559.38	1	8.18	6	476.54	12.62
EZT	2884.05	1716.04	0.3	0.18	1241.24	723.31	1	5.9	6	419.81	15.8
EAB	2163.03	1591.65	0.37	0.23	1569.98	986.39	2	6.62	6	402.33	17.38
ITG	3364.72	1654.42	0.36	0.22	1509.42	912.35	3	6.44	6	464.64	14.25
TOL	4326.07	1782.23	0.26	0.15	1782.23	583.36	0	0	6	440.73	17.68
LEV	3244.55	1589.09	37	0.24	1562.33	983.16	2	6.39	6	460.99	14.31
AET	4326.07	1817.16	0.24	0.13	863.251	475.055	1	7.76	6	478.56	12.33
LTL	2163.03	1668.22	0.29	0.18	1001.93	600.61	1	9.61	5	386.56	14..84
CFI	1922.69	1673.04	0.29	0.18	1065.25	636.72	1	7.07	4	310	14.3
CGS	1922.7	1685.49	0.29	0.17	1411.74	837.58	3	5.32	4	298.82	16.57
FER	2163.03	1751.02	0.29	0.17	1288.93	736.11	2	5.42	4	295.62	17.18
STF	1922.7	1683.71	0.35	0.21	1362.86	809.44	1	7.22	4	305.94	15.17
HEU	2163.03	2163.03	0.29	0.17	1335.5	764.01	2	5.22	4	296.99	16.78
MAZ	2163.03	1661.45	0.32	0.19	1238.34	745.34	2	5.65	4	305.51	15.03
MEP	2763.88	1782.92	0.3	0.17	1129.89	633.73	0	0	4	287.32	19.18
MOR	2884.05	1693.89	0.31	0.18	1265.9	747.33	2	6.2	4	308.35	14.9
MTW	1682.36	1819.05	0.24	0.13	985.58	541.81	1	5.31	4	304.18	14.83
RTH	541.81	1605.31	0.37	0.23	1441.09	897.7	1	7.64	4	307.98	14 58
SFF	1922.7	1780.51	0.32	0.18	1280.5	719.18	1	7.09	4	301.98	16.17
JSW	2884.05	1837.56	0.22	0.12	969.97	527.86	0	0	4	293.48	17.66
ATT	721.01	1704.11	0.3	0.18	1512.12	887.34	2	4.9	4	295.92	18.81
CGS	1922.69	1685.5	0.29	0.17	1411.74	837.579	3	5.32	4	304.09	16.62
ERI	2163.03	1603.86	0.36	0.22	1497.58	933.737	3	6.31	4	312.53	14.47
ESV	2884.05	1770.93	0.28	0.16	1161.71	655.99	1	5.67	4	301.71	16.98
RTH	1922.69	1605.31	0.37	0.23	1441.09	897.7	1	7.63	4	312.948	14.7
AWW	1442.02	1688.96	0.31	0.18	1264.88	748.909	1	6.89	4	303.79	15.14
AFN	1922.7	1735.6	0.25	0.14	1178.22	678.85	1	4.75	3	226.42	17.18
ATN	961.348	1777.69	0.23	0.13	1050.93	591.17	1	5.51	2	143.55	19,19
CHA	1050.92	591.17	0.24	0.13	1050.93	591.17	1	5.51	2	154.593	14.25
DOH	2042.87	1691.73	0.34	0.2	1242.56	734.48	0	0	2	148.4	17.34

LAU	1442.02	1795.55	0.27	0.15	1186.51	660.81	1	5.47	2	148.03	16.91
PHI	1922.69	1634.19	0.32	0.2	1601.13	979.77	3	5	2	147.11	16.53
TON	1442.02	1810.29	0.22	0.12	951.64	525.68	1	5.04	2	147.84	17.04
MTT	2564.75	3230.8	0.09	0.03	534.47	165.43	1	3.23	2	146.41	17.75
GIS	961.35	1635.99	0.31	0.19	1686.03	1030.59	3	4.57	2	149.04	17.85
MFS	2163.03	1740.4	0.28	0.16	1210.58	695.58	2	6.22	2	152.31	14.79
LOS	1442.02	1682.46	0.31	0.18	1220.65	725.51	0	0	2	148.89	16.59
SOD	721.01	1661.65	0.33	0.2	1297.96	781.12	0	0	2	140.9	20.81
BPH	1682.36	1458.96	0.44	0.3	1688.01	1156.99	3	9.11	1	82.23	8.71
CAN	721.01	1685.65	0.29	0.17	1183.81	702.29	1	5.76	1	75.33	15.6
GOO	1922.69	1891.93	0.19	0.1	828.18	437.74	2	3.94	1	73.48	17.45
VET	1021.43	2013.45	0.18	0.09	777.43	386.12	1	5.98	1	76.29	14.65
WEN	1185.69	1629.64	0.32	0.2	1444.93	886.66	3	4.97	1	72.53	18.41
ANA	2884.05	1917.78	0.1	0.05	426.01	222.13	0	0	0	0	0
DFT	480.67	1767.24	0.26	0.15	1125.8	637.04	3	4.19	0	0	0
BIK	721.011	1862.34	0.16	0.09	816.36	438.35	1	3.76	0	0	0
SBN	600.84	1610.87	0.29	0.18	1564.36	971.12	2	4.41	0	0	0
JNT	1922.7	2048.03	0.13	0.06	586.29	286.268	0	0	0	0	0
MON	961.348	1760.77	0.23	0.13	1265.42	718.67	3	3.76	0	0	0
PAR	1986.7	1878.31	0.13	0.07	740.048	393.996	1	3.69	0	0	0
THO	600.84	1570.63	0.31	0.2	1502.63	956.7	3	4.48	0	0	0
VSV	2163.03	1676.33	0.24	0.14	1243.33	741.7	3	3.75	0	0	0
LIT	1506.02	2003.63	0.01,	0.01	0	0	0	0	0	0	0
ITW	1442.02	1768.37	0.27	0.15	1316.49	744.468	1	4.16	0	0	0
JBW	360.505	1873.75	0.17	0.09	847.475	452.287	1	3.86	0	0	0
CAS	1442.02	1871.34	0.15	0.08	661.06	353.25	1	4.44	0	0	0
APD	1922.69	1794.58	0.21	0.12	1014.59	565.36	1	4.22	0	0	0

Appendix 12: Lead (ii) ions data for standard calibration curve

Concentration (ppm)	0.0ppm	1ppm	5ppm	8ppm	10ppm	15ppm	20ppm	30ppm
ABSORBANCE	0.00	0.003	0.015	0.025	0.0301	0.048	0.0624	0.977

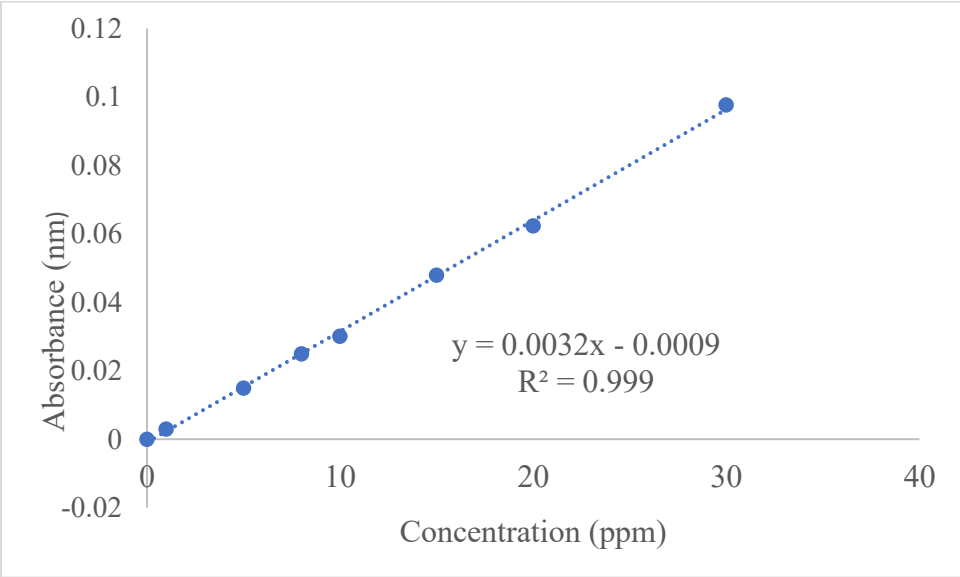

Appendix 13: Cadmium (ii) ions data for standard calibration curve

Concentration (ppm)	0.0ppm	1ppm	1.5ppm	2ppm	3ppm	4ppm	5ppm	8ppm
ABSORBANCE	0.00	0.0158	0.0478	0.0755	0.0935	0.1327	0.1748	0.2635

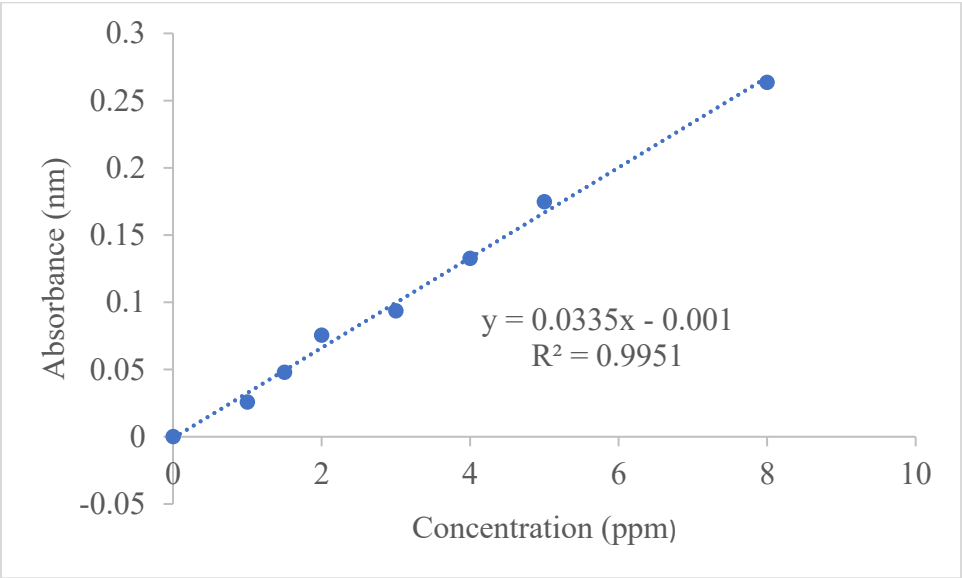

Appendix 14: Phosphate ion data for standard calibration curve

Standard Table

	Sample ID	Type	Ex	Conc	WL880.0	Wgt.Factor	Comments
1	BLK	Standard		0.000	0.000	1.000	
2	1	Standard		1.000	0.117	1.000	
3	2	Standard		2.000	0.243	1.000	
4	3	Standard		3.000	0.342	1.000	
5	4	Standard		4.000	0.472	1.000	
6	5	Standard		5.000	0.570	1.000	
7							

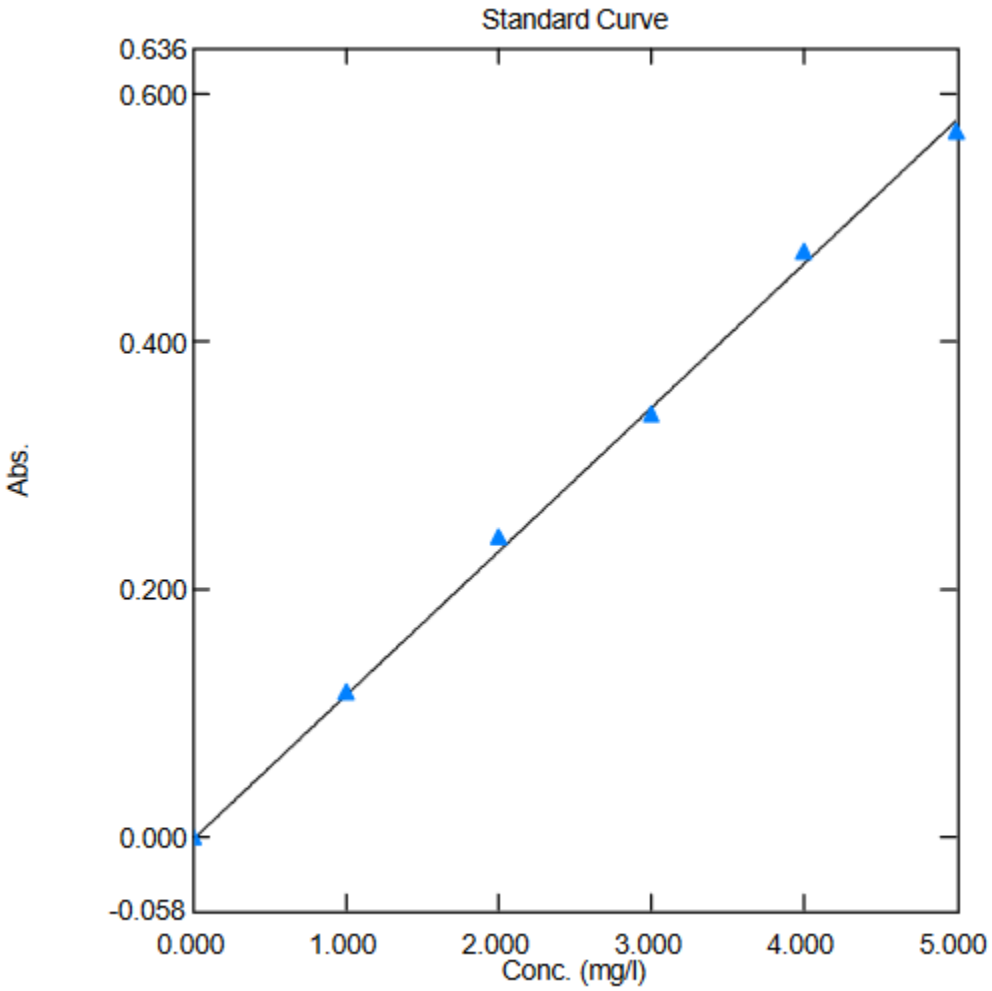

y = 0.11569 x + 0.00000
Correlation Coefficient r2 = 0.99874

Appendix 15: Nitrate ion data for standard calibration curve

Standard Table

	Sample ID	Type	Ex	Conc	WL214.0	Wgt.Factor	Comments
1	BLK	Standard		0.000	0.000	1.000	
2	2	Standard		2.000	0.181	1.000	
3	4	Standard		4.000	0.288	1.000	
4	6	Standard		6.000	0.375	1.000	
5	8	Standard		8.000	0.533	1.000	
6	10	Standard		10.000	0.673	1.000	
7							

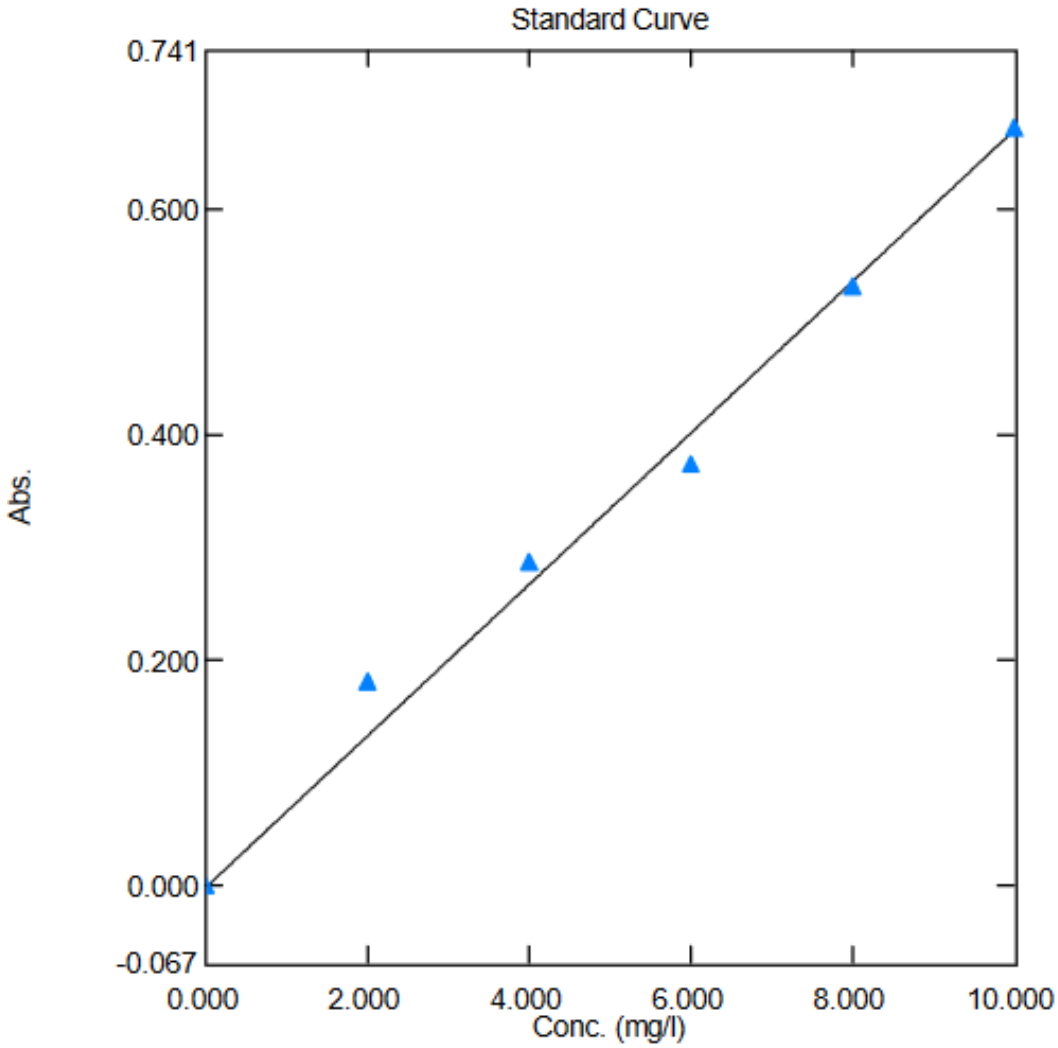

y = 0.06707 x + 0.00000
Correlation Coefficient r2 = 0.99091

Appendix 16: Calibration curve for (a) Imidacloprid and (b) Chlorpyrifos

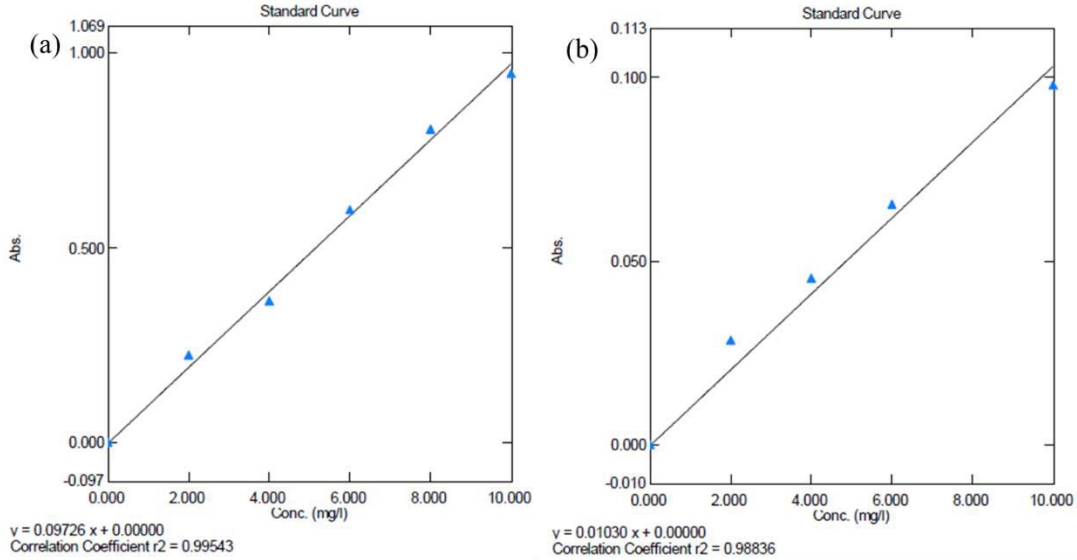

Appendix 17: Calibration curve for pharmaceutical diclofenac, ciprofloxacin and chloramphenicol

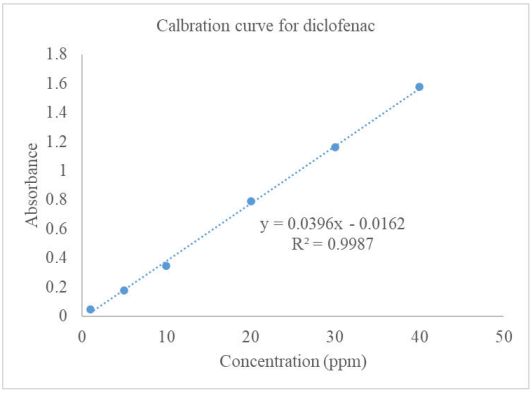

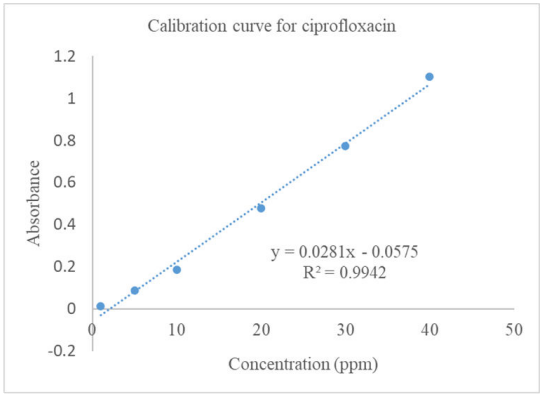

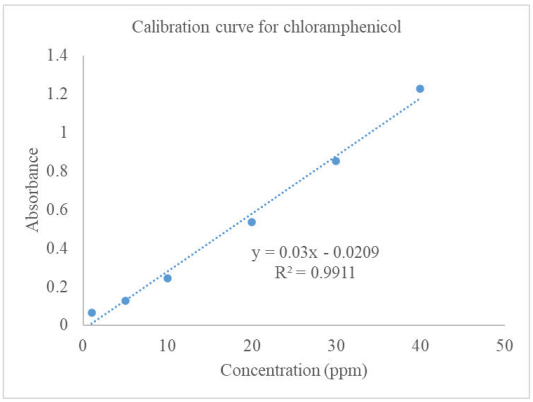

Appendix 18: Adsorption isotherm studies for Lead and Cadmium ions

a) **Freundlich and Langmuir data pb^{2+}**

Co	Ce	qe	Ce/qe	Log qe	Log Ce
5ppm	0.001	0.249	0.004	-0.6	-3
10ppm	0.015	0.4975	0.032	-0.3	1.8
20ppm	9.521	0.5239	18.17	-0.28	0.98
30ppm	20.018	0.5991	40.11	-0.3	1.3
40ppm	30.346	0.5325	56.98	-0.27	1.5
50ppm	40.523	0.6738	85.53	-0.32	1.61

b) Langmuir and Freundlich data Cd^{2+}

Co ppm	Ce ppm	Qemg/g	Ce/qe g/l	Log qe	Log ce
1.0	0.02	0.049	0.41	-1.31	-1.69
1.5	0.34	0.0575	6.09	-1.23	-0.46
2.0	0.97	0.051	19.22	-1.29	-0.01
2.5	1.21	0.051	24.60	-1.30	0.089
3.0	1.83	0.0519	30.84	-1.229	0.26

Appendix 19: Effect of Concentration of Cadmium (ii) ions adsorption

Time	1.00 ppm	1.50 ppm	2.00 ppm	3.00 ppm
0	1.00	1.50	2.00	3.00
30	0.97	1.45	1.91	2.93
60	0.83	1.36	1.85	2.65
90	0.67	1.12	1.56	2.42
120	0.43	0.96	1.41	2.32
150	0.02	0.71	1.17	2.17
180	0.01	0.38	1.01	1.94
210	0.01	0.35	0.98	1.81
240	0.02	0.35	0.98	1.82

Appendix 20: Effect of Concentration of lead (ii) ions adsorption

Time (min)	**Pb^{2+} Concentrations (ppm)**			
0	30.00 ppm	20.00 ppm	10.00 ppm	5.00 ppm
30	27.39	17.13	7.89	2.93
60	24.34	15.32	4.12	0.543
90	24.81	13.27	3.45	0.042
120	21.48	11.59	1.68	0.002
150	20.27	10.42	0.89	0.001
180	20.016	10.02	0.018	0.001
210	20.014	10.01	0.019	0.001
240	20.015	10.016	0.018	0.001

Appendix 21: Effect of adsorbent dosage (grams) on adsorption
Pb^{2+} ion

Dosage of Zeolite	**Grams**	**0.3g**	**0.5g**	**0.8g**	**1g**	**1.5g**	**2g**
pb^{2+}	Co	10	10	10	10	10	10
	Ce	4.23	1.74	1.35	0.016	0.53	1.68
	%	57.7	82.6	86.7	99.8	94.7	83.2

Cd^{2+} ion

Dosage of Zeolite		**0.3g**	**0.5g**	**0.8g**	**1g**	**1.5g**	**2g**
Cd^{2+}	Co	1.5	1.5	1.5	1.5	1.5	1.5
	Ce	1.15	0.956	0.779	0.35	0.62	0.812
	%	23.4	36.0	48.1	76.7	58.7	46.3

Dosage of Zeolite	**0.3g**	**0.5g**	**0.8g**	**1g**	**1.5g**	**2g**
Pb^{2+}	57.7	82.6	86.7	99.8	94.7	83.2
Cd^{2+}	23.4	36.0	48.0	76.7	58.7	46.3

Appendix 22: UV-Vis spectra of pesticides compounds (a) chlorpyrifos (b) diuron and (c) imidacloprid

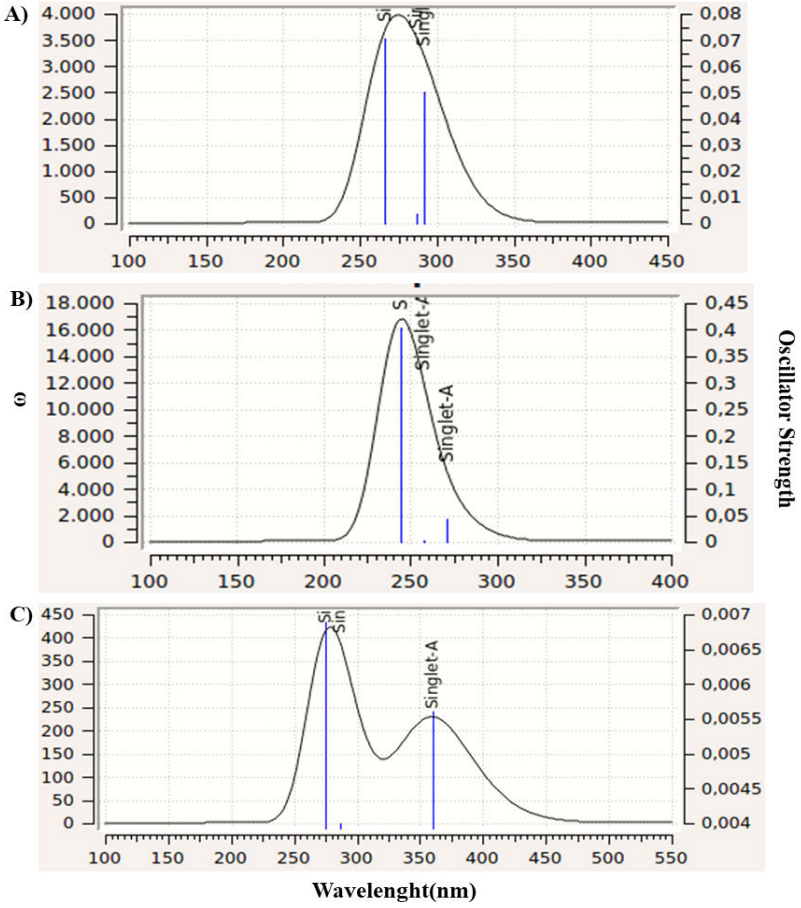

Appendix 23: Chromogram for ciprofloxacin (a) before and (b) after adsorption

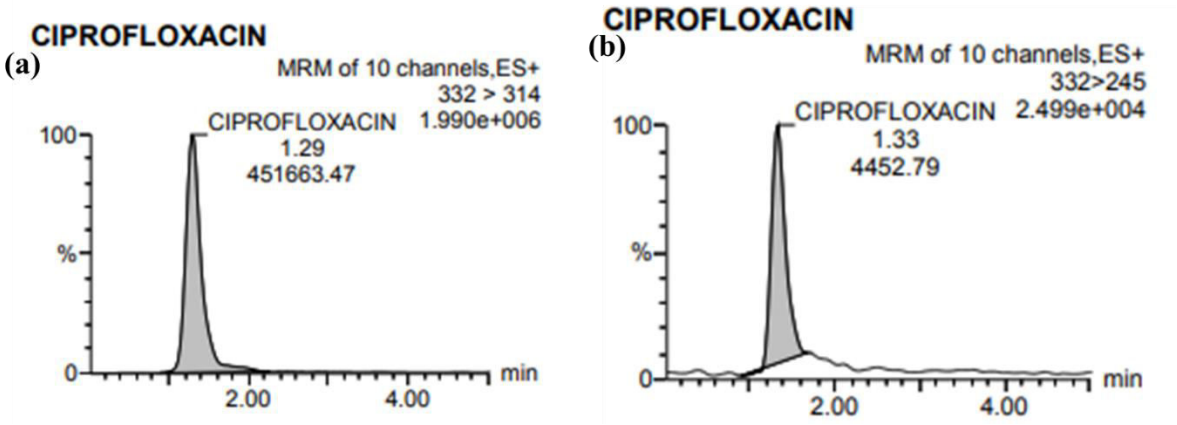

Appendix 24: The LC-MS/MS chromatogram of Imidacloprid (a) before and (b) after adsorption for imidacloprid from real water.

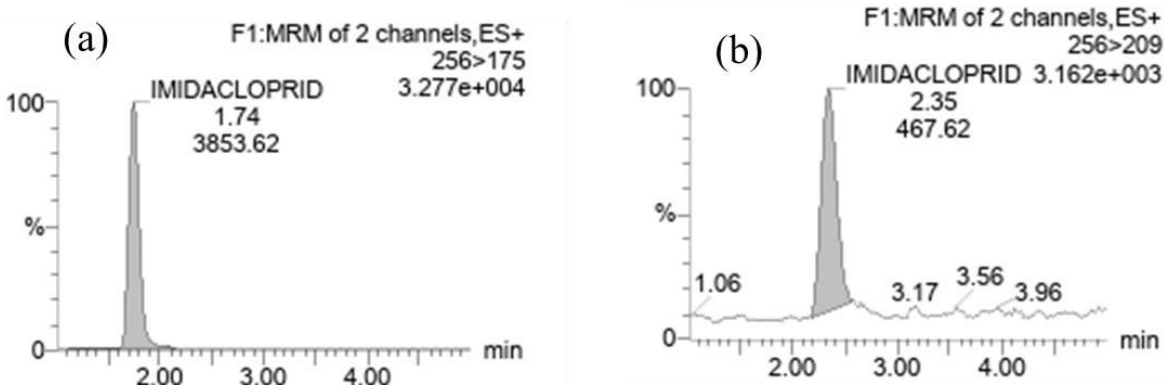

Appendix 25 Calibration curve for (a) Imidacloprid and (b) Chlorpyrifos

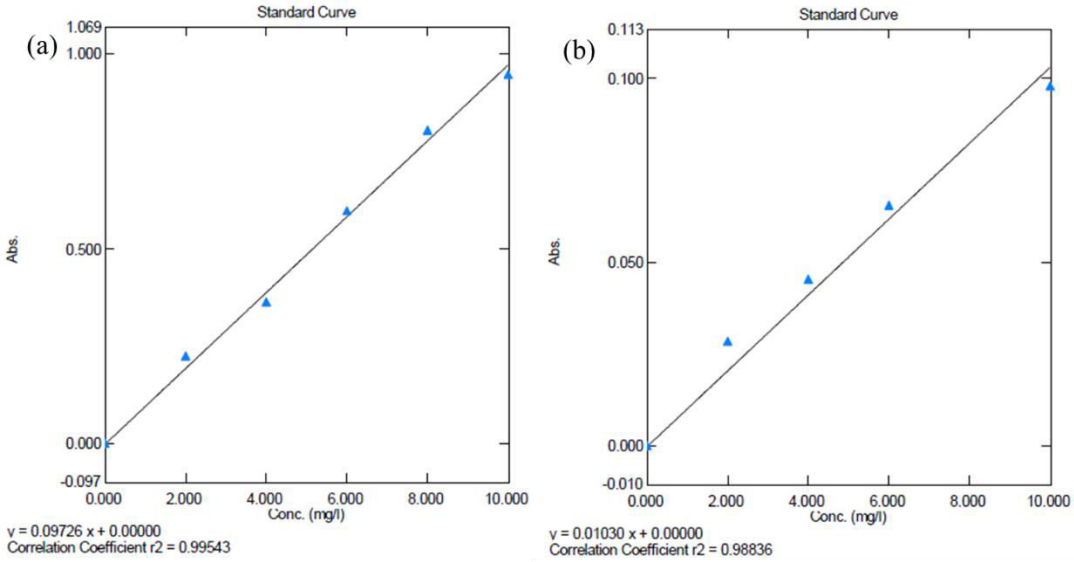

Appendix 26: First published paper

Research Article

Computational screening of zeolites for the adsorption of selected pharmaceutical pollutants

Fred Sifuna Wanyonyi[1] · Anthony Pembere[2] · Gershom Kyalo Mutua[1] · Francis Orata[1] · Hitler Louis[3]

Received: 28 August 2020 / Accepted: 13 October 2020 / Published online: 27 October 2020

Abstract
Molecular simulations have been used as a screening tool to identify promising zeolites for the removal of selected pharmaceutical pollutants. 40 zeolites with different structural and chemical configurations were studied. Galophosphate cloverite (CLO) of the chemical formula, $F_{24}Ga_{96}P_{96}O_{372}(OH)_{24}$, with pores of 20 rings and the lowest observed bulk density, showed exceptionally preferred adsorption of diclofenac [2-(2,6-dichlorophenyl)amino benzeneacetic acid), ciprofloxacin [1,3,7-Trimethylpurine- 2,6-dione] and chloramphenicol [2,2-dichloro-N-[(IR,2IR)-1, 3-dihydroxy-1-(4-nitrophenyl) propan-2-yl acetamide]. This selectivity was attributed to the geometry and structural composition of the cavities. We also investigated the most stable adsorbed compositions of the pollutants in the CLO zeolite. Our calculations show that diclofenac, ciprofloxacin and chloramphenicol molecules are adsorbed into the pores with adsorption energies of − 78.23, − 173.68 and − 84.46 kcal/mol respectively. Additional calculations were also made to obtain detailed information on desorbed products. It is seen that dechlorination is the most energetically preferred process compared to dehydrogenation and dehydroxylation.

Keywords Monte Carlo simulation · Adsorption isotherms · Pharmaceutical pollutants · Zeolites

Appendix 27: Second published paper

Contents lists available at ScienceDirect

Computational Materials Science

journal homepage: www.elsevier.com/locate/commatsci

Role of pore chemistry and topology in the heavy metal sorption by zeolites: From molecular simulation to machine learning

Fred Sifuna Wanyonyi [a,1], Timothy Tizhe Fidelis [b,1], Gershom Kyalo Mutua [a], Francis Orata [a], Anthony M.S. Pembere [c,*]

[a] Department of Pure and Applied Chemistry, Masinde Muliro University of Science and Technology, P.O Box 190, Kakamega 50100, Kenya
[b] Institute of Chemistry, Chinese Academy of Science, Beijing 100190, China
[c] Department of Physical Sciences, Jaramogi Oginga Odinga University of Science and Technology, P.O BOX 210, Bondo 40601, Kenya

ARTICLE INFO

Keywords:
Monte Carlo simulation
Machine leaning
Adsorption isotherms
Heavy metals
Zeolites

ABSTRACT

Zeolite frameworks can provide pores that enable selective heavy metals sorption, making these materials promising for energy-efficient heavy metals capture. In the present study, the adsorption of hazardous heavy metal ions on 242 zeolites have been investigated by employing molecular simulations and machine learning techniques, where the role of pores, topology, and chemical characteristics in the heavy metal sorption has been examined. The molecular simulation results show that only the zeolites with high diameter of pores exhibited appreciable loading of the cations. To unravel the encoded chemical information of the three parameters (total energy, pore size and average volume) on how each influence the loading capacity of the heavy metals, boruta algorithm; a wrapper based built around random forest classier was employed to rank these parameters. In light of the forgoing, total energy accounts for the highest contribution for the sorption of heavy metals. Compared to the pore size, the average volume was rejected by the random forest classier algorithm, which implies that the individual pore size on the surface of each of the best performing zeolite framework is responsible for the adsorption of heavy metals with relatively high sphere diameter instead of total volume of each zeolite.

Appendix 28: Third published paper

Journal of Molecular Liquids

journal homepage: www.elsevier.com/locate/molliq

Simulation guided prediction of zeolites for the sorption of selected anions from water: Machine learning predictors for enhanced loading

Fred Sifuna Wanyonyi [a], Timothy Tizhe Fidelis [b,c], Hitler Louis [d], Gershom Kyalo Mutua [a], Francis Orata [a], Lydia Rhyman [e,f], Ponnadurai Ramasami [e,f], Anthony M.S. Pembere [f,*]

[a] Department of Pure and Applied Chemistry, Masinde Muliro University of Science and Technology, P.O. Box 190, Kakamega 50100, Kenya
[b] Institute of Chemistry, Chinese Academy of Science, Beijing 100190, China
[c] Computational Quantum Chemistry Research Group, Department of Pure and Applied Chemistry, Faculty of Physical Sciences, University of Calabar, 1115 Calabar, Nigeria
[d] Computational Chemistry Group, Department of Chemistry, Faculty of Science, University of Mauritius, Réduit 80837, Mauritius
[e] Centre of Natural Product Research, Department of Chemical Sciences, University of Johannesburg, Doornfontein Campus, Johannesburg 2028, South Africa
[f] Department of Physical Sciences, Jaramogi Oginga Odinga University of Science and Technology, P.O. Box 210, Bondo 40601, Kenya

ARTICLE INFO

Article history:
Received 10 November 2021
Revised 20 February 2022
Accepted 9 March 2022
Available online 18 March 2022

Keywords:
Monte Carlo Simulation
Anions
Zeolites
Machine Learning

ABSTRACT

The development of highly efficient adsorbents, especially those that can harvest anions like CrO_4^{2-}, AsO_4^{3-}, NO_3^- and PO_4^{3-}, is one of the principal challenges in the water treatment field. The current study utilized a screening process involving an initial selection of zeolites based on the pore-limiting diameter, followed by GCMC (Grand Canonical Monte Carlo) simulations to identify high-performing zeolites for anion removal. CLO, LTN, MWF, TSC, ITV, PAU, FAU and DFO zeolites are the best performing in terms of loading while several zeolites like ANA, DFT, BIK, SBN and JNT gave no loading at all. In addition, quantum chemical calculations revealed that after adsorption of the anions on the zeolite, there is charge transfer between the zeolite and the anion. The CLO cluster has a charge of 0.64 before adsorption. After adsorption, it attains a charge of −0.06, suggesting that the phosphate ion acts as an electron donor while the CLO cluster, as an electron acceptor. Finally, machine learning was employed to rank the importance of the various descriptors that have influence on the removal of anions in water. Largest overall cavity diameter, mass and accessible pore volume appeared to be the three most important descriptors, thus, tuning the sphere cavity and inter channel diameter as well as engineering the accessible volume of zeolite architectures are of utmost important toward harvesting the desired anions.

Appendix 29: Accepted paper: Heliyon

Heliyon 10 (2024) e34657

Contents lists available at ScienceDirect

Heliyon

journal homepage: www.cell.com/heliyon

Research article

Application of South African heulandite (HEU) zeolite for the adsorption and removal of Pb^{2+} and Cd^{2+} ions from aqueous water solution: Experimental and computational study

Fred S. Wanyonyi [a], Francis Orata [a], Gershom K. Mutua [a], Michael O. Odey [b], Sizwe Zamisa [d], Sopuruchukwu E. Ogbodo [b,*], Francis Maingi [e], Anthony Pembere [c,**]

[a] Department of Pure and Applied Chemistry, Masinde Muliro University of Science and Technology, P.O Box 190, Kakamega, 50100, Kenya
[b] Computational and Bio-Simulation Research Group, University of Calabar, Calabar, Nigeria
[c] Department of Physical Sciences, Jaramogi Oginga Odinga University of Science and Technology, P.O Box 210, Bondo, 40601, Kenya
[d] School of Chemistry and Physics, University of Kwazulu-Natal, Westville Campus, Private Bag X 54001, Durban, 4001, South Africa
[e] Department of Science, Technology and Engineering, Kibabii University, PO Box 1699, Bungoma, 50200, Kenya

ARTICLE INFO

Keywords:
Adsorption
Pb^{2+}
Cd^{2+}
Heulandite zeolite
Isotherms
Molecular simulation

ABSTRACT

The capacity of South African Heulandite (HEU) zeolite to remove Pb^{2+} and Cd^{2+} ions from aqueous solution was investigated using batch experiments and molecular simulations studies. The effect of different factors on the adsorption of these ions onto the zeolite was investigated; contact time, initial metal ion concentration and the amount of HEU adsorbent. Molecular simulations was done using Monte Carlo and density functional theory. Experimental results obtained indicate that the maximum adsorption for the two ions occur at pH 5 and after 240 min of contact time. The percent removal based on contact time of Pb^{2+} and Cd^{2+} ions from water by the heulandite zeolite were 99.7 and 76.7 %, respectively. The adsorption of two metal ions onto the HEU zeolite follows the Langmuir adsorption isotherm. From the molecular simulation findings, the adsorption of Pb^{2+} ions onto the HEU window is equidistant from the two adjacent oxygen atoms within the HEU structure while the Cd^{2+} ion is adsorbed in the upper left side of the 8-ring HEU window. It was observed that the performance of the zeolite can significantly be improved by doping with germanium, aluminum, thallium indium, and sodium cations. These results indicate that the application of HEU zeolite as an adsorbent holds a great promise in heavy metal removal from aqueous solutions.

Appendix 30: Paper published

Unlocking the adsorptive effectiveness of naturally occurring heulandite zeolite for the removal of PO_4^{3-} and NO_3^- anions from wastewater.

Fred Sifuna Wanyonyi[1], Francis Orata[1], Ponnadurai Ramasami[2,3], Emily Ngeno[1,5], Victor Shikuku[5], Robert O. Gembo[6], Gershom Kyalo Mutua[1], Anthony Pembere[4]*.

[1]*Department of Pure and Applied Chemistry, Masinde Muliro University of Science and Technology, P.O Box 190 Kakamega 50100, Kenya*

[2]*Computational Chemistry Group, Department of Chemistry, Faculty of Science, University of Mauritius, Réduit 80837, Mauritius*

[3]*Centre for Natural Product Research, Department of Chemical Sciences, University of Johannesburg, Doornfontein 2028, South Africa*

[4]*Department of Physical Sciences, Jaramogi Oginga Odinga University of Science and Technology, P.O Box 210 Bondo 40601, Kenya*

[5]*Department of Physical Sciences, Kaimosi Friends University, P.O BOX 385-50309, Kaimosi. Kenya*

[6]*Institute for Nanotechnology and Water Sustainability (iNanoWS), College of Science, Engineering and Technology (CSET), University of South Africa, Florida Science Campus, Johannesburg, South Africa*

*Correspondence Email:apembere@jooust.ac.ke

Abstract

The mitigation of high levels of phosphate (PO_4^{3-}) and nitrate (NO_3^-) and ions in water bodies, particularly in agricultural wastewater, holds paramount importance in curbing eutrophication within aquatic ecosystems. Herein, using experimental and computational techniques, the study explored the potential of naturally occurring South Africa heulandite (HEU) zeolite for the removal of PO_4^{3-} and NO_3^- ions from synthetic wastewater in batch mode. The percentage removal of PO_4^{3-} and NO_3^- was 59.15 and 51.39 %, respectively, whereas the corresponding maximum adsorption capacity of the adsorbent was 0.0236 and 0.0206 mg/g. The adsorption kinetics of both anions by HEU fitted well in the pseudo-first order (PFO) kinetics model indicating a physisorption-mediated rate-determining step. It was revealed that the adsorption process was multi-mechanistic spontaneous and

exothermic. Molecular simulations using Monte Carlo (MC) and density functional theory (DFT) methods also provided insights into the adsorption mechanisms.

Keywords: Adsorption; Anions; Zeolites; Molecular simulation; Thermodynamic parameters